



Kent Academic Repository

Antonio Sanz-Izquierdo, Benito (2006) *Compact multiband antennas for wireless systems*. Doctor of Philosophy (PhD) thesis, University of Kent.

Downloaded from

<https://kar.kent.ac.uk/94637/> The University of Kent's Academic Repository KAR

The version of record is available from

<https://doi.org/10.22024/UniKent/01.02.94637>

This document version

UNSPECIFIED

DOI for this version

Licence for this version

CC BY-NC-ND (Attribution-NonCommercial-NoDerivatives)

Additional information

This thesis has been digitised by EThOS, the British Library digitisation service, for purposes of preservation and dissemination. It was uploaded to KAR on 25 April 2022 in order to hold its content and record within University of Kent systems. It is available Open Access using a Creative Commons Attribution, Non-commercial, No Derivatives (<https://creativecommons.org/licenses/by-nc-nd/4.0/>) licence so that the thesis and its author, can benefit from opportunities for increased readership and citation. This was done in line with University of Kent policies (<https://www.kent.ac.uk/is/strategy/docs/Kent%20Open%20Access%20policy.pdf>). If you ...

Versions of research works

Versions of Record

If this version is the version of record, it is the same as the published version available on the publisher's web site. Cite as the published version.

Author Accepted Manuscripts

If this document is identified as the Author Accepted Manuscript it is the version after peer review but before type setting, copy editing or publisher branding. Cite as Surname, Initial. (Year) 'Title of article'. To be published in **Title of Journal**, Volume and issue numbers [peer-reviewed accepted version]. Available at: DOI or URL (Accessed: date).

Enquiries

If you have questions about this document contact ResearchSupport@kent.ac.uk. Please include the URL of the record in KAR. If you believe that your, or a third party's rights have been compromised through this document please see our [Take Down policy](https://www.kent.ac.uk/guides/kar-the-kent-academic-repository#policies) (available from <https://www.kent.ac.uk/guides/kar-the-kent-academic-repository#policies>).

Compact Multiband Antennas for Wireless Systems

A Thesis Submitted to The
University of Kent at Canterbury
In the Subject of Electronic Engineering
For the Degree
of Doctor of Philosophy

By

Benito Antonio Sanz-Izquierdo
December 2006

To My Family & Gosia

Abstract

The research work to be presented focuses on the study of multiband antennas for wireless indoor communications and wearable transceivers. An introduction to the essential antenna parameters and the theory behind the electromagnetic simulators used for this research sets the background necessary for understanding the procedure used when designing and measuring antennas. A study of the characteristics of textile materials at microwave frequencies using non-resonant transmission methods is later performed. The basis of small antenna design by top loading and the design of the Planar Inverted F Antenna is also covered.

The main research work is divided into two parts. The first part investigates antennas for mobile and wireless indoor communications networks. The antennas are intended for Distributed Antenna Units to be located in buildings. A dual band Planar Inverted F antenna previously developed at the University of Kent is chosen as the prototype to achieve multiband and broadband operations. A parasitic resonator on the ground plane and side resonators are introduced in a study where additional bands are added. The derivation of equivalent function planar antennas from three dimensional multiband PIFAs is also covered.

The second part of the work focus on antennas for wearable applications. The antennas are intended for WLAN on-body communication networks. A novel approach is taken by using metallic button structures to create wearable antennas. Dual frequency band operation is achieved on the button structures by adding a metallic plate on the top of the antenna and a cylindrical via connector. Miniaturization techniques are later applied to the button structure to reduce the size of the antenna while maintaining a match at the 2.4GHz and 5 GHz wireless bands.

Benito Antonio Sanz-Izquierdo

December 2006

Acknowledgements.

I would like to express special gratitude to my supervisor John Batchelor for his guidance, valuable advice and support throughout my research work.

I am also grateful to Prof. Richard Langley, Prof. M. Sobhy, Dr. Nathan Gomes and Dr. Paul Young for their assistance and advice on antennas and microwave devices, measurement techniques, communication systems and electromagnetic simulators.

Thank you also to Dr. Lester Low, Simon Tse, Freddy Koning, Dr. Steve Savia, Ignacio Garcia, Fengxi Huang, Anthony Nkansah, Anjali Das for their valuable technical information and support regarding electromagnetic simulators, antennas, microwaves and communications systems. Also thanks to Chidi Diugwu, John Miller, Nike Folayan, Dr. Charan Litchfield, Dr. Huiling Zhu, Dr Thomaskutty Mathew, Sharon & Simon Bai and all the colleagues in the antennas lab and ex-MSc students who have made my stay at the University enjoyable.

Thank you to Nigel Simpson, Simon Jakes, Clive Birtch, Nigel Bourner and Terry Rockhill for their excellent assistance regarding resources, mechanical aspects of the research and measurement techniques.

Finally, thank you to Gosia for her support and understanding which has helped me to be focused and organized during my research work. Thank you to my parents; Amancio Sanz-Ruiz and Alicia Izquierdo-Perez for providing me continuous encouragement throughout my career, and my sisters: Alicia and Dioni for their constant support.

Publications Arising From This Work.

1. B. Sanz-Izquierdo, J.C. Batchelor, R.J. Langley “Multiband PIFA Antenna with Ground plane Capacitive Resonator” IEE Electronic Letters, Vol. 40, pp. 1391-1392, October 2004
2. B. Sanz-Izquierdo, J.C. Batchelor, R.J. Langley, “Multiband Printed PIFA Antennas for Wireless Picocell Base Stations”, IEEE International Workshop on Antenna Technology (IWAT), Singapore, March 2005
3. B. Sanz-Izquierdo, J.C. Batchelor, R.J. Langley “Broadband Multi-Function Planar PIFA Antenna”, LAPC Conference, Loughborough, pp. 209-212, April 2005
4. B. Sanz-Izquierdo, F. Huang and J.C. Batchelor “Dual-Band button antennas for wearable applications”, IEEE IWAT 2006, New York, March 2006
5. B. Sanz-Izquierdo, F. Huang and J.C. Batchelor, “Wearable Dual Band Button Antennas”, LAPC Conference, Loughborough, pp. 209-212 April 2006
6. B. Sanz-Izquierdo, F. Huang and J.C. Batchelor, “Dual Band Wearable PIFA”, LAPC Conference, Loughborough, pp. 209-212, April 2006
7. B. Sanz-Izquierdo, J.C. Batchelor, R.J. Langley and M.I. Sobhy, “Single and Double Layer Planar Multiband PIFAs”, IEEE Transactions on Antennas and Propagation, Vol.54, No.5, pp.1416-1422, May 2006
8. B. Sanz-Izquierdo, F. Huang, J.C. Batchelor “Covert Dual-Band Wearable Button Antenna”, IEE Electronics Letters, Vol.42, No.12, pp. 668-670, June 8 2006
9. B. Sanz-Izquierdo, F. Huang, J.C. Batchelor, M.I. Sobhy “Compact Antenna for WLAN On-Body Applications”, 35th European Microwave Conference, Manchester, September 2006
10. M.I. Sobhy, B. Sanz-Izquierdo, J.C. Batchelor “System and Circuit Models for Microwave Antennas” 35th European Microwave Conference, Manchester, September 2006
11. B. Sanz-Izquierdo, F. Huang, J.C. Batchelor, “Small Size Wearable Button Antenna”, European Conference on Antennas and Propagation EuCAP06, Nice, France, p. 39, November 2006
12. B. Sanz-Izquierdo, M.I. Sobhy, J.C. Batchelor, “UWB Wearable Button Antenna”, European Conference on Antennas and Propagation EuCAP06, Nice, France, p. 131, November 2006

CONTENTS

Abstract	iii
Acknowledgments	iv
Publication Arising From This Work	v
1. Introduction	1
2. Theoretical Background and Simulation Techniques	7
2.1 Basic Antenna Theory	8
2.1.1 Scattering	8
2.1.2 Radiation Patterns	9
2.1.3 Directivity and Gain	10
2.2 Electromagnetic Simulators	11
2.2.1 IE3D and Method of Moments	12
2.2.2 CST Microwave Studio and Finite Integration Method	14
2.2.3 Comparison between IE3D and CST Microwave Studio	17
References	17
3. Dielectric Measurements and Small Antenna design	19
3.1 Methods of Measuring the Permittivity of Substrates	20
3.1.1 Waveguide method for measuring dielectric textiles	21
3.2 Small Antenna Designs	24
3.2.1 Top Loaded Monopoles	24
3.2.2 Planar Inverted F Antenna	27
3.3 Conclusions	28
References	29

4. Multiband Antennas for Wireless indoor communications	31
4.1 Introduction	31
4.2 Multiband Antennas	33
4.3 Multiband Antenna with Ground Plane Parasitic Resonator	34
4.3.1 Dimensions	36
4.3.2 Measurement Results, Reflection Coefficient	36
4.3.3 Surface Currents	38
4.3.4 Parametric Analysis	40
4.3.5 Radiation Patterns	43
4.4 Multiband Antenna with Side Resonators	47
4.4.1 Dimensions	47
4.4.2 Measurement Results, Reflection Coefficient	48
4.4.3 Surface Currents	49
4.4.4 Parametric Analysis	51
4.4.5 Radiation Patterns	55
4.5 Multiband Antenna with Multi-resonators	59
4.5.1 Dimensions	59
4.5.2 Measurement Results, Reflection Coefficient	60
4.5.3 Surface Currents	61
4.5.4 Parametric Analysis	63
4.5.5 Radiation Patterns	68
4.6 Conclusions	72
References	72
5. Multiband Planar Antennas	74
5.1 Introduction	74
5.2 Multiband Planar Antennas	76
5.3 PIFA Transposition to Planar Form	77
5.3.1 Initial Simulations of the Transposed PIFA	79
5.4 Multiband Planar Antenna on Thin Dielectric Substrate	81
5.4.1 Dimensions	82
5.4.2 Measurement Results, Reflection Coefficient	82
5.4.3 Surface Currents	84

5.4.4	Radiation Patterns	85
5.5	Single Sided Multi-band Planar PIFA on FR4 substrate	88
5.5.1	Dimensions	88
5.5.2	Measurement Results, Reflection Coefficient	89
5.5.3	Surface Currents	90
5.5.4	Double Sided Simulation Study	92
5.6	Double layer Multiband Planar PIFA	93
5.6.1	Dimensions	94
5.6.2	Measurement Results, Reflection Coefficient	95
5.6.3	Surface Currents	97
5.6.4	Parametric Analysis	100
5.6.5	Radiation Patterns	105
5.7	Conclusions	109
	References	109
6.	Wearable Antennas	111
6.1	Introduction	111
6.2	Materials Characterisation	112
6.3	Single Band Metallic Button Antenna (SBMBA)	114
6.3.1	SBMBA Dimensions	115
6.3.2	SBMBA Measured Results, S11	117
6.3.3	SBMBA Surface Currents	117
6.3.4	SBMBA Parametric Analysis	118
6.3.5	SBMBA Radiation Patterns	122
6.4	Dual Band Metallic Button Antenna	123
6.4.1	DBMBA Dimensions	124
6.4.2	DBMBA Measured Results, S11	126
6.4.3	DBMBA Surface Currents	127
6.4.4	DBMBA Parametric Analysis	128
6.4.5	DBMBA Equivalent Circuit Model	135
6.4.6	DBMBA Radiation Patterns	137

6.5 Dual Band Metallic Button Antenna with Microstrip Feed	140
6.5.1 DBMBA with Microstrip Feed – Dimensions	140
6.5.2 DBMBA with Microstrip Feed –Measured Results, S11	142
6.5.3 DBMBA with Microstrip Feed – Radiation Patterns	144
6.6 Conclusions	147
References	147
7. Optimization and Miniaturization of Wearable Antennas	149
7.1 Introduction	149
7.2 DBMBA using a Standard Metallic Button	150
7.2.1 DBMBA using a SMB- Dimensions	151
7.2.2 DBMBA using a SMB – Measured Results, S11	152
7.2.3 DBMBA using a SMB –Surface Currents	154
7.2.4 DBMBA using a SMB- Parametric Analysis	156
7.2.5 DBMBA using a SMB – Radiation Patterns	159
7.3 Miniature Ground Shorted DBMBA	162
7.3.1 Miniature Ground Shorted DBMBA –Dimensions	164
7.3.2 Miniature Ground Shorted DBMBA – Results, S11	165
7.3.3 Miniature Ground Shorted DBMBA –Surface Currents	167
7.3.4 Miniature Ground Shorted DBMBA – Parametric analysis	169
7.3.5 Miniature Ground Shorted DBMBA – Radiation patterns	176
7.4 Summary of Button antennas	179
7.5 Conclusions	181
References	182
8 Conclusions and Future Work	183
8.1 Electromagnetic Simulators	184
8.2 Multiband Antennas for Indoor Communication Systems	185
8.3 Multiband Antennas for Wearable Applications	186
8.4 Future Work on Multiband and Wearable Antennas	187

Chapter 1.

Introduction

Wireless communications have experienced fast growth over the last few decades. This growth has been driven by the rapid development of systems such as: GSM, 3G-UMTS, CDMA2000, Bluetooth- WLAN, hiperlan systems [1] and the strong demand for mobile voice and data services. Mobile communication systems such as: GSM900, DCS1800 and UMTS have been typically supplied by Basestations located on the roof of building or in high towers, creating a cellular system. Recent years, however, have seen an increase in demand for broadband services while on the move. This demand for data services has required closer basestations, creating microcells or even picocells [2]. Picocell basestations are designed to serve a very small area, such as part of a building, a street corner, or an aeroplane cabin.

Wireless networks using the 2.4GHz and 5.25 GHz frequency bands are seen as the most cost effective solution for wireless computing within buildings and commercial

centres with access points that are typically spread around a building and connected directly to the IP network.

Novel approaches to provide wireless computing and mobile communications services within buildings have appeared in recent years. Some tend to provide both services from the same access point and transmit low power. The access points are distributed antenna units which are connected to a common basestation [3]. Distributed antennas systems would typically need multiband antennas working with several communication systems at the same time.

1.1 Multiband antennas for wireless indoor communications

The requirements for antennas working in indoor environments (shopping malls, train stations, public places) are typically less stringent than those outdoors. The reason for that is the rich multipath characteristic of indoor environments that makes the need for single polarization unnecessary.

This work places its emphasis on designing multiband antennas able to operate in an indoor environment and work at as many commercial and wireless systems as possible. The frequency bands targeted for the multiband antennas in this research work have been specifically:

- GSM900 (890-960 MHz) [Europe]
- DCS1800 (1710-1880 MHz) [Europe]
- DECT (1880-1990 MHz) [Europe]
- UMTS (1900–2200 MHz) [Europe]
- Bluetooth (2400 – 2500 MHz, varies between countries) [International]
- Hiperlan bands (5150GHz - 5150-5350, 5470-5725, spectrum used varies between countries) [International]

The multiband antennas in chapters four and five have been developed for a research project entitled “Radio-optical systems Engineering in Transmanche Telecom”(Rosette). The research project covered all aspects in the development of inexpensive technology for antenna units in the distributed antenna systems in radio over fibre Networks with the final work published in [4] and UK patent ... applied for.

Multiband operation was studied in a single antenna for mobile handsets in [5] where a quad-band antenna was achieved by connecting two extra resonators directly to the feed.

Dual band antennas suitable for indoor communications were successfully realised with planar inverted-F antennas in previous development by D.Viratelle and R.J.Langley [6] at the University of Kent. The antennas, initially intended for automotive applications, had two wide band resonant modes and omnidirectional radiation patterns which made them appropriate for the initial study in multiband antennas.

1.2 Wearable antennas

Wearable antennas have been traditionally used at the UHF and TETRA bands for military and emergency services applications. Currently, there is an ongoing trend to add consumer electronics into everyday clothing; i.e: MP3 players that can be sewn directly into shirts or jackets [7] or even shoe trainers [8] with sensors that send pulses wireless on every step to a mp3 player.

On body propagation channels have already been studied and characterised for narrowband [9] and UWB [10] communication systems aiming to understand device to device links as part of a wearable area network (WAN).

Antennas designs for wearable applications have been developed mainly on textile materials, for example metal patches in [11 and 12] and with probe feeds and linear polarization or in [13] with a microstrip feed and circular polarization.

The totally novel approach is taken in the second part of this literature studying the use of metallic buttons as means of radiating structures for wearable applications.

1.3 Thesis Outline

This thesis “Compact Multiband Antennas for Wireless Communications” summarises the research work carried out by the author on multiband antennas for wireless indoor communications and wearable transceivers.

The author begins by providing a general introduction to indoor communication systems and planar inverted F antennas suitable for the environment. It follows with a review on wearable technology, looking at the current trend on wearable electronics and antennas being developed for wearable on body applications. Chapter One is concluded with the Outline of the thesis.

Chapter Two provides a general theoretical background to antenna technology and electromagnetic simulators. It firstly reviews the parameters involved in the design and measurement antennas, such as, S parameters, resonant frequency, bandwidth, input impedance, radiation pattern, polarisation, gain and efficiency. It follows with a discussion on commercial electromagnetic simulators, the methods used in the simulators and the reasons for choosing specific simulators for antenna design.

Chapter Three considers the explicit theory concerning the research study. Firstly, it looks at methods of calculating dielectric permittivity of materials and the method used for calculation of dielectric permittivity of textile substrates. The second part looks at the theory concerning planar inverted F antennas and top loaded monopoles, the two antenna types mostly used in this research work. It finalises with a study of parasitic resonators and the conclusion of the chapter.

Chapter Four studies bandwidth enhancements on a dual band planar inverted F antenna previously developed at the University of Kent [6]. The chapter begins with an introduction on distributed antennas systems and multiband antennas. It follows with the development of a novel technique for bandwidth enhancement of dual band antennas using ground plane parasitic resonators. It continues with a further improvement of the antenna by adding commonly used side resonators. The antenna is finally optimized by rearranging the side resonators and by side extending part of the ground plane.

Chapter Five investigates the transformation of the multiband antenna with a parasitic resonator developed in chapter four into a uni-planar antenna. The first part of the chapter looks at the issues concerning the transformation from a three dimensional antenna into a planar form. It shows how current modes cancelled in the first transformed antenna can be re-established to obtain good input matching by the

rearrangement of the different metal segments of the uni-planar antenna. The second part of the chapter studies the issues concerning the balancing problems at the lower frequency band of the uni-planar antenna and the development of a double layer design to improve the balance. An optimized version of the antenna is finally presented which is able to cover all the systems targeted in section 1.1 of this chapter.

Chapter Six provides an introduction on wearable technology and studies the use of metallic buttons as wearable antennas. The introduction on wearable technology reviews existing wearable technology and previous work done on wearable antennas. It follows with the study and development of a single band metallic button antenna. A further dual frequency version of the metallic button structure is later developed and studied. The dual band version is finally fed by a microstrip transmission line and studied on the human body. The human body study is done through simulation and computational analysis of the S-parameters and radiation patterns of the antenna.

Chapter Seven optimizes the dual band metallic button structure developed in chapter six and presents a novel small size dual band metallic button. The first dual band antenna presented in the chapter is a version of the dual band metallic button antenna in which the top plate connection has been shifted to fit to any solid metallic button. The second and final metallic button antenna uses dielectric material between the top plates and the connection of a centre wire to ground which increases the rigidity of the structure and miniaturizes the antenna while maintaining the two operational bands. A summary table at the end of the chapter provides information about the four metallic button antennas presented in the current research work.

Chapter Eight concludes the work and looks at future developments. The key subjects of the research thesis are summarized and concluded in this chapter. Emphasis is done on future antenna developments for wearable applications.

References

- [1] Hsiao-Hwa Chen , Mohsen Guizani , “Next Generation Wireless Systems and Networks”, John Wiley & Sons, Inc, 2006
- [2] Hamed Al-Raweshidy, Shozo Komaki “Radio Over Fiber Technologies for Mobile Communications Networks”, Chapter 4, pp.186, Artech House, Inc, 2002
- [3] Hamed Al-Raweshidy, Shozo Komaki “Radio Over Fiber Technologies for Mobile Communications Networks”, Chapter 5, pp.231, Artech House, Inc, 2002
- [4] A. Das, A. Nkansah, N.J. Gomes, J.C. Batchelor, D. Wake “Design of Low Cost Multimode Fiber-Fed Indoor Wireless Networks” IEEE Microwave Theory and Techniques, Vol.54, pp. 3426-3432, August 2006
- [5] Yong-Xin, Michael Yan Wah Chia, and Zhin Ning Chen, “Miniature Built-In Multiband Antennas for Mobile Handsets”, IEEE Trans. Antennas Propag. Vol.52, No.8, August 2004, pp. 1936-1943
- [6] Viratelle, D. and Langley, R.J.: “Dual-Band Printed Antenna for Mobile Telephone Applications”, IEE P-Micro., Anten. & Propag., 147, (5), pp.381-384, Oct. 2000.
- [7] J.G. Spooner, “Infineon gets musical with MP3 jacket,” April 27, 2002, 07:31 BST, <http://news.zdnet.co.uk/hardware/chips/0,39020354,2109243,00.htm>
- [8] <http://www.nike.com/nikeplus>
- [9] Y. Nechayev, P. Hall, C. C. Constantinou, Y. Hao, A. Owadally, and C.G. Parini, “Path loss measurements of on-body propagation channels,”in *Proc. 2004 Int. Symp. Antennas and Propagation*, Sendai, Japan, pp. 745–748.
- [10] A. Alomainy; Y.Hao; C.G. Parini; P.S Hall, “Comparison between two different antennas for UWB on-body propagation measurements”, *IEEE Antennas and Wireless Propagation Letters Volume 4, 2005 Page(s):31 – 34*
- [11] P. Salonen; Kim Jaehoon; Y. Rahmat-Samii; “Dual-band E-shaped patch wearable textile antenna”, IEEE Antennas and Propagation Society International Symposium, Volume 1A, 3-8 , p.p. 466 - 469, 2005
- [12] M. Tanaka and J.-H. Jang, “Wearable microstrip antenna”, *IEEE Antennas and Propagation Society International Symposium*, vol: 2, June 2003, pp. 704-707.
- [13] Maciej Klemm, Ivo Locher, Gerhard Tröster “A Novel Circularly Polarized Textile Antenna for Wearable Applications”, *The 34rd European Microwave Conference (EuMC)*, Amsterdam, Netherlands, 11-14 October 2004

Chapter 2.

Theoretical Background and Simulation techniques

The basic antenna theory necessary for antenna design and analysis and the different electromagnetic simulation methods used in the developing of the antennas for this work are covered in this chapter. The aim is to set up a background which defines the parameters considered when designing antennas such as: S-parameters, input impedance, radiation patterns, gain and efficiency. The practical calculation and representation of the main antenna parameters will also be covered. Finally, the theory related to general electromagnetic software modelling and specifically for the software packages used in this research work will be discussed.

2.1 Basic Antenna Theory

Antennas, defined in [1] as a “means of radiating or receiving electromagnetic waves”, are considered as the transition structure between free-space and a guiding device [2].

The general condition for radiation in any antenna is a charge accelerating or decelerating and is expressed by the formula [3]:

$$\dot{I}L = Q\dot{v} \text{ [A m s}^{-1}\text{]} \quad (2.1)$$

Where, \dot{I} is a time-changing current (A s^{-1}), L is the length of a current element (m), Q is the charge (C), and \dot{v} is the time change of velocity which equals the acceleration of the charge (m s^{-2}). The interpretation of the formula is that time changing currents and accelerated charges radiate.

A lossless matched radiating antenna will appear to the transmission line as a resistance R_r , called radiation resistance. It is not related to any resistance in the antenna, but it is a resistance coupled from space to the antenna terminals.

2.1.1 Scattering parameters

Scattering parameters describe the electrical behaviour of linear electrical networks when a signal is applied. The scattering matrix [4] relates the voltage waves incident on the ports to those reflected from the ports. The scattering matrix (S matrix) is defined as:

$$\begin{bmatrix} V_1^- \\ V_1^- \\ \cdot \\ \cdot \\ V_N^- \end{bmatrix} = \begin{bmatrix} S_{11} & S_{12} & \dots & S_{1N} \\ S_{21} & & & \cdot \\ \cdot & & & \cdot \\ \cdot & & & \cdot \\ S_{N1} & & & S_{NN} \end{bmatrix} \begin{bmatrix} V_1^+ \\ V_2^+ \\ \cdot \\ \cdot \\ V_N^+ \end{bmatrix} \quad (2.2)$$

Where V_n^- is the amplitude of the voltage wave reflected from the port n and V_n^+ is the amplitude of the voltage wave incident on the port n .

Any element of the [S] matrix can be determined as

$$S_{ij} = \left. \frac{V_i^-}{V_j^+} \right|_{V_k^+ = 0 \text{ for } k \neq j} \quad (2.3)$$

Thus, S_{ij} is found by driving port j with an incident wave of voltage V_j^+ , measuring the reflective wave amplitude, V_i^- , coming out of port i .

The antennas used in the present research work use a single feed which is considered as a single port network when the antenna is isolated. Thus, the first parameter analysed when designing antennas is the return loss or reflection coefficient (S11). The reflection coefficient of the antenna relates to its input impedance as follows

$$S_{11} = \frac{V_1^-}{V_1^+} = \Gamma = \frac{Z_m - Z_0}{Z_m + Z_0} \quad (2.4)$$

Where Γ is the reflection coefficient, Z_m is the input impedance of the antenna and Z_0 is the characteristic impedance of the system.

The systems used for the antennas in this research have an impedance of 50Ω . This value has also been used in the electromagnetic simulators when calculating the antennas. The graph of the return loss (S11) from the simulation and measurement of the antennas developed for the present research work are presented in decibels (dB), and the antennas have been considered to work at a given frequency band when the S11 is lower than -10dB or 90% of the power is transmitted to the antenna.

2.1.2 Radiation Patterns

The radiation pattern is the graphical representation of the relative field strength transmitting from or received from an antenna. Two main regions of radiation are considered when designing antennas, the near-field and the far-field. The near field is

a region close to the antenna where the angular field distribution is dependent upon the distance from the antenna. It is that part of the radiated field that is within a small number of wavelengths of the diffracting edge or antenna. The far field is the region outside the near-field region, where the angular field distribution is independent of distance from the source. The far field region exists for distances greater than $(2D)^2/\lambda$ where D is the maximum overall dimension of the antenna and λ is the operating wavelength.

The radiation patterns are three-dimensional quantities involving a variation of field or power (proportional to the square of field) as a function of the spherical coordinates theta (θ) and phi (φ) as shown in Fig.2.1. Practically, the radiation pattern will normally be measured in an anechoic chamber as the power received in the antenna when a broadband directional antenna transmits a signal. The measured radiation patterns in this research work are presented through the three main plane cuts of the full three dimensional pattern. The planes, shown in are the XY for $\theta = 90$ (φ from 0 to 360), the XZ for $\varphi = 0$ (θ from 0 to 360) and YZ for $\varphi = 90$ (θ from 0 to 360).

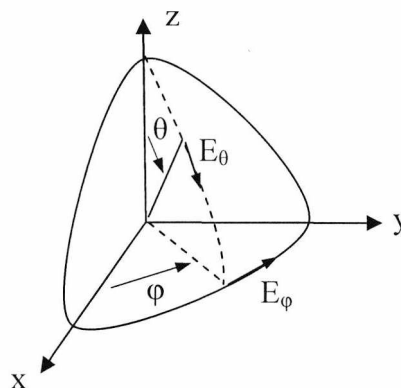


Figure 2.1 Coordinates system for antenna analysis

2.1.3 Directivity and Gain

Directivity and gain [3] are two important parameters of the antenna that can be extracted from the radiation pattern plot. The directivity of an antenna is equal to the ratio of maximum power density $P(\theta, \varphi)_{\max}$ [watts/m²] to its average value over a sphere as observed in the far field of an antenna. Therefore:

$$\text{Directivity from radiation pattern} \quad D = \frac{P(\theta, \phi)_{\max}}{P(\theta, \phi)_{av}} \quad (2.5)$$

The gain G of an antenna is a real quantity which is less than directivity D due to the ohmic losses in the antenna. When transmitting, these losses involve power fed to the antenna which is not radiated but heats the antenna structure. A mismatch in feeding the antenna can also reduce the gain. The ratio of the gain of the antenna to the directivity is the antenna *efficiency factor*. Thus,

$$G = kD \quad (2.6)$$

with k the efficiency factor ($0 \leq k \leq 1$), [dimensionless].

The gain measured at the University of Kent has been calculated by comparing the maximum received power density of the Antenna Under Test (AUT) with that received by a reference antenna of known gain, such as a broadband standard dipole. Thus:

$$\text{Gain} = G = \frac{P_{\max}(AUT)}{P_{\max}(ref.ant)} \times G(ref.ant.) \quad (2.7)$$

The limitation of this method is that, for good accuracy, the standard antenna should have similar gain to the antenna under test.

2.2 Electromagnetic Simulators

There has been a rapid growth in commercial electromagnetic simulator over the last few decades. In the past, the simulators used by scientists and antenna engineers were mostly written in house and for a specific application. Simulations used to be time consuming to code, validated and test were highly costly to produce and were limited to the academic community. The development and expansion of existing commercial electromagnetic software in the 1990's such as Zealand Software's IE3D, HP EEsof's ADS, ANSOFT's Ensemble and HFSS and the introduction of CST microwave studio has facilitated the design of antennas and other microwave related components.

At present, three main mathematic methods seem to be dominant in the commercial electromagnetic software market for antenna applications: Method of Moments

(MoM) [5], Finite Element Method (FEM) [6] and Finite-Difference Time-Domain (FDTD) [7].

The electromagnetic software packages used in this research work are: Zealand IE3D [8-9], based on the Method of Moments and CST Microwave studio, which uses time domain techniques. Both simulation packages and the basic electromagnetic formulation and techniques are discussed in the following sections.

2.2.1 IE3D and Method of Moments

The primary formulation of IE3D [9] is an integral equation obtained through the use of Green's functions. Both the electric current on a metallic structure and a magnetic current representing the field distribution on a metallic structure can be modelled. For reasons of simplicity, the discussion in this section will focus on the formulation of electric current only. The magnetic current is obtained, using a complementing argument.

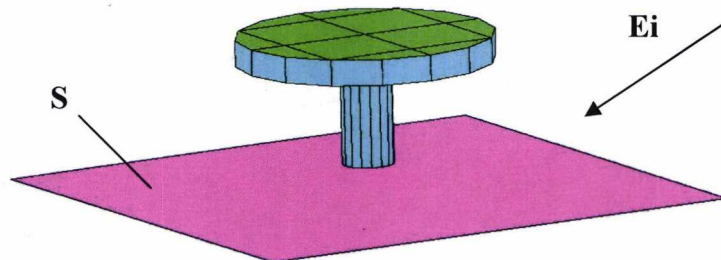


Fig.2.2. An incident field is applied to a metallic structure.

For a general electromagnetic scattering problem, a conducting structure in a stratified dielectric environment is assumed, as shown in the IE3D model in Fig.2.2. An incident field is imposed on the structure, inducing a current distribution on it. The induced current will create a secondary field to satisfy the boundary conditions on the metallic structure. For a typical conducting structure, the induced current is distributed in the conducting surface and the boundary condition is,

$$E(r) = Z_s(r)J(r), \quad r \in S \quad (2.8)$$

Where S is the conducting surface; $E(r)$ is the total tangential field on the surface; $J(r)$ is the current distribution on the surface; $Z_s(r)$ is the surface impedance of the conductor.

When the structure is in a layered dielectric environment, the total field can be written down as [9],

$$E(r) = E_i(r) + \int_S G(r/r') \cdot J(r') ds' \quad (2.9)$$

Where $G(r/r')$ is the dyadic Green's function for the dielectric environment; $E_i(r)$ is the incident field on the conducting surface. $G(r/r')$ satisfies the stratified dielectric boundary conditions except the boundary condition on the conductor S .

Substituting (2.9) in (2.8) yields the integral equation,

$$Z_s(r)J(r) = E_i(r) + \int_S G(r/r') \cdot J(r') ds' \quad (2.10)$$

The incident field and the surface impedance are provided and the Green's function can be derived. The unknown is the current distribution $J(r)$.

By assuming that the current distribution is represented by a set of complete basis functions,

$$J(r) = \sum_n I_n B_n(r), \quad n = 1, 2, \dots \quad (2.11)$$

we obtain

$$Z_s(r) \sum_n I_n B_n(r) = E_i(r) + \sum_n I_n \int_S G(r/r') \cdot B_n(r') ds' \quad (2.12)$$

By taking the Galerkin's procedure, we convert (2.12) into a matrix equation,

$$\begin{aligned} & S_m \int_S ds E_i(r) \cdot B_n(r) \\ & = S_m S_n I_n \left\{ \int_S ds Z_s(r) B_m(r) \cdot B_n(r) + \int_S ds \int_S ds' B_m(r) \cdot G(r/r') \cdot B_n(r') \right\} \quad (2.13) \end{aligned}$$

The above process is to enforce (2.12) with a complete set of test functions and the test functions are the same as the basis functions. A complete set of functions consist of an infinite number of terms. Therefore, (2.13) is an infinite dimensional problem and it can be approximated as a numerical solution. The approximation is to truncate the infinite series with a finite number of terms. Mathematically, the truncation is a

projection process. The actual solution in infinite dimensions is projected to that of finite dimensions. If finite dimensions are chosen so that the major components of the actual solution are all in the finite dimension, the result should be a very good approximation of the solution. After the projection, equation (2.13) becomes an N by N equation,

$$[Zmn][Im]=[Vm] \quad (2.14)$$

Where

$$Z_{mn} = \int_S ds Zs(r) B_m(r) \cdot B_n(r) + \int_S ds \int_S ds' B_m(r) \cdot G(r/r') \cdot B_n(r') \quad (2.15)$$

$$Vm = \int_S ds Ei(r) \cdot B_n(r) \quad (2.16)$$

The solutions of equations (2.15) and (2.16) are the current distribution coefficients. After the current distribution is solved, the s-parameters and radiation pattern can be calculated.

All moment method (or method-of-moment, MOM) formulations, no matter how simple or complex is, take the form of equations (2.14 -2.16). The differences are on the choice of basis functions and the Green's function.

2.2.2 CST Microwave Studio and Finite Integration Method

The antennas developed for this work have been simulated using the Finite difference time-domain calculation (FDTD) included in CST Microwave studio. The FDTD method belongs to a general class of grid-based differential time-domain numerical modeling methods. Maxwell's equations are modified to central-difference equations, discretized, and implemented in software. The electric field is solved at a given instant in time, then the magnetic field is solved at the next instant in time, and the process is repeated over and over again. CST Microwave Studio is an electromagnetic simulator based on the Finite Integration Technique (FIT), first proposed by Weiland in 1976/1977 [10-11]. FIT discretizes the following integral form of Maxwell's equations, rather than the differential one [10]:

$$\oint_{\partial A} \vec{E} \cdot d\vec{s} = - \int_A \frac{\partial \vec{B}}{\partial t} \cdot d\vec{A}, \quad \oint_{\partial A} \vec{H} \cdot d\vec{s} = \int_A \left(\frac{\partial \vec{D}}{\partial t} + \vec{J} \right) \cdot d\vec{A} \quad (2.17)$$

$$\oint_{\partial V} \vec{D} \cdot d\vec{A} = - \int_V \rho \cdot dV, \quad \oint_{\partial V} \vec{B} \cdot d\vec{A} = 0 \quad (2.18)$$

E [V/m] - electric field	H [A/m] - magnetic field
D [q/m ²] - displacement vector	B [Wb/m ²] - mag. Flux density
ρ [q/m ²] - vol. charge density	A [m ²] - element area
V [m ³] - volume	

Equations (2.17) and (2.18) are solved numerically by defining a finite calculation domain enclosing the considered application problem. This domain is divided into several small grid cells as is shown in Fig.2.3. As shown in the figure, for every grid mesh a secondary grid mess is defined orthogonally to the first one. A spatial discretization of Maxwell's equations is performed on the two orthogonal grid systems, where the new degrees of freedom are introduced as integral values as well.

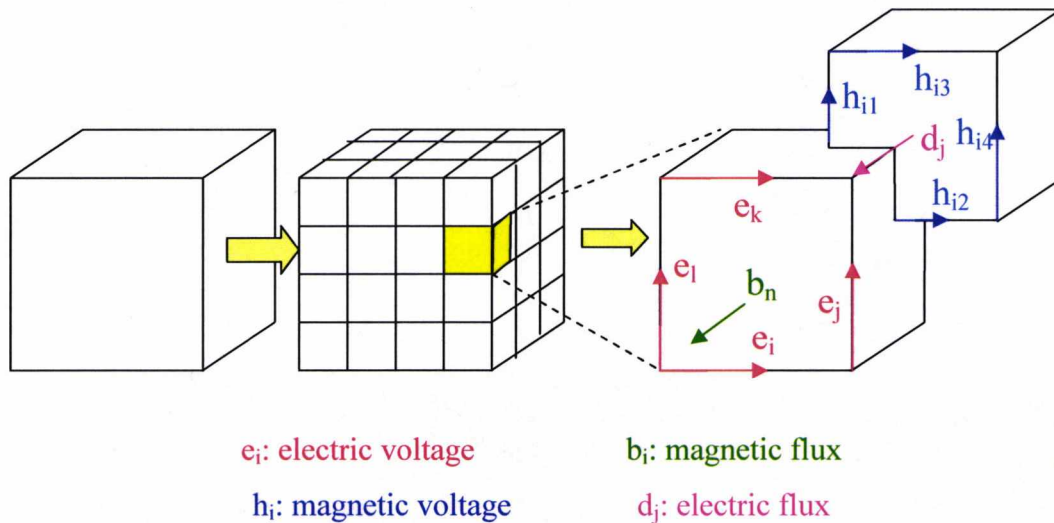


Figure 2.3 Orthogonal grid system used for spatial discretization.

Maxwell's equations are formulated for each of the cell facets separately. Considering Faraday's law the closed integral on the equation left side can be rewritten as a sum of four grid voltages without introducing supplement any errors. Therefore, the time derivative of the magnetic flux defined on the enclosed primary cell facet represents the right side of the equation, as shown in Fig.2.3. By repeating this procedure for all available cell facets, the calculation rule can be summarized in a C matrix as the discrete equivalent of the analytical curl operator.

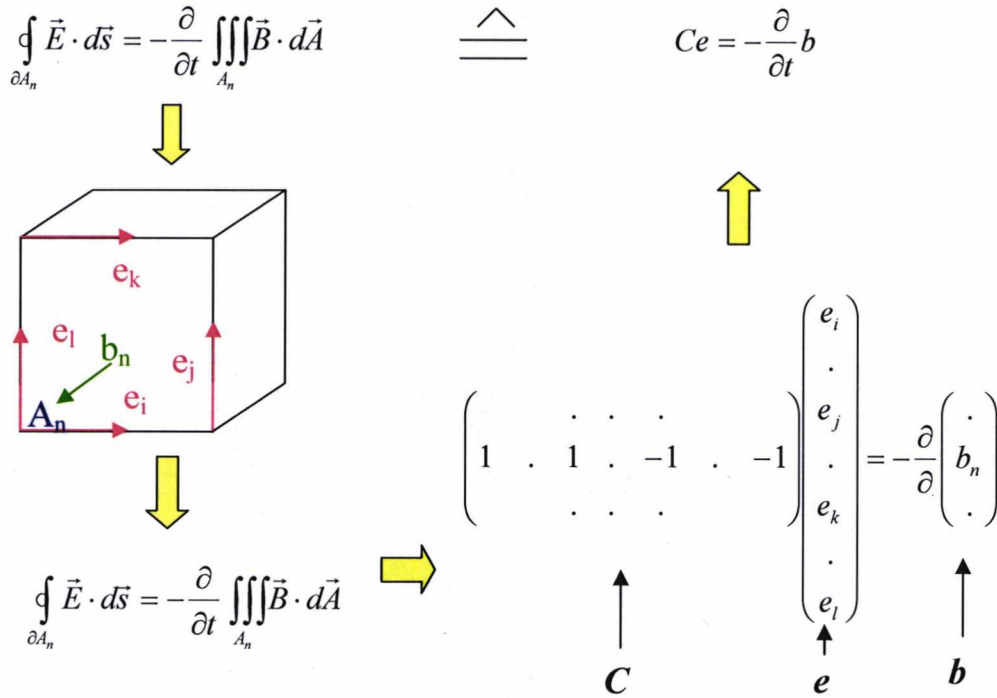


Figure 2.4 Matrix C as the discrete equivalent of the analytical curl

Applying this scheme to Ampere’s law on the dual grid involves the definition of a corresponding discrete curl operator \hat{C} . Similarly the discretization of the divergence equations (2.18) introduces discrete divergence operators S and \hat{S} , belonging to the primary and dual grid, respectively. Finally, the complete discretized set of Maxwell’s Grid Equations are obtained (MGE):

$$C e = -\frac{d}{dt} b, \quad \hat{C} h = \frac{d}{dt} d + j \tag{2.19}$$

$$\hat{S} d = q, \quad S b = 0 \tag{2.20}$$

The FIT discretization still maintains the important properties of the continuous gradient, curl and divergence operators:

$$S C = \hat{S} \hat{C} = 0 \quad \Leftrightarrow \quad \text{div rot} \equiv 0 \tag{2.21}$$

$$C \hat{S}^T = \hat{C} S^T = 0 \quad \Leftrightarrow \quad \text{rot grad} \equiv 0 \tag{2.22}$$

The material equations add numerical inaccuracy due to spatial discretization. By defining the necessary relations between voltages and fluxes their values have to be approximated over the grid edges and cell areas, respectively. Therefore, the resulting

coefficients depend on the average material parameters as well as on the spatial resolution of the grid and are summarized again in correspondent matrices:

$$\hat{D} = \epsilon \hat{E} \qquad d = M_\epsilon e \qquad (2.23)$$

$$\hat{B} = \mu \hat{H} \quad \Rightarrow \quad b = M_\mu h \qquad (2.24)$$

$$\hat{J} = \sigma \hat{E} + \hat{J}_s \qquad j = M_\omega e + j_s \qquad (2.25)$$

The topological and the metric information separated in different equations have had important theoretical, numerical and algorithmic consequences [12] which are the basis of CST Microwave Studio Software package.

2.2.3 Comparison between IE3D and CST Microwave studio

The main differences between IE3D and CST Microwave studio's time domain solver are summarized in the following points:

- CST Microwave Studio uses the Finite Integration Technique while IE3D uses Method of Moments.
- The discretization of geometry in IE3D is 2.5 dimension using triangles and rectangles while CST Microwaves studio uses 3-D cells.
- The projects in IE3D are normally run in open space while boundaries need to be introduced in CST.
- Near to far field approximations are used in CST Microwave studio while IE3D obtains direct far field calculations.
- The results on CST Microwave studio are broadband compared to the single frequency point calculation in IE3D.
- CST Microwave Studio performs well with inhomogeneous structures while IE3D is inefficient for such structures.

References

- 1] IEEE standard definition of Terms for Antennas, IEEE Std 145-1983
- [2] C.A.Balanis, "Antenna Theory"-2nd Edition, John Wiley&Sons 1997.
- [3] John D. Kraus, Ronald J. Marhefka, "Antennas" - 3rd Edition, Mc Graw Hill, 2002

- [4] D.M. Pozar, "Microwave Engineering", 2ndEd, Chapter 4, pp.196, John Wiley&Sons, Inc, 1998.
- [5] R.F.Harrington:"Field computation by Moment Methods", IEEE Press series On Electromagnetics
- [6] O. C. Zienkiewicz, R. L. Taylor, J.Z. Zhu, "The Finite Element Method: Its Basis and Fundamentals", Sixth Edition, Elsevier, 2005
- [7] Karl S. Kunz, Raymond J. Luebbers, "The Finite Difference Time Domain Method for Electromagnetics", CRC Press, 1993
- [8] P.Eskelinen.:"IE3D eleectromagnetic simulation package"
- [9] Zeland Sofware.:"IE3D product literature" -1998
- [10] T.Weiland "A discretization method for the solution of Maxwell's equations for six-components fields", *Electron.Commun.(AEU)*, 31, 116 (1977)
- [11] T. Weiland, 'A numerical method for the solution of the eigenwave problem of longitudinally homogeneous waveguides', *Electron. Commun. (AEU)*, 31, 308 (1977).
- [12] Weiland, T.: "Time Domain Electromagnetic Field Computation with Finite Difference Methods", *International Journal of Numerical Modelling*, Vol. 9, pp. 295-319, 1996.

Chapter 3.

Dielectric measurements and Small Antenna design

The study of the characteristics of materials at microwave frequencies is an essential part of microwave engineering. Through the understanding of the properties of materials it is possible to obtain a better prediction of the electrical behaviour of microwave devices, including antennas. Typically, the responses of materials to electromagnetic fields are determined by the displacement of their free and bounded electrons by electric fields and their atomic moments by magnetic fields [1].

The materials used in this research work can be mainly classified as conductive (copper and brass) and dielectric (PTFE, FR4 and textile materials). Little literature has reported the characteristics of textile materials used for wearable antennas [2]-[3].

In addition, the characteristics of the textile materials can vary regarding the property of the textile and the additions to it, such as colour or any other chemical agents which may change the dielectric permittivity of a specific textile fabric.

To enable the design of wearable antennas it is necessary to characterise the textile on which they are mounted and the first part of this chapter covers the theory behind a dielectric measurement method used for denim and Velcro.

The second part discusses the basic theory related to the specific antennas used in this research which are: the planar inverted F antenna and the top loaded monopole antenna.

3.1 Methods of Measuring the Permittivity of Substrates

The methods for electrical characterisation of materials generally fall into resonant methods and nonresonant methods[1]. The resonant methods are based on the fact that the resonant frequency and the quality factor of a dielectric resonator with given dimensions are determined by its permittivity and permeability. In the nonresonant methods, the properties of the materials are fundamentally deduced from their impedance and the wave velocities in the materials.

Non resonant methods mainly include reflection methods and transmission/reflection methods. In the reflection method, the material properties are calculated on the basis of the reflection from the sample. In the transmission/reflection method, the material properties are calculated on the basis of the reflection from the sample and the transmission through the sample.

Non resonant methods require a means of directing the electromagnetic energy toward the material, and the collecting of what is reflected from the material, and/or what is transmitted through the material. All types of transmission lines can be used to carry the wave for nonresonant methods, such as coaxial line, hollow metallic waveguide, dielectric waveguide, planar transmission line, and free space.

In this research, a hollow waveguide transmission/reflection, broadband, non resonant method has been used and is explained in the following section.

3.1.1 Waveguide Method for Measuring Dielectric Textile

In the transmission method used for the material measurement, the textile material is placed at the centre of a rectangular waveguide [4-5] supported by expanded polystyrene foam. The scattering parameters of the structure with and without the textiles are compared to determine the dielectric constant and the loss tangent. The advantages of this method are:

- The material is supported by the foam and can be accurately placed in the waveguide.
- Since this is a comparison measurement, any mismatch or inaccuracies in the measurements are subtracted.
- The length of the material sample can be increased at will to obtain a bigger difference between the two measurements and thus increase the accuracy.
- Unlike a resonance method, the measurement can be performed over a wide band of frequencies between the cut-off frequencies of the TE_{10} and the TE_{20} modes.

The method has been used to determine the dielectric constants and loss tangents of Velcro and Denim. With reference to Fig. 3.1, in the transverse direction we have a waveguide with equivalent width of a where λ_g is the wavelength of the propagating mode in the longitudinal direction. Thus λ_g represents the cut-off wavelength of the transverse guides.

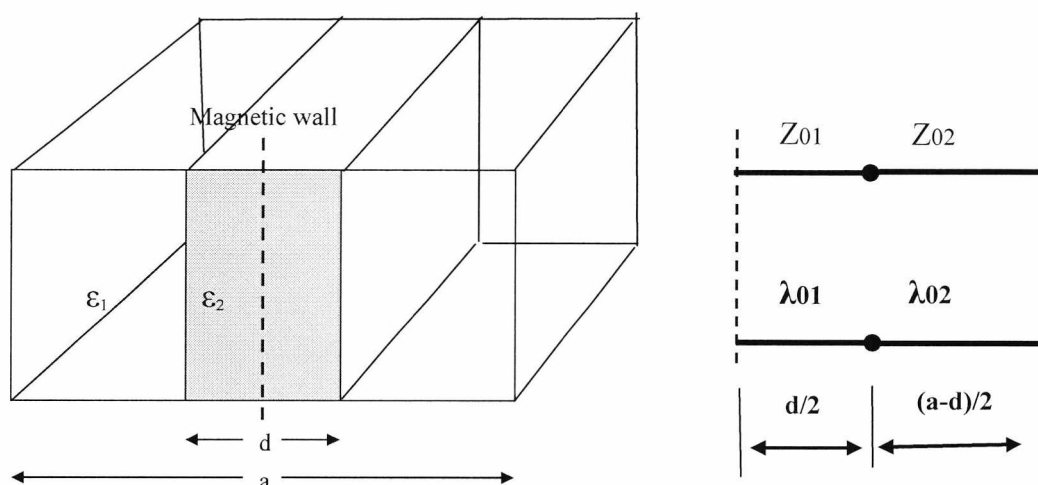


Figure 3.1 Waveguide cross section width a with textile sample width d (left). Equivalent network (right).

At the interface in the transverse direction we have

$$Y_1 = -jY_{01} \cot\left(\frac{\beta_1(d-a)}{2}\right) \text{ and } Y_2 = jY_{02} \tan\left(\frac{\beta_2 d}{2}\right) \quad (3.1)$$

$$\begin{aligned} \beta_1 &= \frac{2\pi}{\lambda_1} \sqrt{1 - (\lambda_1/\lambda_g)^2} \quad , \\ \beta_2 &= \frac{2\pi}{\lambda_2} \sqrt{1 - (\lambda_2/\lambda_g)^2} \quad , \\ \lambda_1 &= \lambda_0/\sqrt{\epsilon_1} \quad , \quad \lambda_2 = \lambda_0/\sqrt{\epsilon_2} \end{aligned} \quad (3.2)$$

and λ_g is the cut-off wavelength of the guide with the dielectric .

The characteristic admittances Y_{01} and Y_{02} are given by [4,5]

$$Y_{01} = \frac{1}{\eta_1} \sqrt{1 - (\lambda_1/\lambda_g)^2} \quad \text{and} \quad Y_{02} = \frac{1}{\eta_2} \sqrt{1 - (\lambda_2/\lambda_g)^2} \quad (3.3)$$

$$\text{where} \quad \eta_1 = \sqrt{\mu_0/\epsilon_1} \quad \text{and} \quad \eta_2 = \sqrt{\mu_0/\epsilon_2} .$$

For propagation to be sustained, resonance must be achieved and we have $Y_1 + Y_2 = 0$ and substituting (3.2) and (3.3) we get

$$\frac{\sqrt{k^2 \epsilon_r - \beta^2} \tan(d\sqrt{k^2 \epsilon_r - \beta^2}/2)}{\sqrt{k^2 - \beta^2} \cot((a-d)\sqrt{k^2 - \beta^2}/2)} = \quad (3.4)$$

where k is the propagation constant in medium 1, $\beta = 2\pi/\lambda_g$ is the propagation constant in the guide with the dielectric and $\epsilon_r = \epsilon_2/\epsilon_1$. If both or either dielectric media are lossy, then ϵ_1 and/or ϵ_2 are complex and β in (3.4) is replaced by $\gamma = \alpha + j\beta$.

For the measurement procedure: the sample is inserted in a C-band waveguide and the transmission parameters S_{21} with and without the sample are measured in amplitude and phase. The measured phase of S_{21} with and without the sample are ϕ_1 and ϕ_2 respectively, where $\phi_1 > \phi_2$ due to the dielectric. The measured phase also includes phase shift due to the length occupied by the sample, any extra length of waveguide, the waveguide to coaxial transitions and the cables connecting to the network analyser. If the same length of waveguide and all the other components are

used with and without the sample, then the difference between the two phase shifts will give us the extra phase due to the sample.

Thus $\phi_1 = \theta_1 + \theta_e$ and $\phi_2 = \theta_2 + \theta_e$ where θ_e is the extra phase shift due the measurement components, θ_1 is the phase shift due to the dielectric sample and θ_2 is the phase shift of the length of waveguide where the sample was placed but after it has been removed. The angles θ_1 and θ_2 are related to the guided wavelengths by $\theta_1 = 2\pi l / \lambda_g$ and $\theta_2 = 2\pi l / \lambda_{g0}$ where λ_g and λ_{g0} are the guide wavelengths with and without the sample.

From measurement of the difference $\Delta\phi$ between the phase angles ϕ_1 and ϕ_2 we calculate λ_g from

$$\lambda_g = \frac{\lambda_{g0}}{1 - \Delta\phi\lambda_{g0} / 2\pi l} \quad (3.5)$$

The attenuation constant is calculated from the ratio of the amplitude of S_{21} with and without the sample. When both λ_g and α are known, equation (3.4) is used to calculate ϵ_r . These equations are also applicable when the slabs are dissipative and characterized by a complex dielectric constant; in which λ_g is complex.

Figure 3.2 and Table II give the results for Velcro and dry denim using a sample length of 40mm. The a and b parameters of the waveguide were 60x28mm. The small fluctuation for the permittivity of denim between 3.5 and 4GHz is due to residual inaccuracies in the measurement.

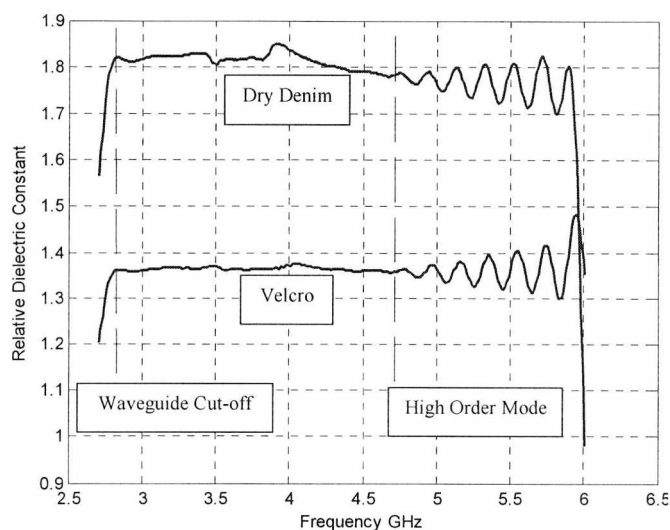


Figure 3.2 Measured dielectric constant of Velcro and dry Denim.

TABLE II
MEASURED RELATIVE PERMITTIVITY AND LOSS TANGENT OF
VELCRO AND DRY DENIM

Material	Relative Permittivity	Loss Tangent
Velcro	1.34	6×10^{-3}
Dry Denim	1.8	7×10^{-2}
PTFE	2.1	5×10^{-3}

Solid PTFE was also measured, giving an average dielectric permittivity of 2.1 and loss-tangent of 5×10^{-4} which approximates the values expected for this material. For tolerance observed for the permittivity calculation using this method was lower than 10%.

3.2 Small Antenna designs

The design of small antennas operating a many frequency bands has become essential in recent years. Size reduction in early antenna designs were achieved by folding the top wire in antennas operating at very long wavelengths [6]. Nowadays, with the wide spread use of wireless and mobile communications, antennas have become part of our everyday life and are embedded onto slim mobile phones, PDA's and laptops. The antennas in these devices are required to be electrically small and be surrounded by complex electronics devices, such us speakers and cameras.

The present research focus on compact antenna designs for wireless and mobile communication systems and the following two sections give an introduction to the basic antenna designs from which many mobile antennas have evolved. The first section (4.4.2) discusses top loaded monopoles which are the basis of the button antennas developed in chapters 6 and 7. The second section (4.4.3) looks at the later developed planar inverted F antennas for mobile communications which is the type of structure used for the antennas in chapters 4 and 5.

3.2.1 Top loaded Monopoles

Electrically small dipole and monopole antennas using top loading metal structures have been employed for many decades. A study of electrically short antennas for very

low frequencies (VLF) using top loading can be found as early as 1965 [6] where the umbrella top-loaded antenna is discussed. Since the height required to achieve self resonant in antennas at VLF was prohibitive, top loading used to be an economical solution to reduce the capacitance reactance and in many cases to increase the radiation resistance for a shortened antenna height [7]. The inverted L antenna (Fig.3.3) provides the simplest example of top loading with early discussion on this antenna and the T (Fig.3.3b) and four elements antenna (Fig.3.3) presented in [8].

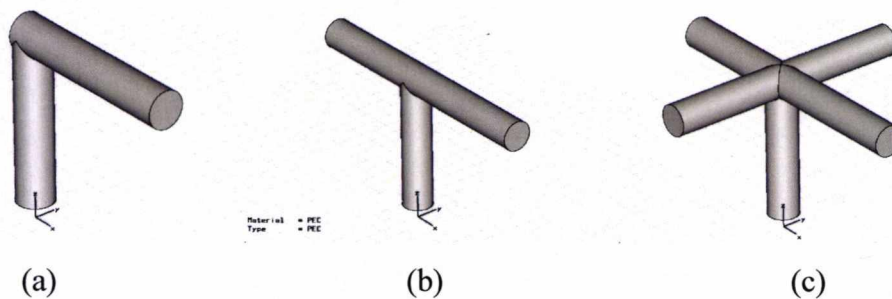


Figure 3.3. Elementary top loading structures with $\theta_A = 90^\circ$. (a) Inverted L antenna, (b) T antenna and (c) Four-element top loaded antenna.

For a given vertical height, resonating the antenna with top loading results in much bigger radiation resistance, of an order of two to four times [8]. The effect of such top loading is to increase the current at the base of the antenna, and also to make the current distribution more uniform [9]. To illustrate this effect, Fig.3.4 shows a simplified schematic of current magnitude in a resonant antenna and the L and T top loaded antennas.

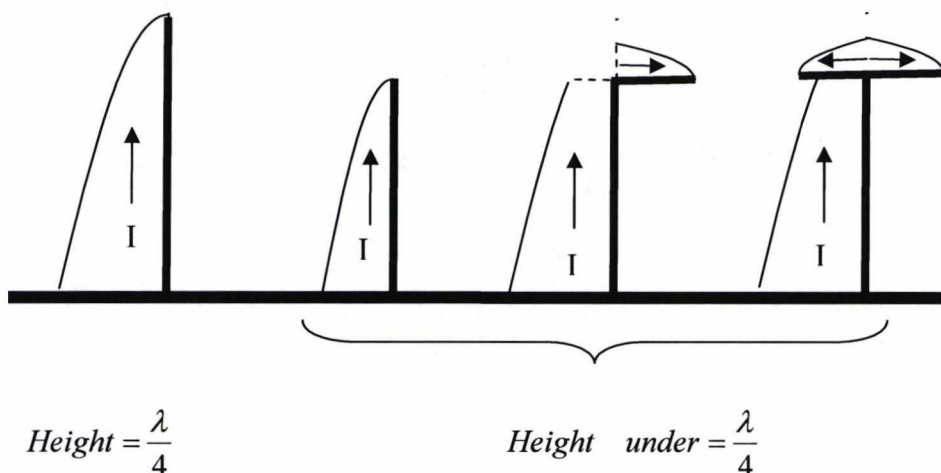


Figure 3.4 Effect of top loading on the current of the antenna.

In [8], the formulation of the capacitance of the top hat antenna with the structure as in Fig.3.5 is as follows:

- The characteristic impedance of a vertical antenna is found by:

$$Z_0 = 60 \left(\ln \left(\frac{4h}{d} \right) - 1 \right) \quad (3.6)$$

Where

h is the length (height) of vertical radiator

d is the diameter of the radiator

- The capacitive reactance for the amount of top loading can be found from

$$X = \frac{Z_0}{\tan \theta} \quad (3.7)$$

Where

X is the capacitive reactance, in ohms [ohms]

Z_0 is the characteristic impedance of the antenna [ohms]

θ is the phase due to electrical loading [degrees]

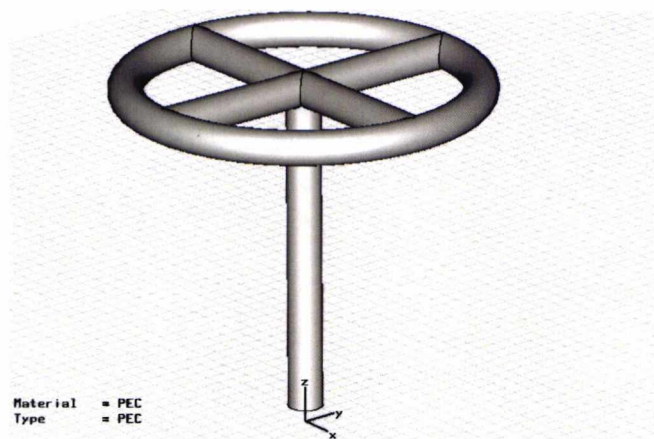


Figure 3.5 Top hat antenna

The button antennas to be presented in chapters 6 and 7 are more complex than the simple structures mentioned here, though the small electrical size of the buttons is mainly due to top loading by a metallic disc. There is an analysis of monopole top loaded by discs in [10] though its formulation is not necessary for the designs to be presented here.

3.2.2 Planar Inverted F Antenna

The Planar inverted F Antenna is currently one of the most common designs used in modern mobile phones. The antenna originated from the inverted L antenna already shown in Fig.3.4. Extending the top part of the Inverted L Antenna (ILA), the antenna will become a very short monopole with a long horizontal wire as is shown in Fig.3.6

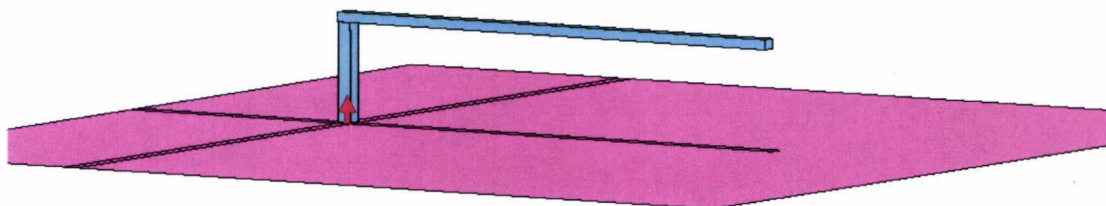


Figure 3.6 ILA antenna with extended long horizontal wire

The length of the horizontal element of the ILA structure is typically a quarter wavelength and has low input impedance. The impedance is given by a very short monopole with the addition of the reactance from the element in closed proximity to the ground.

The Inverted F Antenna or IFA [11], shown in figure 3.7, is a later development of the ILA and is able to achieve higher radiation resistance by shorting the top of the vertical monopole of the structure at a calculated distance from the feed. In [11] the IFA was described as a “shunt-driven inverted L antenna-transmission line with open end”. The IFA has been often applied on moving platforms such as rockets and aircrafts due to its low profile, high strength and easy control of its input impedance matching.

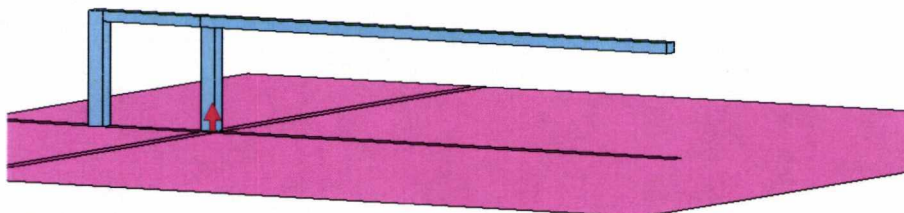


Figure 3.7 IFA antenna

The Planar Inverted F Antenna (PIFA) is an IFA where the top wire has been transformed into a planar structure. A simple PIFA on a large ground plane is shown in Fig.3.8.

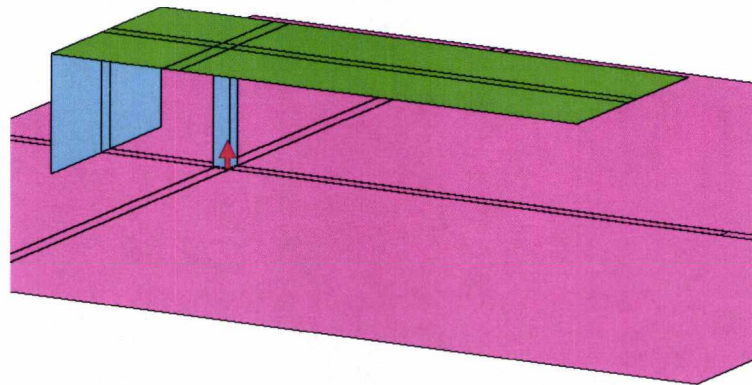


Figure 3.8 PIFA antenna geometry

In [12] it was found that the resonant frequency of a planar inverted-F antenna can be determined approximately from:

$$f_0 = \frac{c}{4(L+W)} \quad (3.8)$$

Where

c is the velocity of the light [m/s]

L is the length of the radiating element [m]

W is the width of the radiating element [m]

The PIFA was initially suggested for use in mobile systems due to its compactness and sensitivity to both horizontal and vertical polarization. The same reason has been considered when choosing PIFAs as multiband antennas for indoor communications as described in chapters 4 and 5.

3.3 Conclusions

Material measurement methods and small antenna designs have been presented in this chapter. The methods to determine the material properties at microwave frequencies have been classified as resonant or nonresonant. The method used here to characterise

the permittivity and loss tangent of textile materials is a nonresonant transmission methods using a rectangular waveguide. The permittivity of Velcro and Denim have been measured and found to be 1.34 and 1.8 respectively.

The basic designs from which antennas in this work evolved have also been discussed in this chapter. Two antennas are considered from which the work originates:

- The top loaded monopole, as precursor to the wearable button antennas in chapter 6 and 7.
- The planar inverted F antenna which has been used as a basis for the indoor communications antennas in chapter 4 and 5.

References

- [1] L.F.Chen, C. K. Ong, C. P. Neo, and V. V. Varadan, "Microwave Electronics: Measurement and Materials Characterization", John Wiley&Sons, Ltd., 2004.
- [2] Yang Taeyoung, W.A Davis,. W.L. Stutzman, "Wearable ultra-wideband half-disk antennas", IEEE International Symposium in Antennas and Propagation, Vol. 3A, pp. 500-503, July 2005
- [3] D. Cottet, J. Grzyb, T. Kirstein and G. Tröster, "Electrical Characterization of Textile Transmission Lines", IEEE Transactions on Advanced Packaging, Vol. 26, No. 2, pp. 182-190, May 2003
- [4] C.G. Montgomery, R.H. Dicke and E. M. Purcell, ' Principles of Microwave Circuits, Chapter 11.
- [5] N. Marcuvitz, ' Waveguide Handbook', Chapter 8.
- [6] A.Gangi, S.Sensiper., G.Dunn, "The characteristics of electrically short, umbrella top-loaded antennas", IEEE Transactions on Antennas and Propagation, Volume 13, Issue 6, p.p. 864 – 871, Nov. 1965
- [7] T. Simpson, "The theory of top-loaded antennas: Integral equations for the currents", IEEE Transactions on Antennas and Propagation, Volume 19, Issue 2, p.p.186-190, Mar 1971
- [8] ARRL, "The ARRL Antenna book", 20TH Edition, 2003
- [9] Kennedy, Davis, "Electronic Communication Systems", Gleoncoe, Fourth Edition 1992

- [10] Morgan, M.A.; Schwering, F.K.; "Eigenmode analysis of dielectric loaded top-hat monopole antennas", IEEE Transactions on Antennas and Propagation, Vol. 42, Issue 1, p.p.54 – 61, Jan. 1994
- [11] R.King, C.W.Harrison, and D.H.Denton, "Transmission-line missile antennas", IRE Trans.Antennas and Propagation, vol.8,. no.1, pp.88-90, 1960.
- [12] K.Ogawa and T.Uwano, "A diversity antenna for very small 800-MHz band band portable telephones", IEEE Transactions on Antennas and Propagation, Vol. 42, pp.1342-1345, Sept.1994.

Chapter 4.

Multiband Antennas for Wireless Indoor Communications

4.1 Introduction

The communications standards being currently used indoors in Europe are typically identically to those used outdoors such as GSM900 [1], DCS1800 [1], GPRS [2], UMTS [3] and those used for wireless computing such as Bluetooth [4] and WLAN [5]. Normally, GSM900, DCS1800 and UMTS communications are supplied throughout a building via a basestation on the roof or a nearby building while WLAN and Bluetooth are supplied by wireless access points inside the building. In some

cases, such as large commercial centres and underground stations, the number of users exceeds the bandwidth of the standard rooftop basestation or there is not full coverage of the building, in which cases the basestation is required to be closer to the users to cope with demand, creating picocell basestations [6].

Distributed Antenna Systems (DAS) [7] have been introduced for indoor picocell applications in many buildings: for example superstores, airports, rail stations.... Most of the second and third generation of the radio cellular systems already use the picocell concept for indoor communications. In addition, some picocell systems are adding WLAN systems which can unify all the indoor communications into one single distributed antenna system.

The multiband antennas to be presented in the present chapter as well as chapter 5 have been developed for a research project entitled “Radio-optical systems Engineering in Transmanche Telecom”. The research project which ended in 2005, covered all aspects in the development of inexpensive technology for antenna units in the distributed antenna systems in radio over fibre Networks.

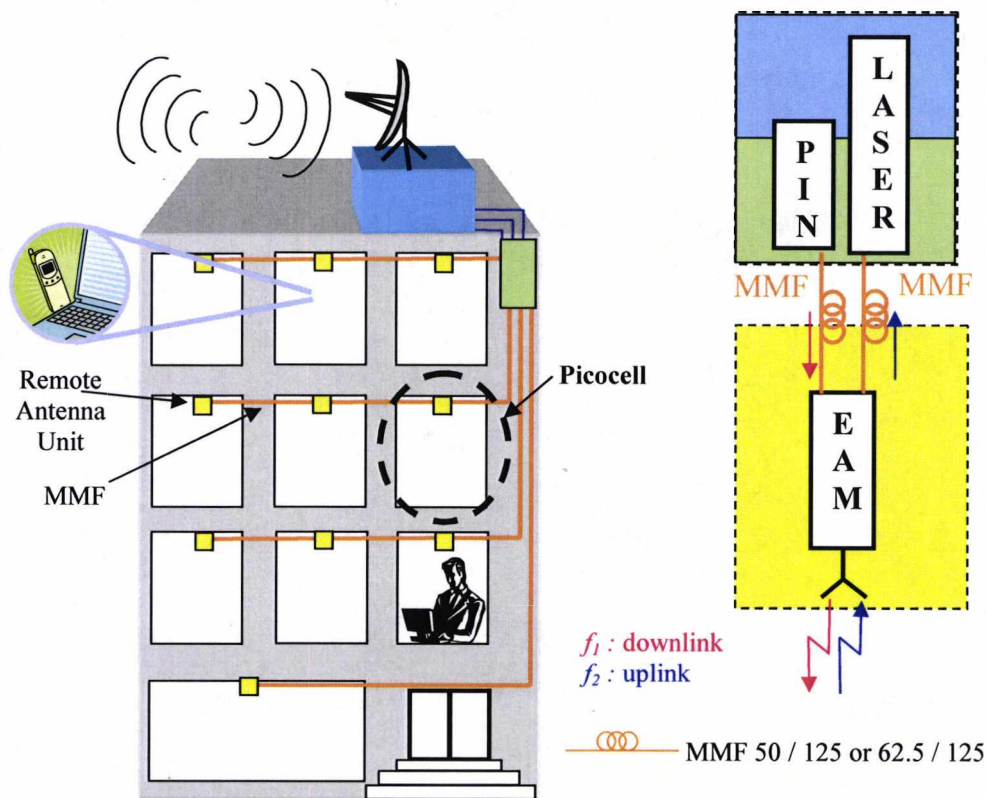


Figure 4.1. Hybrid Fibre Radio Systems in Building

Figure 4.1 shows the basic architecture of a HFR System in a building studied for the ROSETTE project. The main component of the system is a Remote Antenna Unit

(RAU) such as previously reported for single mode fibre (SMF) systems [8] matched to multi-mode fibre (MMF) networks, insensible to the different modulation schemes and carrier frequencies (GSM, GPRS, UMTS, HIPERLAN) and composed of a multiband Antenna and an ElectroAbsorption Modulator (EAM)¹. This EAM acts as a modulator for the uplink and as a Multiple Quantum Well photodetector for the downlink. The EAM will communicate with the pre-installed MULTIMODE FIBRE and use this type of fibre to transmit RF signals in buildings at a low cost.

4.2 Multiband Antennas

Dual band antennas suitable for mobile communications were successfully realised with planar inverted-F antennas in [9]. The antennas in [9] were intended for mobile terminals and used a mobile handset ground and a top metal patch with slots, cuts and via pin connectors to produce the dual band operation. Using a single via connector and rearranging the top metal cuts the antennas in [10] achieved dual band PIFA through multi-resonators with wider bandwidth than that reported in [9].

Multiband operation has also been achieved in a single antenna for mobile handset in [11] where the effect of extra metal elements connected to the feed was also studied. Additionally, it has been shown that parasitically coupled elements in plane with a top patch can be used to broadband antennas, [12].

The initial antenna considered for the present research thesis was the “Dual-band printed antennas” developed by D.Viratelle and R.J.Langley [13] at the University of Kent. The antenna in [13] had two wide band resonant modes and its size and omnidirectional radiation pattern characteristics made it convenient for the radio over fibre systems developed for the ROSETTE project. Extra frequency bands have been incorporated to the antenna in [13] by adding a ground plane parasitic resonator and two capacitive coupling side resonators. The resulted antennas are compact, lightweight, low-cost and cover most of the commercial wireless systems below 3GHz in Europe.

The frequency bands targeted for the antennas in this chapter were specifically:

- GSM900 (890-960 MHz)
- DCS1800 (1710-1880 MHz)
- DECT (1880-1990 MHz)
- UMTS (1900–2200 MHz)
- Bluetooth (2400 – 2500 MHz)

Three antennas will be presented in this chapter, each of them being a further improvement on the previous one. The first antenna is based on the antenna in [13] and incorporates the UMTS band to the already achieved GSM900 and DCS1800 bands by adding a ground plane parasitic resonator. The next antenna includes the Bluetooth band to the GSM900, DCS1800 and UMTS bands by adding side resonators. The final antenna achieves smaller size while maintaining the same characteristics of the antenna by rearranging the extra resonators.

4.3 Multiband Antenna with Ground Plane Parasitic Resonator

The first antenna to be presented in this chapter is a multiband antenna evolved from a previous development at the University of Kent (Fig.4.2a). A photograph of the new antenna is shown in Fig.4.2b and an enlarged representation of the antenna showing the principal elements is shown in Fig.4.3. The multiband antenna uses a novel technique to improve the higher band bandwidth. The increase in the higher band bandwidth is achieved by the addition of a parasitic resonator placed in the ground plane of the antenna developed by Viratelle and Langley [13] and by making further adjustments of the antenna dimensions. The additional parasitic resonator adds two extra modes in the higher frequency band without compromising the existing lower and higher frequency bands which results in an enlargement of the higher band bandwidth of more than 130%.

As for the original antenna in [13], the novel multiband antenna is simple and low cost to construct with the metallic elements printed on a flexible material which is shaped around a honeycomb former.

The novel antenna with the additional resonator is appropriate for the GSM850 (824 - 894 MHz), GSM900 (890-960 MHz), DCS1800 (1710-1880 MHz), DCS1900 (1850-

1990 MHz) DECT (1880-1990 MHz) and UMTS (1900–2200 MHz) cellular telephone system applications. Zealand software's IE3D was used to simulate the antenna with good agreement found between the simulations and practical results.

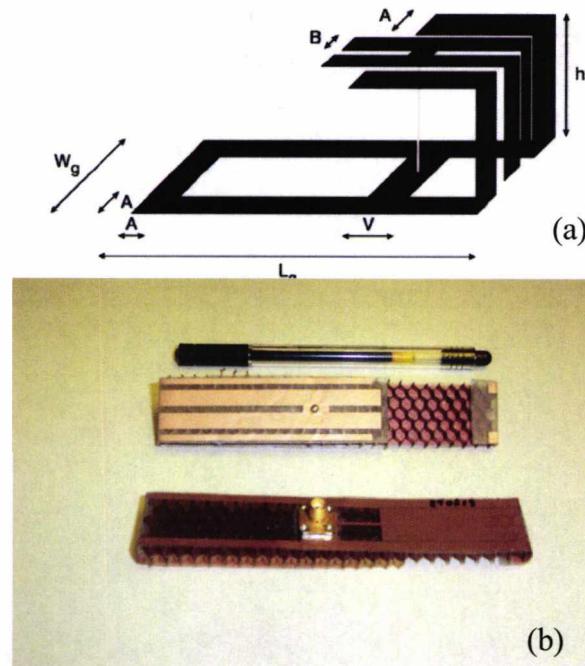


Figure 4.2. (a) Initial antenna. (b) Multiband antenna with ground plane parasitic resonator.

Figure 4.3 shows the geometry of the five-band printed PIFA Antenna with ground plane patch resonator where the honeycomb former has been omitted for clarity. As can be seen from the figure, the feeding probe is connected to the top inner patch of element 2 and the two symmetrical top outer patches of element 1 connect through shorting walls to the ground plane and element 4. The added parasitic element 3 at the bottom plane is not electrically connected to the ground plane and has a rectangular shape.

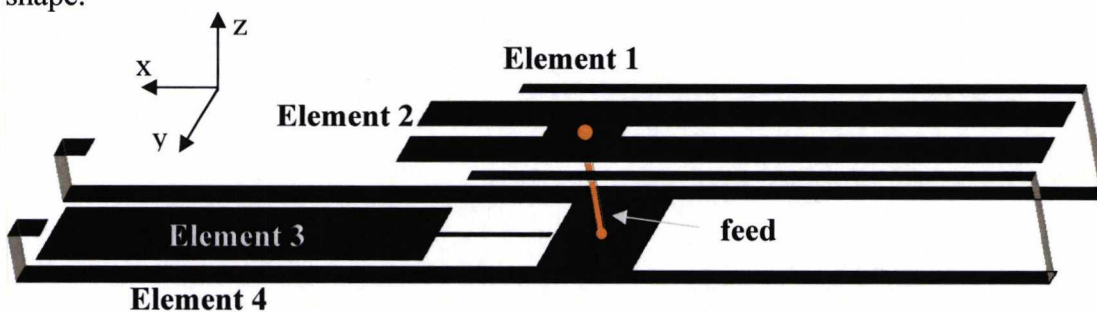


Figure 4.3. Multiband antenna with ground plane parasitic resonator

4.3.1 Multiband Antenna with Ground Plane Parasitic Resonator- Dimensions

The dimensions of the multiband antenna with ground plane parasitic resonator are shown in Fig.4.4 and Table 4.1. The total dimensions of the antenna were 133.0x24.0x9.5mm, which suits well for indoor communications. The dimensions of the ground plane parasitic resonator (element 3) were 15 x 48.5mm. There is a 0.5x15.0mm feed line with a 0.5 mm air gap between the feed ground and element 3.

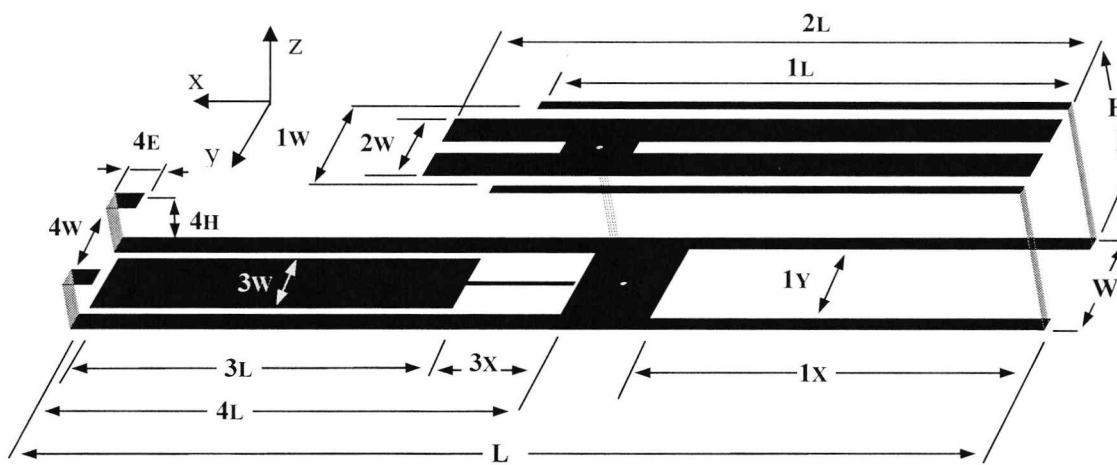


Figure 4.4. Dimensions of the multiband antenna with ground plane parasitic resonator

Element	W	L	H	1L	1w	1x	1Y	2L
Dimensions	24.0	133.0	9.5	75.0	20.0	54.5	18.0	84.0
Element	2w	3L	3w	3x	4L	4w	4E	4H
Dimensions	15.0	48.5	15.0	15.0	65.0	16.0	4.0	6.5

Table 4.1 Dimensions of the multiband antenna with ground plane parasitic resonator

4.3.2 Multiband Antenna with Ground Plane Parasitic Resonator - Measurement Results, Reflection Coefficient

The simulated and measured S11 for the multiband antenna with a ground plane parasitic resonator is shown in Fig.4.5 and Table 4.2. Multiband characteristic are observed with -10dB S11 bandwidth at the lower band of 22.3% and a higher band of

nearly 33%. The IE3D simulation of the antenna compares well with the measurements with -10dB bandwidth of 17.9% in the lower band and 33.4% in the higher band. The measured S11 of the antenna has sufficient bandwidth to cover the GSM850 (824 – 894 MHz), GSM900 (890-960 MHz), DCS1800 (1710-1880 MHz), PCS1900 (1850-1990 MHz) DECT (1880-1990 MHz) and UMTS (1900–2200 MHz). At least 5 different resonant modes were observed in the antenna within the working bandwidth. The working modes are shown Fig.4.6 with the corresponding resonant frequency.

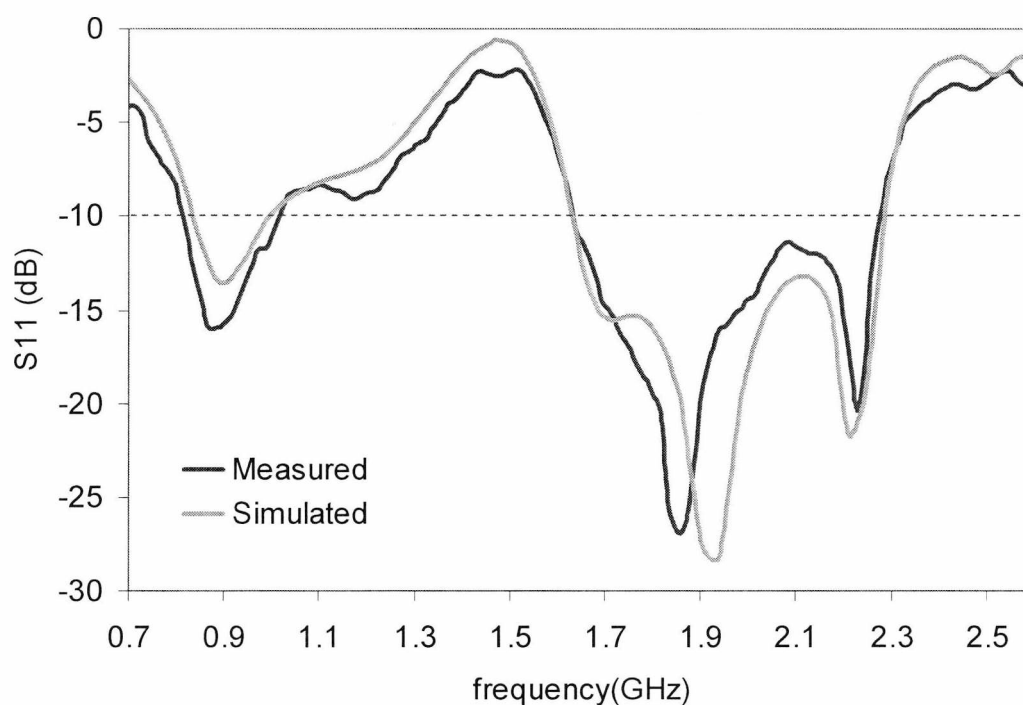


Figure 4.5 Simulated and Measured S11 curves for the multiband antenna with ground plane parasitic resonator

	Low band (MHz)	BW low band (MHz) - %	High band (MHz)	BW high band (MHz) - %
Simulated air	835 - 999	164 - 17.9 %	1631 - 2285	654 - 33.4 %
Measured air	815 - 1020	205 - 22.3 %	1634 - 2275	641 - 32.8 %
GSM 850	824 - 894	70 - 8.1 %		
GSM 900	890 - 960	70 - 7.6 %		
DCS 1800			1710 - 1880	170 - 9.5 %
PCS 1900			1850 - 1990	140 - 7.3 %
DECT			1880 - 1900	20 - 1.1 %
UMTS			1885 - 2200	315 - 15.4 %

Table 4.2 Simulated and Measured S11 for the multiband antenna with ground plane parasitic resonator and comparison with existing mobile communication systems

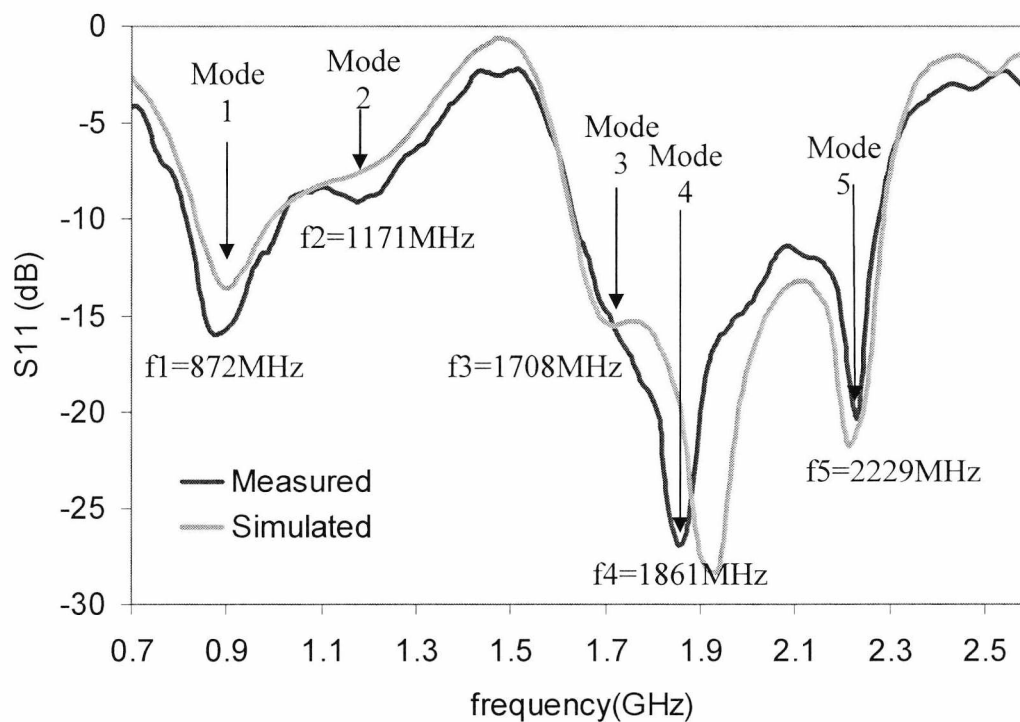


Figure 4.6 Modes and centre frequency in the multiband antenna with ground plane parasitic resonator

4.3.3 Multiband Antenna with Ground Plane Parasitic Resonator – Surface currents

The surface currents of the multiband antenna with ground plane parasitic resonator at 900MHz, 1800MHz, 1900MHz and 2100MHz are shown in Figs.4.7-4.10

At 900MHz (Fig.4.7), there are strong currents in element 1 and element 4 that are coupled through element 2 which is connected to the feed. As the wavelength is larger at 900 MHz, currents tend to flow throughout most of the body of the antenna starting from the feed in element 2, capacity coupling to element1 and connecting through the back metal walls to element 4 which makes the ground of the antenna.

At 1800MHz (Fig.4.8), currents become stronger in the whole element 2, which is still coupling to element 1, but also appears to couple with element 4 and element 3. Element 3 seems to couple higher currents than at the lower frequency band.

At 1900MHz (Fig.4.9), the current density at the back of element 2 becomes weaker, while the side facing element 3 maintains its strength. Currents in element 3 and 4 remain strong, while currents in element 2 weakened slightly.

Finally, at 2100MHz, currents in the parallel elements 3 and 4 become very strong while currents in the other elements weakened significantly.

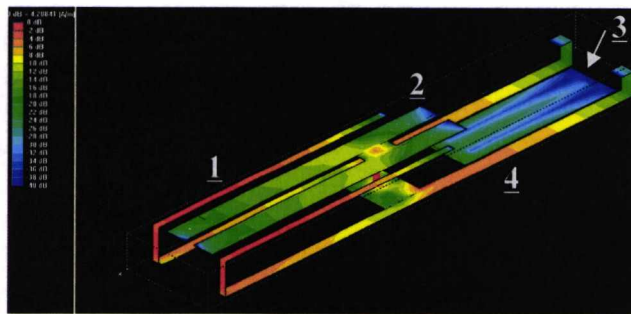


Figure 4.7. Surface currents at 900 MHz

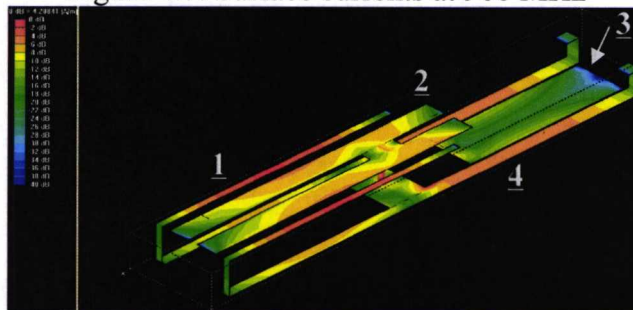


Figure 4.8. Surface currents at 1800 MHz

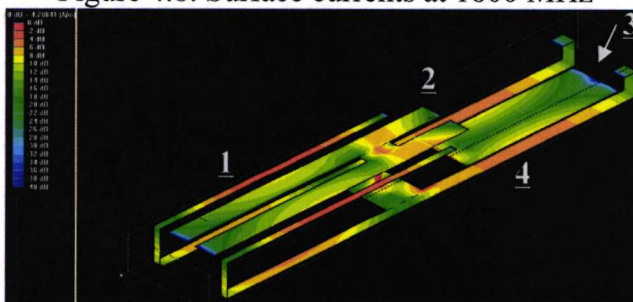


Figure 4.9. Surface currents at 1900 MHz

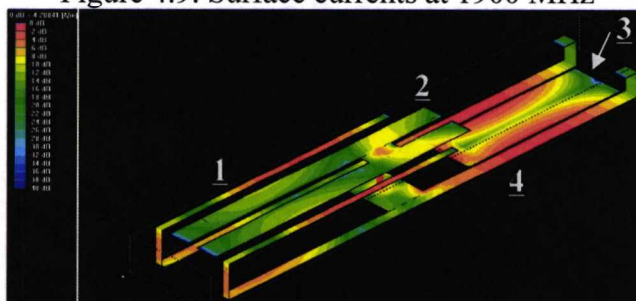


Figure 4.10. Surface currents at 2100 MHz

4.3.4 Multiband Antenna with Ground Plane Parasitic Resonator –Parametric Analysis

A parametric analysis of the multiband antenna with ground plane parasitic resonator was carried out to determine insight into the characteristics of the antenna. The main parameters considered for the analysis were the length of the elements 1, 2, 3 and 4. The parametric analysis is presented through the S11 curves of the existing modes in the antenna as its physical elements are changed. The effect of the changes in the resonant modes is shown with arrows placed in the reflection coefficient S11 (dB) curve.

Figure 4.11 shows the effect on the resonant modes of the antenna as the length of element 1 (1L) is increased from 71mm to 79mm. As can be seen from the figure, the increase in 1L caused a decrease in the resonant frequency of mode2 (M2) of 5.6% which reduced the match in mode1 by 1%. In the higher band, the resonant frequency of mode3 remains almost constant while the frequency of mode4 and mode5 decreased by 2% and 1.7% respectively; increasing the matching of M4 and decreasing the matching of M5.

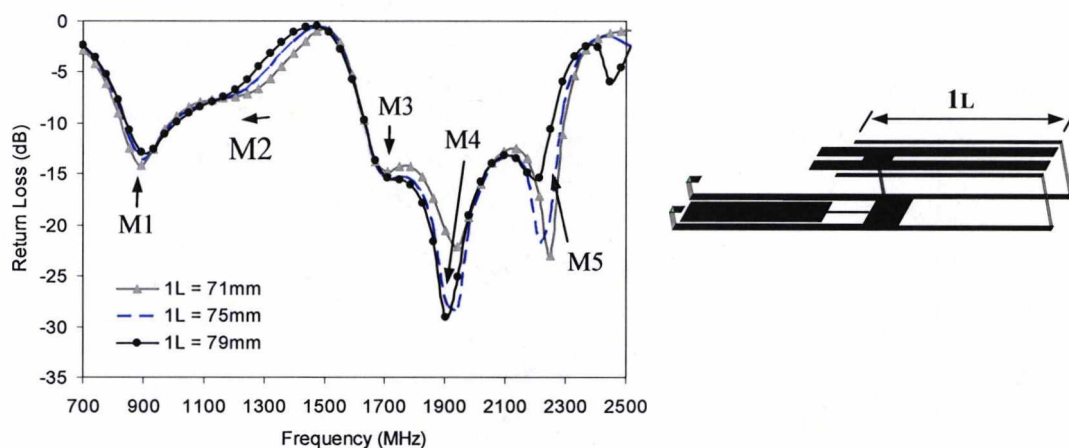


Figure 4.11 Simulated return loss of the antenna (S11) versus frequency for different element 1L lengths

The effect of varying 2L from 82mm to 86 mm on the resonant frequency and bandwidth is shown in Fig.4.12. The increase in 2L increased the matching of mode1 (M1) by 4% while its resonant frequency remained almost constant; M2 did not vary. In the higher band, the effect was considerable on M3 with its resonant frequency decreasing by over 9%. The bandwidth of the combined modes M3, M4 and M5

increased by over 22.4% as there is a higher capacitive excitation from element 2 to the coupling between elements 3 and 4. M4 does not seem to exist for values of $2L$ lower than 82mm. The resonant frequencies of M5 did not change significantly.

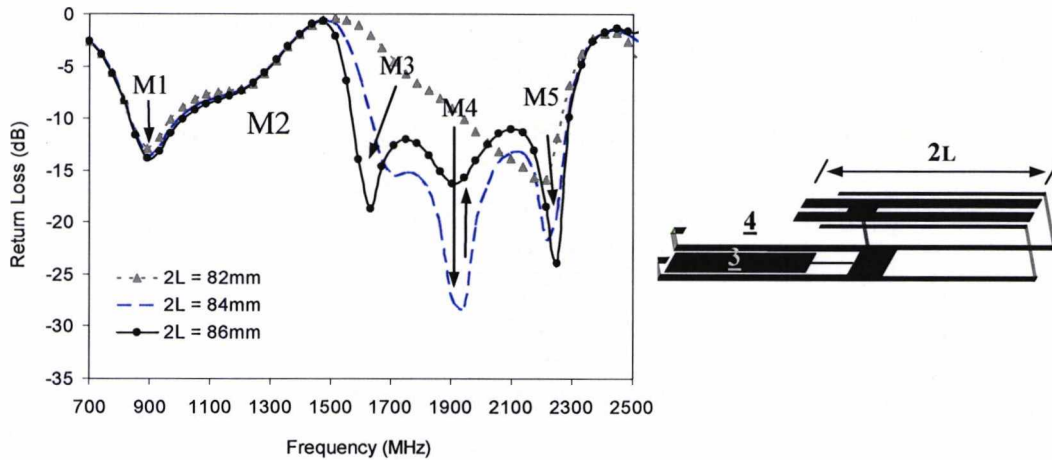


Figure 4.12 Measured return loss of the antenna (S11) versus frequency for different element $2L$ lengths

Figure 4.13 shows the effect of increasing the length $3L$ from 46.5mm to 50.5 mm on the resonant frequency and bandwidth. No changes were observed in the lower band M1 and M2 modes and the M3 mode of the higher band. In the higher band, however, the resonant frequency of mode M5 decreased by 6.7% and its matching improved by -5dB while the resonant frequency of M4 remained constant and its matching decreases by -10dB.

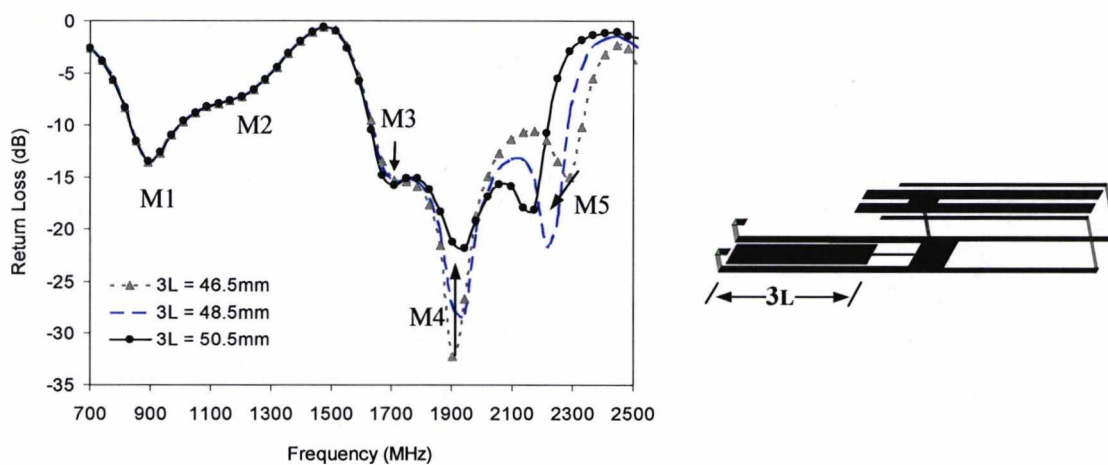


Figure 4.13 Simulated return loss of the antenna (S11) versus frequency for different element $3L$ lengths

The effect of increasing the dimension $4E$ from 0.0mm to 8.0mm on the resonant frequency and bandwidth is shown in Fig.4.14. The increase in $4E$ caused a 2.7%

decrease in the resonant frequency of M1 and increased its bandwidth by 0.5%; M2 did not change significantly. In the higher band, the resonant frequency of M5 decreased by 1.7% whilst the resonant frequency of M3 and M4 remained constant. The matching of M5 and M3 decreased while the matching of M4 increased.

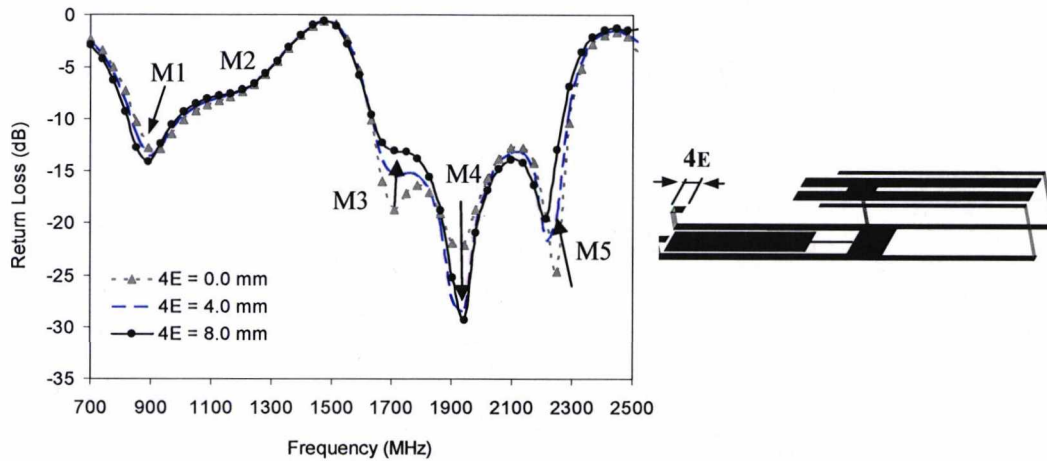


Figure 4.14 Simulated return loss of the antenna (S11) versus frequency for different element 4E lengths

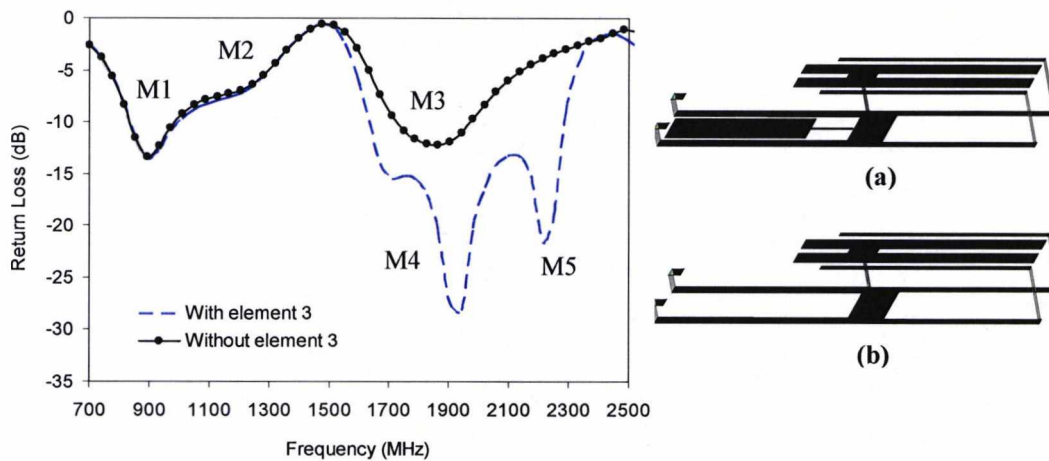


Figure 4.15 Simulated return loss of the antenna (S11) versus frequency with element 3 (a) and without element 3 (b)

Figure 4.15 compares the antenna with and without element 3. The antenna structure without element 3 is, basically, the initial dual band antenna in [13], with sufficient bandwidth to cover both the GSM band and the DCS1800 band. Only three modes (M1, M2 and M3) are observed in the antenna. The introduction of element 3 in the antenna adds M4 and M5, increasing the higher band bandwidth by 19.9%.

Finally, a summary of the parametric analysis is shown in table 4.3. Elements 1L & 4E provide the GSM900 band while 2L controls the DCS1800 band. Element 3L is the proposed new parasitic element that provides the DECT and UMTS bands in association with elements 1L & 4E. Note that the parasitic patch element 3 allows the upper band to be tuned independently of the lower band which simplifies the tuning process.

Element	Increase	Low band (decrease)		High band (decrease)		
		M1	M2	M3	M4	M5
	mm.	%	%	%	%	%
1L	+4.0	-	-2.8	-	-1.0	-0.9
2L	+2.0	-	-	-4.6	-	-
3L	+2.0	-	-	-	-	-6.7
4E	+4.0	-1.4	-	-	-	-0.9

Table 4.3 Summary of the parametric analysis of the multiband antenna with ground plane parasitic resonator.

From the present study, it can be found a manufacture tolerance of 0.5mm necessary to maintain the full performance of the antenna.

4.3.5 Multiband Antenna with Ground Plane Parasitic Resonator – Radiation patterns

The radiation patterns of the multiband antenna with ground plane resonator were measured in the anechoic chamber at the University of Kent and are shown normalized in Figs 4.16-4.24. The XY, XZ and YZ planes of the antenna were measured at 850MHz, 920MHz, 1800MHz and 2100 MHz. The radiation patterns were those of a PIFA antenna on a small ground plane which are similar to dipole patterns. Good omnidirectional radiation was observed in the YZ plane for all the frequency bands which suggests that the antenna is well suited to its intended application as a picocell basestation antenna. The peak gain was also measured for all

bands and was found to vary by only 0.5dBi across the GSM band. The gain at centre frequency of the GSM900, DCS1800, DECT and UMTS bands are 1.9, 3.2, 3.1 and 2.1 dBi respectively. The measured gain never fell significantly below 1dBi.

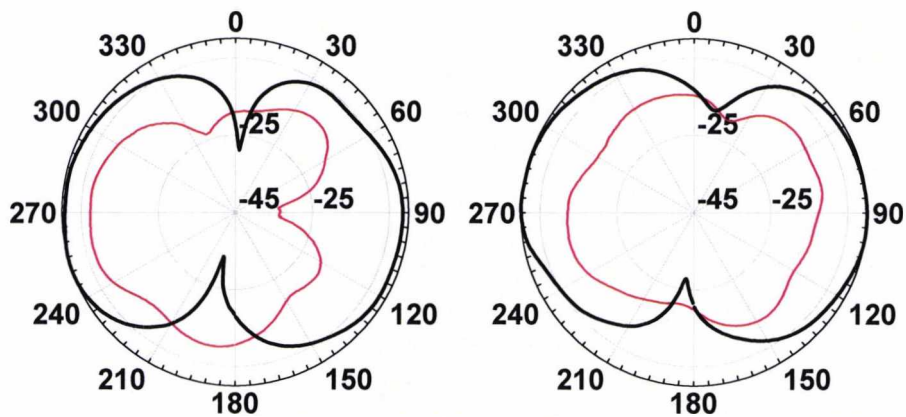


Figure 4.16 Measured far field pattern in the XY plane at 850 MHz (left) and 920 MHz (right). Co-polar (thick line) and cross-polar (thin line)

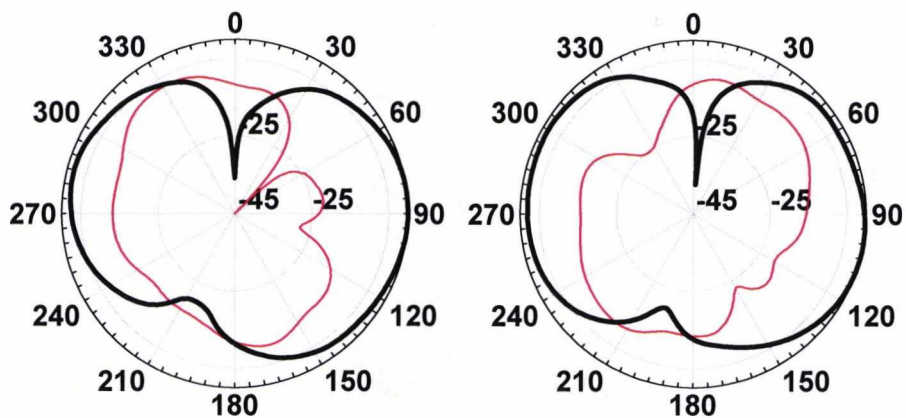


Figure 4.17 Measured far field pattern in the XZ plane at 850 MHz (left) and 920 MHz (right). Co-polar (thick line) and cross-polar (thin line)

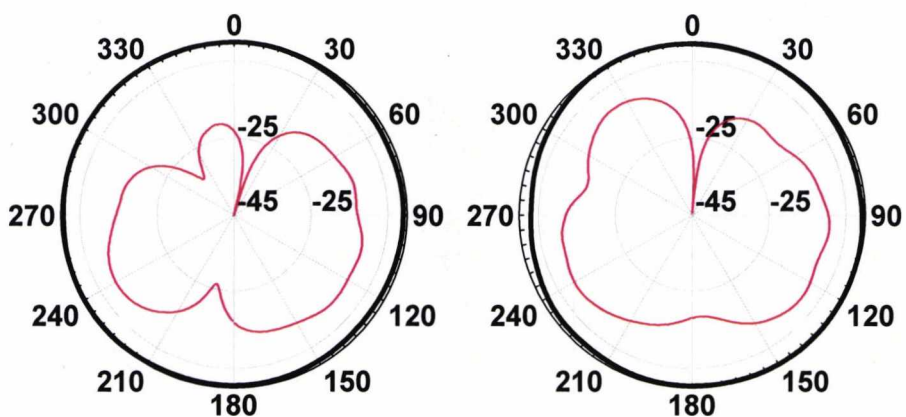


Figure 4.18 Measured far field pattern in the YZ plane at 850 MHz (left) and 920 MHz (right). Co-polar (thick line) and cross-polar (thin line)

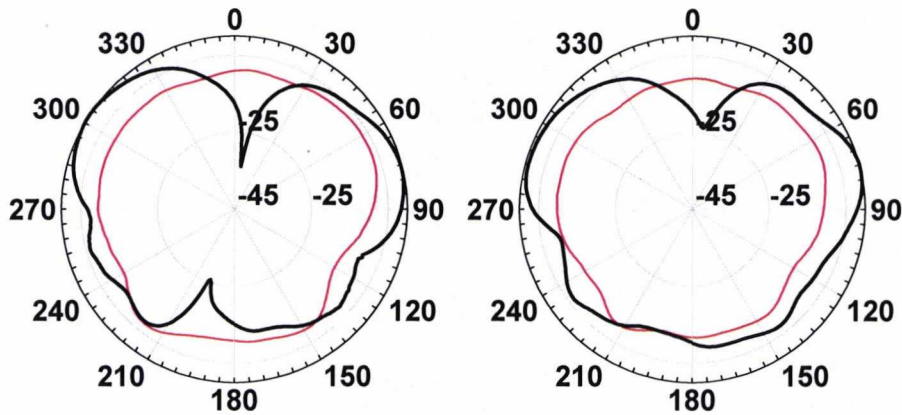


Figure 4.19 Measured far field pattern in the XY plane at 1800 MHz (left) and 1900MHz (right). Co-polar (thick line) and cross-polar (thin line)

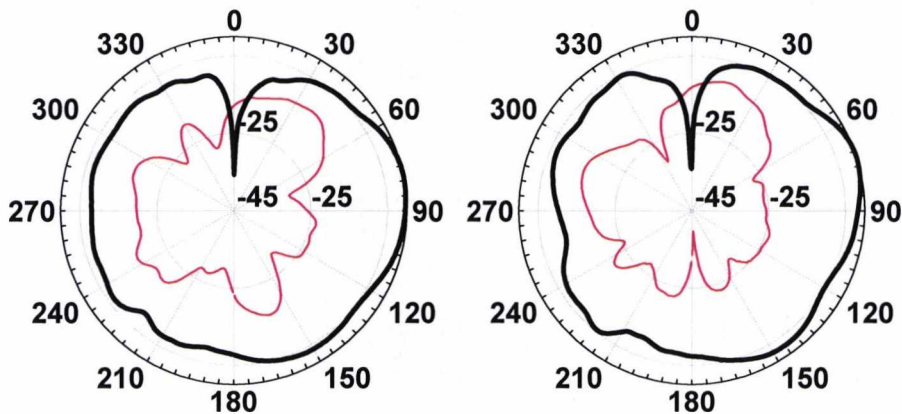


Figure 4.20 Measured far field pattern in the XZ plane at 1800 MHz (left) and 1900MHz (right). Co-polar (thick line) and cross-polar (thin line)

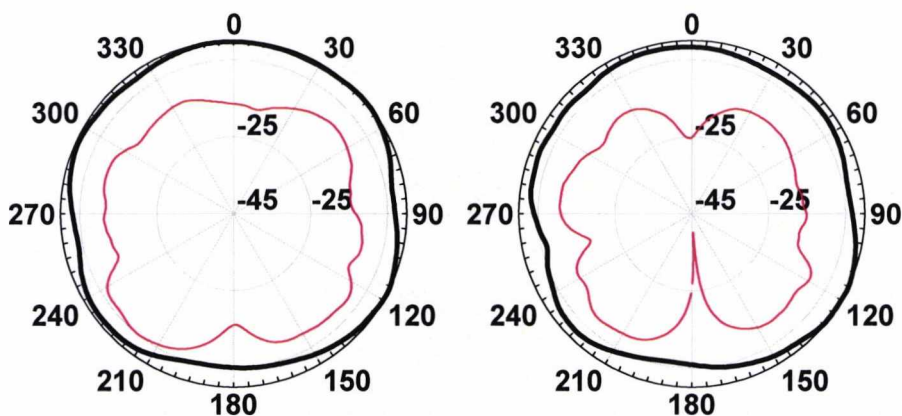


Figure 4.21 Measured far field pattern in the YZ plane at 1800 MHz (left) and 1900MHz (right). Co-polar (thick line) and cross-polar (thin line)

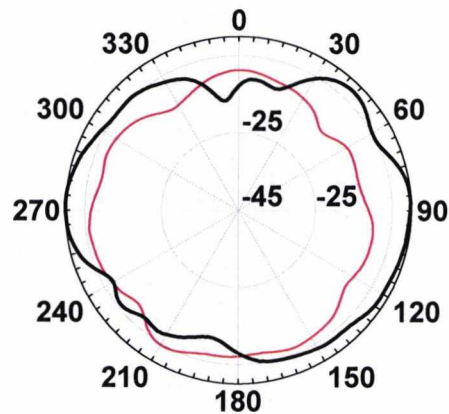


Figure 4.22 Measured far field pattern in the XY plane at 2100 MHz . Co-polar (thick line) and cross-polar (thin line)

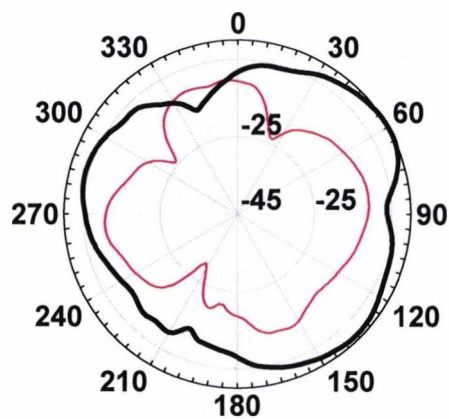


Figure 4.23 Measured far field pattern in the XZ plane at 2100 MHz. Co-polar (thick line) and cross-polar (thin line)

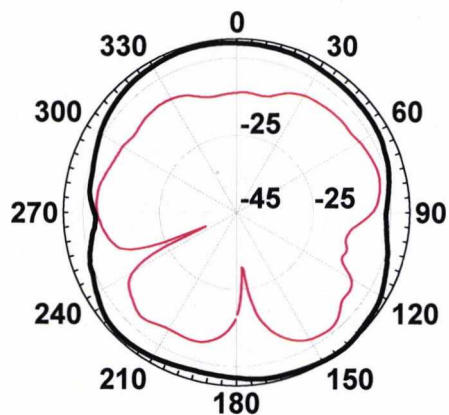


Figure 4.24 Measured far field pattern in the YZ plane at 2100 MHz. Co-polar (thick line) and cross-polar (thin line)

4.4 Multiband Antenna with Side Resonators

In section 4.3 a multiband operation was achieved by adding a ground plane parasitic element to the dual band antenna developed in [13] at the University of Kent. The antenna improved the higher band bandwidth by nearly 20% and was able to cover the GSM850, GSM900, DCS1800, PCS1900, DECT and UMTS bands. In this section, two side resonators are added to increase further the higher band bandwidth and cover the Bluetooth band. The antenna with the added element 5 is shown in Fig.4.25. An identical element 5 is placed on the far side of the antenna not shown in the figure.

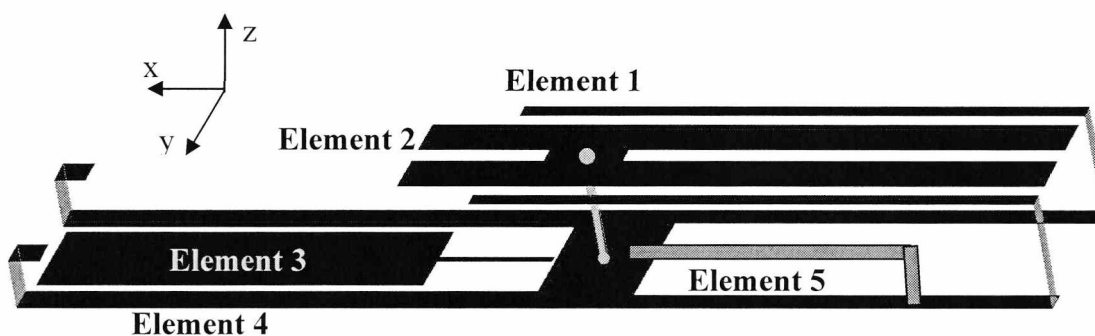


Figure 4.25. Multiband antenna with side resonators

The addition of element 5 increases the higher band bandwidth of the antenna without increasing the volume of the original antenna. The increase in the bandwidth is achieved by adding an extra mode in the higher band without cancelling the currents from the existing modes.

4.4.1 Multiband Antenna with Side Resonators – Dimensions

The dimensions of the multiband antenna with side resonators are shown in Fig.4.26 and Table 4.4. The total dimensions of the antenna are 131x24x9.5 which is 2mm smaller than the antenna in section 4.3. The dimension of the added side elements was 6.5mm x 1.5mm and was placed at 6.5mm from the ground of the antenna. The main changes made on the existing element in the previous antenna are the reduction in the size of element 1L by 6.5mm and element 3L by 2.5mm. The changes in the dimensions were determined by simulation modelling of the antenna using IE3D.

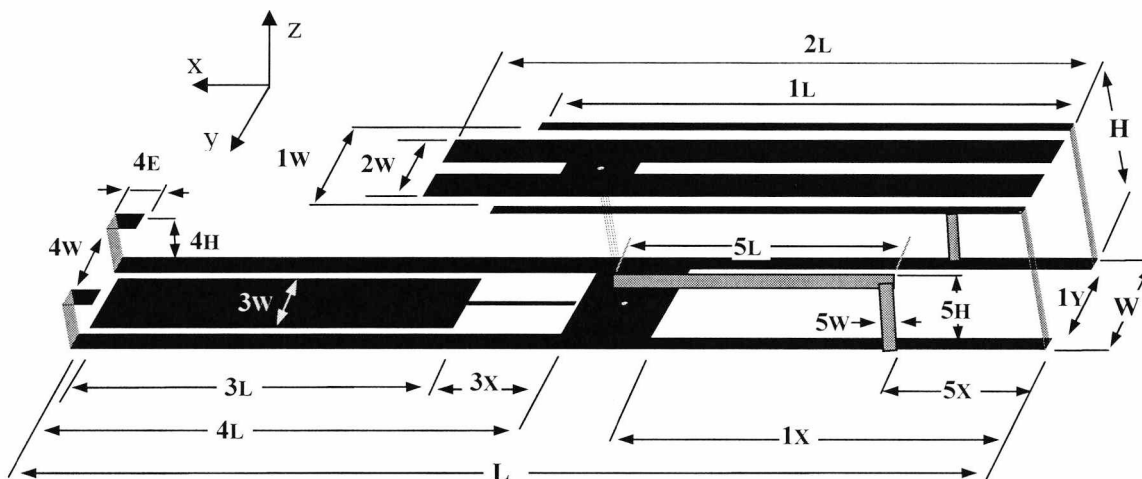


Figure 4.26. Dimensions of the multiband antenna with side resonators

Element	W	L	H	1L	1w	1x	1Y	2L
Dimensions	24.0	131.0	9.5	68.5	20.0	54.5	18.0	83.0
Element	2w	3L	3w	3x	4L	4w	4E	4H
Dimensions	15.0	46	15.0	14.5	64.0	16.0	2.0	6.5
Element	5x	5H	5L	5w				
Dimensions	19.5	6.5	35.0	1.5				

Table 4.4 Dimension of the multiband antenna with side resonators

4.4.2 Multiband Antenna with Side Resonators – Measurement Results, Reflection Coefficient

The simulated and measured S11 curves for the multiband antenna with the added side resonators are shown in Fig.4.27 and Table 4.5. A multiband characteristic is observed with -10dB S11 bandwidth of 13.7% at the lower band and 38.5% at the higher band. The 5.5% increase in the higher band bandwidth is mainly achieved by incorporating the extra mode 6 with the addition of element 5 and shifting up the resonant frequency of mode 4 and mode 5 by 150MHz and 207MHz respectively. The shift in resonant frequency of the modes 4 and 5 is achieved by decreasing the size of element 3 and element 1.

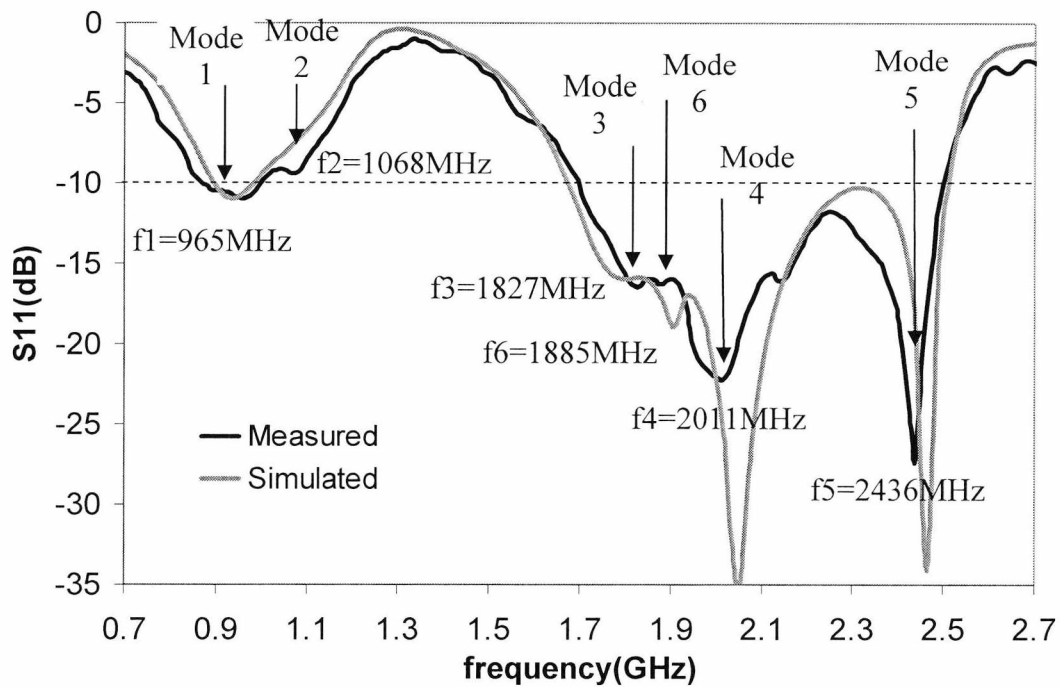


Figure 4.27 Simulated and Measured S11 curves with main modes in the multiband antenna with ground plane parasitic resonator

	Low band (MHz)	BW low band (MHz) - %	High band (MHz)	BW high band (MHz) - %
Simulated air	890 - 982	92 - 9.8 %	1675 - 2510	835 - 39.9 %
Measured air	872 - 1000	128 - 13.7 %	1695 - 2502	807 - 38.5 %

Table 4.5 Simulated and Measured S11 for the multiband antenna with side resonators

4.4.3 Multiband Antenna with Side Resonators – Surface currents

The surface currents of the multiband antenna with the added side resonators at 900MHz, 1800MHz, 1900MHz, 2100 MHz and 2450 MHz are shown in Figs.4.28 to 4.32.

Similar to the original antenna of section 4.3, at 900 MHz (Fig.4.29), there are strong currents in element 1 and 4 being coupled through element 2 connected to the feed.

At 1800 MHz (Fig.4.30), the added side resonators (element 5) become active showing strong currents which are also present in element 1,2 and 4.

At 1900 MHz, the currents in element 5 lose strength while currents in elements 1, 2 and the coupling between elements 3 and 4 become stronger.

At 2100 MHz, the currents in element 1 and 2 appear to be weaker, while currents in the coupling between element 3 and 4 gain strength.

Finally, at 2450 most of the strong currents are concentrated in the coupling between element 3 and 4.

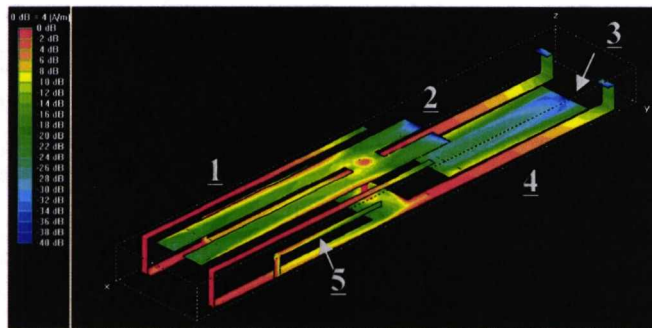


Figure 4.28. Surface currents at 900 MHz

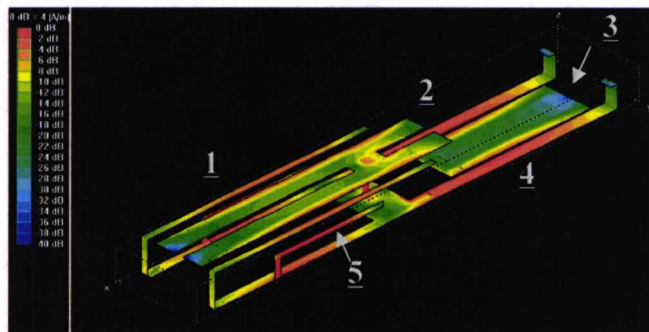


Figure 4.29. Surface currents at 1800 MHz

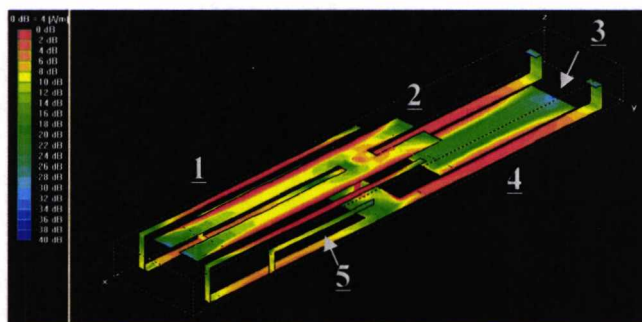


Figure 4.30. Surface currents at 1900 MHz

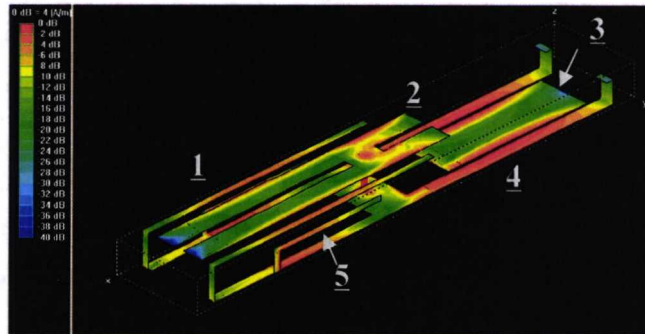


Figure 4.31. Surface currents at 2100 MHz

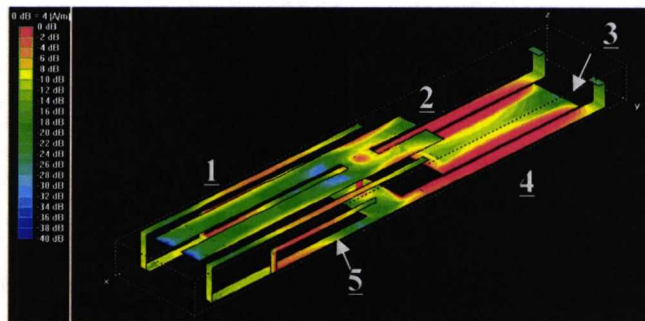


Figure 4.32. Surface currents at 2450 MHz

4.4.4 Multiband Antenna with Side Resonators – Parametric Analysis

A further parametric analysis of the multiband antenna with the added side resonators was carried out to determine the sensitivity of the antenna to changes in its dimensions. The main parameters considered for the analysis were the length of the elements 1, 2, 3, 4 and 5.

Figure 4.33 shows the effect on the resonant modes of the antenna as the length of element 1 (1L) is increased from 64.5mm to 72.5mm. Similarly to the antenna in section 4.4.3, the increase in 1L caused a decrease in the resonant frequency of mode 2 (M2), which decreased by 3.4% and reduced the matching of mode 1 by 4.4%. In the higher band, the resonant frequency of mode 3 remained almost constant while the frequency of M4 and M6 decreased by 1.4% and 5.2% respectively, increasing the matching of M4 and decreasing the matching of M5 and M6.

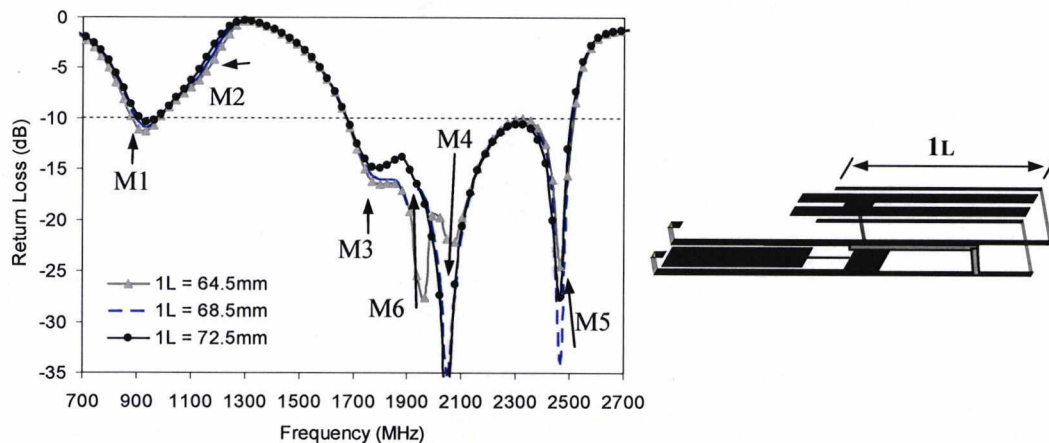


Figure 4.33 Simulated return loss of the antenna (S11) versus frequency for different element $1L$ lengths

The effect of varying $2L$ from 82mm to 84 mm on the resonant frequency and bandwidth is shown in Fig.4.34. The effect was the same as in the original antenna with M3 and M4 decreasing by 3.2% and 1.4% respectively while the other modes and the new mode 6 remained almost constant.

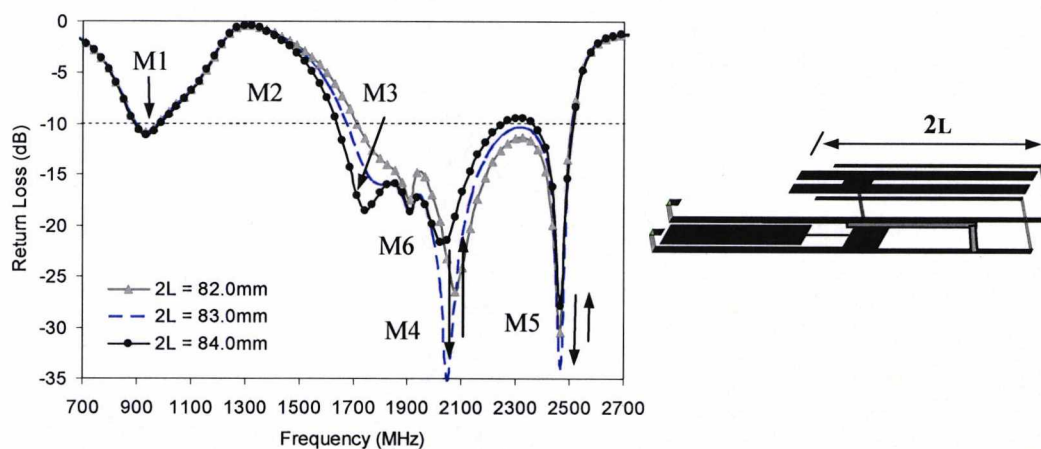


Figure 4.34 Simulated return loss of the antenna (S11) versus frequency for different element $2L$ lengths

Figure 4.35 shows the effect of increasing the length $3L$ from 44mm to 48 mm on the resonant frequency and bandwidth. The same effect on the antenna as in the previous section was observed with only the resonant frequency of mode 5 decreasing by 6.7%.

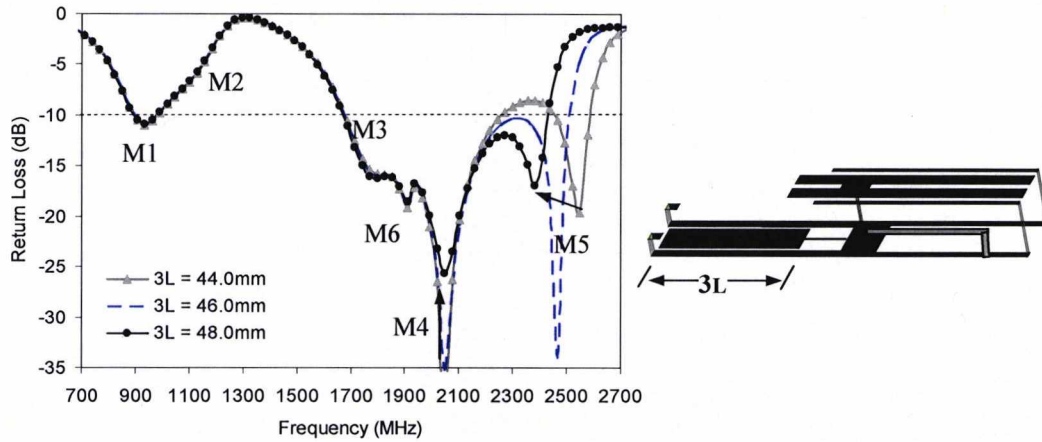


Figure 4.35 Simulated return loss of the antenna (S11) versus frequency for different element 3L lengths

The effect of increasing the dimension 4E from 0.0mm to 4.0mm on the resonant frequency and bandwidth is shown in Fig.4.36. The effect on the modes of the antenna was similar to the one in section 4.3 with less pronounced variations due to the smaller change in the dimensions (4E was varied between 0-8mm in section 4.3). The increase in 4E caused a decrease in the resonant frequency of M1 and M5 of 2.7% and 1.7% respectively; M2 and M6 did not change significantly. The matching of M5 and M3 decreased while the matching of M4 increased. The bandwidth of M1 increased by 2%.

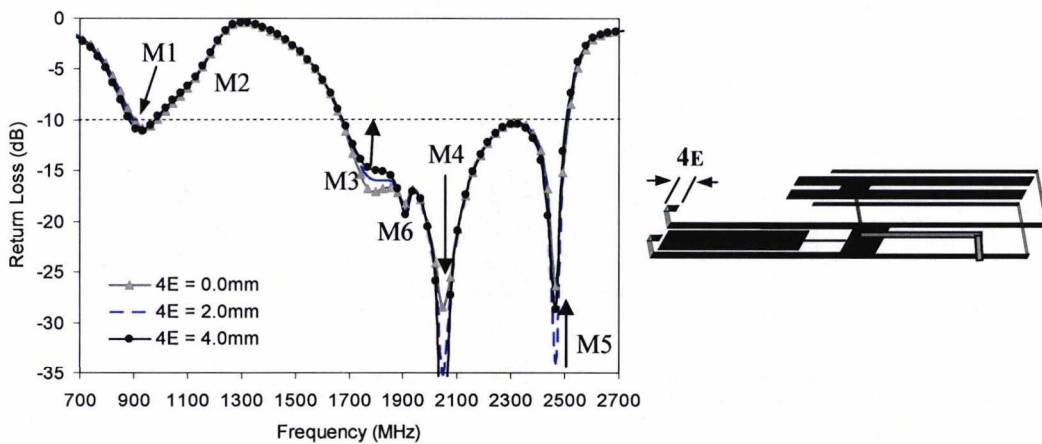


Figure 4.36 Simulated return loss of the antenna (S11) versus frequency for different element 4E length

The effect of increasing the dimensions of the new element 5L from 33.0mm to 37.0mm on the resonant frequency and bandwidth is shown in Fig.4.37. The effect on

the new element is limited to M2 (decreased by 3.2%) and the new mode M6 (decreased by 5.4%) which indirectly affects to the nearby modes 1, 3, 4 and 5.

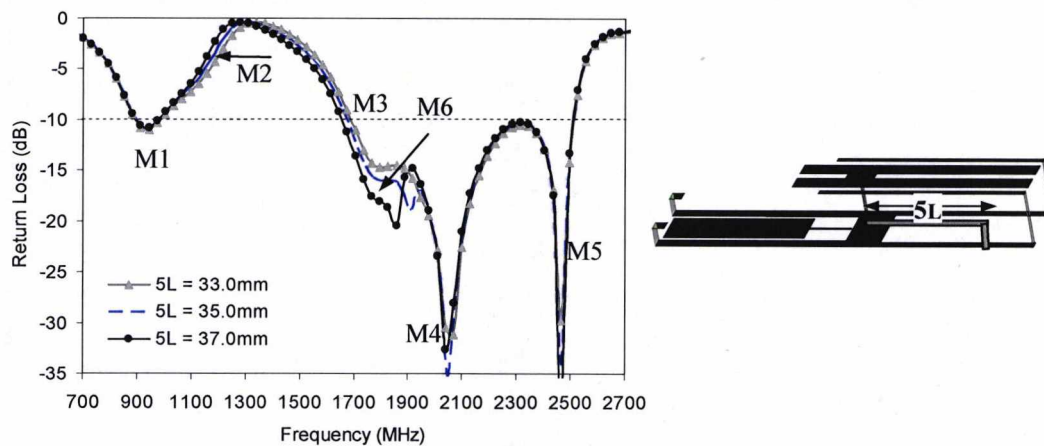


Figure 4.37 Simulated return loss of the antenna (S11) versus frequency for different element 5L length

Figure 4.38 shows the effect of removing totally the new element 5 which eradicated mode 6, decreasing the higher band bandwidth by 5%. There was also a significant effect in mode 2, which increased its resonant frequency by 24% and improved the bandwidth of mode 1 by 2.8%.

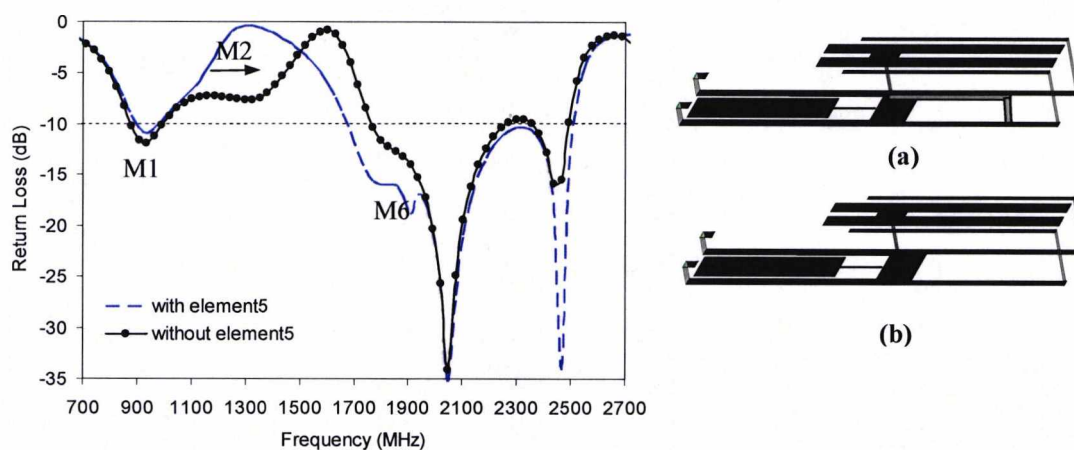


Figure 4.38 Simulated return loss of the antenna (S11) versus frequency with element 5 (a) and without element 5 (b)

Figure 4.39 compares the antenna with and without element 3. The difference from the analysis made in section 4.3 is the presence of the new mode (M6) once element 3 is removed. The higher band bandwidth without element 3 was 18.4% lower than with element 3.

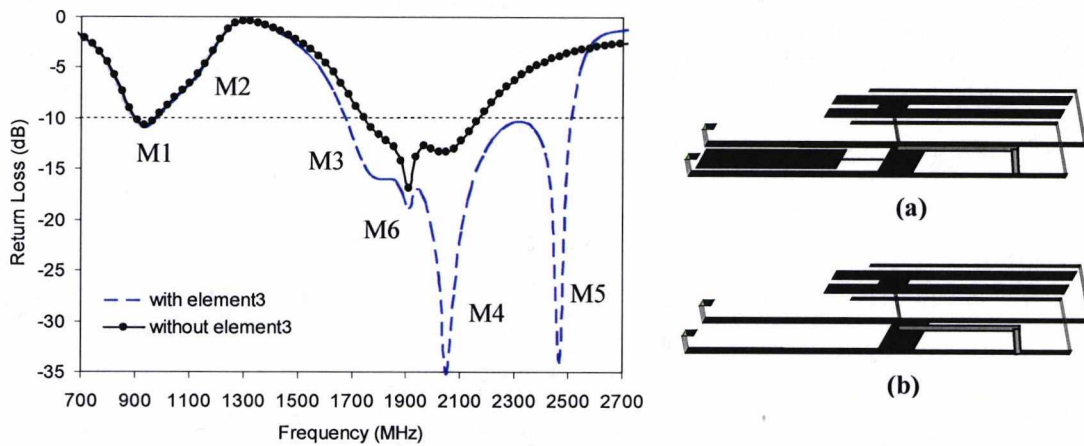


Figure 4.39 Simulated return loss of the antenna (S11) versus frequency with element4 (a) and without element 4 (b)

Finally, a summary of the parametric analysis is shown in table 4.6. The GSM900 band is provided mainly by 4 and 1 with the new element 5 also having some effect in this band. The DCS1800 is controlled mainly by 2L through M3 and the DECT band by the extra element5 through the additional M6. The UMTS band is controlled by elements 2 and 1 through M4 and the Bluetooth band by elements 3 through M5.

Element	Increase mm.	Low band (decrease)		High band (decrease)			
		M1	M2	M3	M6	M4	M5
		%	%	%	%	%	%
1L	+4.0	-	-1.7	-	-2.6	-0.7	-
2L	+2.0	-	-	-3.2	-	-1.4	-
3L	+2.0	-	-	-	-	-	-6.7
4E	+4.0	-2.7	-	-	-	-	-1.7
5L	+4.0	-	-3.2	-	-5.4	-	-

Table 4.6 Summary of the parametric analysis of the multiband antenna with ground plane parasitic resonator.

It can be concluded from table 4.6 that the manufacture tolerance of the antenna will depend on element 3L. Manufacture tolerance of 0.2mm is needed to keep the antenna working at all frequency bands.

4.4.5 Multiband Antenna with Side Resonators – Radiation Patterns

The normalized radiation patterns of the multiband antenna with ground plane parasitic resonator and side resonators at 920MHz, 1800MHz, 1900MHz, 2100MHz and 2450MHz are shown in Figs.4.40 to 4.48. Similar to the antenna in section 4.3, the radiation patterns were those of a PIFA antenna on a small ground plane. Good omnidirectional patterns were observed in the YZ plane for all frequency bands. The gain at centre frequency of the GSM900, DCS1800, DECT, UMTS and Bluetooth bands were 1.7, 3.3, 2.9, 1.9 and 2.1 dBi respectively. The measured gain never fell significantly below 1dBi.

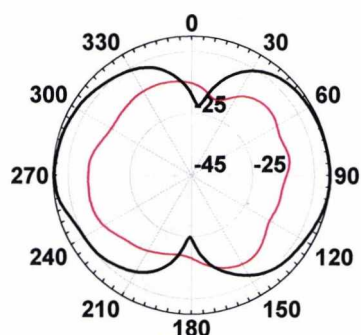


Figure 4.40 Measured far field pattern in the XY plane at 920 MHz. Co-polar (thick line) and cross-polar (thin line)

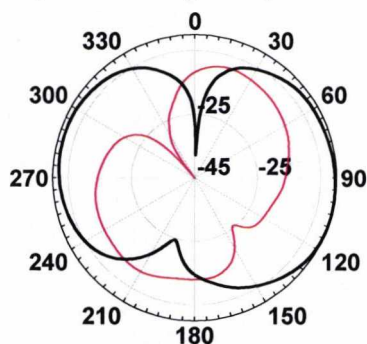


Figure 4.41 Measured far field pattern in the XZ plane at 920 MHz. Co-polar (thick line) and cross-polar (thin line)

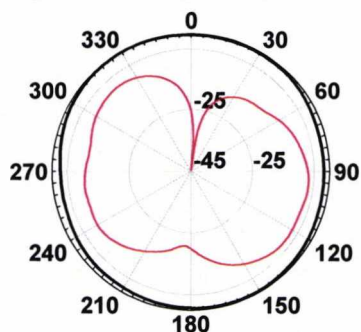


Figure 4.42 Measured far field pattern in the YZ plane at 920 MHz. Co-polar (thick line) and cross-polar (thin line)

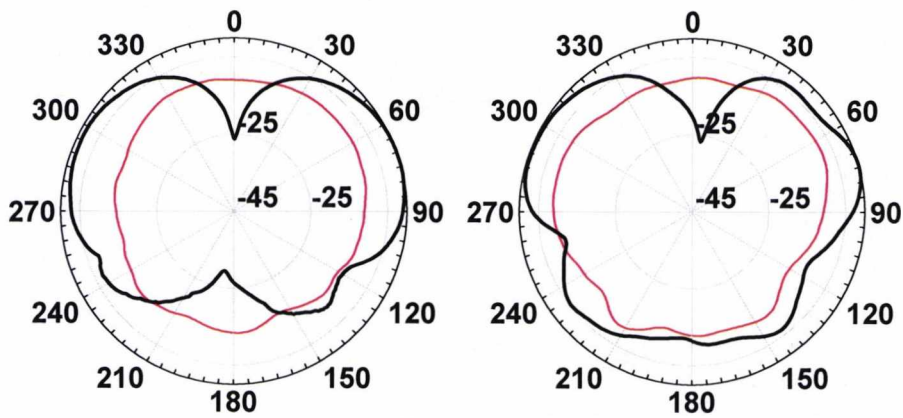


Figure 4.43 Measured far field pattern in the XY plane at 1800 MHz (left) and 1900 MHz (right). Co-polar (thick line) and cross-polar (thin line)

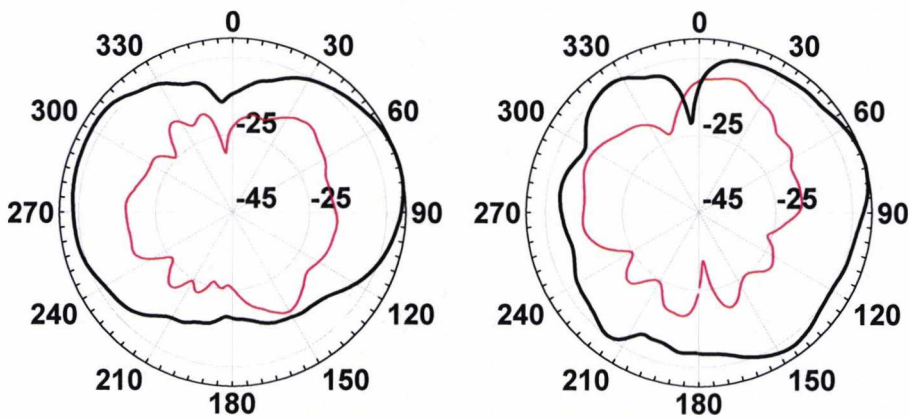


Figure 4.44 Measured far field pattern in the XZ plane at 1800 MHz (left) and 1900 MHz (right). Co-polar (thick line) and cross-polar (thin line)

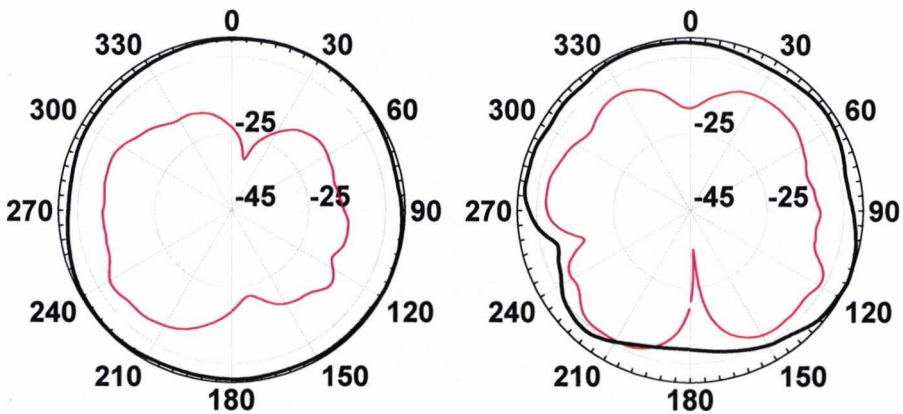


Figure 4.45 Measured far field pattern in the YZ plane at 1800 MHz (left) and 1900 MHz (right). Co-polar (thick line) and cross-polar (thin line)

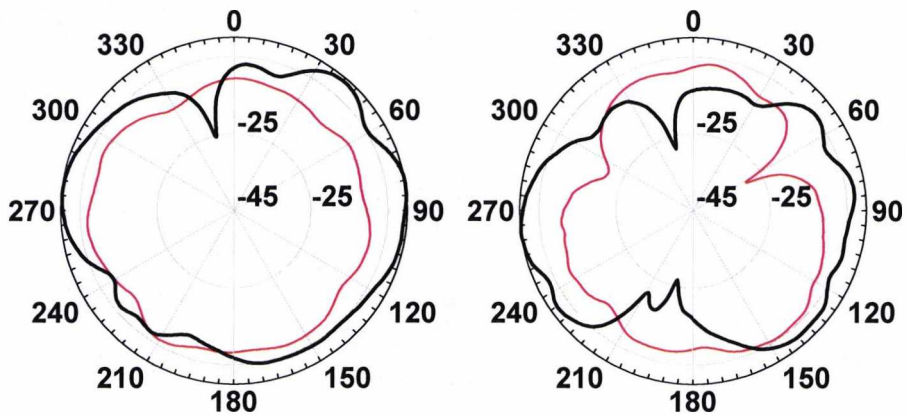


Figure 4.46 Measured far field pattern in the XY plane at 2100 MHz (left) and 2450MHz (right). Co-polar (thick line) and cross-polar (thin line)

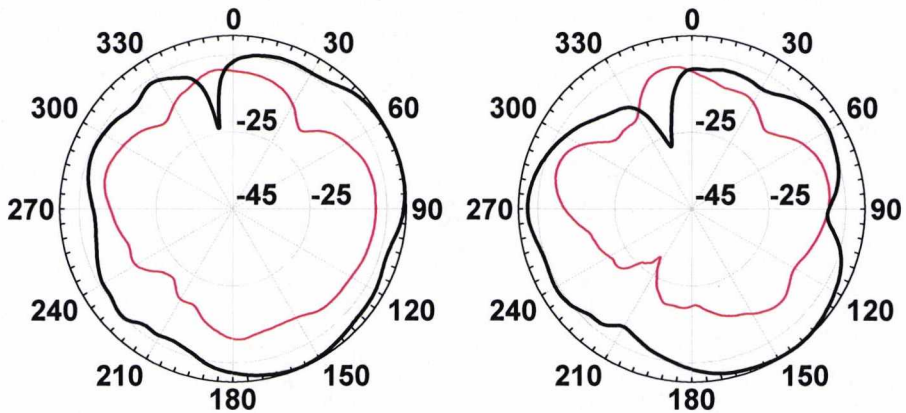


Figure 4.47 Measured far field pattern in the XZ plane at 2100 MHz (left) and 2450MHz (right). Co-polar (thick line) and cross-polar (thin line)

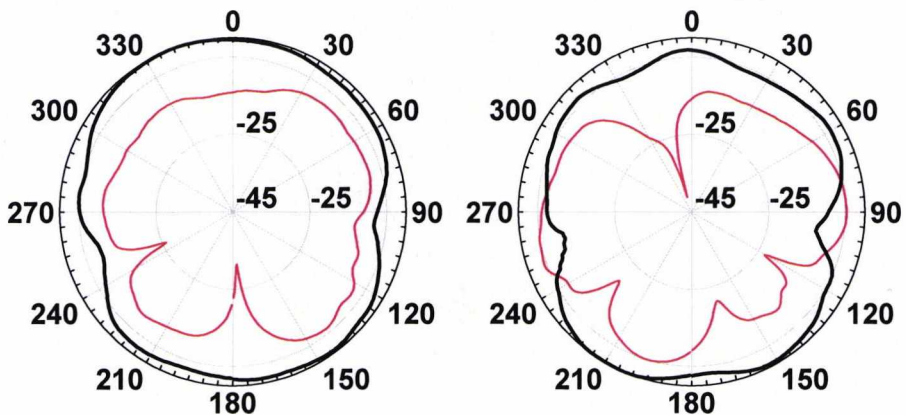


Figure 4.48 Measured far field pattern in the YZ plane at 2100 MHz (left) and 2450MHz (right). Co-polar (thick line) and cross-polar (thin line)

4.5 Multiband Antenna with Multiresonators

The final antenna to be presented in this chapter is a further improvement on the multiband antennas presented in previous sections. The side resonators introduced in section 4.4 have been rearranged and two extra elements 6 have been added as shown in Fig.4.49. The addition of element 6 allows the antenna to be made smaller. Once the antenna is made smaller, a relocation of element 5 is necessary to maintain the bandwidth required at the higher frequency band.

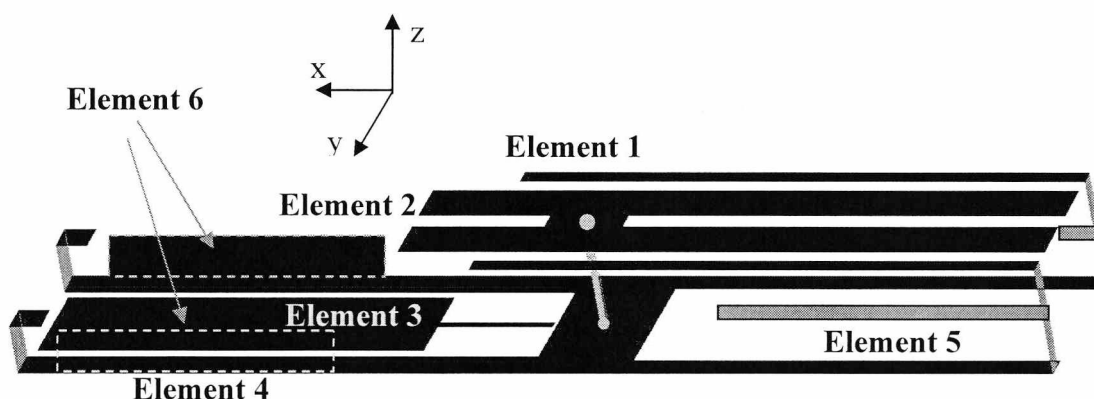


Figure 4.49 Multiband antenna with multiresonators

4.5.1 Multiband Antenna with Multiresonators – Dimensions

The dimensions of the multiband antenna with multiresonators are shown in Fig. 4.50 and Table 4.7. The total dimensions of the antenna are 131x20x8mm which is 30% smaller in volume than the antenna in section 4.4. The reduction in size has been made mainly in the antenna width (4mm smaller) and the antenna height (1.5mm smaller).

The dimensions of the new extension (element6) in the ground were 41mm x 48mm. Other significant changes have been made in 1L which is increased by 3mm, 3L increased by 2.5mm and 5L increased by 5mm.

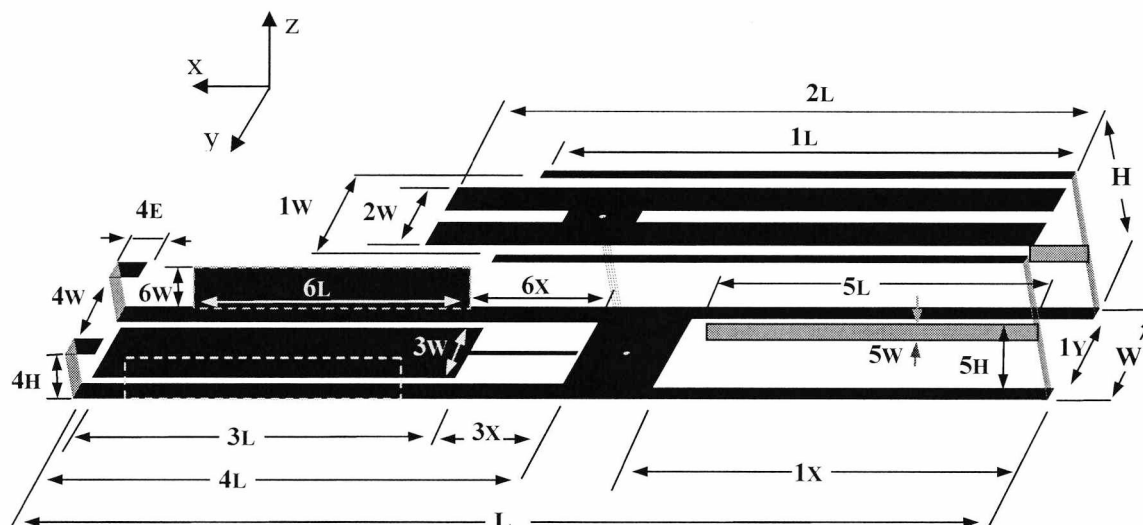


Figure 4.50 Dimensions of the multiband antenna with multiresonators

Element	W	L	H	1L	1w	1x	1Y	2L
Dimensions	20.0	131.0	8.0	71.5	16.0	54.5	16.0	82.0
Element	2w	3L	3w	3X	4L	4w	4E	4H
Dimensions	9.0	48.5	12.0	11.5	64.0	13.0	2.0	6.5
Element	5H	5L	5w	6X	6L	6w		
Dimensions	5.5	40.0	2.5	19.0	41.0	4.8		

Table 4.7 Dimension of the multiband antenna with side resonators

4.5.2 Multiband Antenna with Multiresonators – Measurements Results, S11

The simulated and measured S11 curves for the multiband antenna with multiresonators are shown in Fig.4.51 and Table 4.8. A multiband characteristic is observed with -10dB S11 bandwidth of 22.0% at the lower band and 39.5% at the higher band. The increase in the bandwidth from the antenna in section 4.4 was of 8.3% in the lower band and just 1% in the higher band. The most important changes in the resonant frequency of the modes of the antenna were observed in mode 6 which decreases by 139MHz, with mode 3 increasing by 138 MHz and mode 4 increasing by 104 MHz. It is worth noting that the rearrangement of element 5 and the further adjustments in the antenna have swapped the order of the modes with mode 6 at lower frequency than mode3.

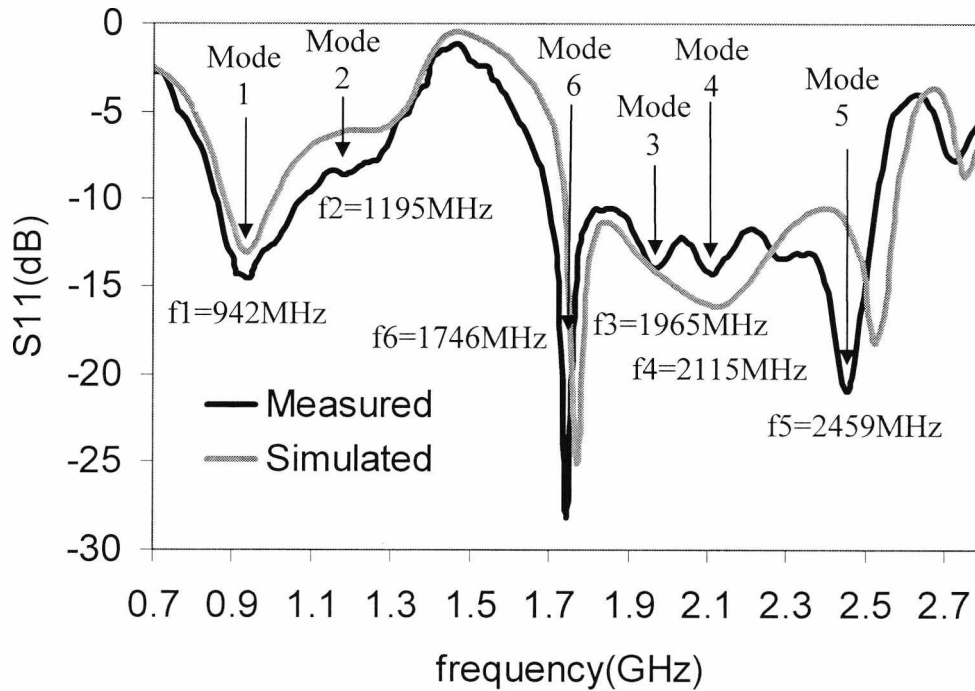


Figure 4.51 Simulated and Measured S11 curves with main modes in the multiband antenna with multiresonators

	Low band (MHz)	BW low band (MHz) - %	High band (MHz)	BW high band (MHz) - %
Simulated air	880 - 1005	125 - 13.3%	1740 - 2575	835 - 38.7 %
Measured air	858 - 1070	212 - 22.0%	1695 - 2530	835 - 39.5 %

Table 4.8 Simulated and Measured S11 for the multiband antenna with multiresonators

4.5.3 Multiband Antenna with Multiresonators – Surface currents

The surface current of the multiband antenna with the added side resonators at 900MHz, 1800MHz, 1900MHz, 2100 MHz and 2450 MHz are shown in Figs.4.52 to 4.56.

Similarly to the antenna in section 4.4, at 900 MHz (Fig.4.52), there are strong currents in element 1&4 being coupled through element 2 connected to the feed. There is also high current density at the edges of element 6.

At 1800 MHz (Fig.4.53), the side resonators (element 5) become active showing strong currents which are also present in elements 1, 2, 4 and 6.

At 1900 MHz, the currents in elements 1,2 and 5 lose strength while currents in the coupling between elements 3 and 4 become stronger.

At 2100 MHz, the currents in element 1 and 2 appear to be weaker, while the coupling between element 3 and 4 gain strength.

Finally, at 2450 MHz most of the strong currents are concentrated around the gap between element 3 and 4.

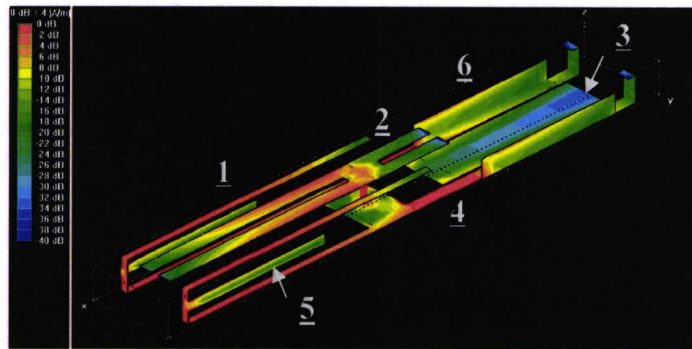


Figure 4.52 Surface currents at 900 MHz

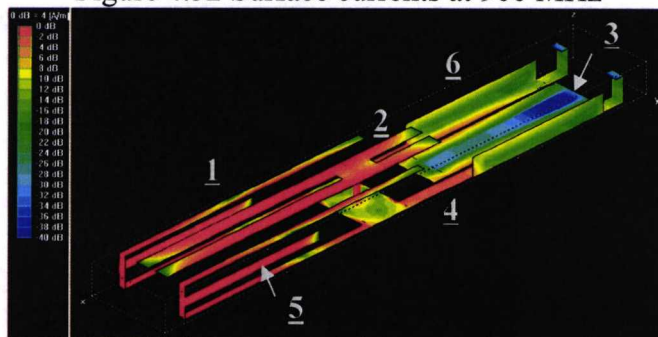


Figure 4.53 Surface currents at 1800 MHz

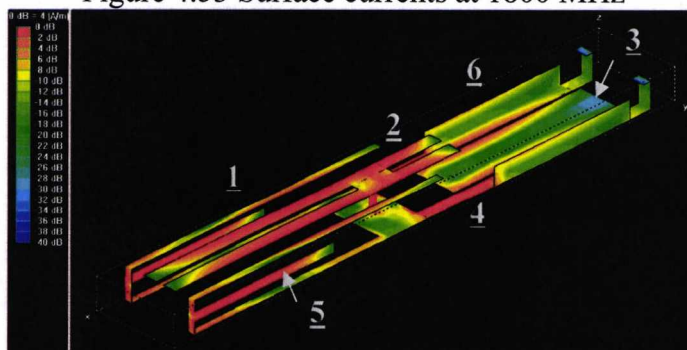


Figure 4.54 Surface currents at 1900 MHz

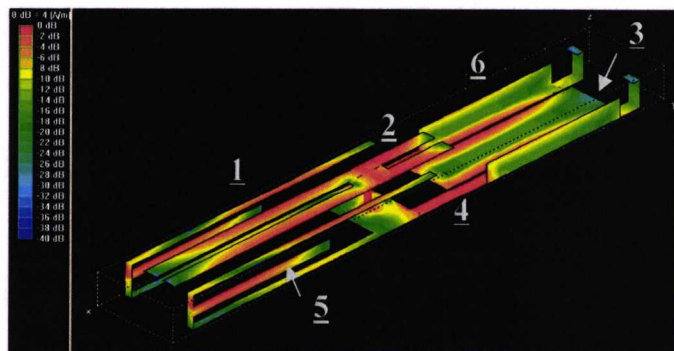


Figure 4.55 Surface currents at 2100 MHz

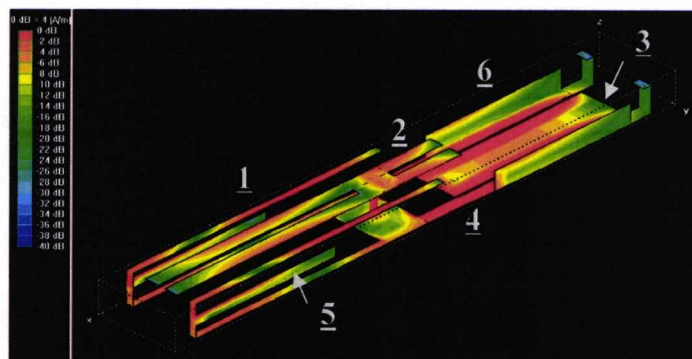


Figure 4.56 Surface currents at 2450 MHz

4.5.4 Multiband Antenna with Multiresonators – Parametric Analysis

A parametric analysis of the multiband antenna with ground plane parasitic resonator was carried out to determine insight into the characteristics of the antenna. The main parameters considered for the analysis were the length of the elements 1, 2, 3, 4, 5 and 6.

Figure 4.57 shows the effect on the resonant modes of the antenna as the length of element 1 ($1L$) is increased from 69.5mm to 73.5mm. As can be seen from the figure, an increase in $1L$ caused the same effect to previous two antennas with a decrease in the resonant frequency of mode2 (M2) of nearly 3% and a reduction in the bandwidth of mode1 of 2.3%. In the higher band, the resonant frequency M6 and M3 remained almost constant while the frequency of M5 decreased by 2.1%, increasing the matching of M5 and decreasing the matching of M4 and M3.

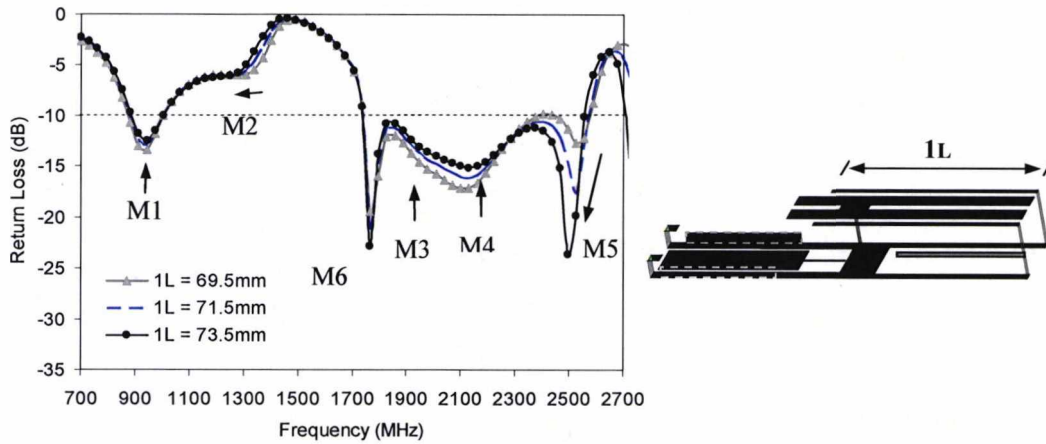


Figure 4.57 Measured return loss of the antenna (S11) versus frequency for different element 1L lengths

The effect of varying 2L from 81mm to 83mm on the resonant frequency and bandwidth is shown in Fig.4.58. The effect is similar to the antenna with side resonators (section 4.4), with the resonant frequency of M3 decreasing by 5.6% while the other modes and the new M6 remained almost constant. M5 decreased its matching.

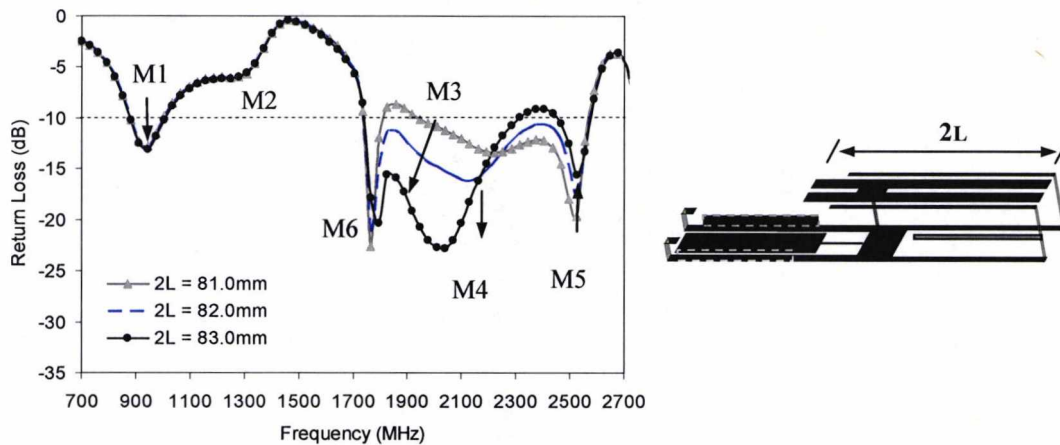


Figure 4.58 Measured return loss of the antenna (S11) versus frequency for different element 2L lengths

Figure 4.59 shows the effect of increasing the length 3L from 46.5 mm to 50.5 mm on the resonant frequency and bandwidth. The same effect to the one in the original antenna is observed with only the resonant frequency of mode 5 decreasing by 4.8%. The drop in the resonant frequency of M5 decreased the bandwidth of the higher frequency band by 5.2%.

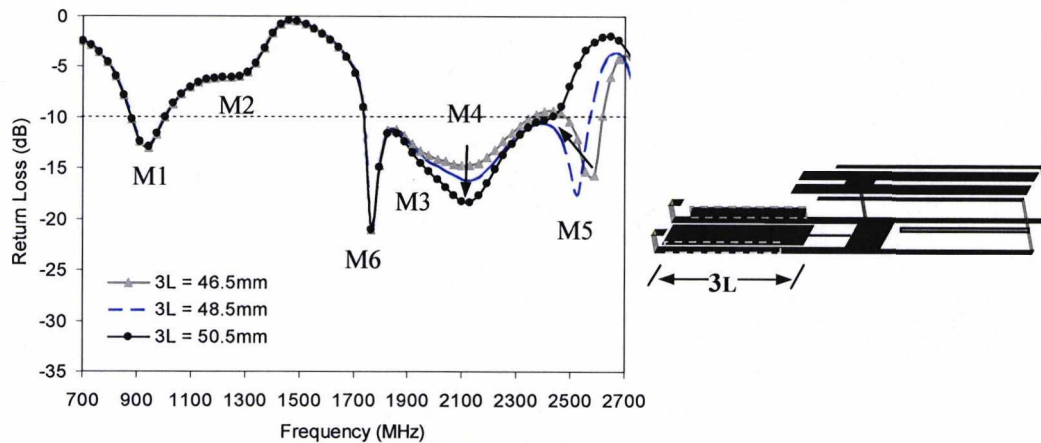


Figure 4.59 Measured return loss of the antenna (S11) versus frequency for different element 3L lengths

The effect of increasing the dimension 4E from 0.0mm to 4.0mm on the resonant frequency and bandwidth is shown in Fig.4.60. Increasing 4E caused a similar but less pronounced effect to that in the antennas of sections 4.3 and 4.4. The increase in 4E caused a decrease in the resonant frequency of M1 of 1.1%. M2, M6 and M5 did not change significantly. The matching of M5 and M3 decreased while the matching of M4 increased.

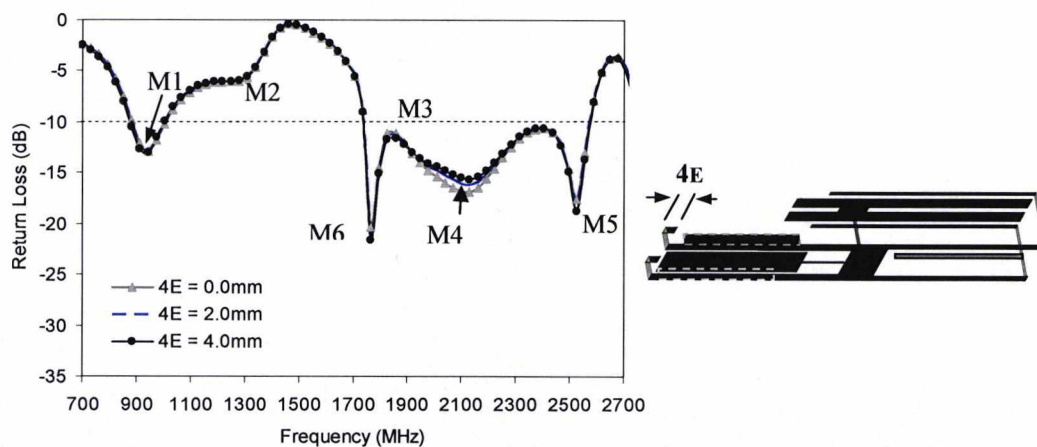


Figure 4.60 Measured return loss of the antenna (S11) versus frequency for different element 3L lengths

The effect of increasing the dimensions of the relocated element 5L from 38.0mm to 42.0mm on the resonant frequency and bandwidth is shown in Fig.4.61. The effect of the increase in 5L was limited to M2 which resonant frequency decreased by 2.2%

and the new mode M6 with a 2.8% decrease in resonant frequency. The changes in M2 and M6 indirectly affected the matching of nearby modes M1, M3, M4 and M5.

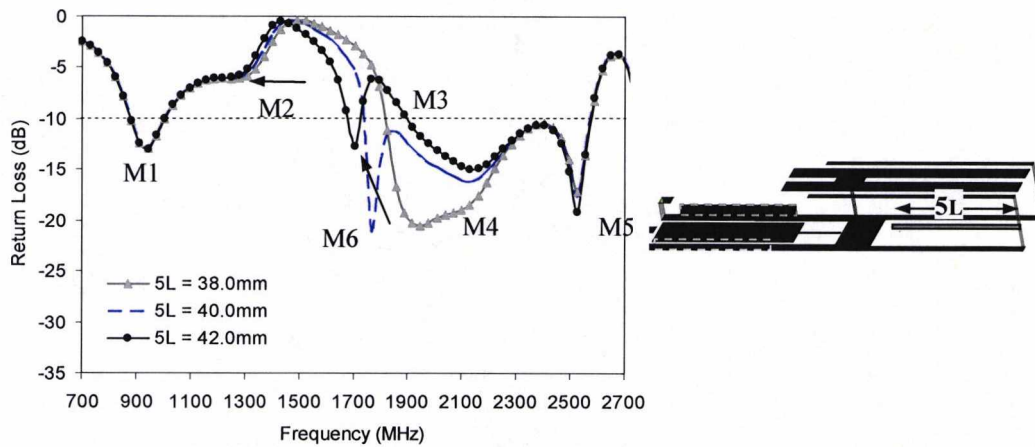


Figure 4.61 Measured return loss of the antenna (S_{11}) versus frequency for different element 5L lengths

Figure 4.62 compares the antenna with and without element 3. The difference from the analysis made in section 4.4 is that mode M6 is the only mode matched in the higher band once element 3 is removed, reducing the bandwidth by 35.3%.

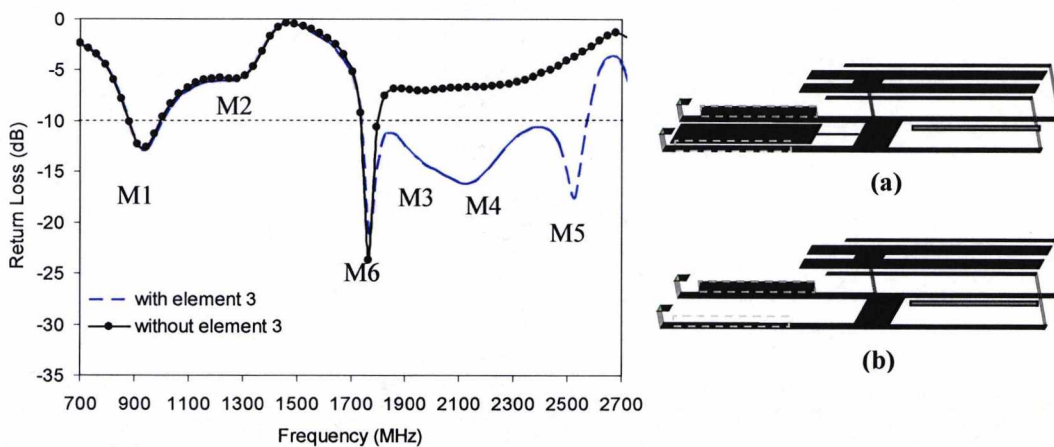


Figure 4.62 Measured return loss of the antenna (S_{11}) versus frequency with element 3 (a) and without element 3 (b)

Figure 4.63 shows the effect of removing totally the relocated element 5. The changes eradicated mode 6, decreased the matching of M3 and M4 and therefore reduced the higher band bandwidth by 10.5%. There was also a significant effect in mode 2, which increased its resonant frequency by 6.3% and improved the bandwidth of M1 by 0.5%.

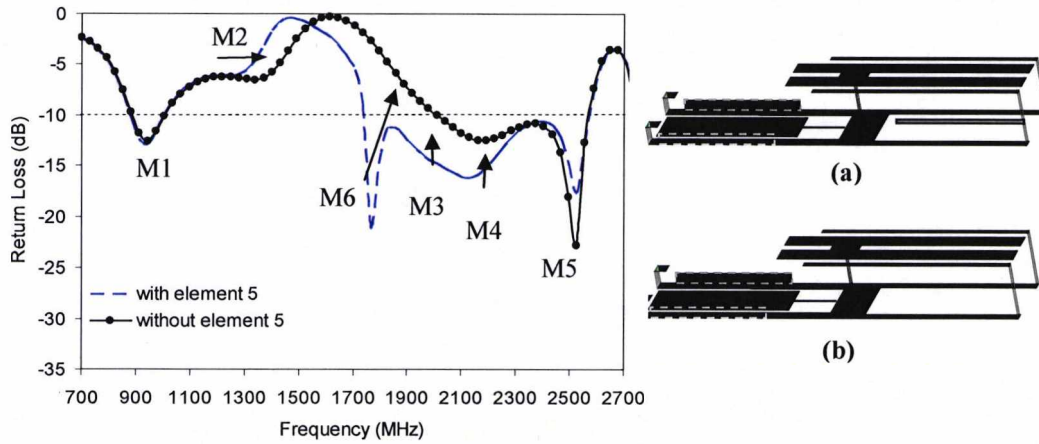


Figure 4.63 Measured return loss of the antenna (S11) versus frequency with element 5 (a) and without element 5 (b)

Figure 4.64 compares the antenna with and without element 6. The presence of element 6 improved the matching of the lower mode M1 by 3.8% which allowed for a smaller antenna size. The effect in the higher band was less pronounced, increasing the resonant frequency of M5 and improving the matching of M3&M4 which increased the higher band bandwidth by 1%.

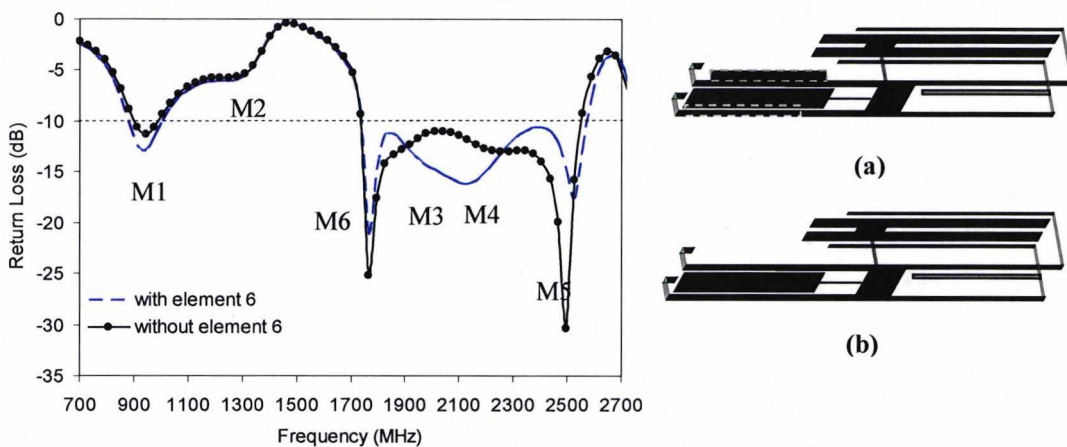


Figure 4.64 Measured return loss of the antenna (S11) versus frequency with element 6 (a) and without element 6 (b)

Finally, a summary of the parametric analysis is shown in Table 4.9. The GSM900 band is provided by elements 1L, 4E and 5. The DCS1800 is controlled by 5L through M6 and 2L through M3, the DECT band is controlled by element 2 through M3. The UMTS and Bluetooth bands are controlled by elements 1&3 through M4 and M5.

Some matching effect on M4 and M5 were observed with changes in 1L, 2L, 3L, 4E and 6.

Element	Increase	Low band (decrease)		High band (decrease)			
		M1	M2	M6	M3	M4	M5
	mm.	%	%	%.	%	%	%
1L	+4.0	-	-2.9	-	-	-	-2.1
2L	+2.0	-	-		-5.6	-	-
3L	+2.0	-	-	-	-	-	-2.4
4E	+4.0	-11	-	-	-	-	-
5L	+4.0	-	-2.2	-2.8	-	-	-

Table 4.9 Summary of the parametric analysis of the multiband antenna with multi resonators.

4.5.5 Multiband antenna with multi resonators – Radiation Patterns

The normalized radiation patterns of the multiband antenna with ground plane parasitic resonator and side resonators at 920MHz, 1800MHz, 1900MHz, 2100MHz and 2450MHz are shown in Figs.4.65 to 4.73. Similarly to the antennas in section 4.3 and 4.4, the radiation patterns were those of a PIFA antenna on a small ground plane. Good omnidirectional patterns were observed in the YZ plane for all frequency bands. The peak gain was also found to vary by only 0.5dBi across the GSM band. The gain at centre frequency of the GSM900, DCS1800, DECT, UMTS and Bluetooth bands were found to be 1.9, 2.8, 2.9, 3.0 and 1.6 dBi respectively.. The measured gain never fell significantly 0.5dBi.

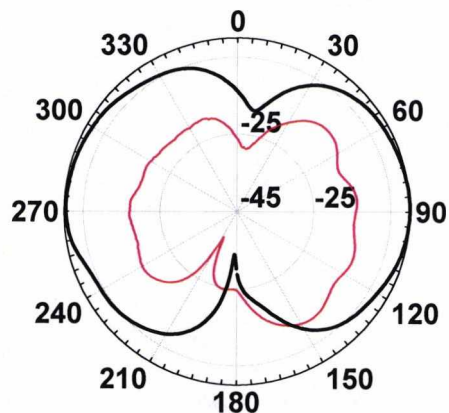


Figure 4.65 Measured far field pattern in the XY plane at 920 MHz . Co-polar (thick line) and cross-polar (thin line)

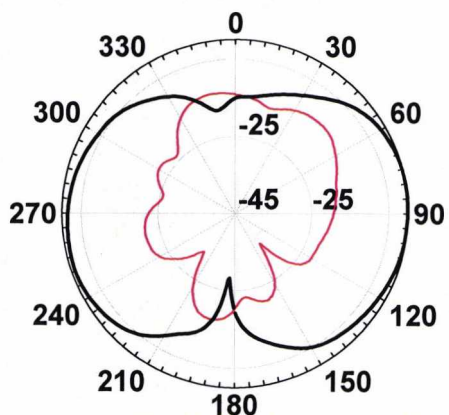


Figure 4.66 Measured far field pattern in the XZ plane at 920 MHz. Co-polar (thick line) and cross-polar (thin line)

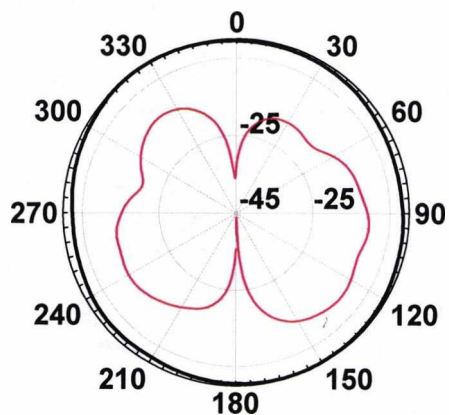


Figure 4.67 Measured far field pattern in the YZ plane at 920 MHz. Co-polar (thick line) and cross-polar (thin line)

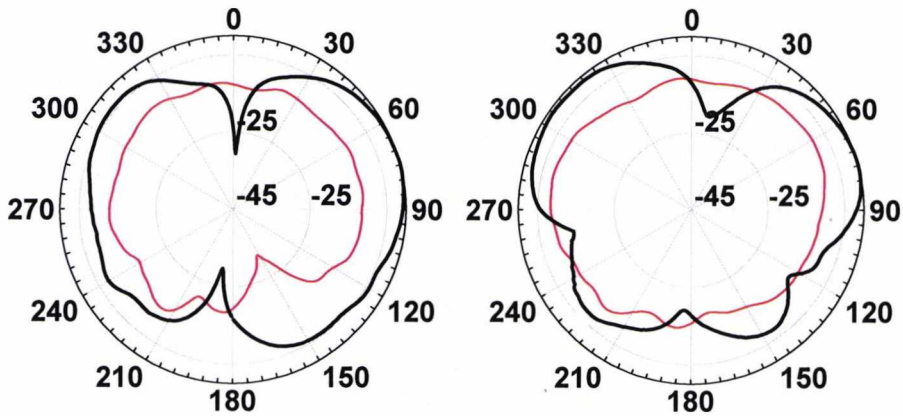


Figure 4.68 Measured far field pattern in the XY plane at 1800 MHz (left) and 1900 MHz (right). Co-polar (thick line) and cross-polar (thin line)

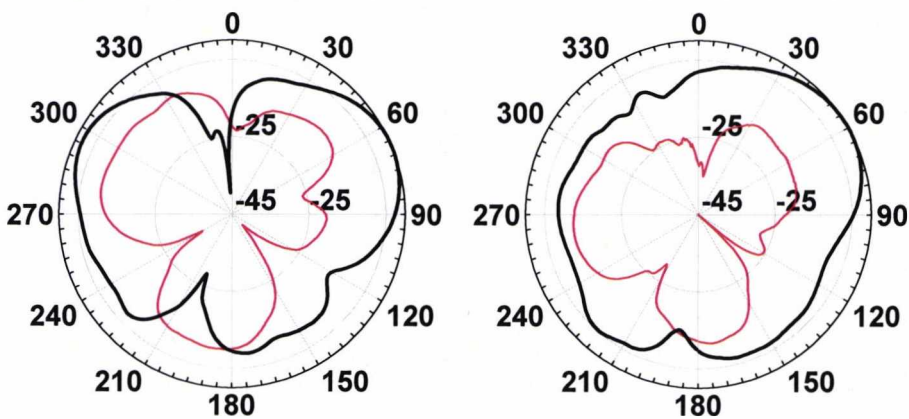


Figure 4.69 Measured far field pattern in the XZ plane at 1800 MHz (left) and 1900 MHz (right). Co-polar (thick line) and cross-polar (thin line)

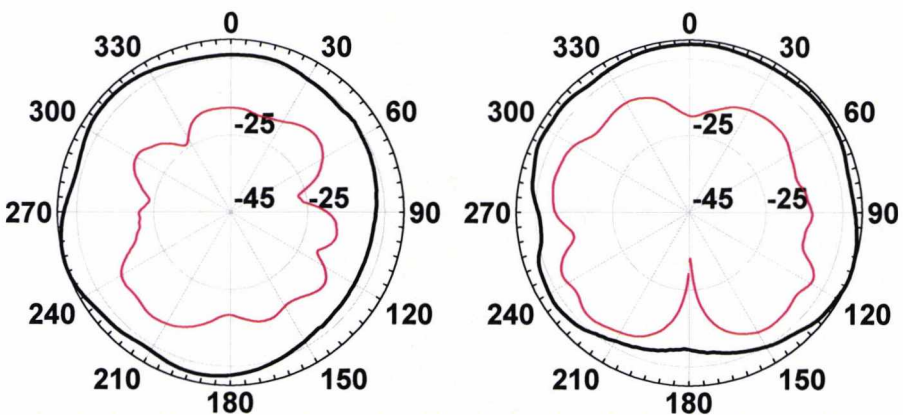


Figure 4.70 Measured far field pattern in the YZ plane at 1800 MHz (left) and 1900 MHz (right). Co-polar (thick line) and cross-polar (thin line)

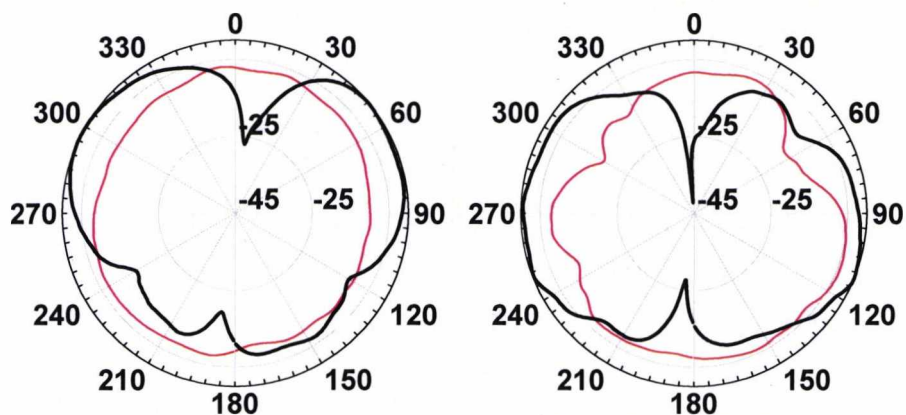


Figure 4.71 Measured far field pattern in the XY plane at 2100 MHz (left) and 2450MHz (right). Co-polar (thick line) and cross-polar (thin line)

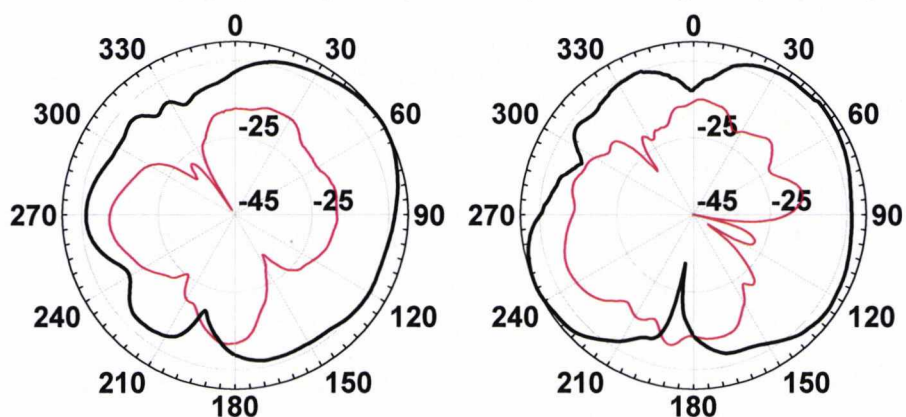


Figure 4.72 Measured far field pattern in the XZ plane at 2100 MHz (left) and 2450MHz (right). Co-polar (thick line) and cross-polar (thin line)

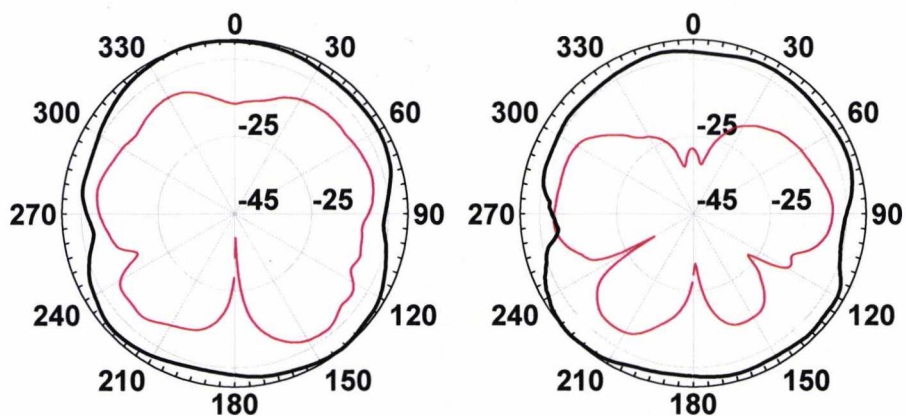


Figure 4.73 Measured far field pattern in the YZ plane at 2100 MHz (left) and 2450MHz (right). Co-polar (thick line) and cross-polar (thin line)

4.6 Conclusions

Three multiband antennas for wireless indoor communications have been presented in this chapter. The antennas follow a sequential order each being a further development on the previous one. The antennas are a considerable improvement on an initial dual band antenna developed at the University of Kent which covered only the GSM900 and DCS1800 mobile phone bands. The new multiband antennas incorporate resonators which allow increased the bandwidth by adding new modes without cancelling the existing ones.

The first antenna developed adds a ground plane resonator which enhances the higher band bandwidth to additionally cover the UMTS band. The following antenna includes side resonators to improve further the higher band bandwidth to accommodate the Bluetooth band. The final antenna achieves a considerable size reduction (30% on the original) by folding the ground plane and rearranging the side resonators. Good quality radiation patterns were observed at all bands.

References.

- [1] <http://www.gsmworld.com/technology/what.shtml>
- [2] <http://www.gsmworld.com/technology/gprs/class.shtml>
- [3] Hsiao-Hwa Chen , Mohsen Guizani , “Next Generation Wireless Systems and Networks”, Chapter 3, pp.117, John Wiley & Sons, Inc, 2006
- [4] <http://www.bluetooth.com/bluetooth/>
- [5] Hsiao-Hwa Chen , Mohsen Guizani , “Next Generation Wireless Systems and Networks”, Chapter 4, pp.205, John Wiley & Sons, Inc, 2006
- [6] Hamed Al-Raweshidy, Shozo Komaki “Radio Over Fiber Technologies for Mobile Communications Networks”, Chapter 4, pp.186, Artech House, Inc, 2002
- [7] Hamed Al-Raweshidy, Shozo Komaki “Radio Over Fiber Technologies for Mobile Communications Networks”, Chapter 5, pp.231, Artech House, Inc, 2002
- [8] D.Wake, D.Moodie, and Frank Henkel “The electroabsorption modulator as a combined photodetector / modulator for analogue optical systems”, Workshop

Electron Devices for Microwave and Optoelectronic Applications, 24-25 November 1997, King's College London

[9] Dong Liu, Z., Hall, P.S. and Wake, D.: "Dual-frequency planar inverted-F antenna", IEEE Trans. Antennas Propag. 1997, 45, (10) pp. 1451-1457

[10] C.W. Chiu and F.L. Lin "Compact dual-band PIFA with multi-resonators", Electronics Letters, 6th June 2002. Vol.38, No.12.

[11] Yong-Xin, Michael Yan Wah Chia, and Zhin Ning Chen, "Miniature Built-In Multiband Antennas for Mobile Handsets", IEEE Trans. Antennas Propag. Vol.52, No.8, August 2004, pp. 1936-1943

[12] C.K.Wu and K.L. Wong "Broadband microstrip antenna with directly coupled and gap-coupled parasitic patches", Microwave Opt. Technol. Lett 22 348-349, Sep. 5. 1999

[13] Viratelle, D. and Langley, R.J.: "Dual-Band Printed Antenna for Mobile Telephone Applications", IEE P-Micro., Anten. & Propag., 147, (5), pp.381-384, Oct. 2000.

Chapter 5.

Multiband Planar Antennas

5.1 Introduction

This chapter describes multiband planar antennas suitable for deployment in an indoor repeater system for personal communications and WLAN. The proposed system is the one explained in section 4.1 which utilizes a centralized base station with distributed antenna units and is intended for environments such as shopping malls or airports where there may be a heavy localized traffic demand across a variety of user services. The main aim is to create a relatively low cost distributed network solution by requiring only one centralized multi-system repeater station. The antenna units would be wall or ceiling mounted and the connection to the base station is made by

optical fiber with an Electro-Absorption Modulator (EAM) serving as both optical-to-electrical and electrical-to-optical transducer in the down and up links respectively [1]. The broadband nature of the optical link from base station to antenna unit makes it feasible to include all the major personal communications systems subject to creating a sufficiently multiband antenna. The systems for which the proposed planar antennas have been designed are given in Table 5.1; all these services fall within the wireless communications frequency bands used in Europe, i.e. 890-960 MHz, 1710-2175 MHz and 2400-2483.5 MHz and 5150-5725 MHz for Bluetooth and WLAN applications.

System	Frequency Band (MHz)
GSM	890-960
DCS-1800	1710-1880
DECT	1880-1900
UMTS	1920-2170
Bluetooth/WLAN	2400-2483.5
HiperLAN/2	5150-5350 5470-5725

Table 5.1 European wireless bands

Although the antenna has been tuned for European systems, it would also be possible to re-tune to the US and Japanese frequencies, the main differences being at the lower band which are 824-894 MHz and 810-956 MHz respectively. The systems are predominantly vertically polarized.

Various approaches to creating multiband antennas for personal communication systems have been reported in recent years. These are often aimed at handset applications and can broadly be defined as:

- (i) Fractal or Sierpinski Gasket Antennas over ground planes [2], [3], [4] and in [5] where fractalization has been used to achieve size reduction.
- (ii) Modified Printed Inverted-F Antennas (PIFAs) [6], and [7] where a PIFA with slots cut on the radiating element was described. An increased bandwidth at the DCS-1800 band was achieved.

This chapter reports a new compact multiband planar PIFA's which has evolved from the dual band design described in [8] that covered the GSM and DCS bands and

possessed dipole type radiation patterns. The antenna size was reduced by removing metallization in areas of low current density. The construction was simple with the metal etched from a thin mylar sheet folded around a honeycomb former. A series of design innovations made to the original PIFA of [8] were reported in chapter 4 [9]. In all cases Zeland's IE3D software has been used to theoretically study and optimize the design of the new planar antennas. As a final part in this chapter, a system model will be introduced as a first stage to developing an equivalent circuit of the multiband antenna.

5.2 Multiband Planar Antennas

In chapter 4 [9] it has been reported that an extra band could be added to the dual band PIFA of [8], Fig.5.1, by including a parasitic resonator in the ground plane. This patch, labeled element 3 in Fig.5.1, had no direct connection to the PIFA and was parasitically coupled to element 4. The tuning of the frequency bands was achieved by altering the element lengths as shown in Table 5.2.

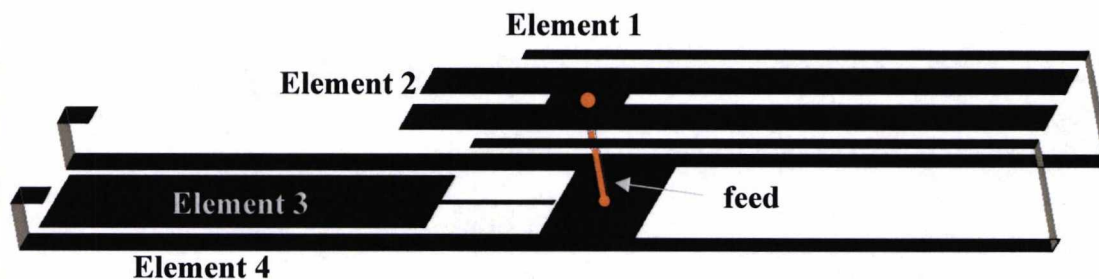


Figure 5.1 Multiband antenna with ground plane patch resonator

Frequency Band	Tuning Element (Predominant, secondary)
Lower	1,4
Upper (lower frequency)	2
Upper (mid frequency)	3,4,1
Upper (upper frequency)	3,1,4

Table 5.2 Multiband PIFA with ground plane resonator tuning elements

A beneficial feature of this design was the predominance of element 1 in tuning the lower band while having only a minor effect on the upper. This reduced the complexity of the tuning process. The radiation patterns remained of good quality and were similar to those of a dipole at all frequency bands. The measured peak gain varied by 0.5, 3.3, 1.1 and 2 dBi across the GSM, DCS1800, DECT and UMTS bands respectively and never fell significantly below -1dBi.

It has been shown that multiband antennas can be successfully implemented in planar form. Wong and Chiou [10] describe the design of an original planar antenna fed by single layer microstrip and serving GSM, DCS, PCS and UMTS. The planar antenna was fabricated on an FR4 substrate 0.4mm thick with no rear ground plane. The antenna area was 30mm x 12mm. Current flow was found to be directed such that, at higher frequencies, modes combined to form a single band with a large matched bandwidth. The patches operated at a quarter-wavelength fundamental mode which reduced the patch size. The radiation patterns were generally good but had some nulls of more than 10-15dB depth. Leelaratne and Langley [11] have developed a planar triple band PIFA for automotive applications and a related technique will be shown here to transpose the PIFA of Fig.5.1 into planar form.

5.3 PIFA Transposition to Planar Form

Figure 5.2 presents the plan and elevation views of the PIFA shown in Fig.5.1. The upper and lower levels are drawn separately for clarity. Figures 5.2 to 5.5 graphically illustrate how the original PIFA was transformed into an equivalent planar design. In Fig.5.3 the upper and lower planes are bisected along the x - z plane of symmetry and half of each layer is removed on opposing sides of the bisecting plane. Figure 5.4a shows the structure after the lower plane has been translated to the upper plane. The section of element 1 aligned along the z -axis is rotated to maintain a connection between points A' and B in the x - y plane, Figs.5.4(b) & (c).

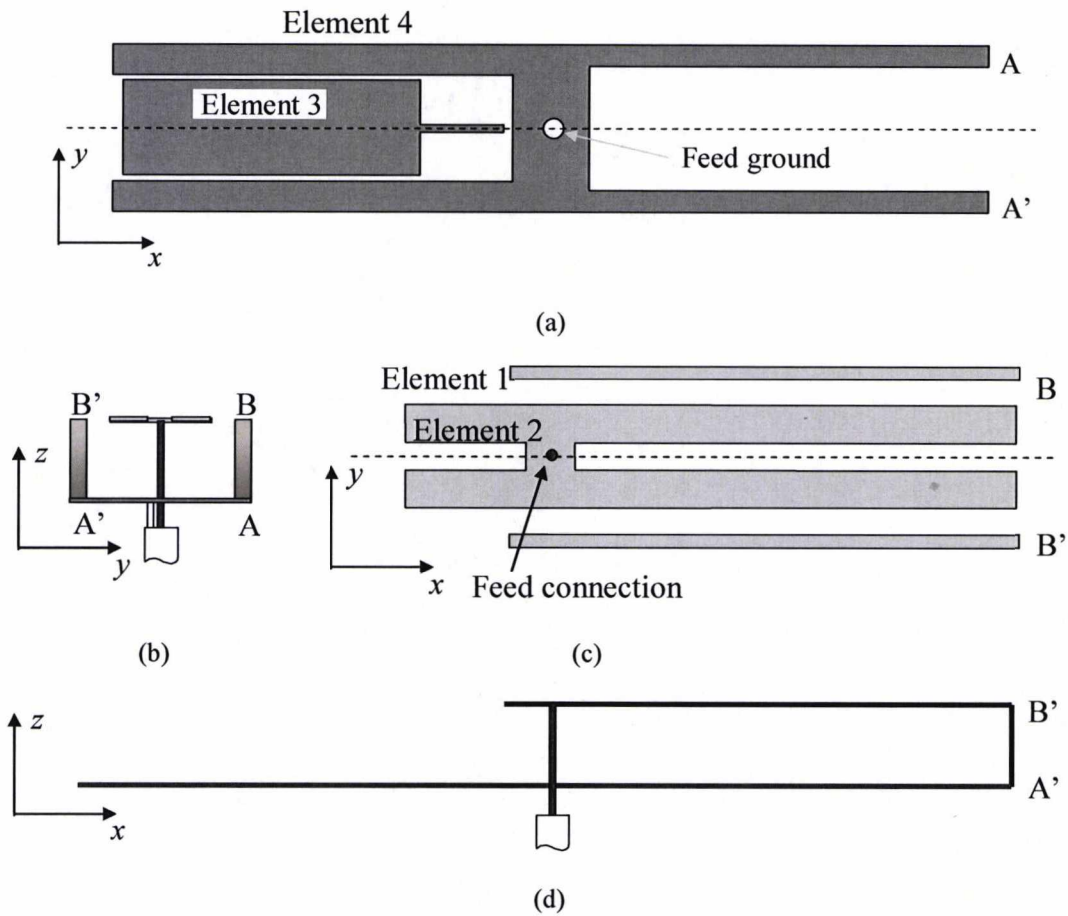


Figure 5.2 Multiband PIFA of Fig.5.1 with geometry of upper and lower levels shown separately for clarity. (a) lower level plan view; (b) end elevation; (c) top level plan view; (d) side elevation.

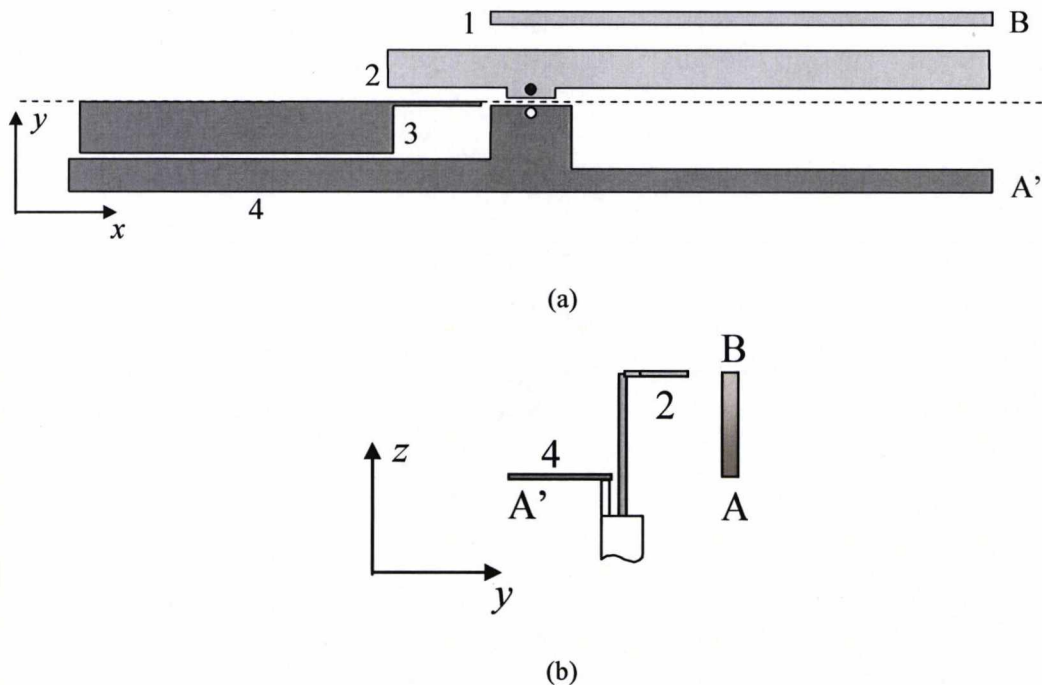


Figure 5.3 PIFA of Fig.2, bisected along x - z plane of symmetry. (a) plan view of upper and lower levels; (b) end elevation.

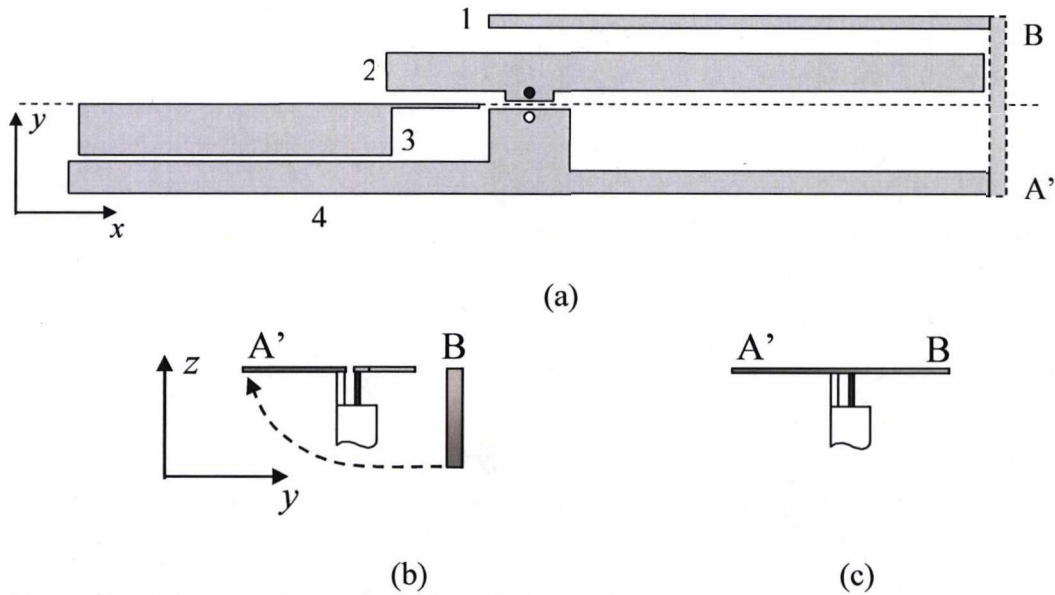


Figure 5.4 (a) plan view of PIFA with lower layer translated to upper layer; (b) end elevation; (c) segment of element 1 is rotated to complete connection between A' and B in the x - y plane

5.3.1 Initial Simulations of the Transposed PIFA

The electromagnetic simulator IE3D was used to simulate the multiband planar antennas resulted from the transposition. The first planar structure derived from the transposition described in Figs.5.2 to 5.4 is shown in Fig.5.5. The total dimensions of this antenna are 142.0mm x 22.0mm and it is intended to be etched in the metal cladding of a 0.1mm thick Mylar substrate. The feeding point is placed in the same location as in the initial antenna in Fig.5.1 which is indicated with a vertical arrow in the antenna design in Fig.5.5. The return loss (S11) curve resulting from the computer simulation of design 1 is shown in Fig.5.7. It shows a good bandwidth (S11=-10dB) at the lower band, however, the matching in the higher band does not drop below -6dB which will not cover the intended applications.

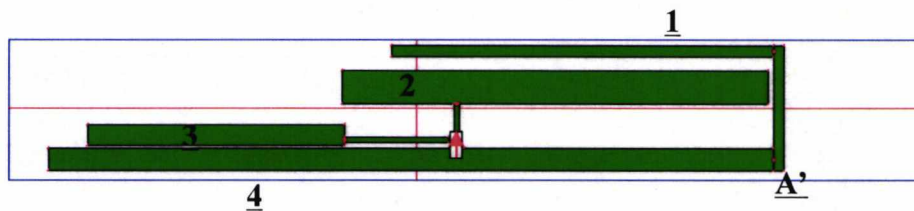


Figure 5.5 Planar antenna design 1

The best results for designs of similar characteristics to the one in Fig.5.5 was obtained for the antenna in Fig.5.6. In this antenna the ground plane (4) and top patch (1) have been made thicker. The total dimensions of the antenna are 156mmx41mm and it was also designed for a Mylar substrate.

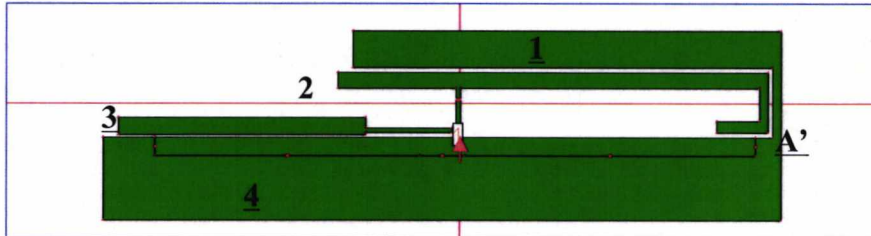


Figure 5.6 Planar antenna design 2

The simulated reflection coefficient (S_{11}) for antenna design 2 in Fig.5.6 is shown in Fig.5.7. There is sufficient bandwidth in the lower band to cover the GSM900 system while the matching in the higher band has been improved considerably from the first antenna design.

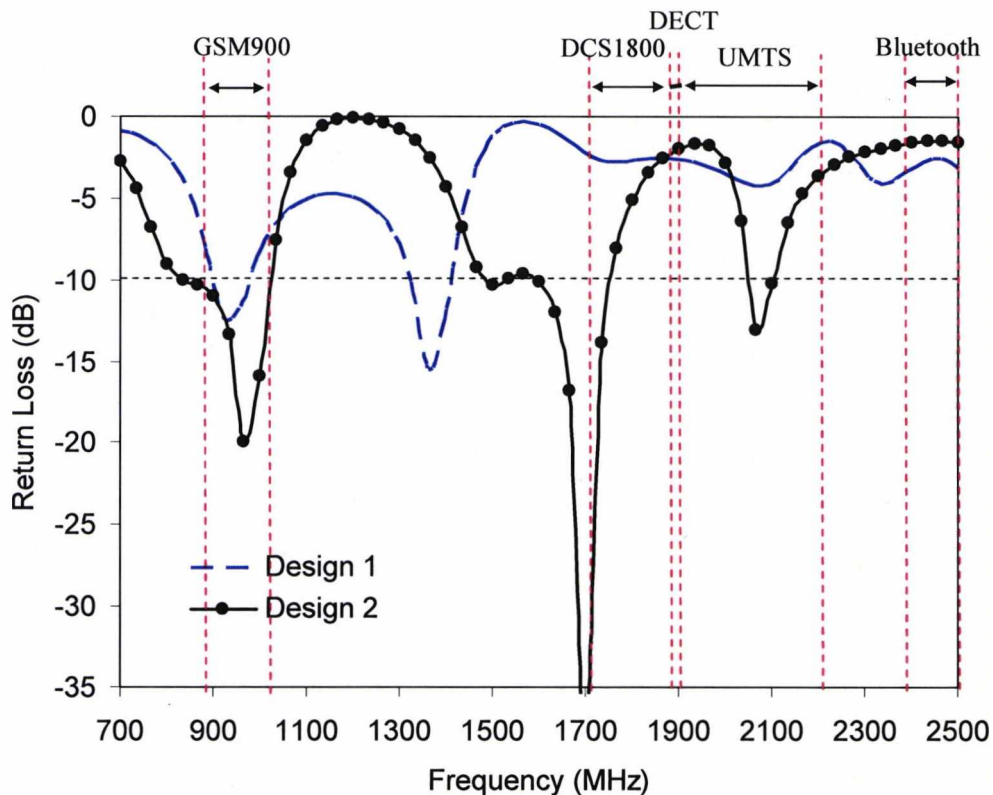


Figure 5.7. Simulated S_{11} curves for the transposed multi-band antenna and the antenna design 2. The frequency bands targeted are also included in the graph.

All the antennas designed using a similar shape to those of Figs.5.5 and 5.6 showed cancellation in the higher band matching when different resonant modes were closed to each other. The behaviour is different to the one in the original 3D Multi-band PIFA where three resonant modes (M3, M4 and M5) join together to create enough bandwidth to support the DCS1800, DECT and UMTS standards. This problem has been overcome as described in the following section.

5.4 Multiband Planar Antenna on Thin Dielectric Substrate

The IE3D simulator was used to tune each element and simultaneously reduce the overall antenna size. A parametric analysis was initially employed and the resulted antenna was later optimized. The derived geometry is shown in Fig.5.8 and was printed onto Mylar, 0.1mm thick. The connection point A' in Figs.5.5 and 5.6 was moved from the end of element 4 to a position part way along its length. This was necessary to provide a current path sufficiently long to support the lower frequency mode without making the antenna unduly large. The shape of element 1 required that element 2 was folded to avoid overlap. Also, folded stub element 5 was added to increase the overall length of element 4 and allow the extension of the matched region to include the DCS1800, DECT and UMTS bands.

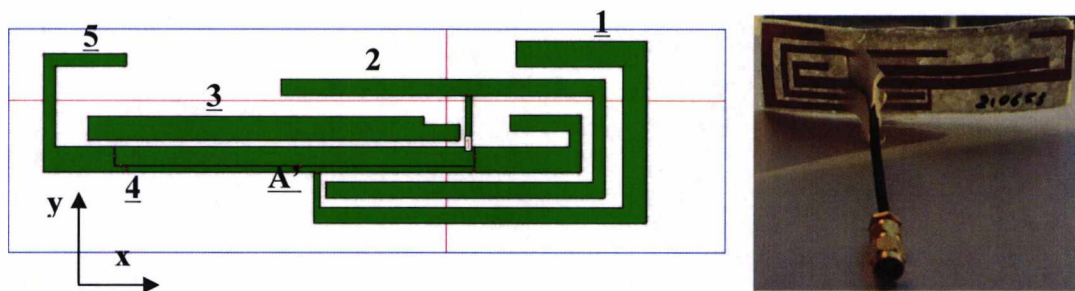


Figure 5.8 Multiband planar antenna on thin substrate; (left) antenna structure, (right) photograph of the antenna with feeding connexion.

The first Multi-band Planar PIFA was fabricated in a thin Mylar substrate and 2mm-thick foam was used to give it a slightly more rigid characteristic.

5.4.1 Multiband Planar Antenna on Thin Dielectric Substrate. Dimensions

The principal dimensions of the design are given Fig.5.9. The overall dimensions of the planar PIFA antenna are 102mm x 29mm making it 53.7% smaller than the antenna design 2 in Fig.5.6. More insight into the exact tuning process will be given in section 5.5.4.

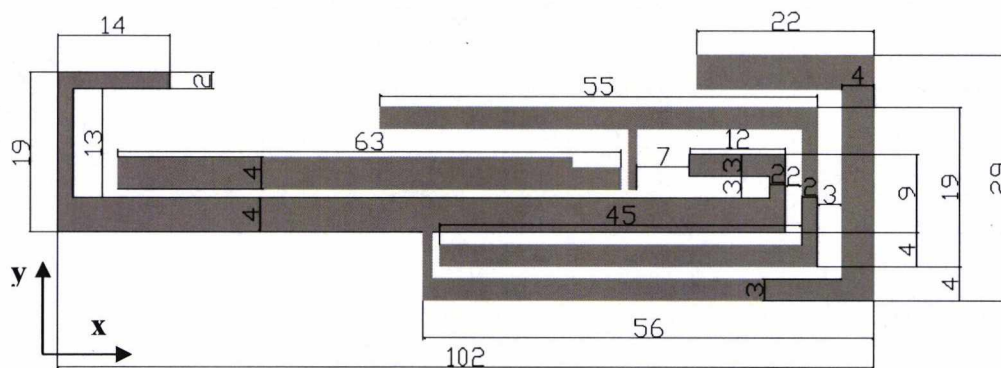


Figure 5.9 Dimension of the multiband antenna on thin dielectric substrate

5.4.2 Multiband Planar Antenna on Thin Dielectric Substrate. Measurement Results, Reflection Coefficient

The simulated and measured S_{11} curves for the multiband planar antenna on a thin dielectric substrate are shown in Fig.5.10 and Table 5.3. A multiband characteristic is observed with measured -10dB S_{11} bandwidths of 8.6% at the lower band and 35.9% at the higher band. The measured bandwidths were 1% wider than the simulated in the lower band and 11.3% wider in the higher band.

Although successfully simulated, the design in Fig.5.9 proved difficult to feed in practice as it was unbalanced. The exact length and connection angle of the feed cable was critical in achieving a good match at all bands. This is clearly undesirable in a practical antenna. Furthermore, implementing a multiband planar balun in limited space would be a significant design challenge. In the case of the multiband antenna in thin dielectric substrate a good matching was obtained by bending the feeding cable by 10mm in the direction of the longer ground plane segment.

	Low band (MHz)	BW low band (MHz) - %	High band (MHz)	BW high band (MHz) - %
Simulated air	890 - 960	70 - 7.6%	1710 - 2190	480 - 24.6%
Measured air	890 - 970	80 - 8.6 %	1530 - 2200	670 - 35.9%
GSM 900	890 - 960	70 - 7.6 %		
DCS1800-UMTS			1710 - 2200	490 - 25.1%

Table 5.3 Simulated and Measured S11 for the multiband planar antenna on thin dielectric substrate and comparison with existing mobile communication systems bandwidth

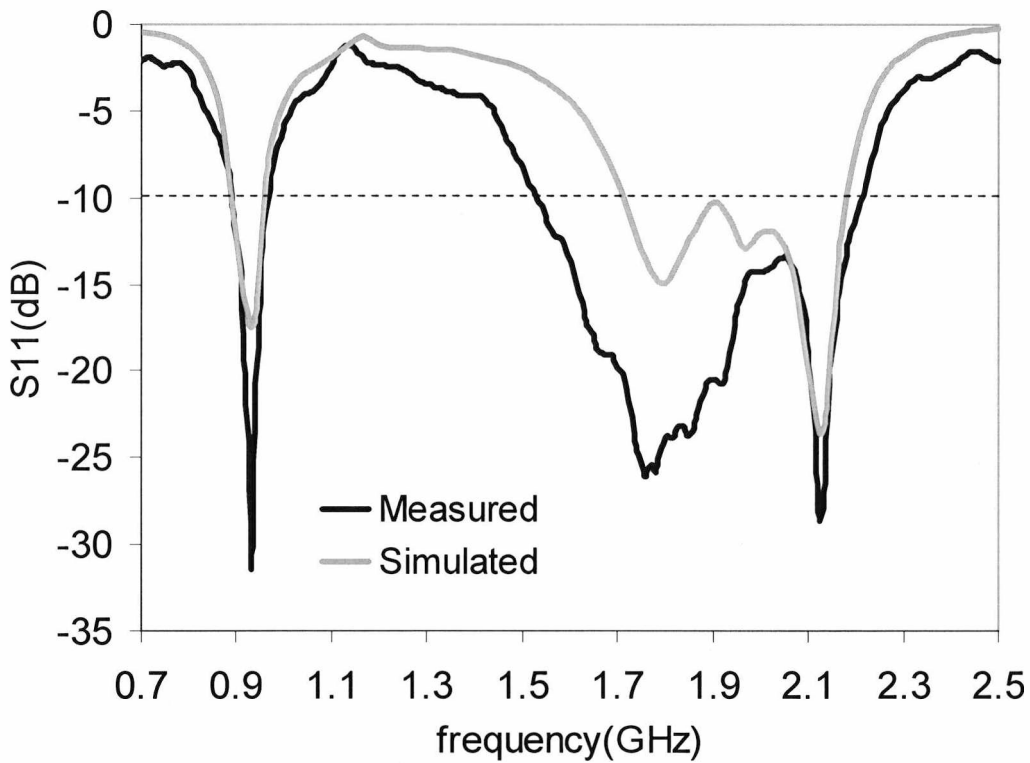


Figure 5.10 Simulated and measured S11 curves for the multiband antenna on thin dielectric substrate

5.4.3 Multiband Planar Antenna on Thin Dielectric Substrate. Surface Currents

The surface current of the multiband planar antenna on thin dielectric substrate resonator at 920MHz, 1800MHz, 1900MHz and 2100MHz are shown in Figs.5.11-5.14. It can be observed from the surface current that it bears a considerable similarity to the original 3D multiband antenna from which it originates [9], also described in section 4.3.3 (Figs. 4.7 to 4.10).

At 900MHz (Fig.5.11), there are strong currents in the section of element 1 which connects with element 4. These currents are coupled through element 2 which is connected to the feed. At larger wavelengths (900 MHz), currents tend to flow throughout most of the body of the antenna starting from the feed in element 2, capacity coupling to element 1 and connecting through A' to element 4 and ending in element 5.

At 1800MHz (Fig.5.12), currents become stronger in the section of element 2 closest to element 3. Element 3 and 4 seem to be excited by the currents in element 2 and also show strong currents.

At 1900MHz (Fig.5.13), the currents in the section of element 2 closest to elements 3 and 4 remain strong while currents in elements 3 and 4 become stronger. The section of element 2 that interweaves with elements 1 and 4 appears to have higher current density.

Finally, at 2100MHz, currents in the parallel elements 3 and 4 become very strong, currents extend to element 5.

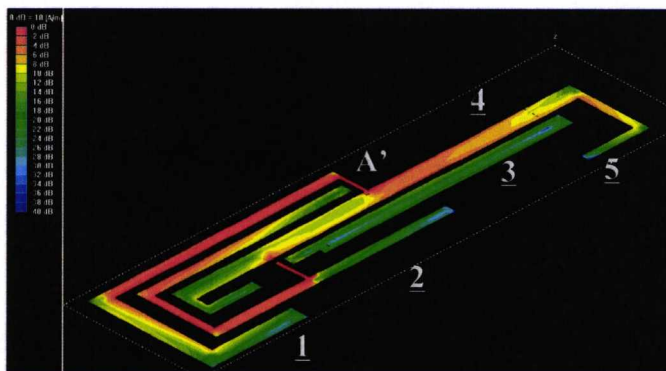


Figure 5.11 Surface currents at 920 MHz

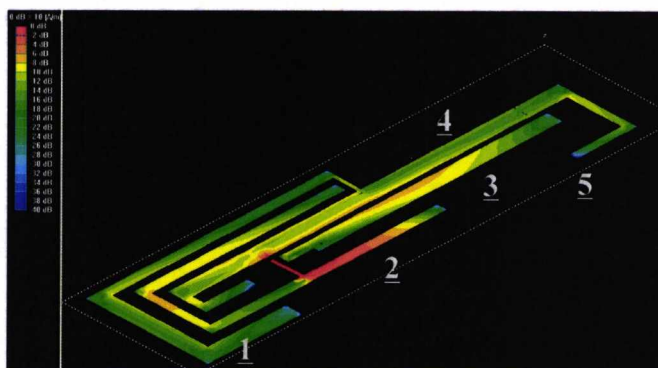


Figure 5.12 Surface currents at 1800 MHz

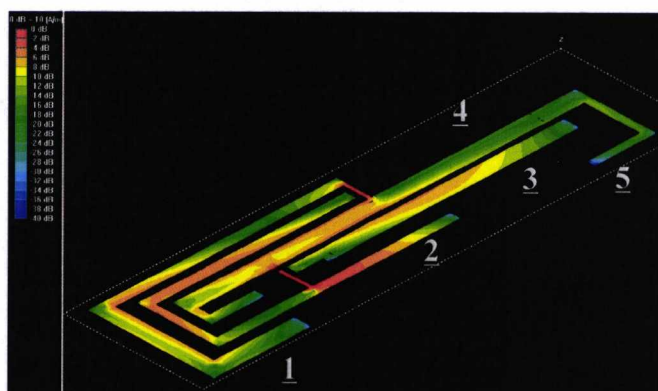


Figure 5.13 Surface currents at 1900 MHz

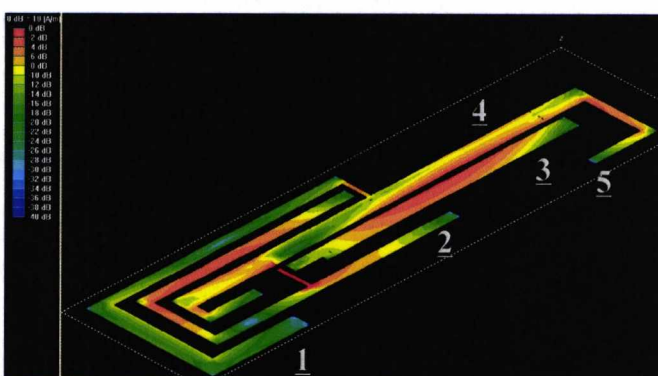


Figure 5.14 Surface currents at 2100 MHz

5.4.4 Multiband planar antenna in thin dielectric substrate. Radiation Patterns

The radiation patterns of the multiband antenna in thin dielectric substrate were measured in the anechoic chamber at the University of Kent and are shown normalized in Figs.5.15-5.19. The XY, XZ and YZ planes of the antenna were measured at 920MHz, 1800MHz and 2100 MHz. The radiation patterns were those of a printed dipole with some alterations in the position of the nulls at the higher band. Good omnidirectionality was observed in the YZ plane for all the frequency bands

which suggests that the antenna is well suited to its intended application as a picocell basestation antenna. The peak gain was also measured for all bands and was found to be between 0.7 to 2 dBi at the GSM band. The peak gain across the DCS1800, DECT and UMTS bands was 2.4, 1.8 and 2.4 dBi respectively. The measured gain never fell below 0.7 dBi.

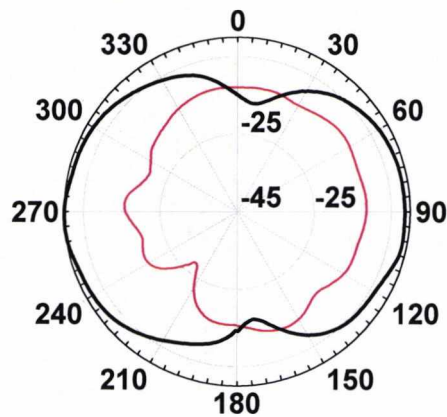


Figure 5.15 Measured far field pattern in the XY plane at 920 MHz. Co-polar (thick line) and cross-polar (thin line)

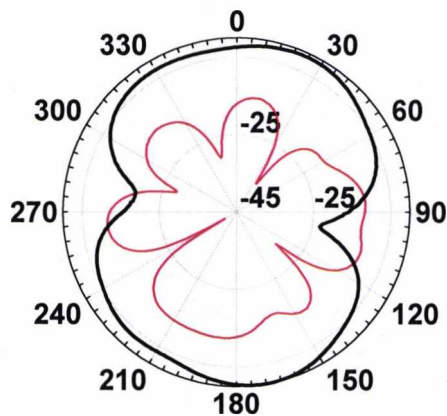


Figure 5.16 Measured far field pattern in the ZX plane at 920 MHz. Co-polar (thick line) and cross-polar (thin line)

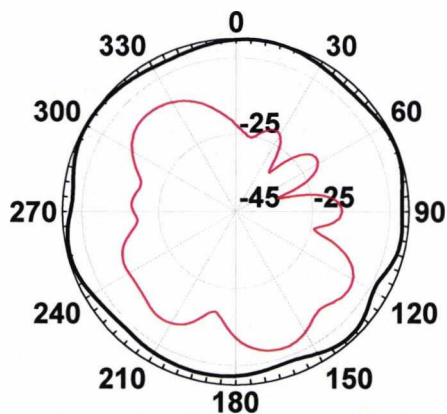


Figure 5.17 Measured far field pattern in the YZ plane at 920 MHz. Co-polar (thick line) and cross-polar (thin line)

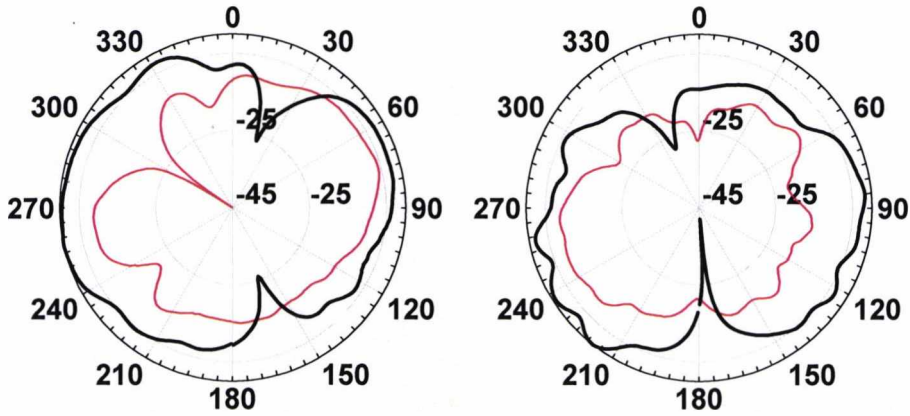


Figure 5.18 Measured far field pattern in the XY plane at 1800 MHz (left) and 2100 MHz (right). Co-polar (thick line) and cross-polar (thin line)

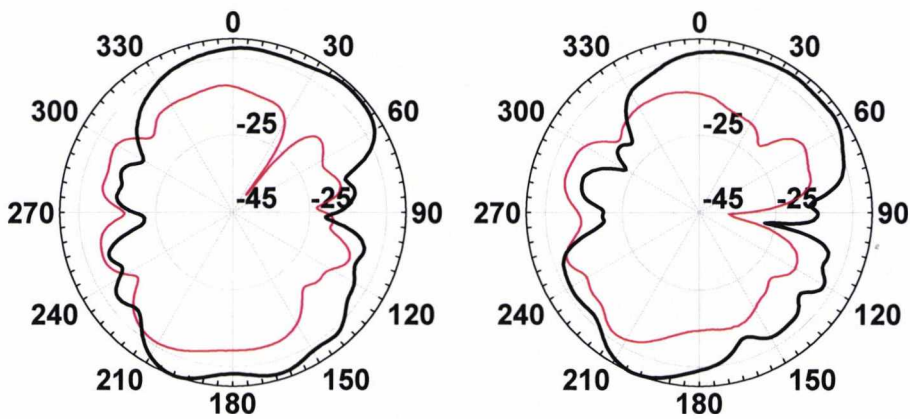


Figure 5.19 Measured far field pattern in the ZX plane at 1800 MHz (left) and 2100 MHz (right). Co-polar (thick line) and cross-polar (thin line)

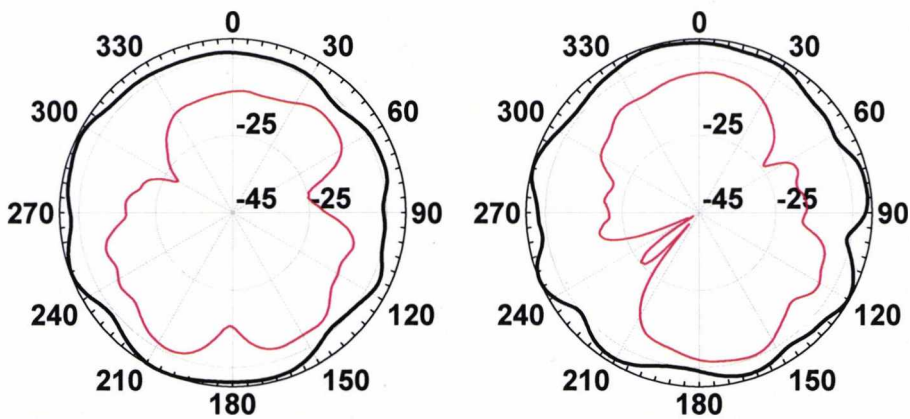


Figure 5.20 Measured far field pattern in the YZ plane at 1800 MHz (left) and 2100 MHz (right). Co-polar (thick line) and cross-polar (thin line)

5.5 Single Sided Multi-band Planar PIFA on FR4 Substrate

A multiband planar PIFA antenna was designed to be etched in the metal cladding of a 0.8mm FR4 substrate and is shown in Fig.5.21. The antenna on FR4 substrate is based in the design in section 5.3 (Fig.5.8) and achieves smaller size, higher rigidity and lower manufacture cost. The main differences from the design on thin dielectric in Fig.5.9 are: the reduction in size of element 4 in its section closest to the feed and the introduction of element 6. The size reduction of element 4 is needed to achieve the tuning required for the antenna on higher permittivity substrate and the addition of element 6 allows a further miniaturization of the antenna.

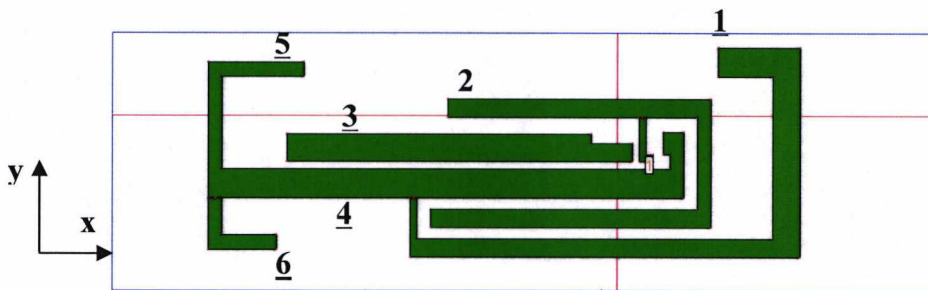


Figure 5.21 Single sided Multiband planar PIFA design

5.5.1 Single Sided Multi-band Planar PIFA on FR4 Substrate - Dimensions

The main dimensions of the single sided multiband planar PIFA antenna on FR4 are shown in Fig.5.22. The overall dimensions of the antenna are 87mmx29mm which is 14.7% smaller in surface area than the previous antenna printed on thin dielectric substrate (section 5.3). The new element 6 had dimensions 2mmx10mm.

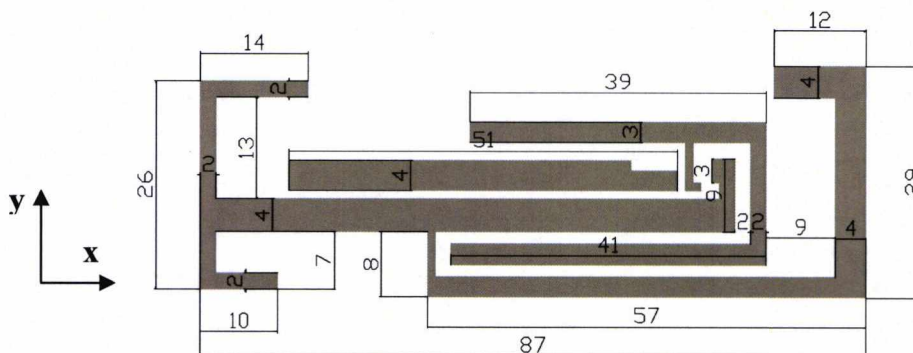


Figure 5.22 Dimensions of the single sided multiband planar PIFA in FR4 substrate

5.5.2 Single Sided Multi-band Planar PIFA on FR4 Substrate. Results – Reflection Coefficient

The simulated and measured S11 curves for the single sided Multi-band planar PIFA on FR4 substrate are shown in Fig.5.23 and Table 5.4.

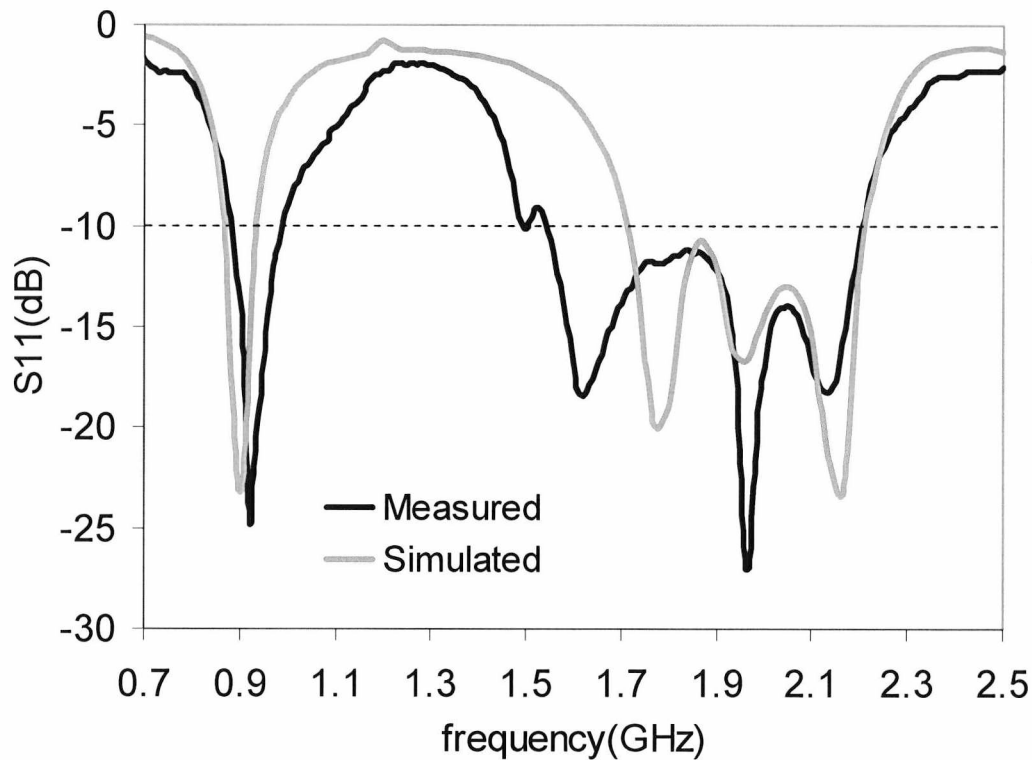


Figure 5.23 Simulated and Measured S11 curves of the single-sided multiband planar PIFA on FR4 substrate

A multiband characteristic is also observed with -10dB S11 bandwidths of 10.7% at the lower band and 35.6% at the higher band. The measured bandwidth was 3% wider than the simulations in the lower band and 10% wider in the higher band. The main difference between the measurements and simulations appears to be in the lower mode of the higher band, which has a measured resonant frequency of 1613MHz compared to a simulated 1767MHz; the bandwidth of this mode is also wider in the measurements.

	Low band (MHz)	BW low band (MHz) - %	High band (MHz)	BW high band (MHz) - %
Simulated air	870 - 940	70 - 7.7%	1710 - 2213	503 - 25.6%
Measured air	880 - 980	100 - 10.7 %	1540 - 2208	668 - 35.6%
GSM 900	890 - 960	70 - 7.6 %		
DCS1800-UMTS			1710 - 2200	490 - 25.1%

Table 5.4 Simulated and Measured S11 for multiband planar PIFA on FR4 substrate comparison with existing mobile communication systems bandwidth

5.5.3 Single Sided Multi-band Planar PIFA on FR4 Substrate -Surface currents

The surface current of the single sided multiband antenna with a ground plane parasitic resonator at 920MHz, 1800MHz, 1900MHz and 2100MHz are shown in Figs. 5.24-5.27. The surface currents are similar to the antenna pattern printed on thin substrate in section 5.3.3 where element 6 is not present.

At 900MHz (Fig.5.24), strong currents are observed in the lower part of element 1 and in element 4. These currents are coupled through element 2 which is connected to the feed. As the wavelength is larger at 900 MHz, currents tend to flow throughout most of the body of the antenna starting from the feed in element 2, capacity coupling to element1 and connecting through A' to element 4 and ending in elements 5 and 6.

At 1800MHz (Fig. 5.25), currents become stronger in the section of element 2 closest to element3. Element 3 and 4 seem to be excited by the currents in element 2 and also show strong currents.

At 1900MHz (Fig. 5.26), the currents in the section of element 2 closest to elements 3 and 4 remains. Currents in elements 3 and 4 are also strong. The section of elements 1 and 2 that interweaves with element 1 and 4 appears to have high current density.

Finally, at 2100MHz, currents in the parallel elements 3 and 4 become very strong, and extend to element 5.

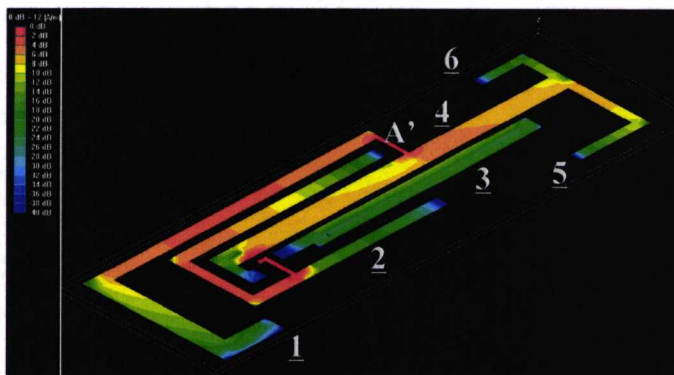


Figure 5.24 Surface currents at 920 MHz

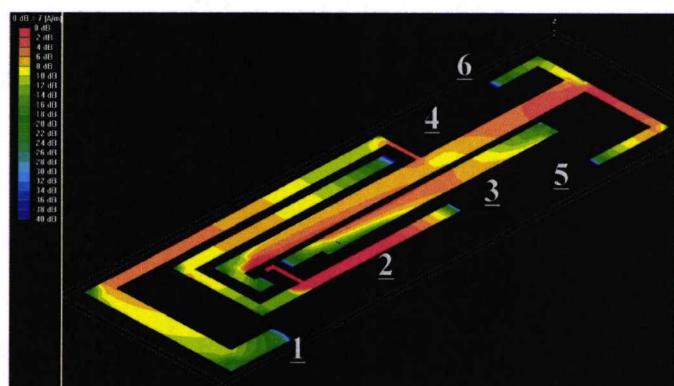


Figure 5.25 Surface currents at 1800 MHz

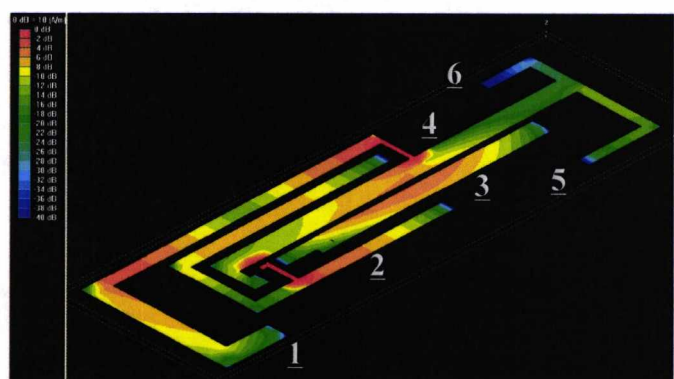


Figure 5.26 Surface currents at 1900 MHz

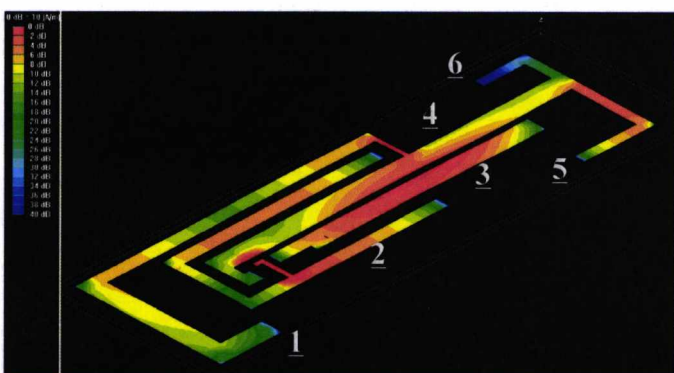


Figure 5.27 Surface currents at 2100 MHz

5.4.4 Double-Sided Simulation Study

A further simulation study of the effect of printing an image metal pattern on the further side of the FR4 substrate of the antenna was carried out to determine the double sided effect on the electrical characteristics of the antenna. The double sided printing was decided after finding significant variations in the lower band matching for different angles and length in the coaxial feeding cable. In most of the cases, the best matching was observed when the feeding cable was parallel to element 4, which gave rise the assumption that and image pattern would create a parallel conductor without the need of bending the cable. The simulated reflection coefficient of the antenna as a single sided multiband planar PIFA and the comparison with the double sided version of the antenna is shown in Fig.5.28 and Table 5.5. The metal patterning was identical in both the single and double layer planar PIFAs in order to allow for a direct performance comparison. Double siding the antenna produced a beneficial increase in the bandwidth of nearly 1% in the lower band and 2% in the higher band. The centre frequency, however, increased by 3.9% in the lower band and 3.5% in the higher band.

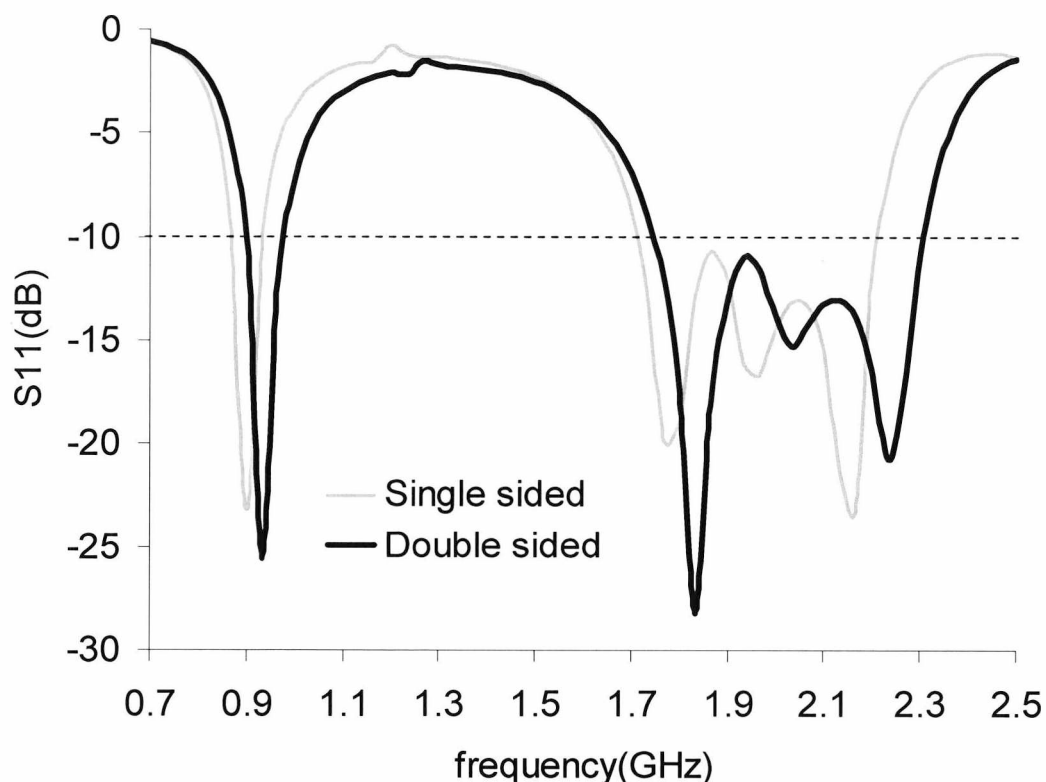


Fig 5.28 Effect of printing an image pattern on the single-sided multiband planar PIFA in FR4 substrate

	Low band (MHz)	BW low band (MHz) - %	High band (MHz)	BW high band (MHz) - %
Single sided	870 - 940	70 - 7.7%	1710 - 2213	503 - 25.6%
Double sided	900 - 980	80 - 8.5 %	1750 - 2310	560 - 27.6%

Table 5.5 Effect of printing an image pattern on the single-sided multiband planar PIFA in FR4 substrate

The double sided version of the planar antenna was tuned further in order to cover the communication systems required for the photonic antenna units in the ROSETTE project. The antenna resulted from the tuning and the fabrication of the novel double sided multiband planar PIFA is presented in the following section.

5.6 Double Layer Multiband Planar PIFA

The double layer multiband PIFA of section 5.4.5 was further improved to cover the GSM, DCS1800, UMTS, Bluetooth and Hiperlan band required for the ROSETTE project. A photograph of the antenna with its coaxial feeding cable is shown in Fig.5.29.

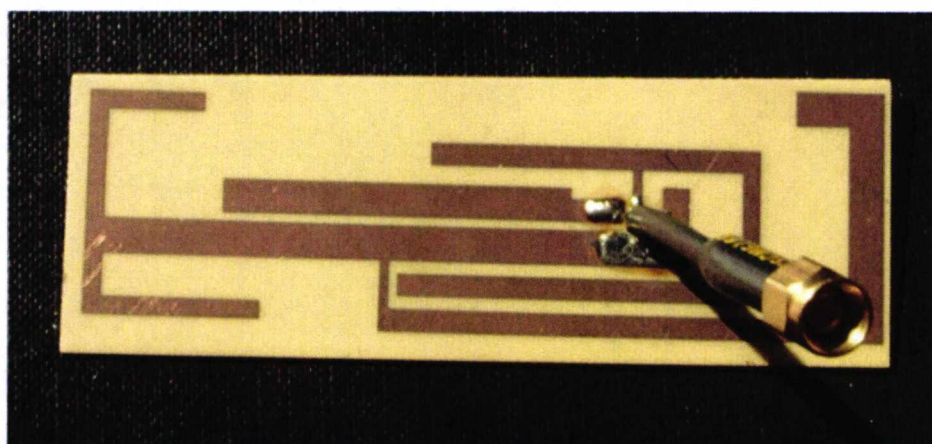


Figure 5.29 Photograph of the double layer multiband PIFA antenna

To create the more balanced system a double layer PIFA (or double-sided PIFA) was fabricated on the underside of the substrate (FR4 0.8mm thick with a relative permittivity of 4.4). It should be noted that the 2 layer design was not balanced in the true sense as the layers were not excited symmetrically; this is shown in Fig.5.30

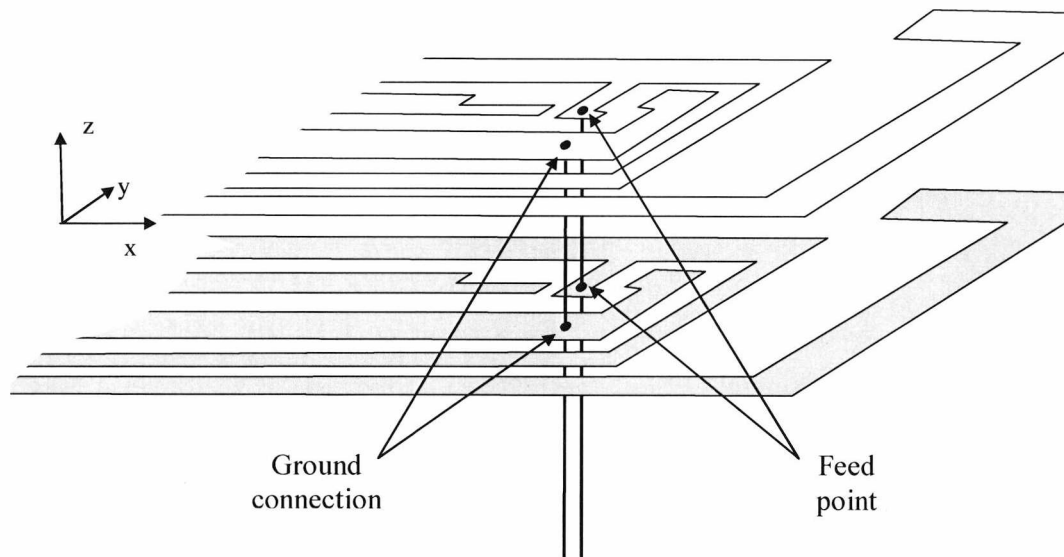


Figure 5.30 Feed connections to double sided PIFA design 2. Layer separation has been expanded for clarity

5.6.1 Double Layer Multiband Planar PIFA – Dimensions

The dimensions of the double layer multiband planar PIFA are shown in Fig.5.31 and Table 5.6. The total dimension of the antennas was $91\text{mm} \times 29\text{mm} \times .8\text{ mm}$, which suits well for indoor communications. The multiband antenna was 4.4% bigger than the single sided version in section 5.4.2 which was necessary to achieve a good tuning at the lower frequency band.

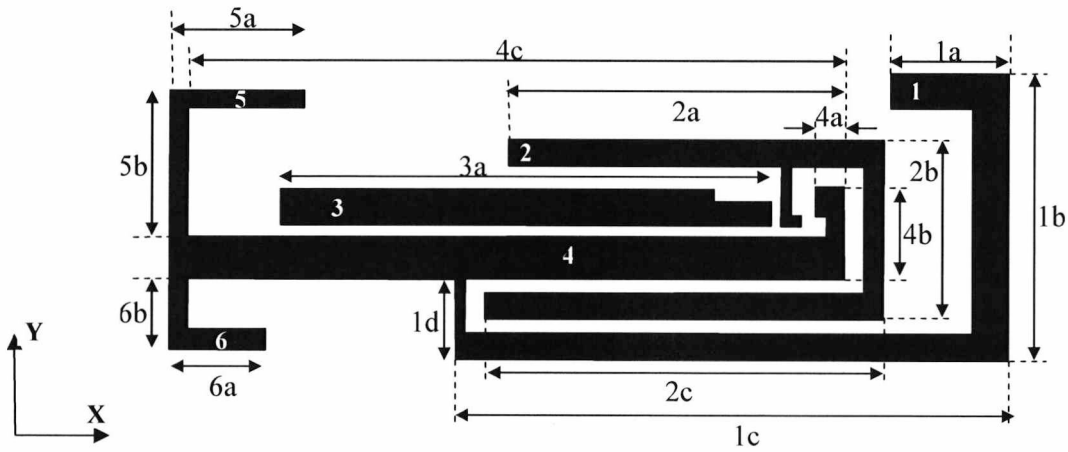


Figure 5.31 Dimensions of the double layer Multiband planar PIFA

Element	Dimension	LENGTH (MM)	Width (mm)
1	1a	12	4
	1b	29	
	1c	57	
	1d	8	
2	2a	39	3
	2b	17	
	2c	41	
3	3a	51	4
4	4a	3	4
	4b	9	
	4c	68	
5	5a	14	2
	5b	13	
6	6a	10	2
	6b	5	

Table 5.6 Dimensions of the double layer multiband planar PIFA

5.6.2 Double Layer Multiband Planar PIFA – Measured S11

The simulated and measured S11 curves for the double layer Multi-band planar PIFA in FR4 substrate are illustrated in Fig.5.32 and Table 5.7. Three wide frequency bands were observed with -10dB S11 bandwidths of 11.3%, 51.5% and 26.4% at the lower,

middle and higher band respectively. The measured bandwidth was 3.3%, 17.5% and 5.5% wider than the simulations at each band. The multiband planar antenna meet the specifications and covers the GSM900, DCS1800, DECT, UMTS, Bluetooth and Hiperlan bands.

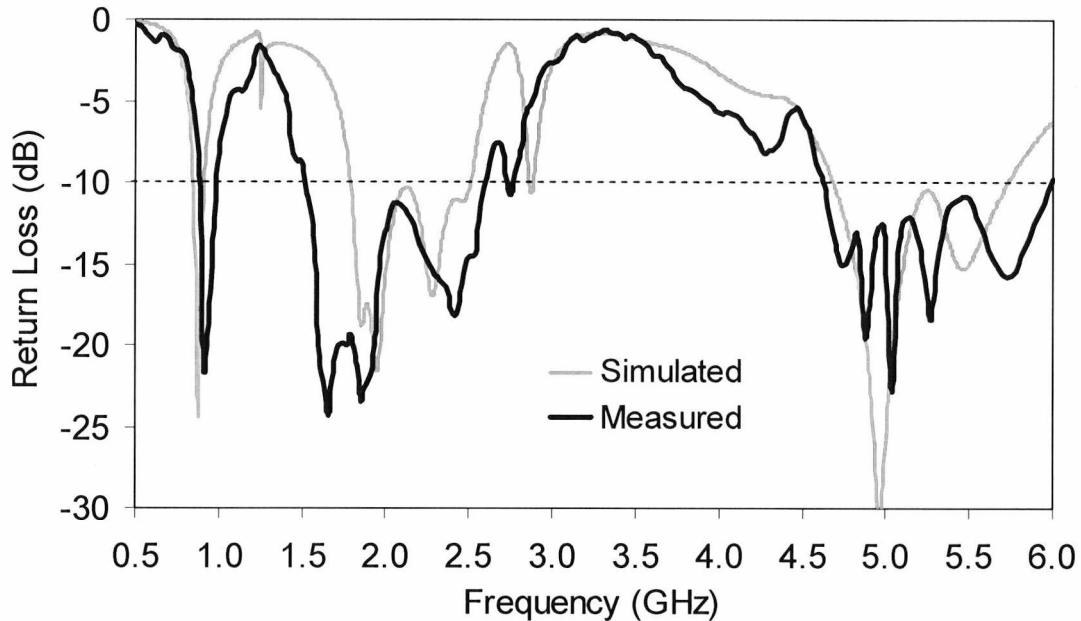


Figure 5.32 Simulated and Measured S11 curves of the single-sided multiband planar PIFA in FR4 substrate

	Low band (MHz)	BW low band (MHz) - %	Mid band (MHz)	BW mid band (MHz) - %	High band (MHz)	BW high band (MHz) - %
Simulated	845-915	70 - 8.0%	1780-2510	730-34.0%	4700-5800	1100-20.9%
Measured	880-985	105-11.3 %	1530-2590	1060-51.5%	4600-6000	1400-26.4%
GSM 900	890-960	70 - 7.6 %				
DCS1800 -UMTS- Bluetooth			1710-2485	1060-36.9%		
HIPERLAN 2					5150-5725	575-10.6%

Table 5.7 Simulated and Measured S11 for multiband planar PIFA in FR4 substrate comparison with existing mobile communication systems bandwidth

Connection of the single and double layer designs to a Hewlett Packard 8722ES network analyzer demonstrated that for the single layer designs in the previous sections, curvature in the feed cable gave rise to a definite degradation in the lower band match and in the worst case the GSM band was lost altogether. There was no discernable change at the upper band. In the double layer case no significant alteration was observed at any band when the feed cable was flexed. Additionally no loss of match at any band was observed when the antenna was connected to cables of different length.

5.6.3 Double layer Multiband Planar PIFA – Surface Currents

The surface current of the double layer Multiband planar PIFA at 920MHz, 1800MHz, 1900MHz, 2100MHz, 2450 MHz, 4960 MHz and 5500 MHz are shown in Figs.5.33-5.39. A considerable similarity can be observed in the surface currents to the original 3D multiband antenna from which it originates [9], also described in section 4.3.3. At the lower band (Fig.5.33), current flows predominantly in elements 1, 2 and 4 as explained in the 3D version of the antenna [9]. At the middle frequency band: At 1800MHz (Fig.5.34), currents become stronger in the section of element 2 closest to element 3. Element 1, element 3 and the section of 4 parallel to element3 also show strong currents; at 1900MHz (Fig.5.35), the currents in the section of element 2 closest to elements 3 and 4 remains strong while currents in elements 3 and 4 are spread more uniformly along the segments; at 2100MHz (Fig.5.36), the currents become stronger in element 5. Elements 1, 2, 3 and 4 remain with strong current density; at 2450MHz (Fig.5.37), the currents become stronger in element 6 while currents in elements 1, 2, 3, 4 and 5 remain strong. At the higher frequency band: At 4960 GHz (Fig.5.38) section 4b of element 4 becomes resonant and shows high current density. There are also high current density in the section of element 2 closest element 4b. Finally, at 5500 GHz (Fig.5.39) the current in section 4b becomes weaker while the surface currents are stronger in the rest of element 4 and elements 2 and 3.

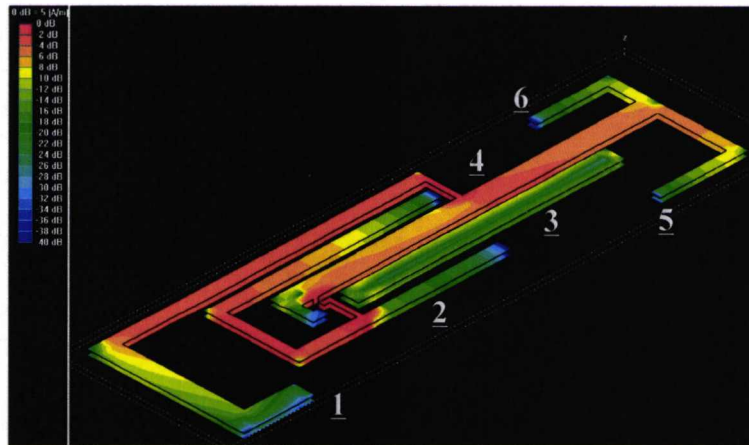


Figure 5.33 Surface currents at 920 MHz

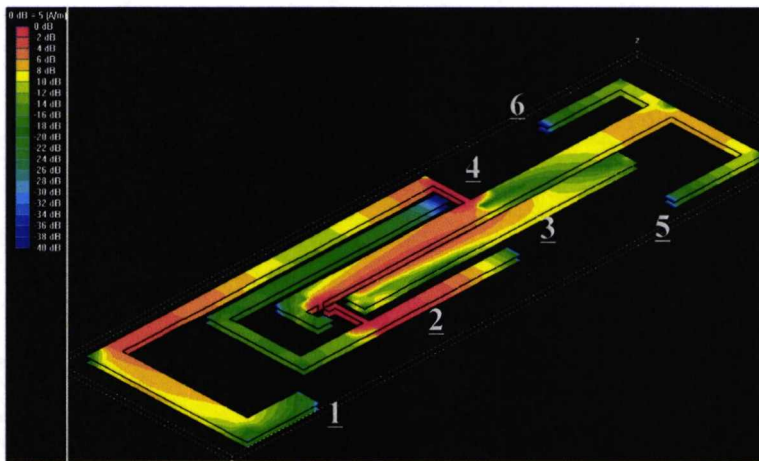


Figure 5.34 Surface currents at 1800 MHz

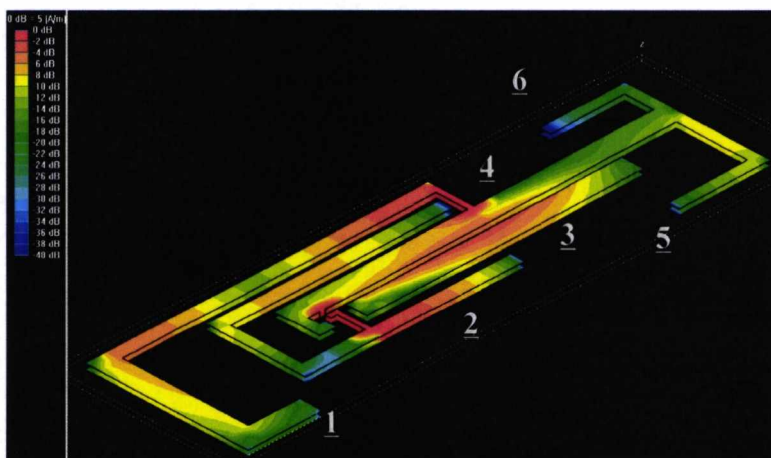


Figure 5.35 Surface currents at 1900 MHz

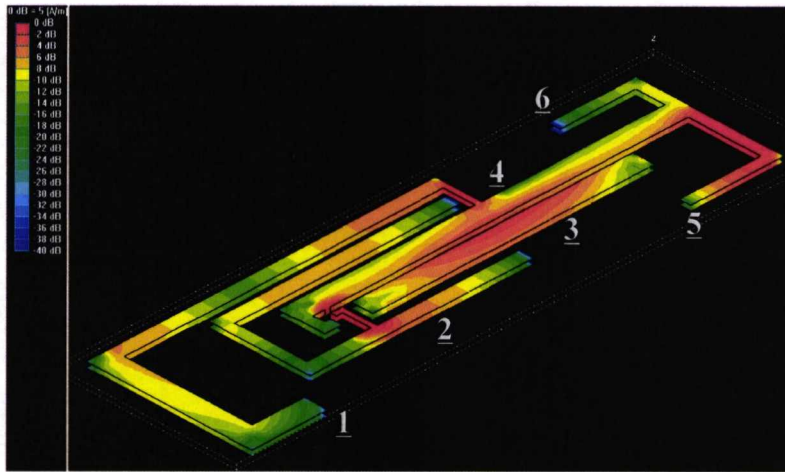


Figure 5.36 Surface currents at 2100 MHz

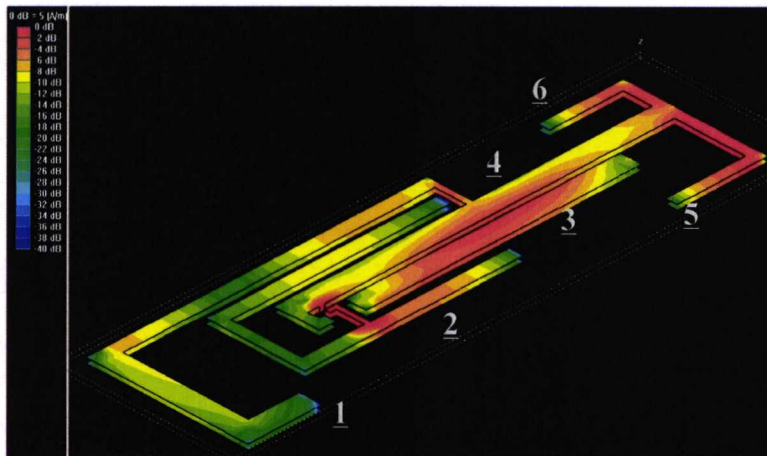


Figure 5.37 Surface currents at 2450 MHz

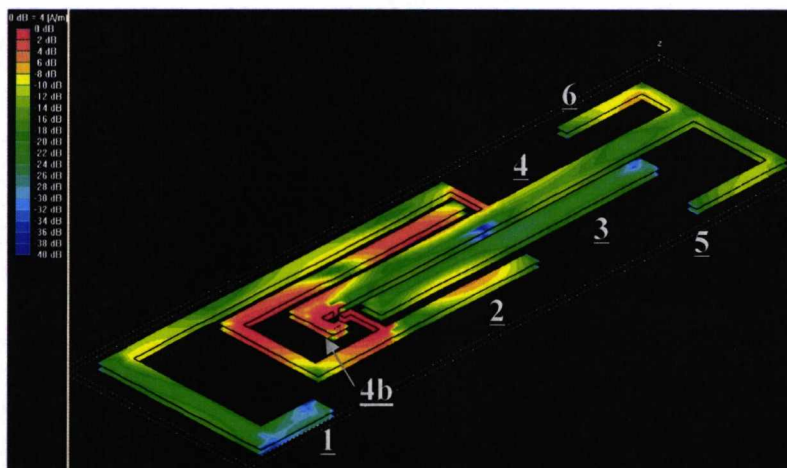


Figure 5.38 Surface currents at 4960 MHz

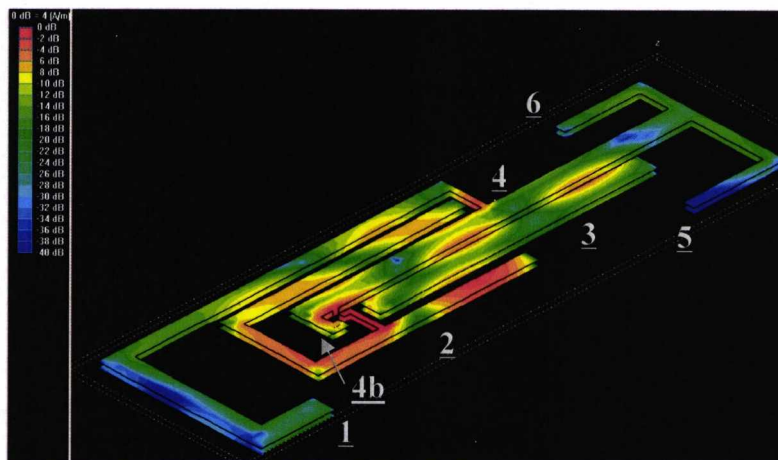


Figure 5.39 Surface currents at 5500 MHz

5.6.4 Double layer Multiband planar PIFA – Parametric Analysis

The multiband antenna consists of 6 elements as indicated in Fig.5.39. The mutual interactions between these tightly coupled elements make the operation of the antenna difficult to describe because loading effects significantly modify the current distribution on adjacent elements. The aim of this section is to give insight into the operation and design of the antenna by presenting a parametric tuning study of the various elements that comprise the multiband planar PIFA. The parametric study was carried out by simulation with IE3D where the length of individual elements was varied to establish the effect on the different frequency bands.

Starting with the initial tuned multiband antenna of Fig.5.31, elements 1 to 6 were modified to show their relative sensitivity to change in length. Practically, a 50Ω matched coaxial cable fed the two sides of the antenna. For the parametric study, the coaxial feed was substituted with a 50Ω planar port to simplify the simulation. The parametric analysis resulted in computed S11 curves giving resonant frequencies for each mode.

Figure 5.40 shows the simulated S11 curves for the lower and middle bands of the antenna where element 1 has been varied. It can be seen that from the initial simulation that the lower band consists of a single mode: (mode 1, at 880MHz), while the middle band contains of 4 modes: (mode 3 at 1860MHz; mode 4 at 1950MHz; mode 5 at 2280MHz and mode 6 at 2480MHz). Trimming element 1 by +-2mm

produced a maximum variation in the resonant frequency of the lower band mode (M1) of 1.2%. In the middle frequency band the variation was of 1.9% for M3, 0.9% for M4 and 2.1% for M5. No significant variations were observed in M6 and in the higher band modes.

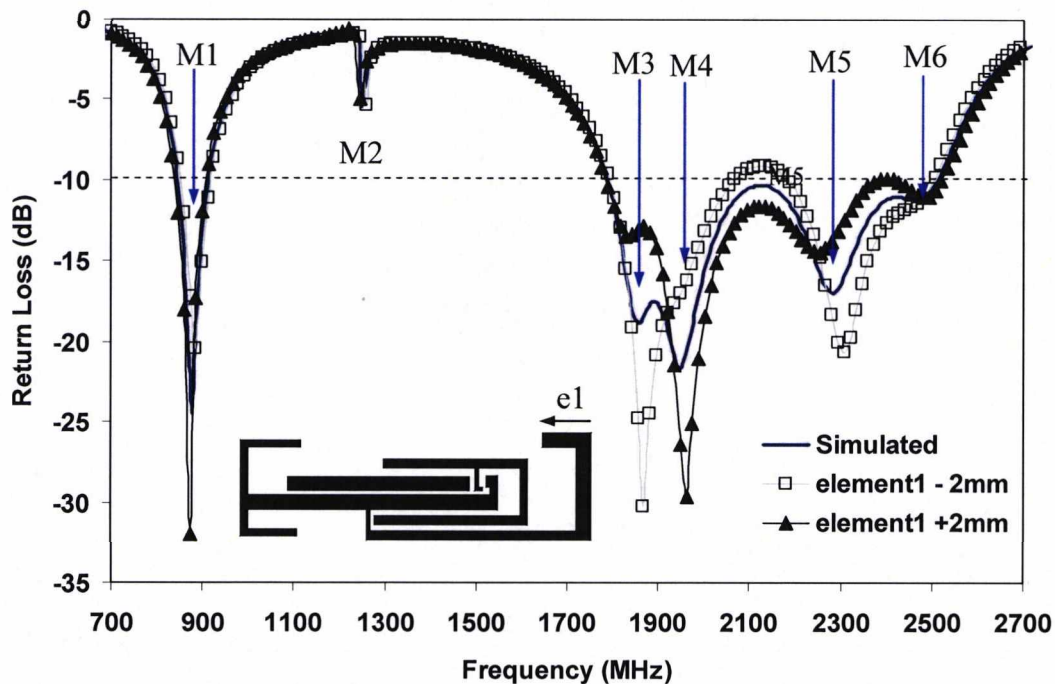


Figure 5.40 Simulated return loss of the antenna (S11) versus frequency for different element 1 length

Figure 5.41 (a) shows the simulated S11 curves for the lower and middle bands of the antenna where element 2 has been tuned. The unbroken line represents the return loss for the tuned antenna while the other two curves show the effect of trimming element 2 by $\pm 2\text{mm}$. Figure 5.41 (b) gives similar curves for the upper band which consists of 2 modes: (mode 6 at 4960MHz and mode 7 at 5460MHz). No significant variation was observed at the lower band mode M1. In the middle band, however, M3 varied by over 3.5%, M4 by 2.5%, M5 by 1% and M6 by 2.5%. In the higher band, the highest variation was observed in mode M8 (6%) while M7 changed 0.7%.

The simulated S11 curves for the lower, middle and higher bands of the antenna for changes in the length of element 3 are shown in Fig.5.42 (a) and (b). Trimming element 2 by $\pm 2\text{mm}$ did not have significant effect in the lower band mode M1. In the middle band, M3 varied by 2%, M4 varied by 2.5%, M5 by 0.8% and M6 by 3.3%. In the higher band, M8 varied by 2% while M7 did not change significantly

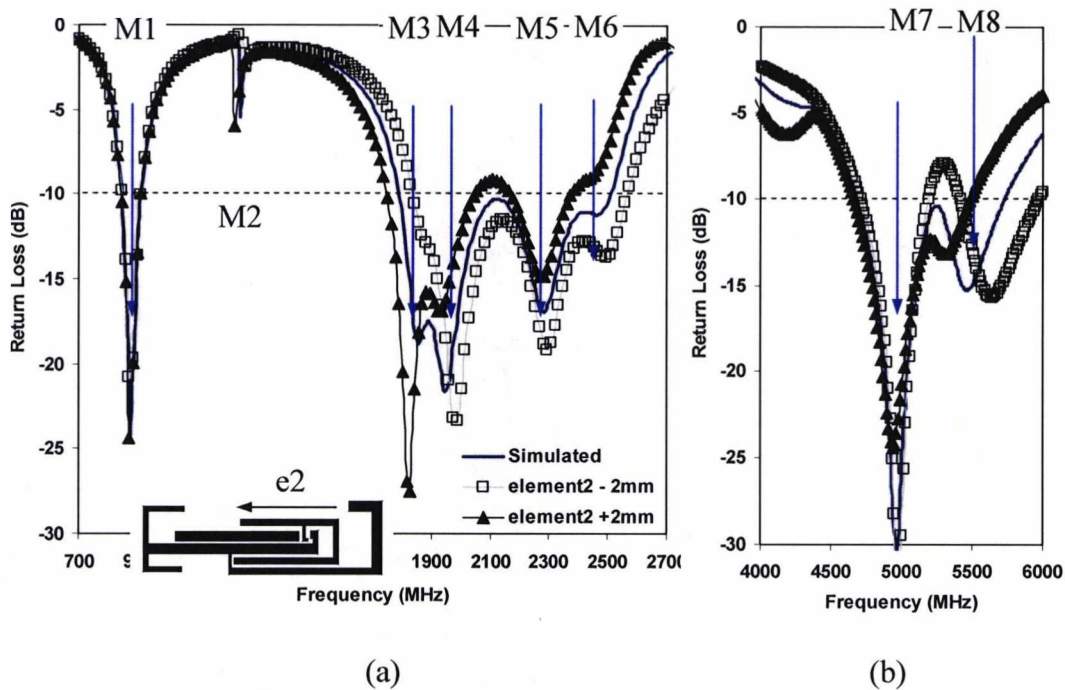


Figure 5.41 Simulated return loss of the antenna (S11) versus frequency for different element 2 length. (a) lower and middle band (b) higher band

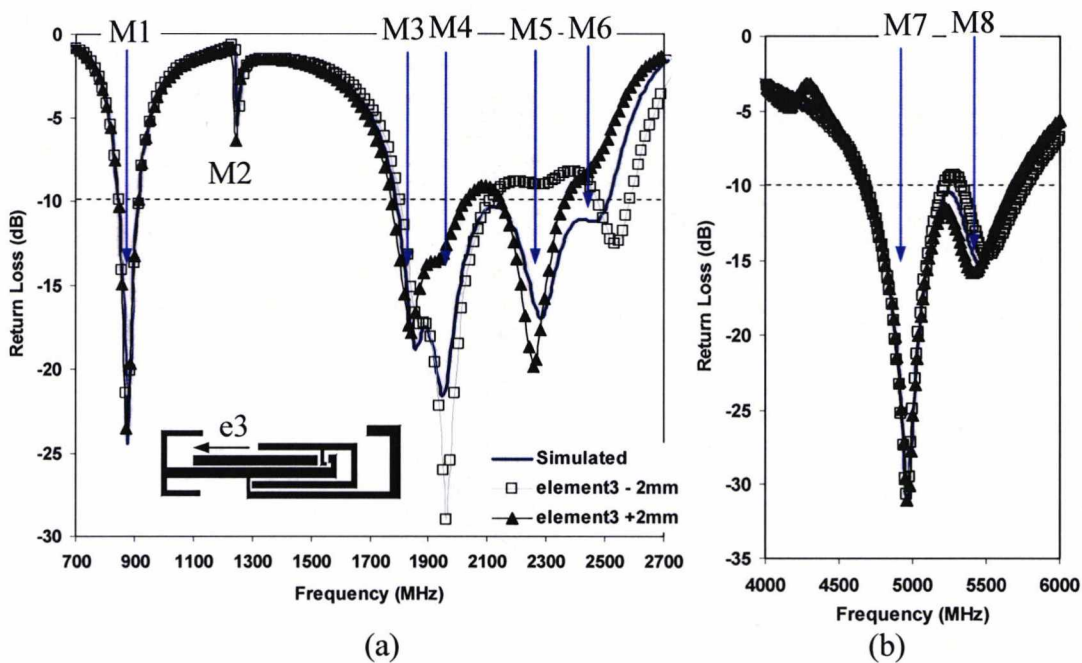


Figure 5.42 Simulated return loss of the antenna (S11) versus frequency for different element 3 length. (a) lower and middle band (b) higher band

Figure 5.43 shows the simulated S11 curves for the lower and middle bands (a) and the higher band (b) of the antenna where element 4b has been tuned. No significant variations were observed in the resonant frequencies of the lower and middle band mode for variations in element 4b of $\pm 2\text{mm}$. In the higher band, M7 varied by over 9.5% while M8 did not vary.

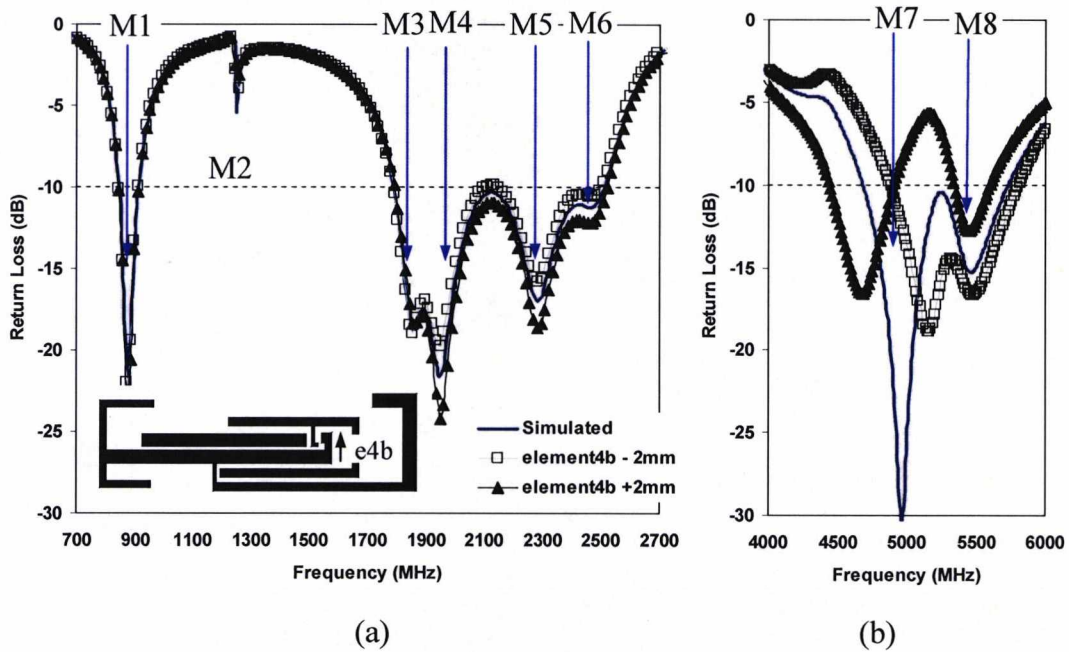


Figure 5.43 Simulated return loss of the antenna (S11) versus frequency for different element 4b length. (a) lower and middle band (b) higher band

The simulated S11 curves of the antenna for changes in the length of element 5 are shown in Fig.5.44 (a) and (b). Trimming element 5 by $\pm 2\text{mm}$ changed the resonant frequency of the lower band mode M1 by 1.8%. The change in the middle band was as follows: M3 varied by 0.8%, M4 varied by 1.5%, M5 by 6.9% and M6 by 6.2%. In the higher band, M7 varied by 0.5% and M8 by 1.4%.

Figure 5.45 shows the simulated S11 curves for the lower and middle bands (a) and the higher band (b) of the antenna where element 6 has been tuned. No significant variations were observed in the resonant frequencies of the lower and higher band modes for variations in element 6 of $\pm 2\text{mm}$. In the middle band, M6 varied by 4.7% while M3, M4, M5 and M6 did not vary.

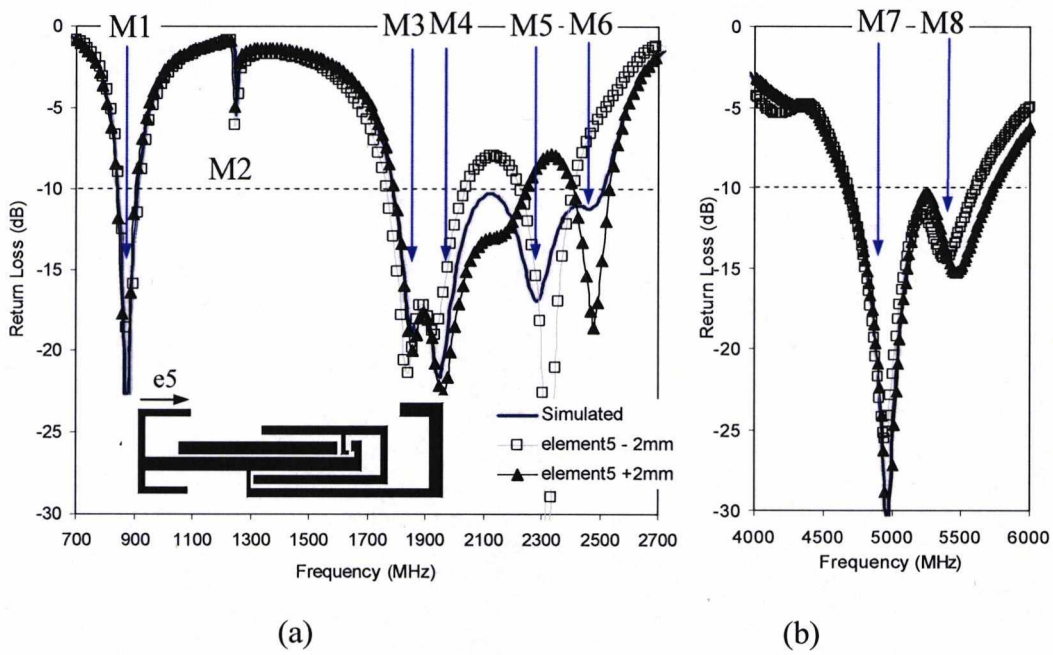


Figure 5.44 Simulated return loss of the antenna (S11) versus frequency for different element 5 length. (a) lower and middle band (b) higher band.

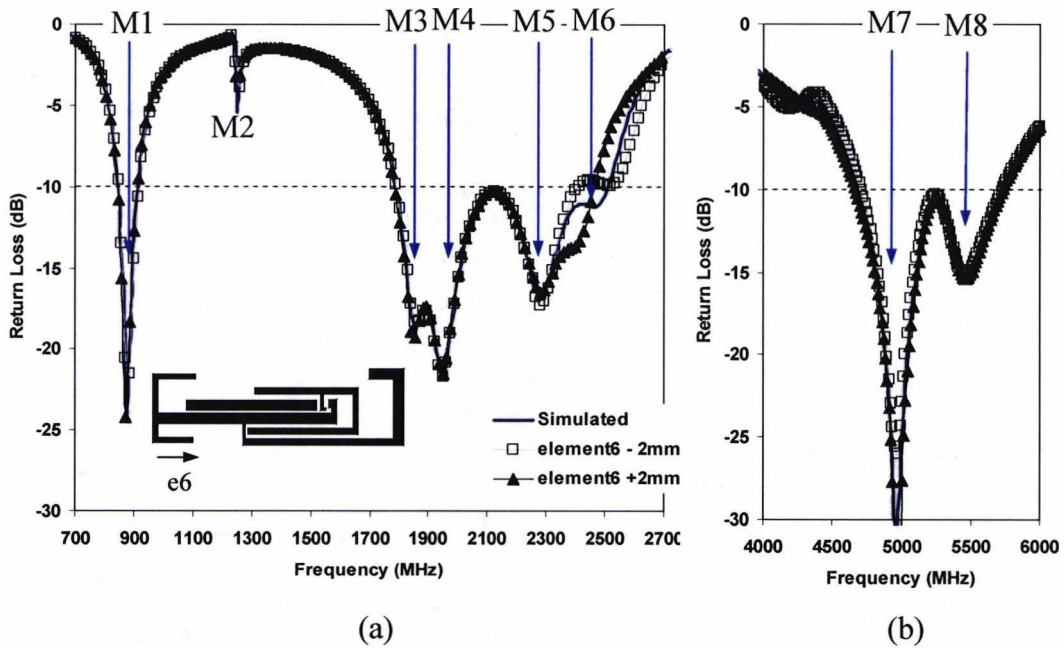


Figure 5.45 Simulated return loss of the antenna (S11) versus frequency for different element 6 length. (a) lower and middle band (b) higher band

The generated S11 curves for the case of each element being tuned in length and the effect on mode frequencies is summarized in Table 5.8 where the total frequency deviation across each element tuning range is given.

Percentage Frequency Deviation								
Band	Mode	Tuned Frequency (MHz)	Element 1 (± 2 mm)	Element 2 (± 2 mm)	Element 3 (± 2 mm)	Element 4b (± 2 mm)	Element 5 (± 2 mm)	Element 6 (± 2 mm)
Lower	1	880	1.2	0	0	0	1.8	0
Middle	2	1860	1.9	3.6	2.0	0	0.8	0
Middle	3	1950	0.9	2.5	2.5	0	1.5	0
Middle	4	2280	2.1	1.0	0.8	0	6.9	0
Middle	5	2480	0	2.5	3.3	0	6.2	4.7
Upper	6	4960	0	0.7	0	9.6	0.5	0
Upper	7	5460	0	6.0	2.0	0.6	1.4	0

Table 5.8 Percentage change in mode frequency caused by tuning the elements of the double sided multiband PIFA

Observation of Table 5.6 and Figs.5.41 to 5.46 show that element 1 is dominant for tuning the lower band, while the middle band depends mainly on elements 2, 3 and 5. Finally, the upper band is primarily tuned by elements 4 and 2. The relative independence of the elements at different bands makes the multiband tuning process achievable

5.6.5 Double layer Multiband Planar PIFA – Radiation Patterns

The radiation patterns for each band were measured in an anechoic chamber and are shown in Figs.5.46 to 5.54 where good omni-directionality can be observed for each band in the y-z plane. Only in the 5 GHz band do significant nulls of about 10 dB form. The antenna patterns are essentially those of a dipole. Although some nulls are present, significant problems are not envisaged as the antenna is intended for operation in an indoor multipath rich environment. Measured gains ranged between 1.0 and 3.0dBi.

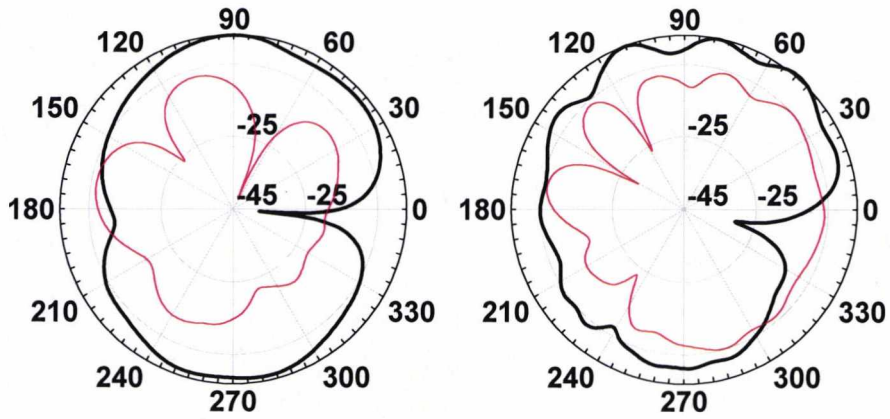


Figure 5.46 Measured far field pattern in the XY plane at 920 MHz (left) and 1800 MHz (right). Co-polar (thick line) and cross-polar (thin line)

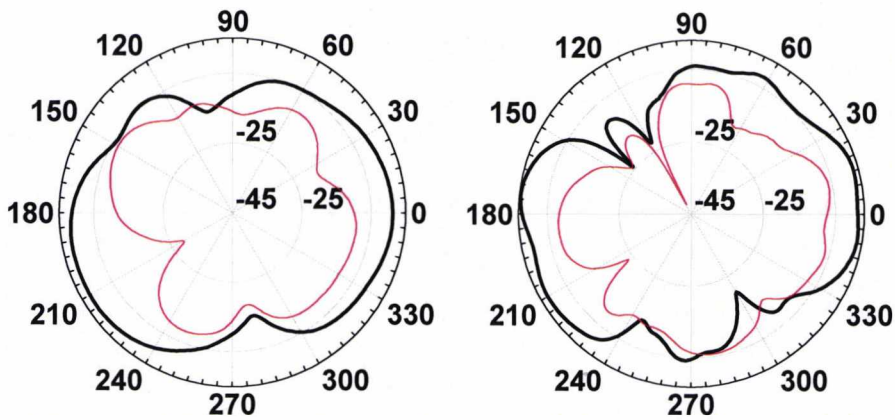


Figure 5.47 Measured far field pattern in the ZX plane at 920 MHz (left) and 1800 MHz (right). Co-polar (thick line) and cross-polar (thin line)

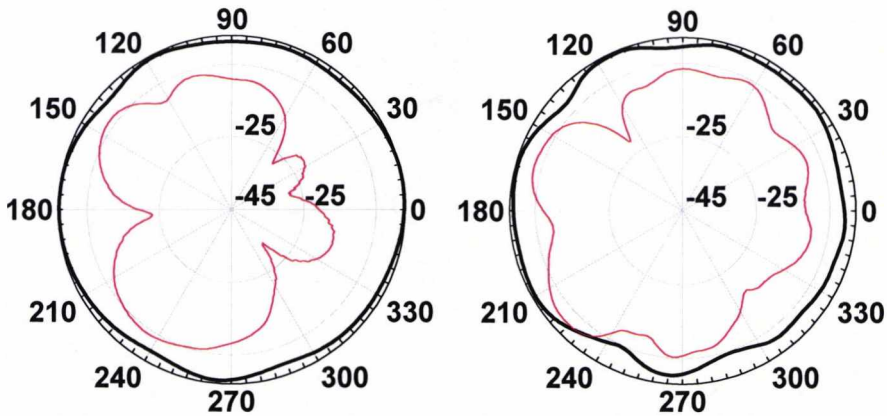


Figure 5.48 Measured far field pattern in the YZ plane at 920 MHz (left) and 1800 MHz (right). Co-polar (thick line) and cross-polar (thin line)

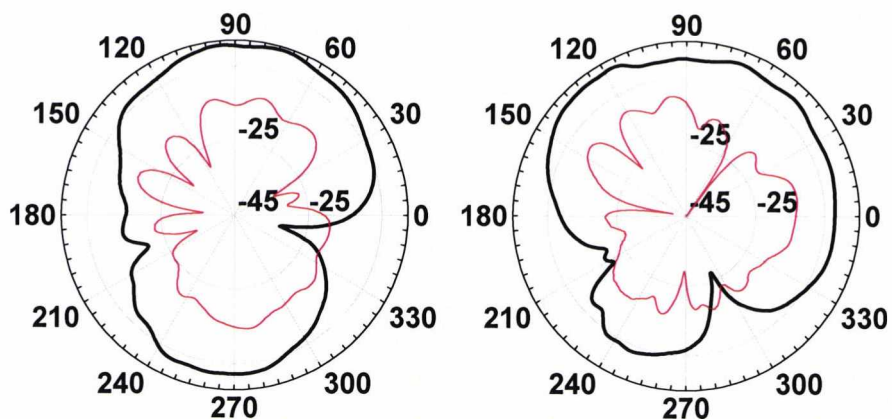


Figure 5.49 Measured far field pattern in the XY plane at 2100 MHz (left) and 2450 MHz (right). Co-polar (thick line) and cross-polar (thin line)

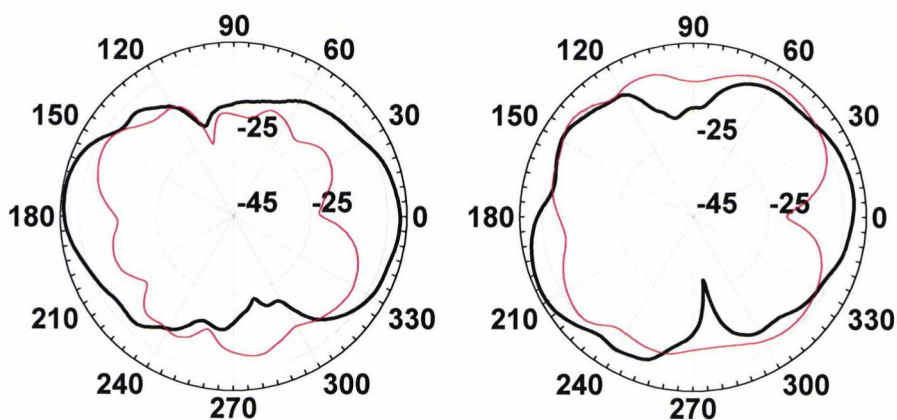


Figure 5.50 Measured far field pattern in the ZX plane at 2100 MHz (left) and 2450 MHz (right). Co-polar (thick line) and cross-polar (thin line)

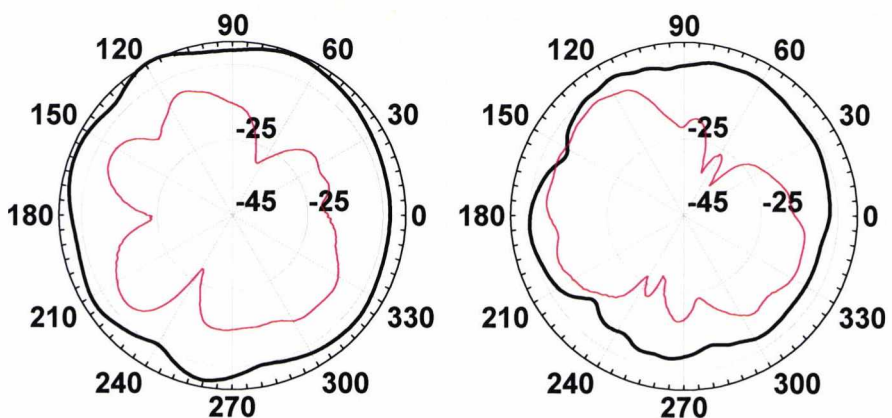


Figure 5.51 Measured far field pattern in the YZ plane at 2100 MHz (left) and 2450 MHz (right). Co-polar (thick line) and cross-polar (thin line)

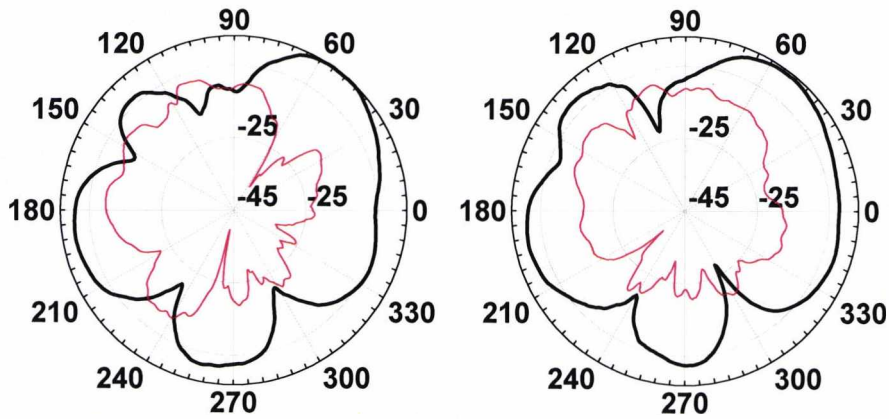


Figure 5.52 Measured far field pattern in the XY plane at 5250 MHz (left) and 5600 MHz (right). Co-polar (thick line) and cross-polar (thin line)

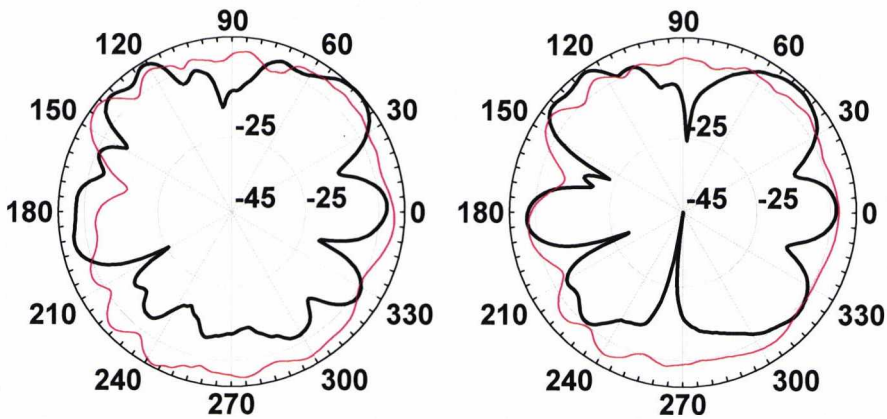


Figure 5.53 Measured far field pattern in the XZ plane at 5250 MHz (left) and 5600MHz (right). Co-polar (thick line) and cross-polar (thin line)

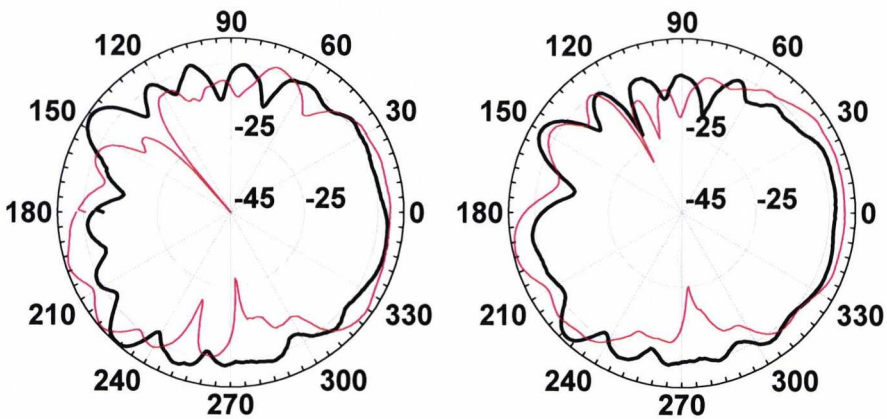


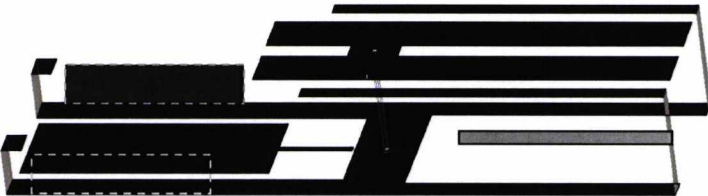
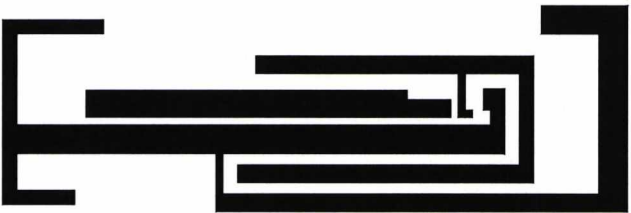


Figure 5.54 Measured far field pattern in the YZ plane at 5250 MHz (left) and 5600MHz (right). Co-polar (thick line) and cross-polar (thin line)

5.7 Summary Table

Table 5.8 presents a summary table of the antennas described in chapter 4 and 5.

TABLE 5.8		S11 (%)		Gain
Antenna	SIZE Button (mm)	Low band BW	Mid- High BW	Frequency (Gain)
Multiband Antenna with Ground Plane Parasitic Resonator 	133 x 24 x 9.5	22.3%	33.0%	920 MHz (1.9 dBi) 1800 MHz (3.2dBi) 1900 MHz (3.1 dBi) 2100 MHz (2.1 dBi)
Multiband Antenna with Side Resonators 	131 x 24 x 9.5	13.7%	38.5%	920 MHz (1.7 dBi) 1800 MHz (3.3dBi) 1900 MHz (2.9 dBi) 2100 MHz (1.9 dBi) 2450 MHz (2.1 dBi)
Multiband Antenna with Multiresonators 	131 x 20 x 8.0	22.0%	39.5%	920 MHz (1.9 dBi) 1800 MHz (2.8dBi) 1900 MHz (2.9 dBi) 2100 MHz (3.0 dBi) 2450 MHz (1.6 dBi)
Double layer Multiband PIFA 	91 x 29 x 0.8	11.3%	51.5% 26.4%	920 MHz (1.7 dBi) 1800 MHz (2.1dBi) 1900 MHz (2.8 dBi) 2100 MHz (1.7 dBi) 2450 MHz (2.4 dBi) 5350 MHz (2.9 dBi) 5500 MHz (2.5 dBi)

As can be seen from Table 5.8 the Double layer Multiband PIFA achieves the smallest size all four antennas presented. However, the GSM900 band bandwidth is lowest for this antenna with 11.3%, which is 11% lower than bandwidth obtain for the Multiband Antenna with ground plane parasitic resonator (22.3%). The Planar Antenna has the widest middle band bandwidth (51.4%) of the four antennas and is the only antenna that resonates at the Hiperlan bands with 26.4% bandwidth. The measured gain of the four antennas at the GSM900 band was similar for the three antennas. At the middle band, however, the average gain was around 0.2dB lower for the Planar Antenna than for the 3D Multiband Antennas.

5.7 Conclusions

A dual band PIFA covering the GSM and DCS bands was enhanced with the addition of a parasitic element 3 in the ground plane in chapter 4. This element added a new mode making the 2GHz band much wider and incorporates all systems between 1690 and 2210 MHz Additional tuning allowed coverage to be extended across GSM, DCS, DECT, UMTS and Bluetooth bands.

In this chapter the PIFA has been redesigned in planar form and the performance at all bands has been maintained. Adding stub elements 5 and 6 to the ground element 4 of the planar PIFA made it possible to achieve further bandwidth enhancements for the upper frequencies. Initially, the planar PIFA was difficult to excite in practice due to balancing problems which made the feed cable position and length critical factors in achieving a good match. This issue was resolved by creating a 2 layer planar PIFA on a thin substrate to create a more balanced design and the feed line was consequently found to be less critical in obtaining a good match at all bands. In addition, the resulted double layer antenna was able to cover the GSM, DCS, DECT, UMTS, Bluetooth and Hiperlan bands. The radiation patterns and gain of the double layer PIFA were dipole like with gains of around 2dB measured at all matched bands. The patterns were comparable with those of the single layer antenna.

References.

- [1] D. Wake, "Trends and Prospects for Radio over Fibre Picocells", *IEICE Electronics Society, International Topical Meeting on Microwave Photonics, MWP* November, Awaji, Japan, 2002, pp.21-24.
- [2] J. Soler, D. Garcia, C. Puente and J. Anguera, "Novel combined MOD-P Multiband Antenna Structures inspired by Fractal Geometries", *Microw. And Opt. Tech. Letts.*, Vol.41, 5, June 2004, pp.423-426.
- [3] C.T.P. Song, P.S. Hall, H. Ghafouri-Shiraz, "Shorted fractal Sierpinski Monopole Antenna", *IEEE Trans. Antenn. And Propag.* Vol.52, 10, October 2004, pp.2564-2570.
- [4] J. Yeo, R. Mittra, "Design of conformal multiband antennas based on Fractal concepts", *Microw & Opt. Tech. Letts.*, vol.36, 5, March 2002.
- [5] H. Elsadek, D. Nashaat and H. Gahli, "Multiband Miniturized PIFA for Compact Wireless Communication Applications", *Microw. And Opt. Tech Letts. Vol.42*, 3, August 2004, pp. 230-234.
- [6] P. Cias, R. Staraj, G. Kossiavas and C. Luxey, "Compact internal multiband antenna for mobile phone and WLAN standards", *IEE Electron. Letts.* July 2004, Vol.40, 15, pp.920-921.
- [7] C.W. Chiu, and F.L. Lin,, "Compact dual-band PIFA with multi-resonators", *IEE Electron. Letts.*, Vol.38, 12, June 2002, pp.538-540.
- [8] D. Viratelle and R.J. Langley: 'Dual-band printed antenna for mobile telephone applications', *IEE proc. Microw. Anten. Propag.*, 147, No.5, October 2000, pp.381-384.
- [9] B. Sanz-Izquierdo, J.C.Batchelor and R.J. Langley, "Multiband PIFA antenna with ground plane capacitive resonator", *IEE Electron. Letts.* Vol.40, 22, October 2004, pp.1391-1392.
- [10] K-L, Wong, G-Y, Lee, and T-W Chiou., "A low profile planar monopole antenna for multiband operation of mobile handsets", *IEEE Trans. Ant & Propag.*, 51, No.1, January 2003.
- [11] R. Leelaratne and R.J. Langley: 'Multiband PIFA Vehicle Telematics Antennas', *IEEE Trans. Vehicular Tech.*, 54, No.2, March 2005, pp.477-485.

Chapter 6

Wearable antennas

6.1 Introduction

Recent technological advances have driven the rapid development of communication standards, such as Bluetooth, WIFI, ZigBee and UWB. Convergence of wired and wireless networks has played an important role in this development. In addition, electronics devices have been becoming more and more compact, lightweight and easier to carry.

Wearable computing and wearable electronics is seen as the next step in the integration of electronic devices into the daily environment. The main aim of wearable computing is to integrate technology while minimizing the human-device interface, device size and physical connections [1]. Numerous wearable devices and systems have been developed over the last decade; such as displays and cameras mounted in the frames of ordinary

glasses [2], MP3 players that can be sewn directly into shirts or jackets [3] and even a wearable sensor system [4] consisting of accelerometers, gyroscopes and magnetic field sensors attached to the body..

Wireless on body networks promise a further integration of computing and peripheral devices into our everyday clothing. Research in [5] and [6] has already characterized on-body propagation channels for narrowband [5] and UWB [6] communication systems to understand device to device link as part of a wearable area network (WAN).

Antennas designs for wearable applications have been developed mainly in textile material as metal patches i.e. in [7-10]; in [7- 9] with probe feeds and liner polarization or in [10] with a microstrip feed and circular polarization. The advantage of the antennas fabricated using flexible metal patches is the easy adaptability to the human body contour and the high level of camouflage within the garment. However, any metal patch antenna placed within the clothes is likely to suffer from frequent bending and flexing due to the natural human movements which will periodically detune the antenna and may degrade its physical structure over time.

The wearable antennas proposed in this chapter use the physical characteristics of ordinary metal buttons to create rigid antennas that can be camouflage within the clothing and avoid the use of metal patches which are subject to flexing and detuning of the antenna.

The chapter is divided into different sections; firstly the material measurement technique used to characterise the substrates and textiles will be discussed, this will be followed by the study of single frequency and dual frequency metal button antennas. Finally, a equivalent circuit model will be introduced and the effect of the human body proximity will be studied.

6.2 Materials Characteristics

In order to design wearable antennas the properties of textiles at microwave frequencies must be determined. The transmission method described in section 3.1.1 has been used to determine the dielectric characteristics of the textile materials employed in the present research work. The material under test is placed at the centre of a rectangular waveguide

and supported by expanded polystyrene foam. The scattering parameters of the waveguide with and without the textiles are compared to determine the dielectric constant. The advantages of this method are:

- The material is supported by the foam and can be accurately placed in the waveguide.
- Since this is a comparison measurement, any mismatch or inaccuracies in the measurements are subtracted.
- The length of the material sample can be increased at will to obtain a bigger difference between the two measurements and thus increase the accuracy.
- The measurements can be performed over a wide band of frequencies between the cut-off frequencies of the TE_{10} and the TE_{01} modes.

The method has been used to determine the dielectric constant of Velcro and the result is shown in Fig. 6.1 and 6.2

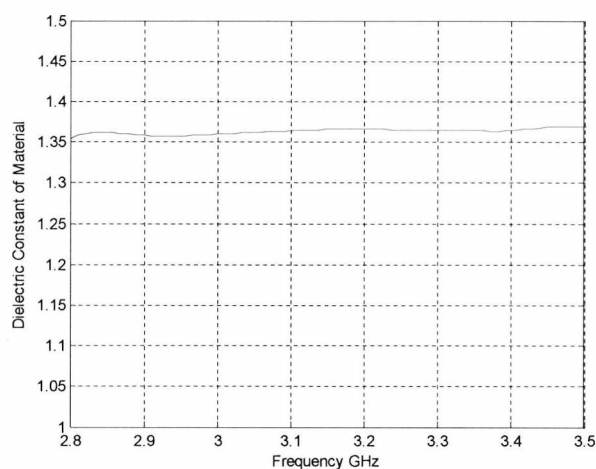


Figure 6.1 Dielectric constant measurements at 2.8 – 3.5 GHz

The average effective permittivity obtained for the Velcro material was 1.37 with little variation at the 2.8 GHz to 3.5 GHz frequency band and the 5.5 GHz to 8 GHz band. It has been deduced that little variations would be observed at the 2.4GHz to 2.5GHz Bluetooth band and 5GHz to 6GHz WLAN band target. Thus, a constant permittivity 1.37 has been assumed for the Velcro material in the computer calculation of the wearable antennas developed in the following sections.

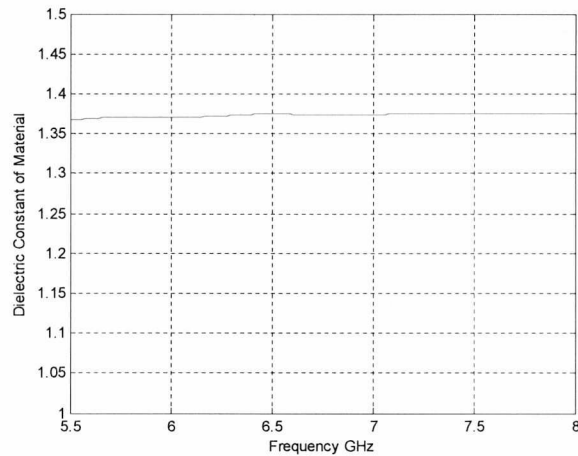


Figure 6.2 Dielectric constant measurements at 5-6 GHz

6.3 Single Band Metallic Button Antenna (SBMBA)

The characteristic denim jeans button, which resembles a top loaded short monopole antenna, allows for designing wearable antennas with a rigid solid structure. The single band metallic button antenna is basically a standard metal button that is placed on a Velcro substrate and fed by a coaxial feed line as shown in Fig.6.3 and 6.4.

The rationale for designing an antenna of this structure is as follows:

- a) Clothing fabric is not used as an integral substrate to fill a resonant cavity as could be the case in a microstrip patch. This alleviates the performance issues coupled with substrate compression, poor electrical characterization of textile material and variable losses associated with moisture uptake.
- (b) The small surface area of the antenna means that it is not required to be flexible so that surface distortion will not alter the input impedance and radiation patterns.
- (c) The antenna does not require a large flat ground plane
- (d) the antenna structure is very simple to incorporate into clothing by conventional construction methods, and it is even possible to fit retrospectively.

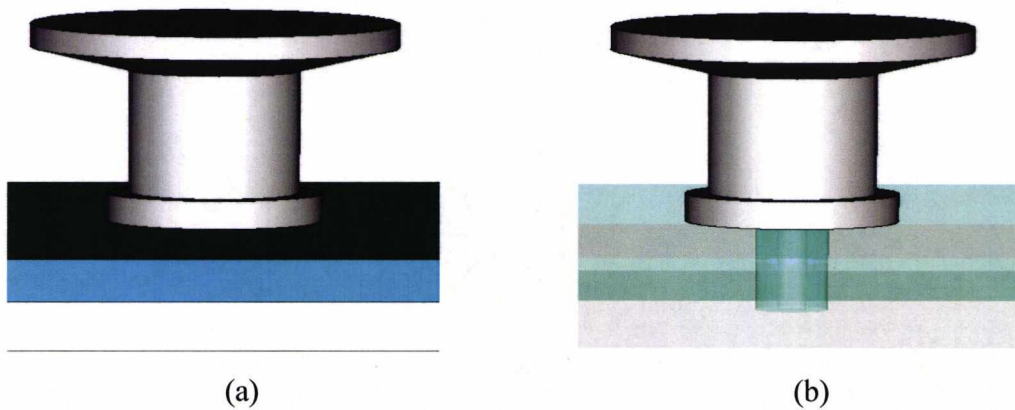


Figure 6.3. Single band wearable metallic button antenna structure (SBMBA) coaxial fed (a) SBMBA with velcro substrate shown (b) SBMBA with Velcro substrate translucent to show coaxial feed



Figure 6.4. SBMBA. Left, top view. Right, side view

6.3.1 SBMBA - Dimension

The dimensions of the single band metallic button antenna using an ordinary jeans button are shown in Fig.6.5 and Table 6.1 which also indicates the electrical dimensions. The antenna is a standard jeans button which is usually brass, iron or compressed metal. The antenna is mounted on a Velcro substrate over a metallic ground of 50x50mm.

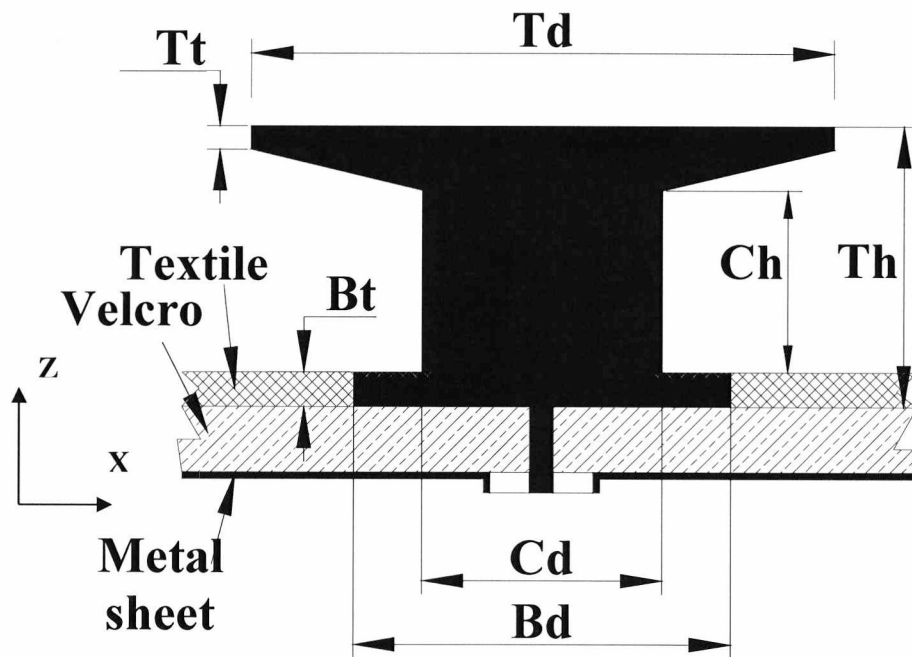


Figure 6.5 Principal dimensions of the SBMBA

Antenna Parameters	Values	Electrical length
Tack button height, T_h	8.50 mm	0.142λ
Tack button top disc diameter, T_d	16.00 mm	0.267λ
Tack button top disc thickness, T_t	1.00 mm	0.017λ
Tack button base diameter, B_d	9.40 mm	0.157λ
Tack button base thickness, B_t	1.20 mm	0.02λ
Tack button outer cylinder diameter, C_d	7.40 mm	0.123λ
Tack button inner cylinder height, Ch	5.30 mm	0.088λ
Substrate height	1.80 mm	0.03λ
Ground plane length	40 mm	0.833λ
Ground plane width	40 mm	0.833λ
Substrate material	Velcro ($\epsilon_r \sim 1.37$)	

Table 6.1 Dimensions of the SBMBA

6.3.2 SBMBA Measurement Results, S11

The S11 curves for the SBMBA are given in Fig.6.6 where it can be seen that the antenna is resonant within the 5 GHz band with a measured 45.6% bandwidth. Simulations and measurements compared well with a 5.2% wider bandwidth obtained for the measurements. The results are summarized in Table 6.2.

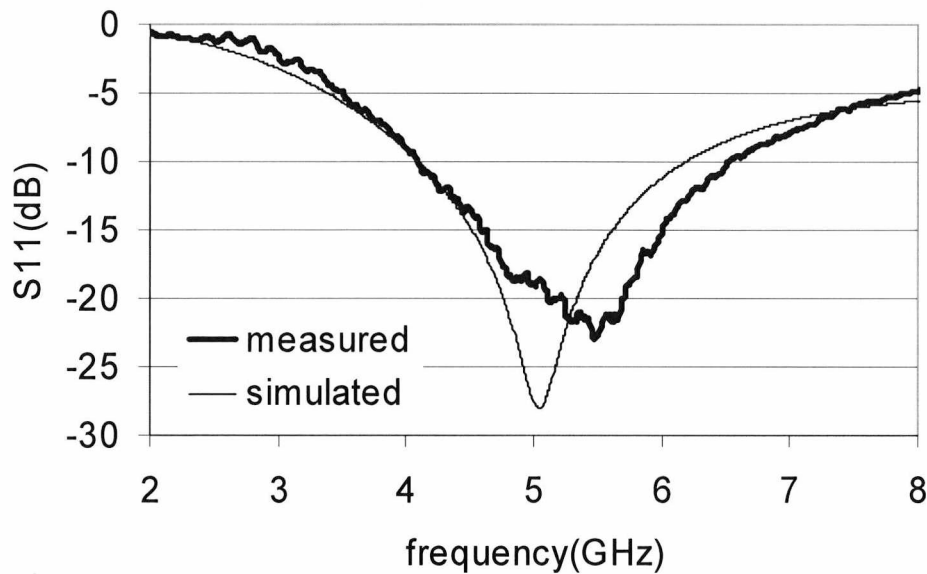


Figure 6.6. S11 curves for the single frequency button antenna.

	Frequency Band (MHz)	Bandwidth (MHz) - (%)
Simulation	4100 - 6200	2100 - 40.7%
Measurement	4100 - 6520	2420 - 45.6%

Table 6.2 .Simulated and Measured S11 for the SBMBA

6.3.3 SBMBA Surface Currents

Figure 6.7 shows the simulated surface currents of the SBMBA at 5 GHz. As can be seen from the surface currents in the antenna, there is a strong current in the bottom disc and in

the middle cylinder that spreads all the way to the edges of the top plate. There is a current null at the centre of the top disc.

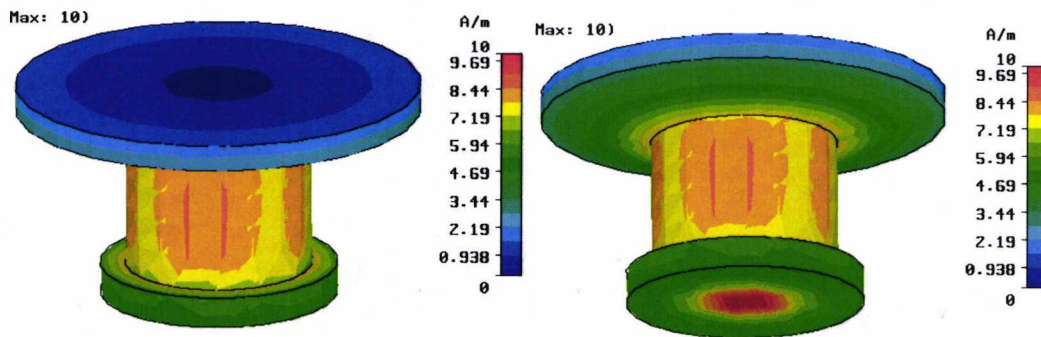


Figure 6.7 Surface currents at 5GHz.

6.3.4 Parametric analysis of the SBMBA

Altering the principal dimensions of the SBMBA gives insight into the operation and design process. The dimensions considered for the parametric analysis were the antenna height T_h , the top disk diameter T_d , the base cylinder diameter B_d and the middle cylinder diameter C_d . Apart from the dimensions considered for parametric variation, all other dimensions are as given in Table 6.1.

Figure 6.8 shows the effect of varying the height of the antenna (T_h) between 5mm and 12mm on the resonant frequency and the fractional bandwidth of the SBMBA. The effect of varying T_h is as follows:

- At a height T_h of 5mm, the antenna is equivalent to a thick monopole with a conical taper between the middle cylinder and the top disc. The antenna achieves -10dB bandwidth of nearly 70% and is resonant at 8GHz.
- As the antenna height increases the capacitance between the top disc and the ground plane decreases and the resonant frequency decreases, which also results in a decrease in the bandwidth. The effect of the antenna height on the resonant frequency and bandwidth is dramatic until a height of approximately 7.2mm ($f = 5.7$ GHz and $BW = 43.3\%$) with a decrease in resonant frequency and bandwidth of 29% and 25% respectively.

- For a height between 7.2mm and 12mm the bandwidth does not decrease significantly (3%) and the resonant frequency curve slope also moderates, decreasing from 5.7GHz to 3.8GHz.
- The last range studied is between 12mm and 15mm with a 3% decrease in bandwidth and 18% decrease in resonant frequency.

It can be concluded from the study of T_h , that the height of the standard button used ($T_h = 8.5\text{mm}$) is optimal since it is within the range of moderate bandwidth change (7.2 to 12mm), where the bandwidth is stable around 40% which is sufficient for applications such as 5 GHz WLAN. The frequency is moderately tunable by altering T_h .

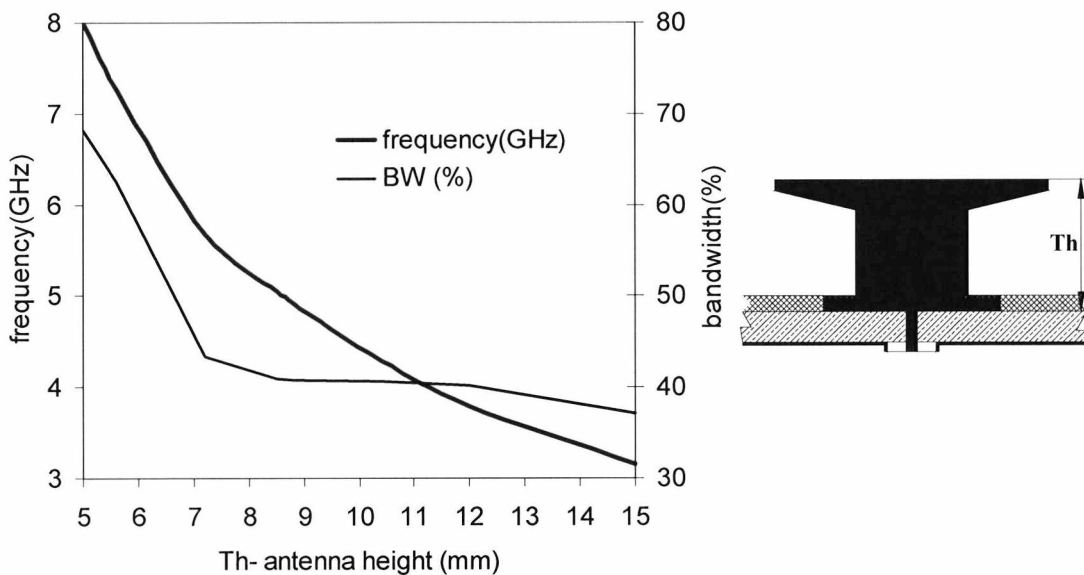


Figure 6.8. Simulated SBMBA resonance as a function of the antenna height (T_h)

Figure 6.9 shows the change of resonant frequency and bandwidth as the top disc diameter (T_d) is varied from 8mm to 20mm. As can be seen from the figure, the resonant frequency of the SBMBA decreases from 6.6 GHz ($T_d = 8\text{mm}$) to 5.5 GHz ($T_d = 10\text{mm}$) with a fairly constant slope. However, the bandwidth BW seems to increase constantly from $T_d = 8\text{mm}$ ($BW = 22$) to $T_d = 14.5\text{mm}$ ($BW = 39\%$) but the slope continually reduces from this point to $T_d = 20\text{mm}$ ($BW = 43\%$).

The dimension of the upper disc diameter (T_d) of the standard jeans buttons used (being for most standard jeans buttons between 16mm to 18mm) is 16mm which is optimal since

the slope of the bandwidth is not as pronounced as for the 8mm to 16mm range while the change of the resonant frequency is constant.

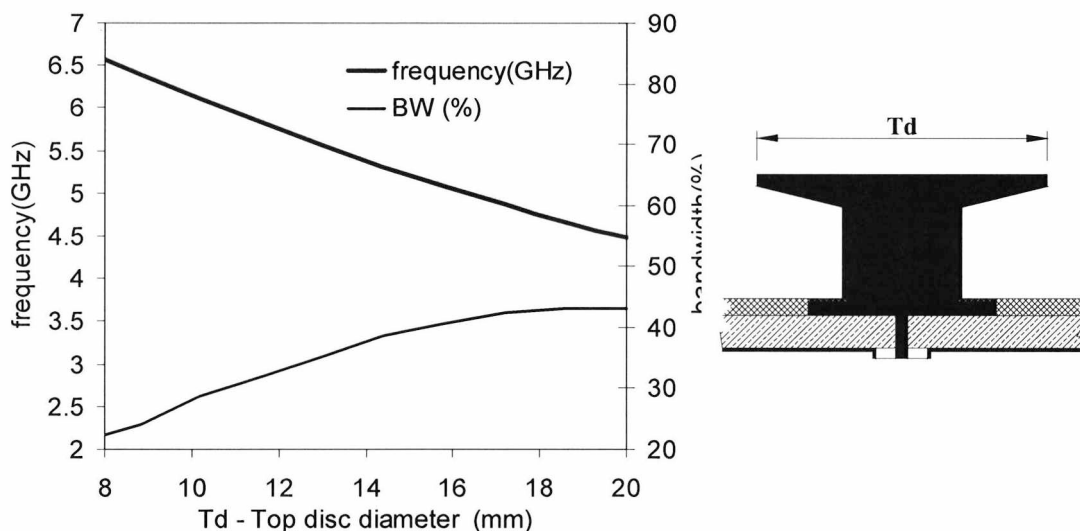


Figure 6.9. Simulated SBMBA resonance as a function of the top disc diameter (Td).

Figure 6.10 shows the effect of varying the diameter of the base Bd of the SBMBA from 7mm to 14mm. The resonant frequency remains almost constant for the range considered for the study, with an average value of 4.97 GHz and maximum deviation of -2% for Bd equals 7mm. The bandwidth remains almost constant up to Bd = 8.8mm, from where the bandwidth decreases sharply and falls to 0 for Bd = 13.6mm where the -10dB match is lost.

The dimensions for the diameter of the base of a standard button used (Bd = 9.4mm) falls just within the range of decaying bandwidth, which, although not desirable, the bandwidth is only 5% lower than the best possible bandwidth. A possible solution to this problem is to use 8.8mm nail (lower part of a standard jeans button with diameter Bd) for best bandwidth performance without compromising the function of the nail in clothing (it should be greater than the diameter of main cylinder = 7.4mm to provide good attachment).

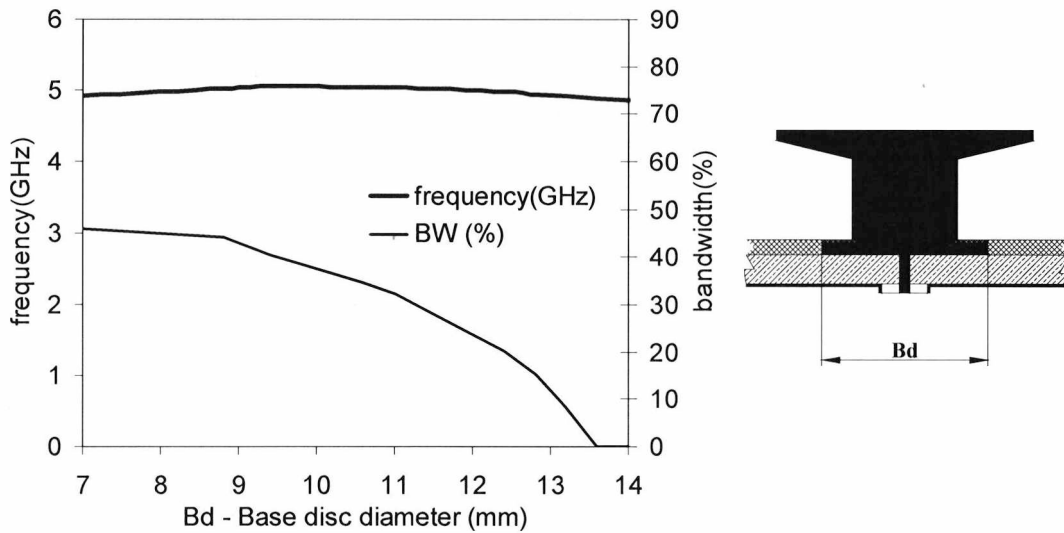


Figure 6.10. Simulated SBMBA resonance as a function of the base disc diameter (Bd).

The effect of varying the diameter of the centre cylinder of the SBMBA on the frequency and bandwidth is shown in Fig.6.11. The resonant frequency increases at an almost constant rate of 0.275GHz/mm. The bandwidth, however, increases rapidly between 2mm to 4mm, slows down between 4mm to 9mm and becomes almost constant between 9 to 10mm. A 40.7% bandwidth is obtained for a standard metal button of 7.4mm middle cylinder diameter..

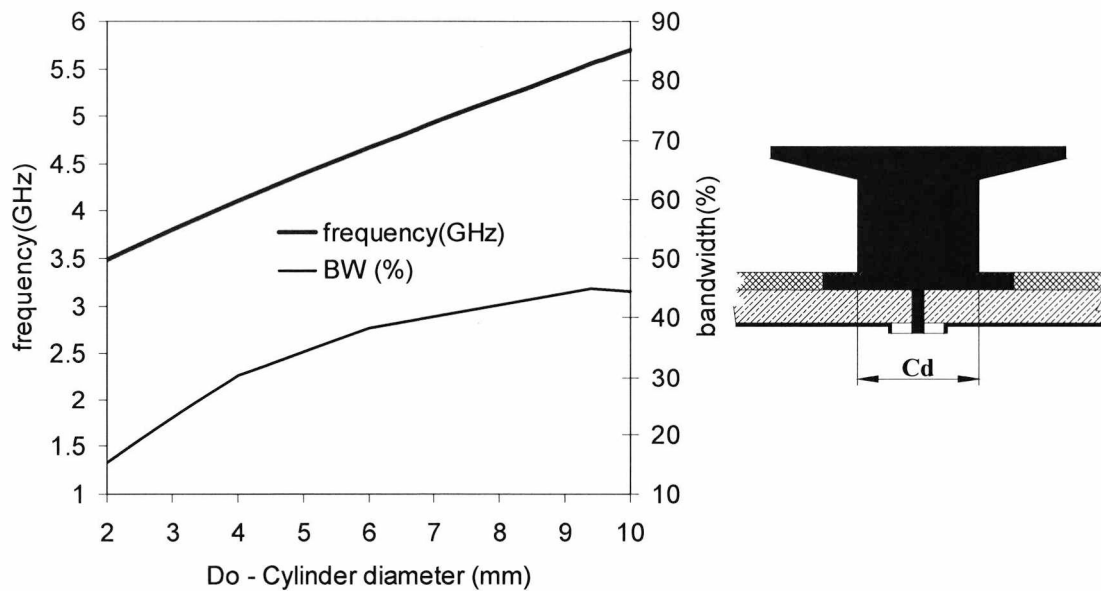


Figure 6.11. Simulated SBMBA resonance as a function of the cylinder diameter (Cd).

To sum up, the parametric study presented in this section for SBMBA antenna height, T_h , top disc diameter, T_d , base disc diameter, B_d , and cylinder diameter C_d , shows that the antenna is tunable but not overly sensitive to dimensions which could lead to poor manufacturing reproducibility. No significant variation was observed in the resonant modes with the addition of the extra textile layer wrapped around the metallic button.

6.3.5 SBMBA Radiation Patterns

The SBMBA radiation patterns were measured in an anechoic chamber, with the SBMBA on a ground plane of 5cm by 5cm ($0.92\lambda \times 0.92\lambda$) in the X-Y plane. Feeding was via a coaxial feed through the ground plane. The radiation patterns were measured at 5.25GHz and 5.5 GHz and are shown in: figure 6.12 for the XY plane, Fig.6.13 for the XZ plane and Fig.6.14 for the YZ plane. The resulted radiation patterns are as for a monopole on a finite ground plane.

No significant variation in pattern shape was discernable across the HiperLAN/2 band of 5.15-5.725GHz and good symmetry was observed for the 2 phi cuts. The gain was measured to be 3.8dBi.

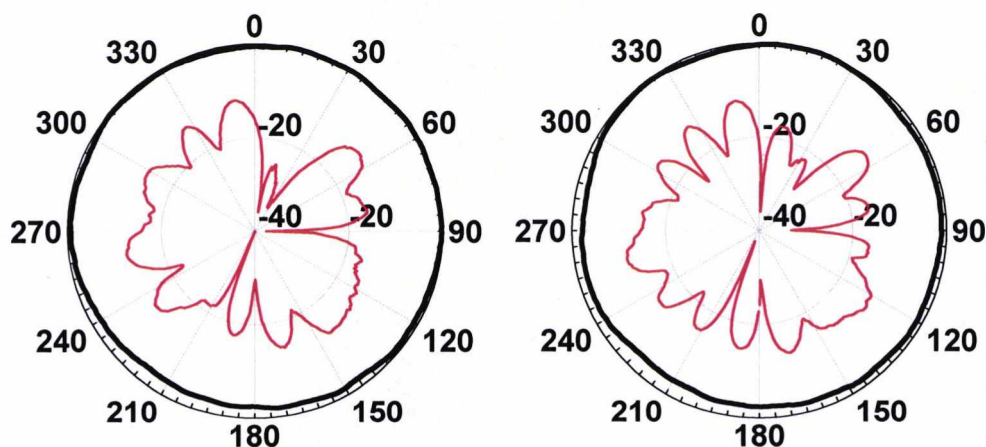


Figure 6.12 Measured far field pattern in the XY plane at 5.25GHz (left) and 5.5 GHz (right). Co-polar (thick line) and cross-polar (thin line)

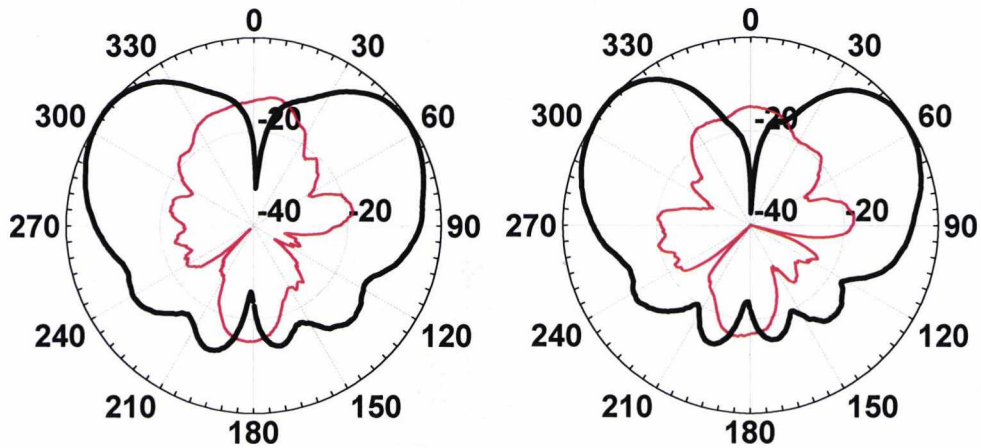


Figure 6.13 Measured far field pattern in the XZ plane at 5.25GHz (left) and 5.5 GHz (right). Co-polar (thick line) and cross-polar (thin line)

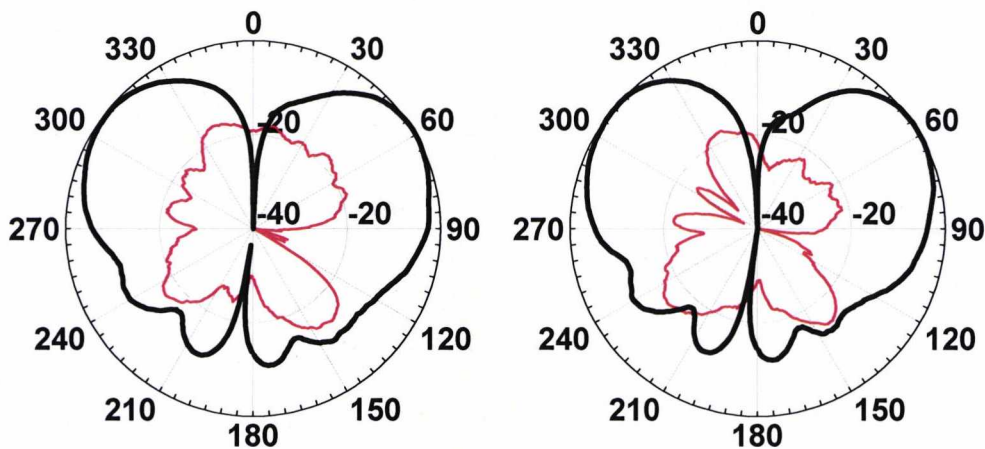
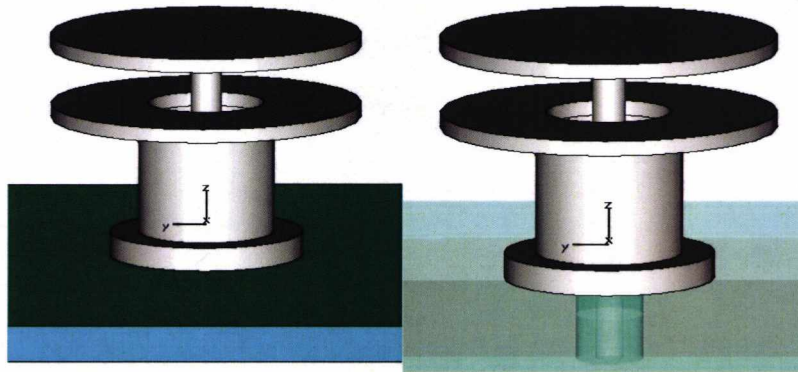


Figure 6.14 Measured far field pattern in the YZ plane at 5.25GHz (left) and 5.5 GHz (right). Co-polar (thick line) and cross-polar (thin line)

6.4 Dual Band Metallic Button Antenna (DBMBA)

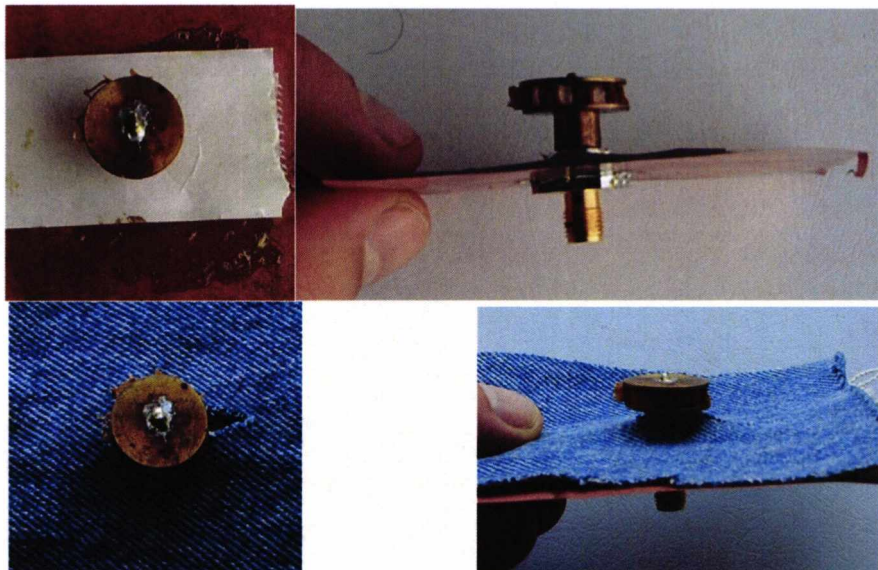
The first dual-band metallic button antenna DBMBA presented is a double top loaded monopole whose dimension has been kept to the approximate dimensions of a jeans button. The antenna is shown in Fig.6.15 and is made up of two parts. The first and lower part of the antenna is a button shaped top loaded monopole with an empty cylinder inside which is similar to the SBMBA. The higher part of the antenna is a disc which connects

to the antenna through a metal via. Honeycomb spacer is used between the additional top disc and the SBMBA structure. As for the SBMBA, the dual band antenna was placed on a 1.8mm height Velcro substrate and fed by a 50 Ω SMA coaxial feeding connected to the ground plane and to the centre of the antenna.



(a)

(b)



(c)

(d)

Figure 6.15 Dual band wearable button antenna with coaxial feed

(a) DBMBA with Velcro substrate shown (b) DBMBA with Velcro substrate translucent to show coaxial feed (c) top view photograph of the antenna (d) side view photograph of the antenna

6.4.1 DBMBA Dimensions

The dimensions of the dual band metallic button antenna and the electrical length at the lower and higher frequency band are shown in Fig.6.16 and Table 6.3. The total height of the button is 10.9mm (0.089λ for the lower band and 0.208λ for the higher band) and the top disc diameter is 16mm (0.130λ and 0.305λ). The top of the DBMBA consists of 2 discs of diameters D_d and T_d . Disc D_d is shorted to the base of the button of diameter B_d by a metal via of diameter V_d .

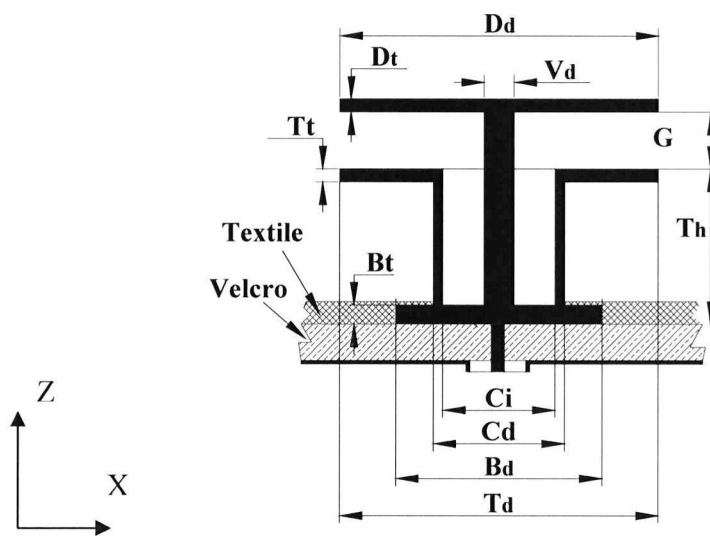


Figure 6.16. Cross-section of the DBMBA with the main dimensions

Antenna Parameters	Values	Electrical length lower band	Electrical length higher band
Disc diameter, D_d	16	0.130λ	0.305λ
Top disc diameter, T_d	16	0.130λ	0.305λ
Base diameter, B_d	10	0.080λ	0.191λ
Cylinder outer diameter, C_d	7	0.060λ	0.133λ
Cylinder inner diameter, C_i	6	0.049λ	0.114λ
Centered via diameter, V_d	1.6	0.013λ	0.031λ
Disc thickness, D_t	0.7	0.006λ	0.013λ
Tack button height, T_h	7.9	0.064λ	0.151λ
Gap between disc and lower button, G	3	0.024λ	0.057λ
Top disc thickness, T_t	0.7	0.006λ	0.013λ
Base thickness, B_t	0.7	0.006λ	0.013λ
Substrate height	1.8	0.015λ	0.034λ

Table 6.3. Main dimensions of the DBMBA.

6.4.1 DBMBA Measured Results, S11

The simulation and measured S11 curves for the DBMBA are shown in Fig.6.17 and Table 6.4. Dual band characteristic is demonstrated with a minimum S11 of -13.3dB at 2.44 GHz for the lower band and -28.33dB at 5.72 GHz for the higher band. The measured antenna achieves -10dB S11 bandwidth at the lower band of almost 12% and a higher band of nearly 35%. Although reduced in bandwidth, the CST simulation of the antenna compares well with the measurements and the antenna achieves sufficient bandwidth to cover the 2.4 GHz Bluetooth, 5.250 WLAN and 5.5 GHz Hiperlan 2 bands.

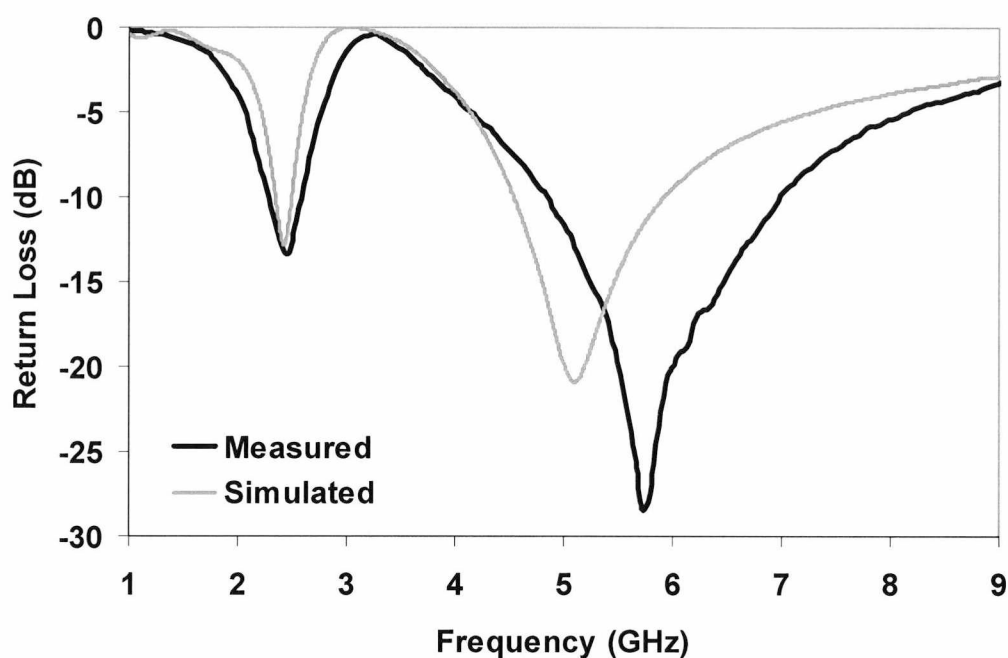


Figure 6.17 Simulated and Measured S11 curves for the DBMBA

	Lower Band (MHz)	Bandwidth (MHz) - (%)	Higher band (MHz)	Bandwidth (MHz) - (%)
Simulation	2350-2500	150 - 6.2%	4580-5950	1370 - 26%
Measurement	2300-2590	290 - 11.9%	4900-6950	2050 - 34.6%
Bluetooth/WLAN/ HIPERLAN 2 bands	2400-2500	100 - 40.8%	5150-5725	575 - 10.6%

Table 6.4. Simulated and measured DBMBA and Bluetooth , WLAN and HIPERLAN 2 bands.

6.4.2 DBMBA Surface currents

The surface current of the DBMBA with coaxial feed are shown in Fig.6.18 (a) and (b) for the lower frequency band and Fig.6.19 (a) and (b) for the higher frequency band. The substrate and ground have been omitted for clarity.

At the lower frequency band the top discs Dd and Td are strongly capacitive and current flows down the centre via to the base disc Bd. The inductance of the inner via and the coaxial cylinder is highly significant at the lower band. At the upper band the most significant fields are between the base disc Bd and the disc Td as described for the single band metallic button antenna (SBMBA) in section 6.3.2.

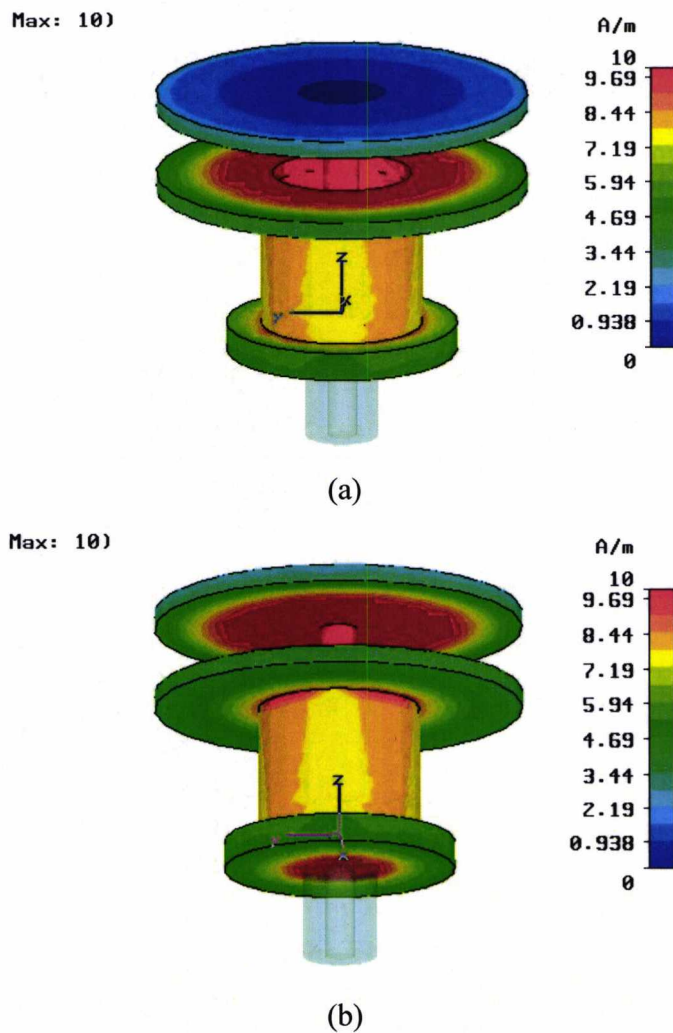


Figure 6.18. Surface currents at 2450 MHz

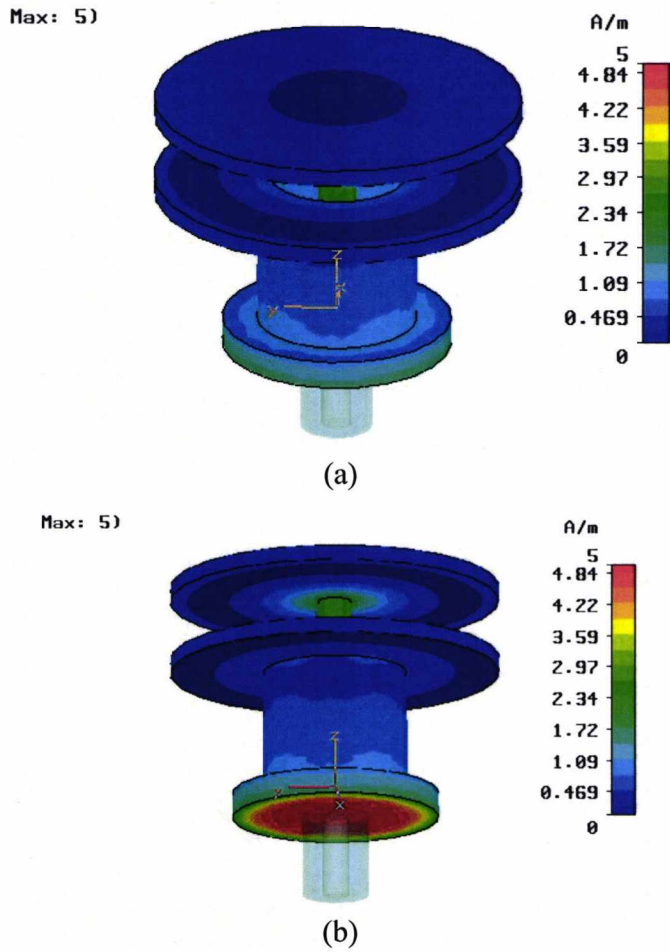


Figure 6.19 Surface currents at 5000 MHz.

6.4.4 DBMBA Parametric analysis

Similarly to the analysis for the SBMBA in section 6.3.3, a parametric analysis of the DBMBA has been carried out to determine insight into the characteristics of the dual band antenna. The main parameters considered for the analysis were the top discs' diameters D_d and T_d , the diameter of the base B_d , the diameter of the cylinder C_d , the diameter of the via connector V_d , the height of the antenna T_h and the gap G between the top discs D_d and T_d .

Fig.6.20 shows the effect on the resonant modes of the antenna as the top disc of the antenna D_d is varied from 4 to 20mm. As can be seen from the figure, the top disc diameter does not have significant effect on the higher frequency band for D_d diameters between 12mm to 19mm. However, the lower band varies considerably for the same range, which allows an almost independent tuning of the lower band over the range.

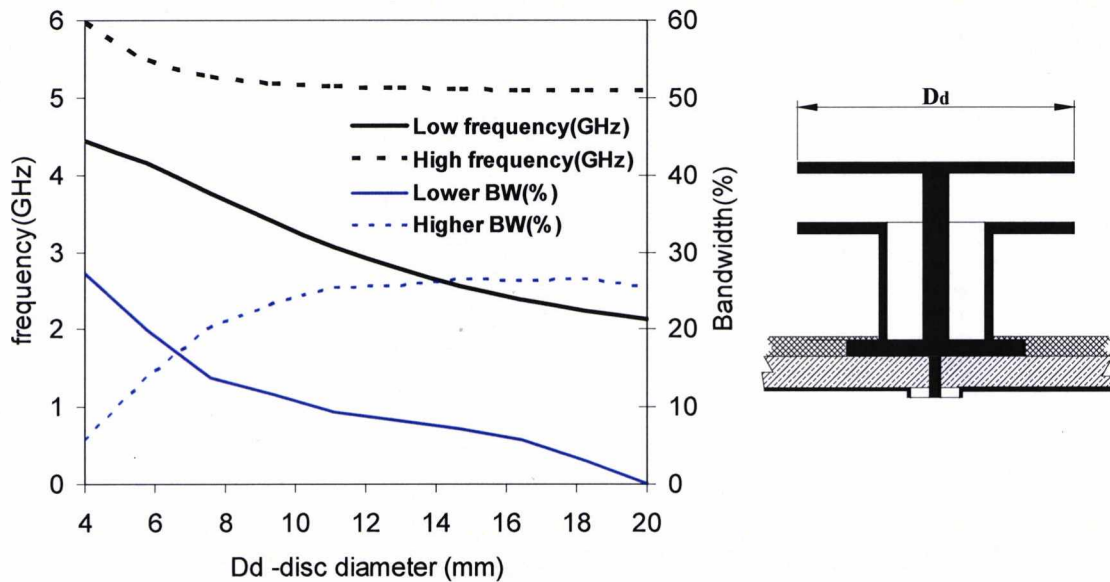


Figure 6.20 Simulated DBMBA resonances as a function of the top disc D_d diameter.
Resonant frequency (black line) and bandwidth (blue line)

Figure 6.21 shows the effect on the resonant modes of the antenna as the lower top disc T_d is varied from 7mm to 20mm. Only a small variation was found in the lower resonant frequency with an average value of 2.46GHz and deviation of $\pm 3\%$, while the average bandwidth was 6.08% with a deviation of $\pm 0.5\%$. On the other hand, the higher resonant mode experiences a significant decrease from a resonant frequency of over 8GHz for 7mm disc diameter to just under 4.5GHz for a T_d disc diameter of 20mm. There is also significant variation in the higher band bandwidth, which starts unmatched with 0% (BW bandwidth -10dB) for any diameter lower than 10mm to nearly 30% for a diameter of 19-20mm. It can be also found from Fig.6.21 that there is an optimal tuning for dimensions

close to 18mm where both higher and lower bandwidth are relatively constant while the higher frequency is moderately tunable.

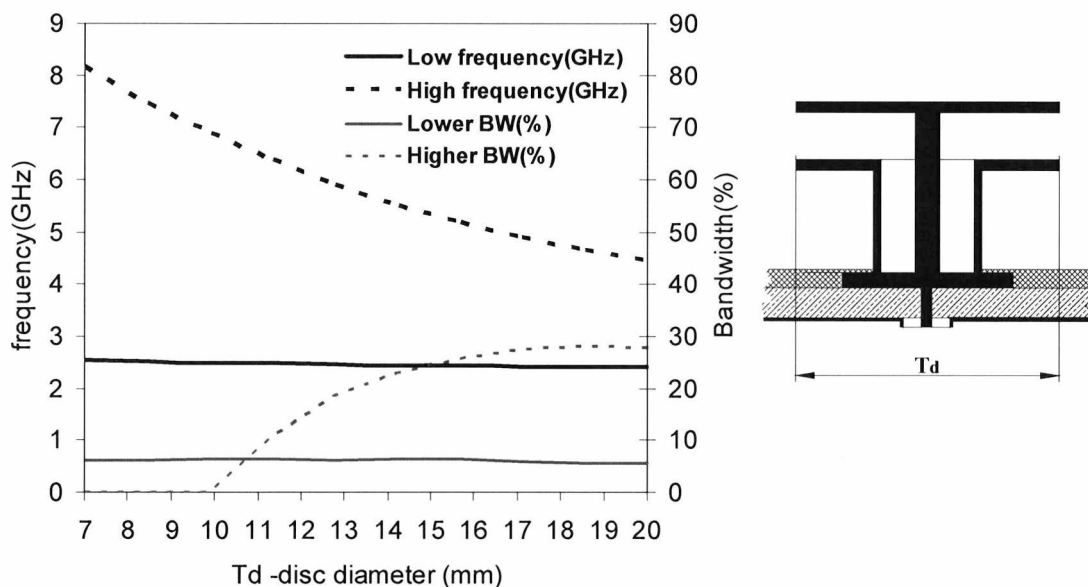


Figure 6.21 Simulated DBMBA resonances as a function of the top disc T_d diameter.
Resonant frequency (black line) and bandwidth (blue line)

The effect of varying the diameter of the base of the antenna B_d on the frequency and bandwidth is shown in Fig.6.22. There is not a match at the lower frequency band for a value of B_d equal to the center cylinder diameter C_d (7mm); however, the bandwidth of the higher frequency band is maximum for the same dimension. As the diameter of the base increases, the lower band becomes matched (-10dB) and its bandwidth increases up to B_d equals to 13mm (BW = 7%) when it becomes level before falling to 5.8% for B_d equal to 16mm. The same variation of B_d (7mm to 16mm) produces a continual decrease in the higher band bandwidth and the match vanishes totally for any dimension of B_d larger than 13mm. Both higher and lower centre frequencies do not vary significantly for the B_d range between 7 mm to 16mm with average frequencies and deviations of 2.42GHz and less than 1% for the lower band and 5.02GHz and 3% for the higher band. The value of B_d equal to 10mm chosen for the button is close to the value of the base of the standard button and at the same time allows the lower frequency band to exist while the higher band bandwidth maintains a reasonable width.

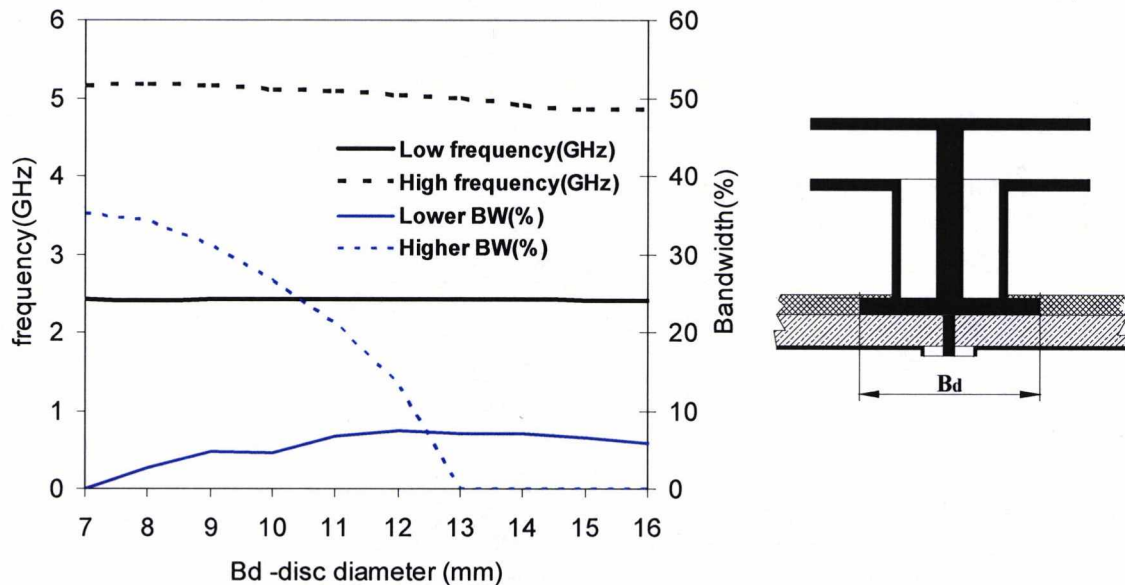


Figure 6.22 Simulated DBMBA resonances as a function of the base disc B_d diameter
Resonant frequency (black line) and bandwidth (blue line)

The effect of varying the diameter V_d of the via connecting the top plate with the base is shown in Fig.6.23. As can be seen from the figure, values of V_d higher than 2mm produce a moderate increase in the lower band resonant frequency and bandwidth and a dramatic decrease in the higher band bandwidth. The effect is also accentuated when the V_d diameter is close to the inner diameter (C_i) of the center cylinder C . The antenna structure is changed when V_d equals 6mm as the via touches the inside of the cylinder with diameter C_i . The value of $V_d = 1.6\text{mm}$ used for final DBMBA design falls within the range V_d from 1.5mm to 2.8mm in which the lower frequency bandwidth is greater than 5% and the higher frequency bandwidth no lower than 20%.

Figure 6.24 shows the effect of varying the gap G between the top plates D_d and T_d as the height T_h remains constant. No match (-10 dB) was found at the lower frequency band for values of G lower than 1.2mm and this bandwidth was not greater than 2% for values lower than 1.6mm. The value chosen for the button $G = 3\text{mm}$ produces a lower frequency bandwidth greater than 5% without compromising the small size of the

antenna. Any value within the range 0mm to 5mm studied would suit for the higher frequency band and bandwidth required (WLAN and Hiperlan). It is interesting to note that the lower frequency does not change significantly for values of G between 1.6 to 5mm. This is due to the decrease capacitance between the upper discs being compensated by an increased inductance associated with the centre via.

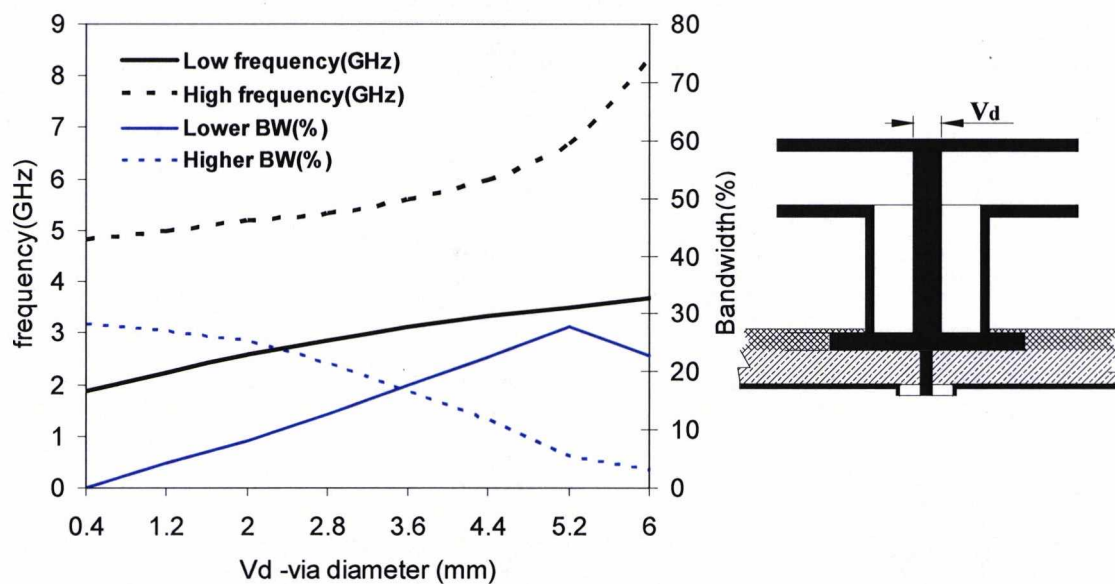


Figure 6.23 Simulated DBMBA resonances as a function of the via connector Vd.
Resonant frequency (black line) and bandwidth (blue line)

The effect of changing the height of the antenna cylinder height T_h while maintaining the gap G between plates constant is shown in Fig.6.25. As the antenna height increases from 5mm to 10mm, both lower and higher frequencies decrease as well as the higher frequency bandwidth. The lower frequency bandwidth fluctuates around a bandwidth level of 6.3% and deviation of $\pm 0.5\%$.

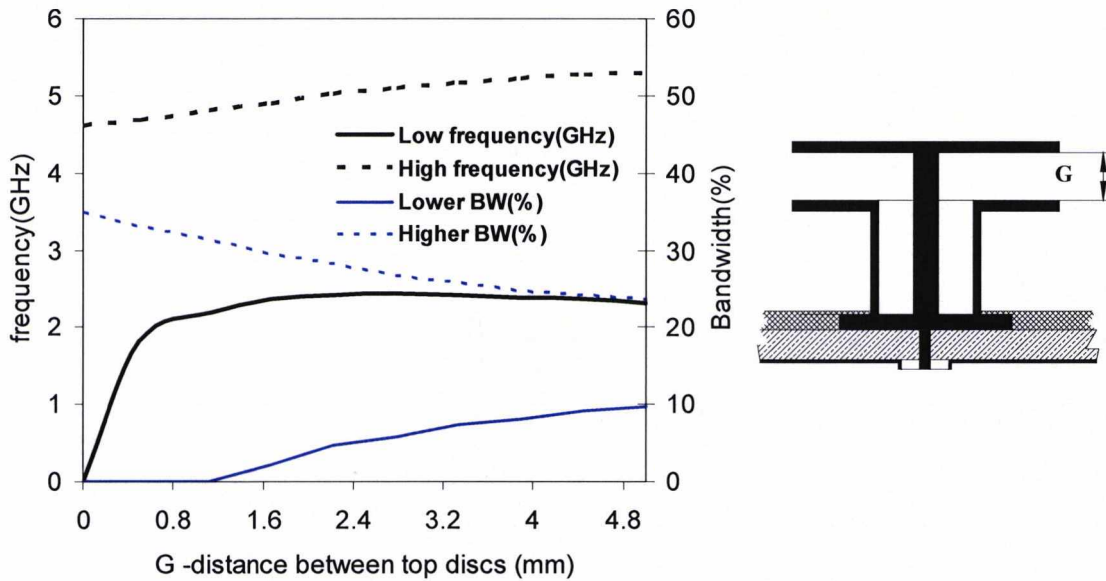


Figure 6.24 Simulated DBMBA resonances as a function of the base disc G diameter.

Resonant frequency (black line) and bandwidth (blue line)

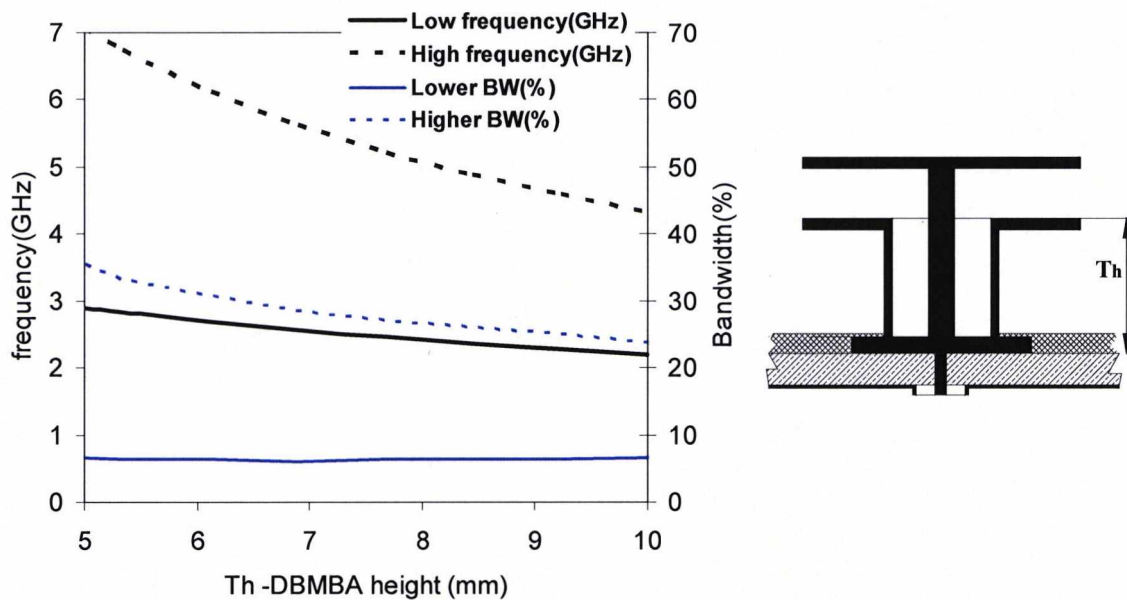


Figure 6.25 Simulated DBMBA resonances as a function of the height Th .

Resonant frequency (black line) and bandwidth (blue line)

Finally, the effect of varying the cylinder diameter Cd while keeping the thickness of the cylinder $Cd - Ci$ on the resonant frequency and bandwidth is shown in Fig.6.26. As Cd

increases from 2.6mm to 10mm, the lower frequency band and bandwidth decrease almost linearly. On the other hand, as C_d increases the higher frequency band decreases sharply and the bandwidth increases dramatically up to a value of C_d equal to 6.5mm. There is an inflection point at 6.5mm and from the value of D_o (6.5mm) to 8.5mm the higher resonant frequency increases as well as its bandwidth. From 8.5mm to 10mm the higher frequency bandwidth decreases as it approximates to the dimensions of the base diameter B_d equals to 10mm. The dimension chosen for the cylinder diameter $C_d = 7$ mm (as for a standard button) falls within the range of lower fluctuation for the higher resonant frequency and bandwidth, hence making the button tunable but not susceptible to poor manufacturing tolerances.

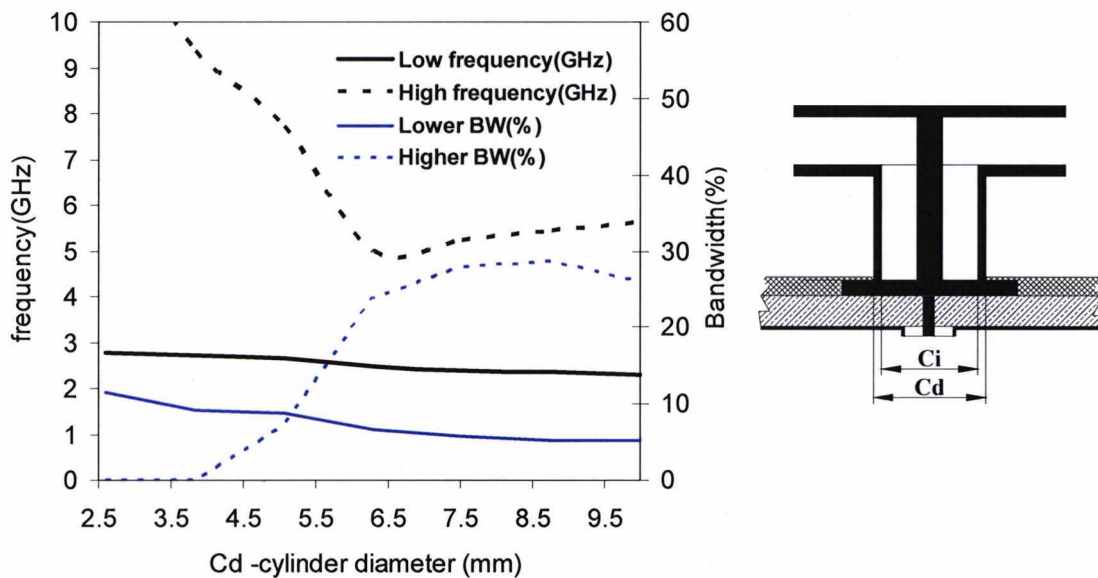


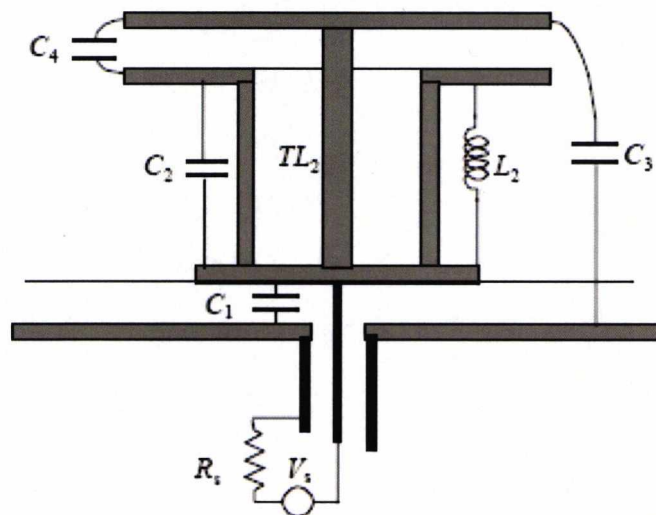
Figure 6.26 Simulated DBMBA resonances as a function of the cylinder diameter C_d .

Resonant frequency (black line) and bandwidth (blue line)

The parametric analysis of the DBMBA has shown that for the dimensions chosen, which closely approximate those of normal jeans buttons, offer the ability to tune the antenna without making it highly sensitive to small fluctuations in physical dimensions. No significant variation in the resonant mode was found by button up the antenna with textile material.

6.4.5 DBMBA – Equivalent circuit model

Modelling of an antenna starts by deciding on a suitable topology and then finding the appropriate element values to reduce the amplitude of the measured S_{11} realised in the frequency range of interest. In the case of the Button Antenna, there are two main resonances which suggests that the minimum order of an equivalent circuit model is four. However, if the minimum order is used it is likely that some of the circuit elements will be negative. Such a circuit could model the antenna response, but the element values would have no physical meaning. Furthermore, microwave circuits cannot be entirely represented by lumped circuits since they also contain distributed structures. For these reasons, it was decided to use a model of eighth order and with a distributed element at the input to compensate for any phase error introduced by the measurement process. The model for the Button antenna is shown in Fig.6.28 which relates to the button structure as shown in Fig.6.27. The element values have been chosen by an optimization process using code developed at the University of Kent [12]. The measured S_{11} amplitude and phase as used as the input and the code varies component values until the circuit response matches that of the input.



6.27 Button antenna structure with electrical model representation

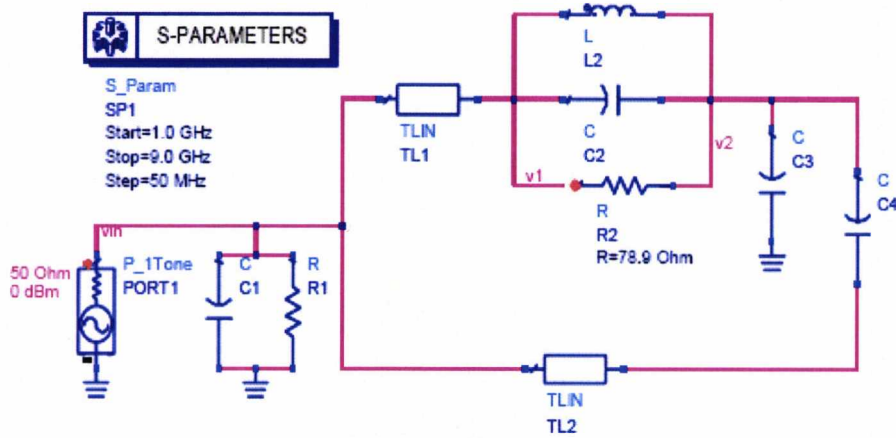


Figure 6.28 Equivalent circuit model for the Button antenna.

Figure 6.28 shows a comparison of the amplitude and phase of S_{11} of both the model. A very close match is observed suggesting the model offers a good representation of the DBMBA. This model may be used for system modeling of wireless link.

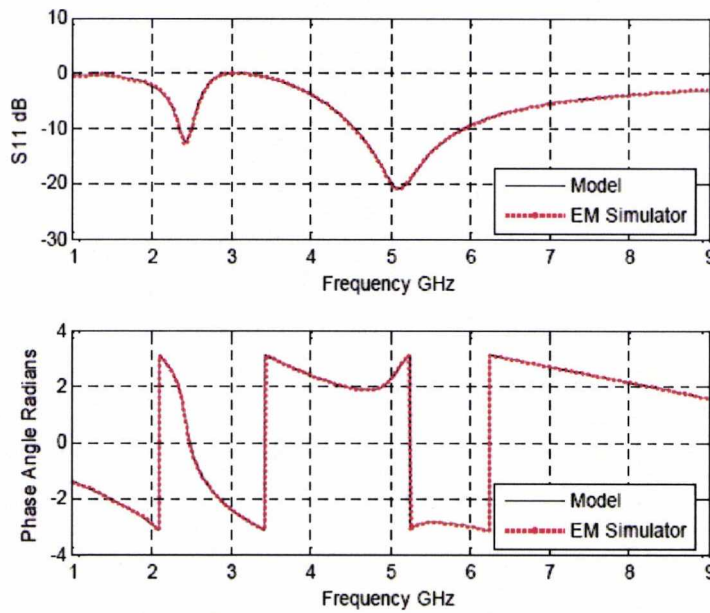


Figure 6.28. Comparison of S_{11} from measurements and model.

6.4.6 DBMBA – Radiation patterns

The measured radiation patterns of the antenna in the X-Y, Y-Z and X-Z at 2.45 GHz, 5.25 GHz and 5.5 GHz are shown in Fig.6.30-6.35. Monopole antenna patterns with polarization in the Z direction were obtained for the dual band button antenna coaxial fed. The gains measured were 2.2dB at 2.45GHz; 3.6dB at 5.2GHz and 1.8dB at 5.5GHz. Good omnidirectional pattern is observed at every band, together with symmetry in the phy cuts.

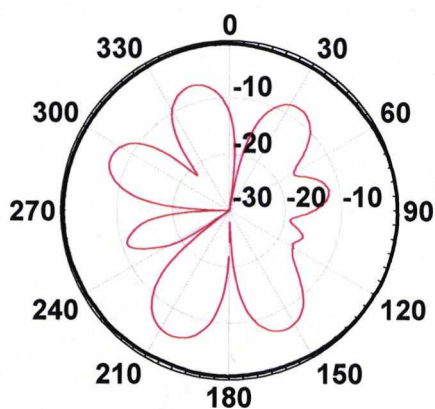


Figure 6.30 Measured far field pattern in the XY plane at 2.45 GHz . Co-polar (thick line) and cross-polar (thin line)

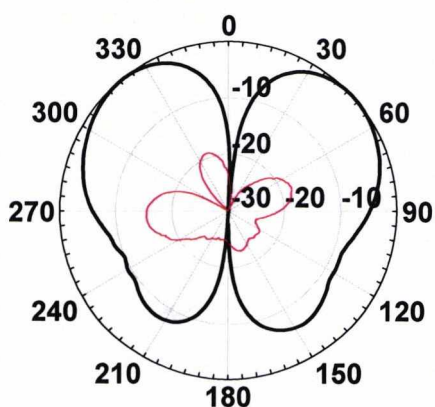


Figure 6.31 Measured far field pattern in the XZ plane at 2.45 GHz. Co-polar (thick line) and cross-polar (thin line)

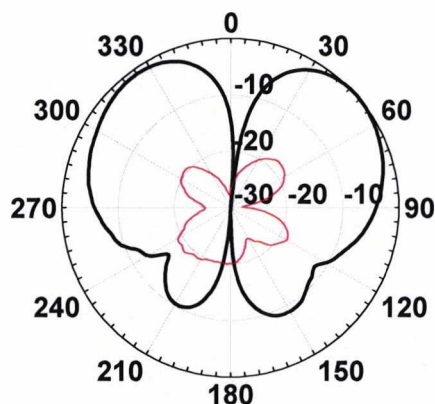


Figure 6.32 Measured far field pattern in the YZ plane at 2.45GHz. Co-polar (thick line) and cross-polar (thin line)

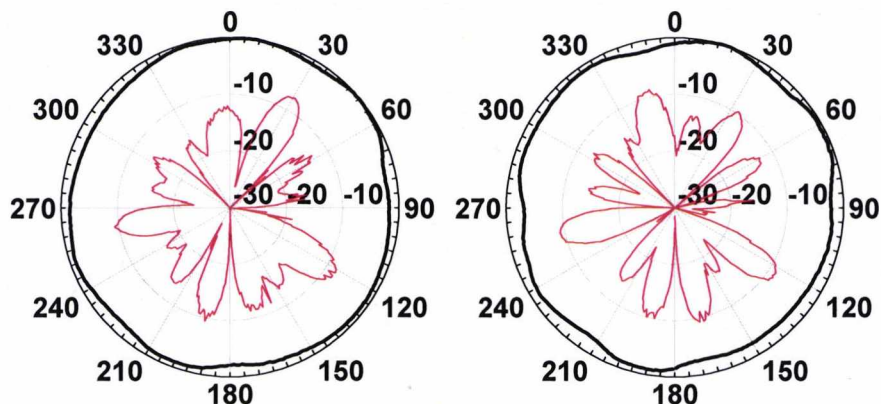


Figure 6.33 Measured far field pattern in the XY plane at 5.25GHz (left) and 5.5 GHz (right). Co-polar (thick line) and cross-polar (thin line)

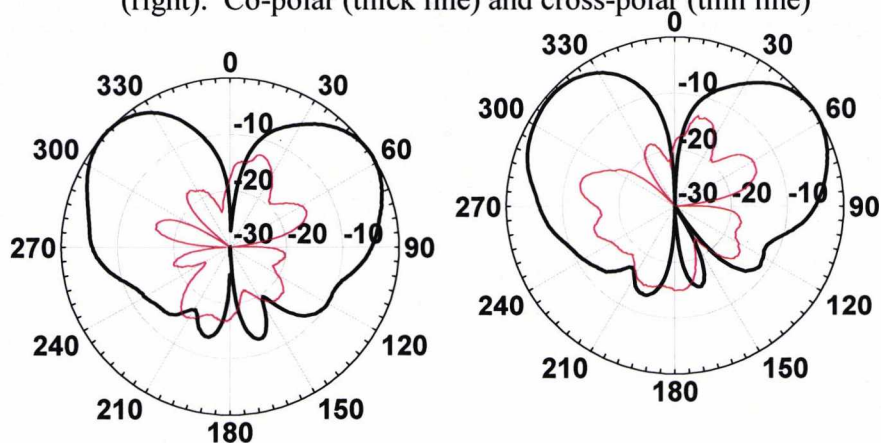


Figure 6.34 Measured far field pattern in the XZ plane at 5.25GHz (left) and 5.5 GHz (right). Co-polar (thick line) and cross-polar (thin line)

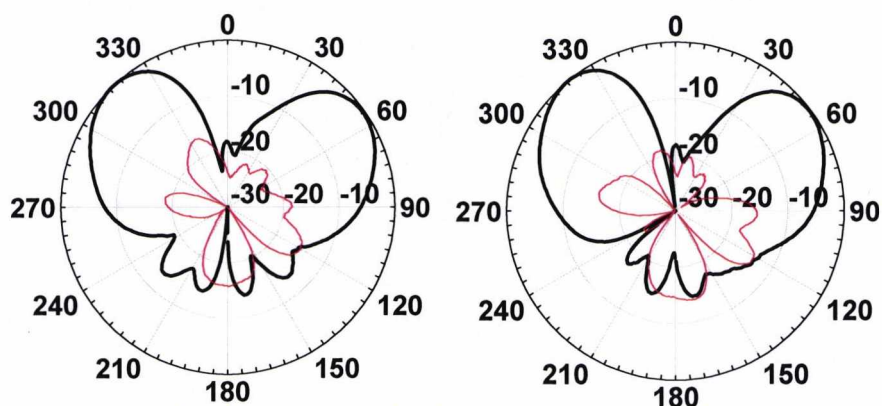


Figure 6.35 Measured far field pattern in the YZ plane at 5.25GHz (left) and 5.5 GHz (right). Co-polar (thick line) and cross-polar (thin line)

6.5 Dual Band Metallic Button Antenna with Microstrip Feed

The DBMBA with coaxial feed could be a good solution when the wearable antenna is backed by circuitry or a transmission line connecting to the transceiver. However, it is not the best solution for an antenna on a human body since the ground plane should lie on the body. For this reason, it was decided to study the antenna with side feeding, specifically a 50ohms microstrip line, as shown in figure 6.36. The electrical behavior of the antenna with the side microstrip transition line, the step transition to SMA connector and the SMA connector were simulated with CST Microwave Studio and compare with the experimental results.

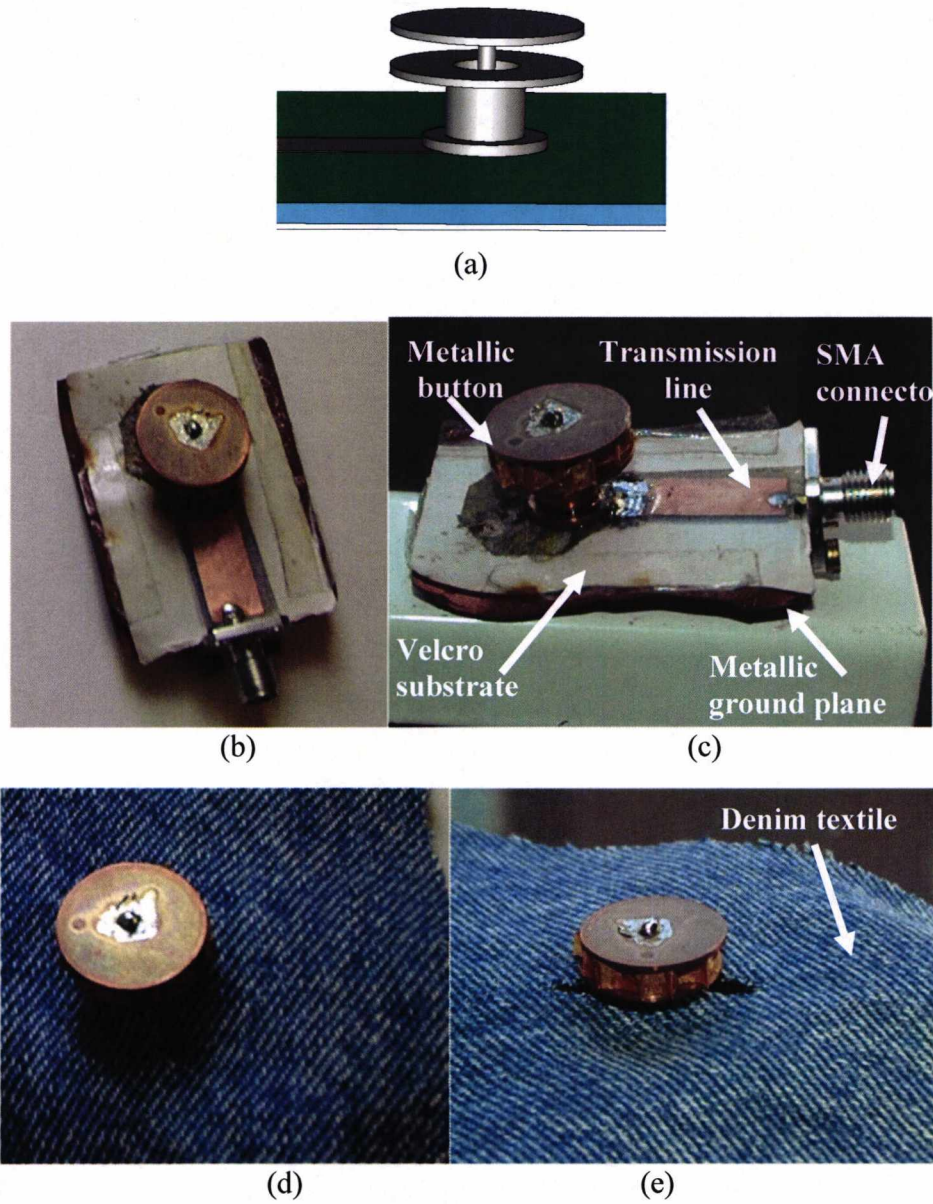


Figure 6.36 DBMBA with microstrip feed. (a) CST Microwave Studio model of the antenna.

(b) and (c) Photograph of the antenna without textile material

(d) and (e) Photograph of the antenna with textile material

6.5.1 DBMBA with Microstrip Feed- Dimensions

A small retuning was necessary and the dimensions of the DBMBA with microstrip feed are shown in figure 6.37 and table 6.5.

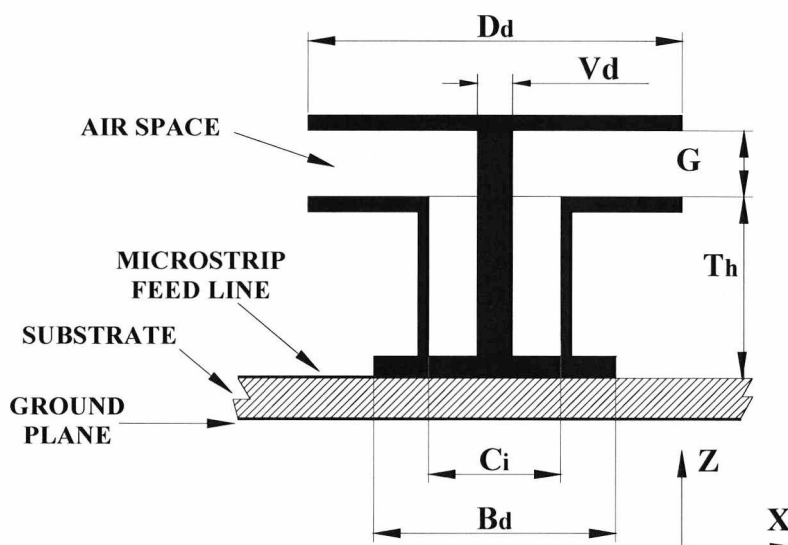


Figure 6.37 DBMBA with microstrip feed dimensions

Antenna Parameters	Values
Disc diameter, D_d	17.0
Top disc diameter, T_d	17.0
Base diameter, B_d	10.0
Cylinder outer diameter, C_d	7.0
Cylinder inner diameter, C_i	6.0
Centered via diameter, V_d	1.6
Tack button height, T_h	8.0
Gap between disc and button, G	3.0
Substrate height	1.8
Ground plane dimensions	50x40

Table 6.5 DBMBA with microstrip feed dimensions

6.5.2 DBMBA with Microstrip Feed -Measured Results, S11

To study the effect of proximity of the human body on the antenna, the antenna was placed directly onto the waist-band of a pair of denim jeans which were worn by an adult male. For the analysis, simulation and measurements of the antenna on and off body were compared. Similarly to the work done in [13], a three-tissue human body model was chosen for simulation as shown in Fig.6.38. The three body layers considered were: a skin layer of 1-mm thickness, a fat layer of 3-mm thickness and a muscle layer of 44-mm thick. The dimensions of the body chosen was $120 \times 120 \times 40 \text{mm}^3$. An investigation carried

out on the dispersive characteristics of the human tissue over the frequency range 3 GHz to 10 GHz [12] led to the assumption that the electrical parameters of the tissues are non-dispersive. The values at the centre (of the DBMBA) 4 GHz for the skin are: $\epsilon = 38$, $\sigma = 2.34[\text{S/m}]$; fat $\epsilon = 5.1$, $\sigma = 0.18[\text{S/m}]$; muscle $\epsilon = 50.8$, $\sigma = 3[\text{S/m}]$. These were obtained from [14] based on [14]. CST Microwave studio was used for the simulation of the antenna on and off the body.

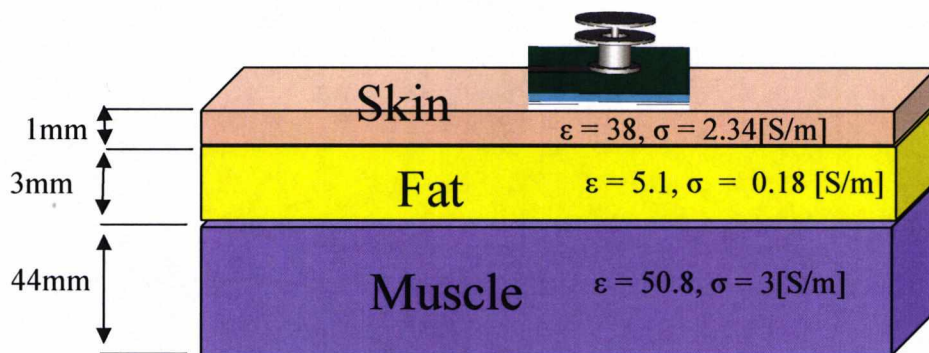


Figure 6.38. Three layers model body model with button antenna

The results of the antenna on/off body are shown in figure 6.38 (for a range 2GHz to 6.5GHz) and figure 6.39 (detail of the lower band - 2.2 GHz to 2.6 GHz) and summarized in table 6.10. The antenna was tuned to cover the 2.45GHz and 5.25GHz and 5.5GHz bands either on or off body, which allows placing the antenna either attached or at a certain distance from the human body.

The simulated and measured S11 curves for the DBMBA microstrip fed are shown in Fig.6.38, Fig.6.39 and Table 6.6. The measured bandwidth of the antenna off body was 5.7% for the lower band and 27.1% at the higher band which compares well with the predicted 4.5% and 27.2% from the computer computation. In the case of placing the antenna on the body, the centre frequency of the lower band was shifted down by just 1% while the lower band bandwidth increased by only 0.1%. The effect of the proximity to the human body shifted up the higher frequency by 1.3% and, although the higher band bandwidth decreased 6.9%, it maintained sufficient bandwidth (20.2%) to cover the Hiperlan2 bands. There was an accurate relationship between the simulation and measurement results.

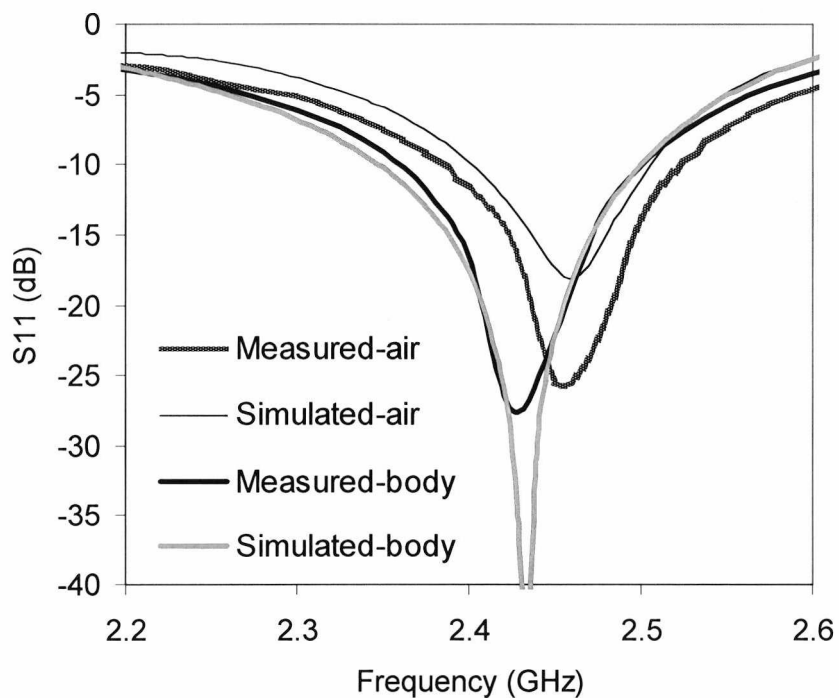
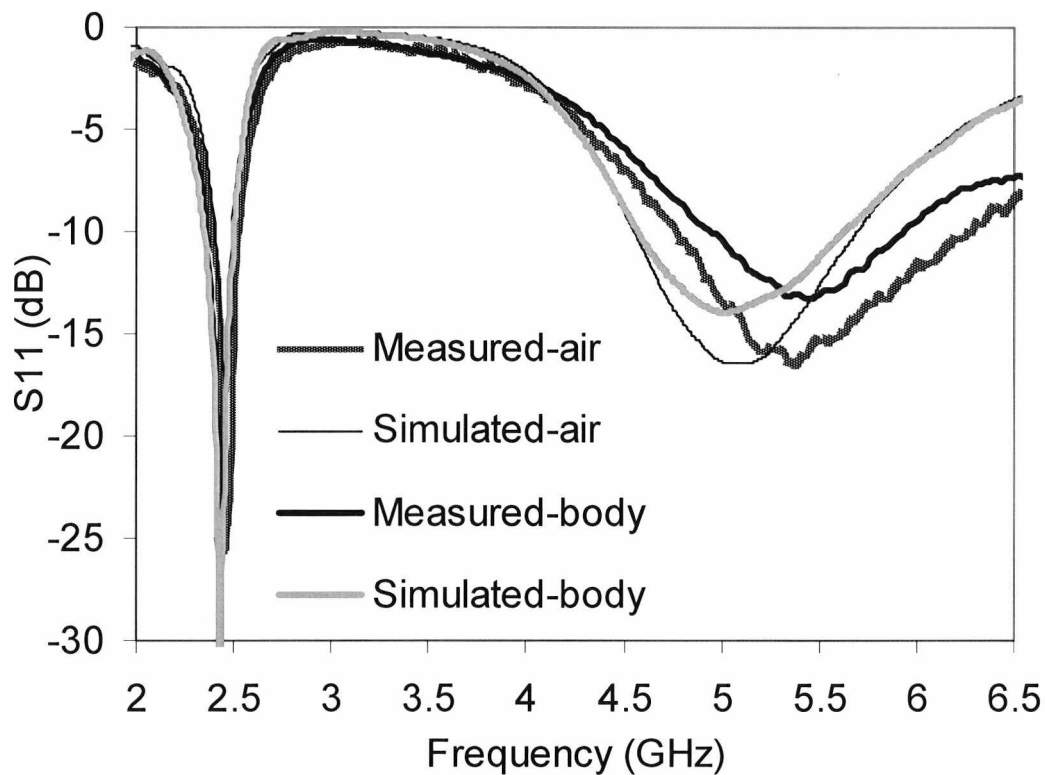


Figure 6.39 Simulated and Measured S_{11} of the microstrip fed button antenna on-off body

	LOW BAND	BW	HIGH BAND	BW HIGH
Simulated air	2400-2510	110 - 4.5%	4540 - 5700	1460 -27.2%
Measured air	2385-2525	140 - 5.7%	4775 - 6275	1500 - 27.1%
Simulated body	2350-2500	150 - 6.2%	4570 - 5630	1160 - 22.7
Measured body	2360-2500	140 - 5.8%	4950 - 5950	1010 - 20.2%

Table 6.6 Simulated and measured S11 on/off body

6.5.3 DBMBA with Microstrip Feed - Radiation Patterns

The measured radiation patterns of the DBMBA with microstrip feed on/off body are shown in Fig.6.40-6.45. The radiation patterns were measured on an adult male and compared with the antenna in free space. The antenna is proposed for use in Personal Area Networks (PAN) where communication is necessary both to devices on body and to external, off-body network nodes. With the antenna mounted as a waist height front trouser button there is a good coverage at the front of the user’s body providing connections to other worn devices. The plane cutting the user’s waist shows there to be reasonable forward coverage with a centre null of around 20dB and there is a deep null in the rear direction.

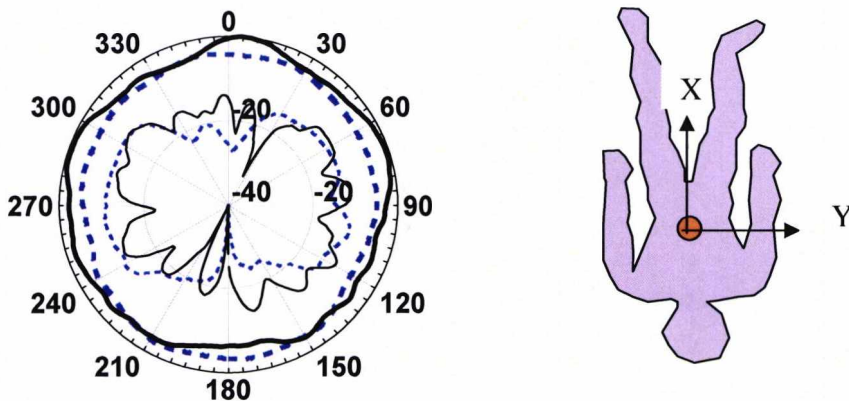


Figure 6.40 Measured far field pattern in the XY plane at 2.45GHz: Co-polar (thick line) and cross-polar (thin line). On body (continuous line), off -body (discontinuous).

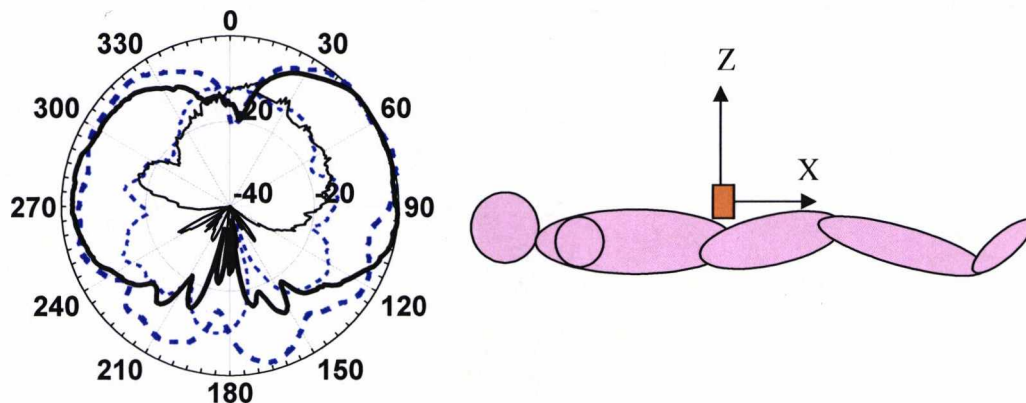


Figure 6.41 Measured far field pattern in the XZ plane at 2.45GHz: Co-polar (thick line) and cross-polar (thin line). On body (continuous line), off -body (discontinuous).

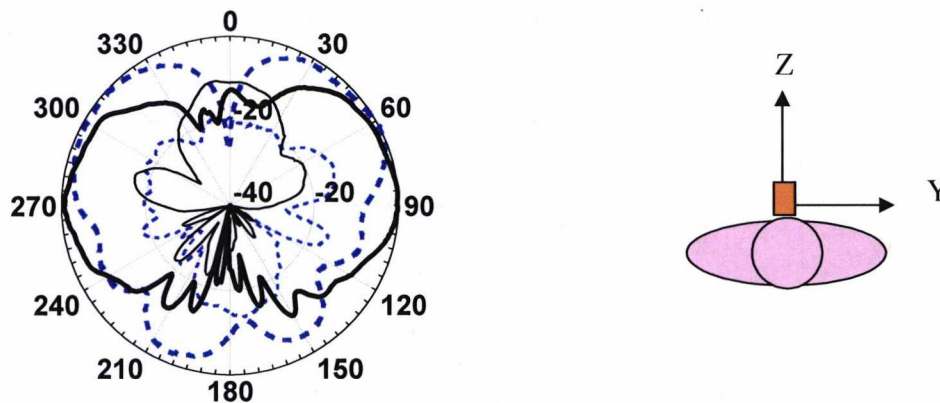


Figure 6.42 Measured far field pattern in the YZ plane at 2.45GHz: Co-polar (thick line) and cross-polar (thin line). On body (continuous line), off -body (discontinuous).

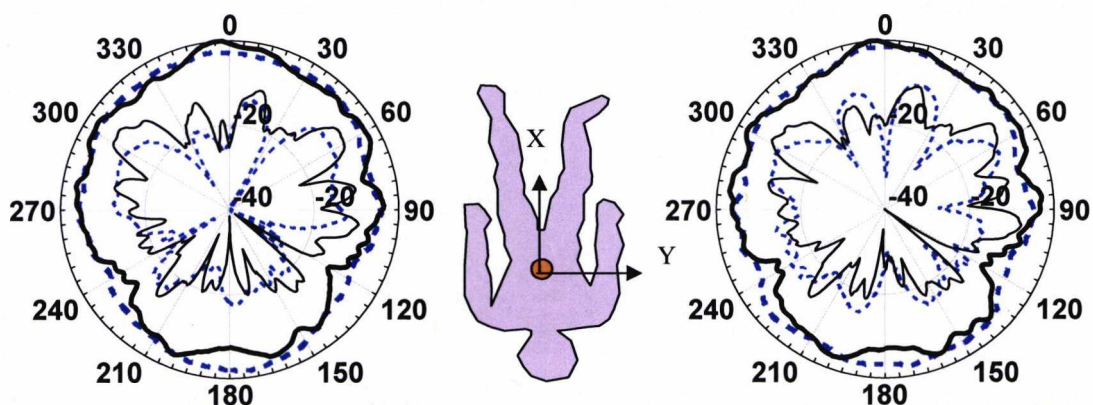


Figure 6.43 Measured far field pattern in the XY plane at 5.25 GHz(left) and 5.5GHz(right): Co-polar (thick line) and cross-polar (thin line). On body (continuous line), off -body (discontinuous).

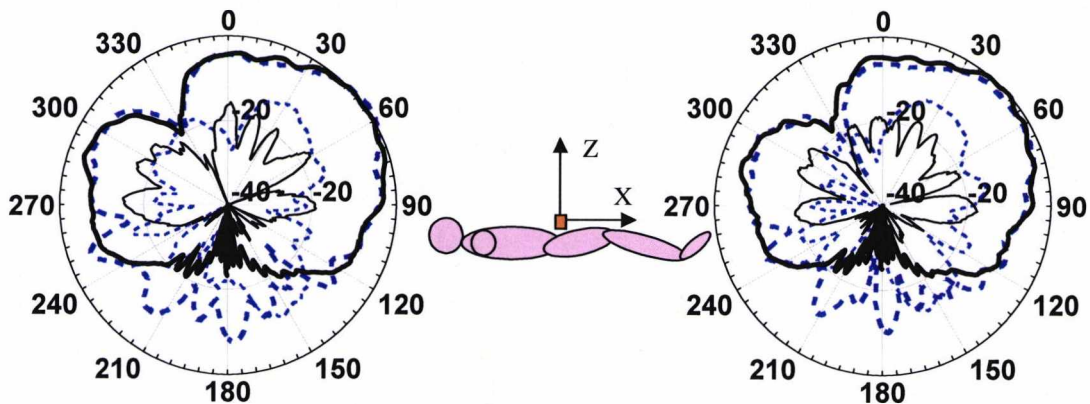


Figure 6.44 Measured far field pattern in the XZ plane at 5.25 GHz(left) and 5.5GHz(right): Co-polar (thick line) and cross-polar (thin line). On body (continuous line), off -body (discontinuous).

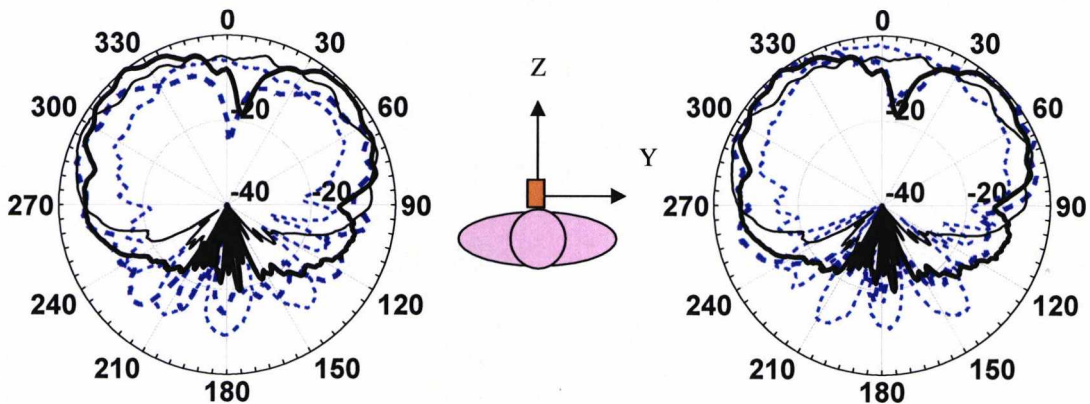


Figure 6.45 Measured far field pattern in the YZ plane at 5.25 GHz(left) and 5.5GHz(right): Co-polar (thick line) and cross-polar (thin line). On body (continuous line), off -body (discontinuous).

The gain obtained for the DBMBA with microstrip feed was 2.18dB at 2.45GHz, 4dB at 5.25GHz and 4.2dB at 5.5GHz. The side feeding caused the gain to be higher for the DBMBA microstrip fed at the 5GHz band as the width of the microstrip line creates an asymmetry in the radiating structure in the XZ and YZ planes as shown in Figures 6.44 and 6.45.

Placing the antenna on the human body increased the gain by 0.5dB at 2.45GHz, 1.2dB at 5.25GHz and 1.3 dB at 5.5GHz. However, the gain difference was not uniform in all the angles and while for some angles the gain increase, the backward radiation decreased an average of 20dB.

6.6 Conclusions

A new antenna proposed for use in Personal Area Networks (PAN) has been introduced with the appearance and dimensions of a standard jeans button. The antenna has been realized in both single and double band versions covering WLAN and Hiperlan/2 bands. The antenna tuning is strongly determined by the capacitance between the various discs that make up the structure and frequencies can be controlled by varying the disc diameter or separations according to the parametric study presented. The radiation currents mainly flow axially along the central post of the structure giving it the radiation characteristics of a monopole on a small ground plane. The measured scattering parameters of the antenna are captured and used to create an equivalent circuit of lumped elements which accurately describes the frequency response.

References

- [1] W. Barfield and C. Thomas, eds., “Fundamentals of Wearable Computers and Argumented Reality”, Lawrence Erlbaun, 2000.
- [2] www.eecg.toronto.edu/~mann
- [3] J.G. Spooner, “Infineon gets musical with MP3 jacket,” April 27, 2002, 07:31 BST, <http://news.zdnet.co.uk/hardware/chips/0,39020354,2109243,00.htm>
- [4] Lukowicz, P.; Büren, T.V.; Junker, H.; Stäger, M.; Tröster, G. „WearNET: A Distributed Multi-Sensor System for Context Aware Wearables“, in Proc. 4th Int. Conf. On Ubiquitous Computing, Göteborg, Schweden, 2002.
- [5] Y. Nechayev, P. Hall, C. C. Constantinou, Y. Hao, A. Owadally, and C.G. Parini, “Path loss measurements of on-body propagation channels,” in *Proc. 2004 Int. Symp. Antennas and Propagation*, Sendai, Japan, pp. 745–748.
- [6] A. Alomainy; Y.Hao; C.G. Parini; P.S Hall, “Comparison between two different antennas for UWB on-body propagation measurements”, *IEEE Antennas and Wireless Propagation Letters Volume 4, 2005 Page(s):31 - 34*

- [7] P. Salonen; Kim Jaehoon; Y. Rahmat-Samii; “Dual-band E-shaped patch wearable textile antenna”, *IEEE Antennas and Propagation Society International Symposium*, Volume 1A, 3-8 , p.p. 466 - 469, 2005
- [8] P. Salonen and H. Hurme, “A novel fabric WLAN antenna for wearable applications”, *IEEE Antennas and Propagation Society International Symposium*, vol: 2, June 2003, pp. 700-703.
- [9] M. Tanaka and J.-H. Jang, “Wearable microstrip antenna”, *IEEE Antennas and Propagation Society International Symposium*, vol: 2, June 2003, pp. 704-707.
- [10] Maciej Klemm, Ivo Locher, Gerhard Tröster “A Novel Circularly Polarized Textile Antenna for Wearable Applications”, *The 34rd European Microwave Conference (EuMC)*, Amsterdam, Netherlands, 11-14 October 2004
- [11] Maciej Klemm, Istvan Z. Kovacs, Gert F. Pedersen, Gerhard Tröster , “Novel Small-Size Directional Antenna for UWB WBAN/WPAN Applications”, , *IEEE Transactions on Antennas and Propagation* , vol.53, issue 12, Dec. 2005, pages: 3883-3896;
- [12] Mohamed I. Sobhy, Benito Sanz-Izquierdo and John C. Batchelor “System and circuit models for microwave antennas,” 35th European Microwave Conference, Manchester 2006.
- [13] <http://niremf.ifac.cnr.it/tissprop/htmlclie/htmlclie.htm> .*ITALIAN NATIONAL RESEARCH COUNCIL Institute for Applied Physics "Nello Carrara" - Florence*
- [14] C. Gabriel, “Compilation of the dielectric properties of body tissues at RF and microwave frequencies,” , *AL/OE-TR-1996-0037 Rep.*, Jun.1996.

Chapter 7

Optimization and Miniaturization of Wearable Button Antennas

7.1 Introduction

The introduction of the GSM [1] and the American IS-54 [2] mobile communication standards in the end of 1980's and beginning of 1990's supposed a starting point in the revolution of personal mobile communications [3]. With the further evolution and development of personal communications systems, wireless communications have become part of our everyday life.

The initial personal mobile communications devices in the 1980's were brick size and only able to make phone calls. However, further advancements in miniaturization of

electronics devices allowed the development of what one can find today as a standard, slim mobile phone for multiple purposes (camera, agenda, game console...).

The evolution and miniaturization of devices have demanded antennas to have small size and be easier to implement in an increasingly complex mobile device. Most of the antennas used in early devices were helical monopole antennas [4], later miniaturized to dielectric loaded helical monopole antennas [5]. The introduction of the inverted F antenna (IFA) [6], later transformed into a planar inverted F antenna (PIFA) [7] allowed a further miniaturization, together with a reduction in radiation towards the human head.

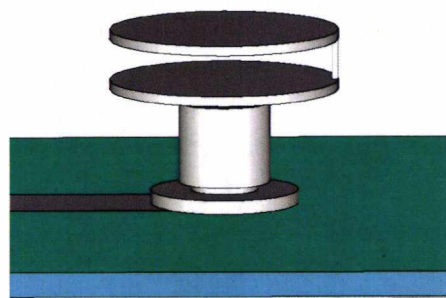
Dual band PIFA antennas [8], [9] meant a further breakthrough as a solely internal antenna can operate at many frequency bands. The dual band antennas have become multi-band [10] antennas as the new systems such as 3G, Bluetooth and WLAN have required them. In addition, the antenna efficiency has been improved by using dielectric resonator antennas in mobile devices [11].

Chapter 6 introduced the concept of using button structures to create wearable antennas and demonstrated the feasibility of making them truly wearable with the SBMBA and DBMBA resonating at the 2.45GHz and 5 GHz Bluetooth and WLAN bands. This chapter will look at the optimization and miniaturization of the wearable button antennas. For the optimization, some of the already mentioned miniaturization techniques will be studied and implemented.

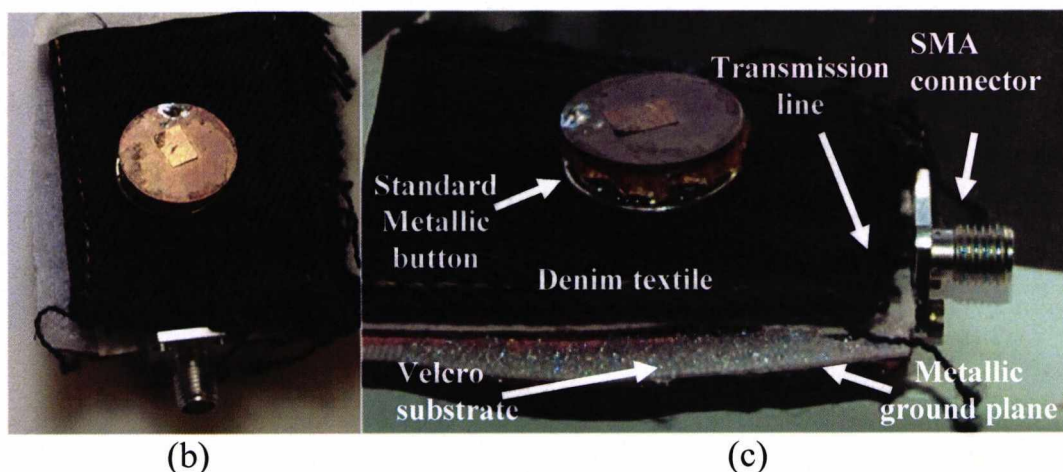
7.2 DBMBA using a Standard Metallic Button

The DBMBA design used in chapter 6, utilized the dimensions of buttons to develop a dual band antenna design capable of covering both Bluetooth and WLAN bands. In this section, however, a standard metallic button structure is used as the base for the antenna which also needs a top plate and via connector to create a DBSMBA (dual band standard metallic button antenna). The operation principle is similar to the operation of the DBMBA described in chapter 6, however, the arrangement allows the use of a standard denim jeans button with the sole addition of the metal disc and a via connection located at the edge of the top metal disc. The antenna design is shown in Fig. 7.1. Similarly to the

previous DBMBA the antenna is fed by a microstrip line to facilitate on human body measurements.



(a)



(b)

(c)

Figure 7.1 DBMBA using a standard metallic button (DBSMBA) (a) CST Microwave Studio model

(b) and (c) Photograph of the dual band antenna

7.2.1 DBMBA using a SMB– Dimensions

The dimensions of the DBSMBA are shown in Fig.7.2 and Table 7.1. The total height of the visible metallic button was 12.2mm which is equivalent to 0.1λ at the lower centre frequency and 0.22λ at the higher centre frequency. The diameter of the top metallic plate was 17mm which is equivalent to 0.14λ at the lower frequency and 0.311λ at the higher frequency.

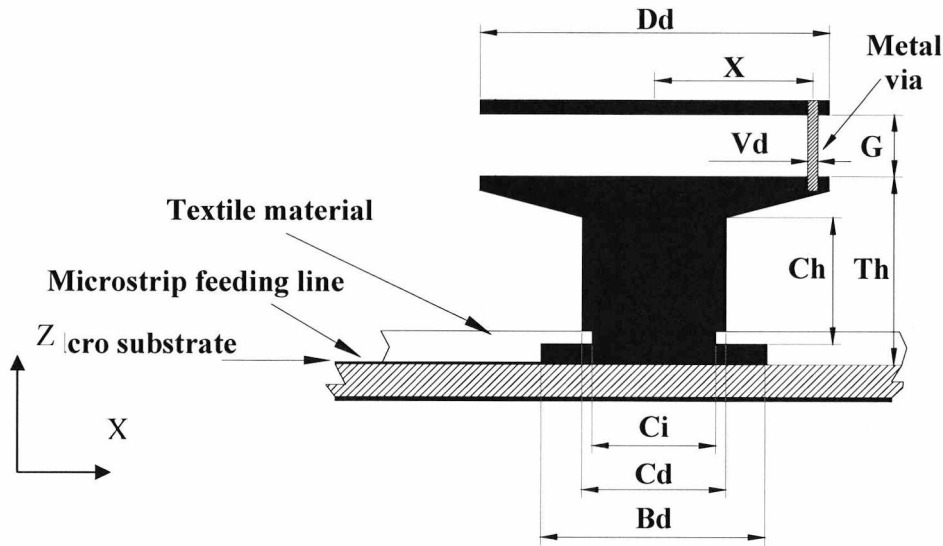


Figure 7.2. Dimension of the DBMBA standard button.

Antenna Parameters	Values	Electrical length lower band	Electrical length higher band
Disc diameter, D_d	17	0.140λ	0.311λ
Top disc diameter, D_t	17	0.140λ	0.311λ
Base diameter, B_d	11	0.090λ	0.202λ
Cylinder outer diameter, C_d	7	0.057λ	0.128λ
Cylinder inner diameter, C_i	6	0.049λ	0.110λ
Centered via diameter, V_d	0.8	0.007λ	0.015λ
Tack button height, T_h	8.5	0.070λ	0.156λ
Cylinder height, C_h	5.5	0.045λ	0.101λ
Gap between disc and button, G	3	0.025λ	0.055λ
Disc thickness, D_t	0.7	0.006λ	0.013λ
Top disc thickness, Z_t	0.7	0.006λ	0.013λ
Base thickness, B_t	1.0	0.008λ	0.018λ
Substrate height	1.8	0.015λ	0.033λ
Ground plane length	50	0.493λ	1.100λ
Ground plane width	40	0.493λ	1.100λ
Coaxial impedance, Z_p	50Ω		
Substrate material	Velcro ($\epsilon_r \sim 1.4$)		

Table 7.1 Main dimensions of the DBMBA standard button

7.2.2 DBMBA using a SMB –Measured results, S11

The simulated and measured S11 on and off body of the DBMBA standard button is shown in Figs.7.3 and 7.4. Similar to the analysis done in section 6.8.1, the computed effect of the human proximity was studied using a three-tissue human body model as in [12]. The three body layers were: a skin layer of 1mm thickness, a fat layer of 3 mm thickness and a muscle layer of 44mm thickness. The dimension of the body chose was $120 \times 120 \times 40 \text{mm}^3$. The values at the centre frequency 4 GHz of skin: $\epsilon = 38$, $\sigma = 2.34[\text{S/m}]$; fat $\epsilon = 5.1$, $\sigma = 0.18[\text{S/m}]$; muscle $\epsilon = 50.8$, $\sigma = 3[\text{S/m}]$ were obtained from [13] based on [14]. CST Microwave studio was used for the simulation of the antenna on and off body. The antenna was placed on the waist band of a pair of denim jeans which were worn by a male adult. The results were compared to the measurements obtained for the antenna in free space.

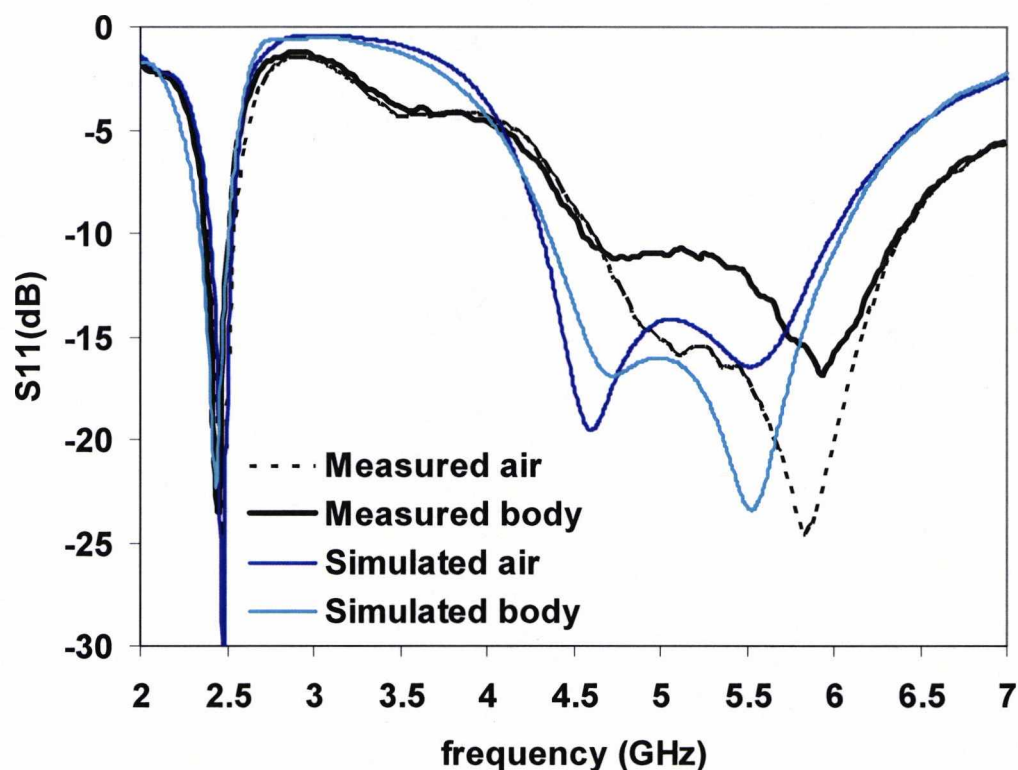


Figure 7.3. Simulated and Measured of the microstrip fed button antenna on-off body

	Low band	BW	High band	BW high
Simulated air	2400-2530	130 - 5.3%	4350-6000	1650 -31.8%
Measured air	2390-2540	150 - 6.1%	4600-6400	1800 - 32.7%
Simulated body	2350-2510	160 - 6.6%	4310-6050	1740 - 33.6%
Measured body	2370-2510	140 - 5.8%	4550-6380	1830 - 33.5%

Table 7.2 Simulated and measured S11 of the DBSMBA on/off body

Measured -10dB S11 bandwidths of the antenna on air were 6.1% and 31.8% at 2.4GHz and 5.2GHz respectively which is suitable for the Bluetooth and WLAN bands. In the case of placing the antenna on the human body waist the -10dB S11 bandwidths for the lower band (2.4 GHz) decreased to 5.8% while the higher band increased to 33.5%, sufficient to cover the WLAN bands. Simulation and measurements compared well, with the Bluetooth and WLAN bands covered in all the cases both on and off body.

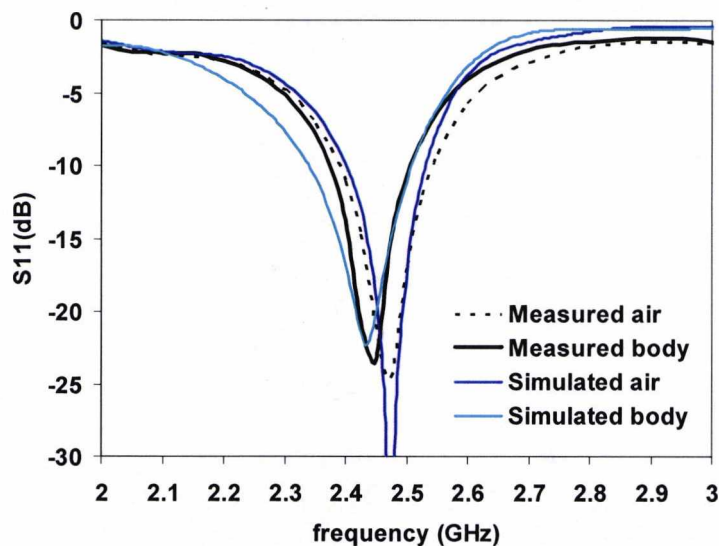


Figure.7.4 S11 Simulated and Measured S11 at the lower band of DBSMBA on-off body

7.2.3 DBMBA using a SMB – Surface Currents

Figures 7.5, 7.6 and 7.7 show the surface currents of the antenna at 2.45 GHz, 5 GHz and 5.5 GHz respectively. At 2.45 GHz there is a strong current flowing between the two parallel plates and through the via connector. At 5GHz the strong current is concentrated

in the base and middle cylinder that spreads to the edges of the top plate of the lower part of the SBMBA (single band metallic button). The current between the two top plates has decreased considerably and there is a weaker current flowing through the displaced via. At 5.5 GHz, the current concentrates mainly in the lower base and middle cylinder and very little current flows through the via connector.

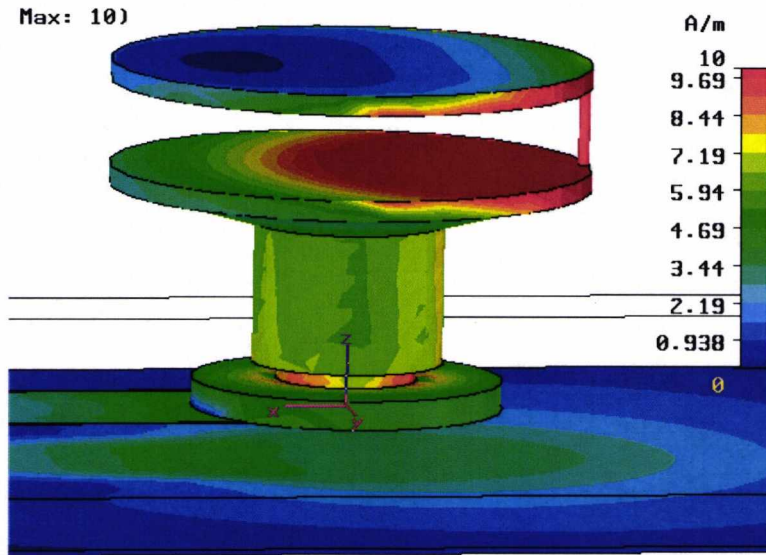


Figure 7.5 Surface currents at 2.45 GHz

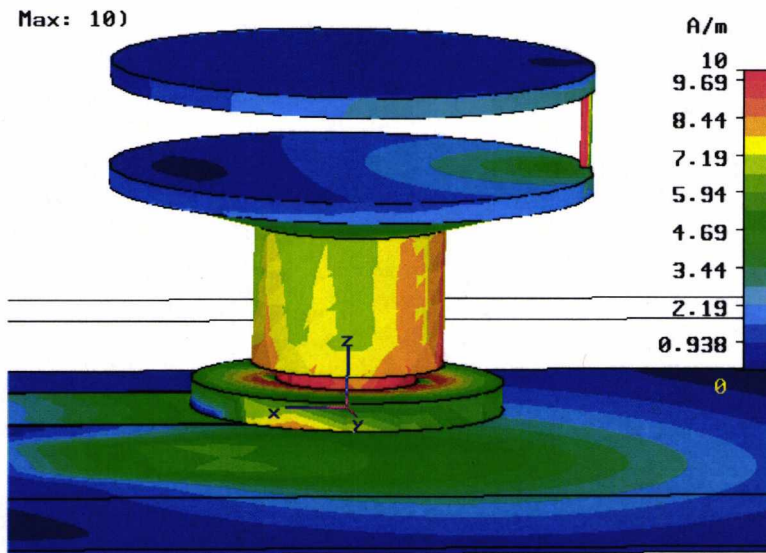


Figure 7.6 Surface currents at 5.0 GHz

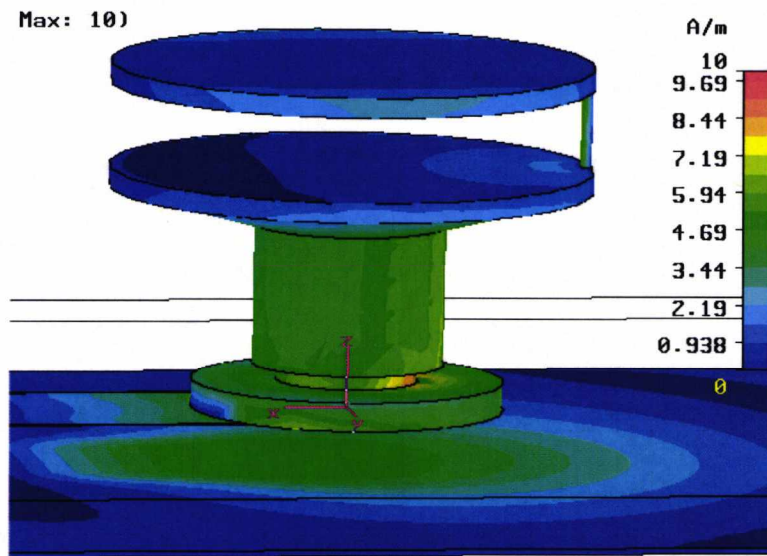


Figure 7.7 Surface currents at 5.5 GHz

7.2.4 DBMBA using a SMB – Parametric Analysis

The DBSMBA has similar characteristics to the DBMBA analyzed in chapter 6 and most of the parameters have comparable effects on the resonant frequency and bandwidth to the parametric analysis carried out in section 6.5.1., with changes in C_d , B_d , T_h and V_d having a similar response. The parameters considered for analysis for the DBSMBA are the position of the metal via connector X , the via thickness V_d and the top disc diameter D_d .

The effect of changing the position of the via connector X is shown in Fig.7.8. As can be seen from the figure, as the via position increases from the initial position at the centre of the two parallel plates, the resonant frequency of the lower band and the higher frequency band decreases. The drop in frequency for a displacement from the centre of the plates ($X=0$) to the optimal position ($X=8.3$) is of nearly 14% for the lower frequency band and 4.3% for the higher frequency band. The decrease is enough to tune the antenna at the lower frequency band from the initial 2.86GHz to the 2.46GHz that covers the Bluetooth band. Although, the lower band bandwidth decreases from 6.6% to 5.4%, it remains

sufficient to cover the WLAN systems. The higher band bandwidth increases from 26.2% to 32.6% and covers the HIPERLAN/2 band for any via position.

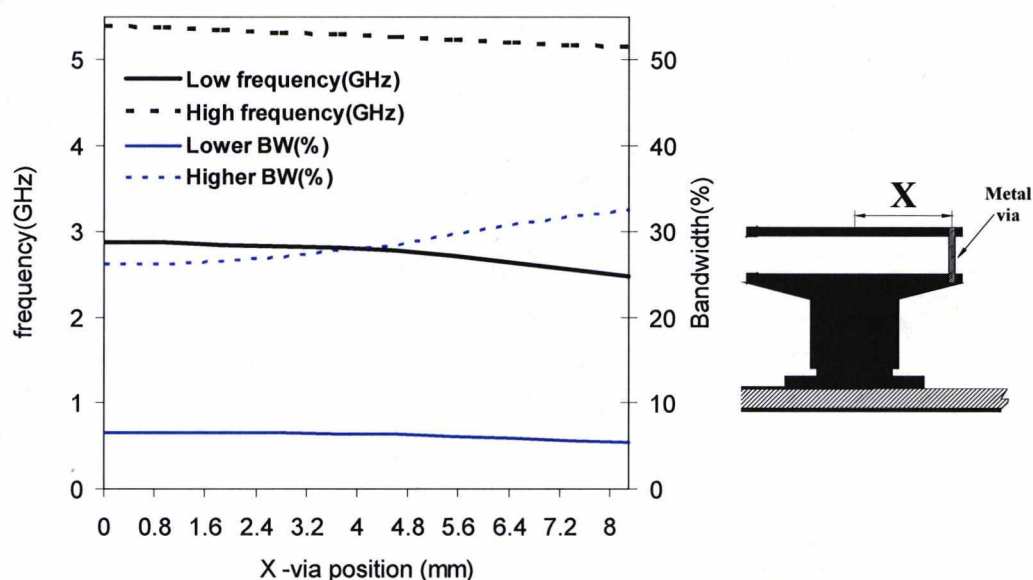


Figure 7.8 Simulated DBSMBA resonances as a function of the via position X.

Resonant frequency (black line) and bandwidth (blue line)

The effect of varying the via diameter on the resonant frequency and bandwidth is shown in Fig.7.9. To simplify the analysis, the via position has been kept at the edge of the two top metal plates Td and Dd. As can be seen from the figure, an increase in Vd between 0.3 to 1.2mm does not cause significant changes in the higher frequency (1% max) and bandwidth (1% max.) while the lower frequency (10% max) and bandwidth increase. The finding allows the lower band to be tuned while maintaining the higher frequency and higher band bandwidth for the range between 0.3 to 1.5mm. Values of Vd higher than 1.5mm cause a rapid increase in the higher resonant frequency and a dramatic decrease in the higher band bandwidth, while the lower frequency and bandwidth increase. The effect of varying Vd on the resonant frequency and bandwidth for the DBSMBA is similar to the effect of the via in the DBMBA in section 6.5.1, shown in Fig.6.23 with changes observed in the slope of the curves and higher resonant frequencies for the same via diameter.

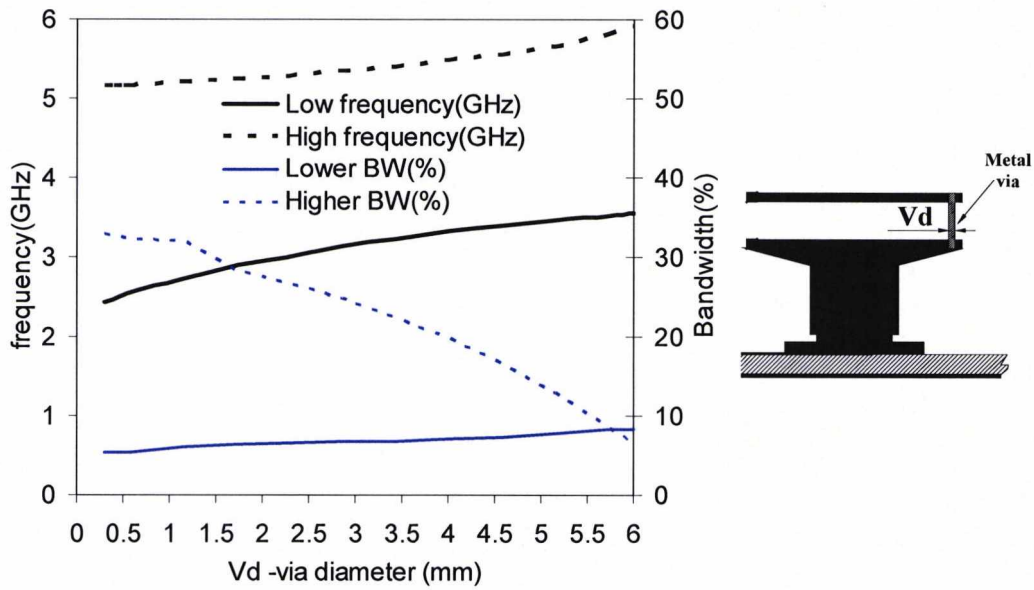


Figure 7.9 Simulated DBSMBA resonances as a function of the via diameter V_d . Resonant frequency (black line) and bandwidth (blue line)

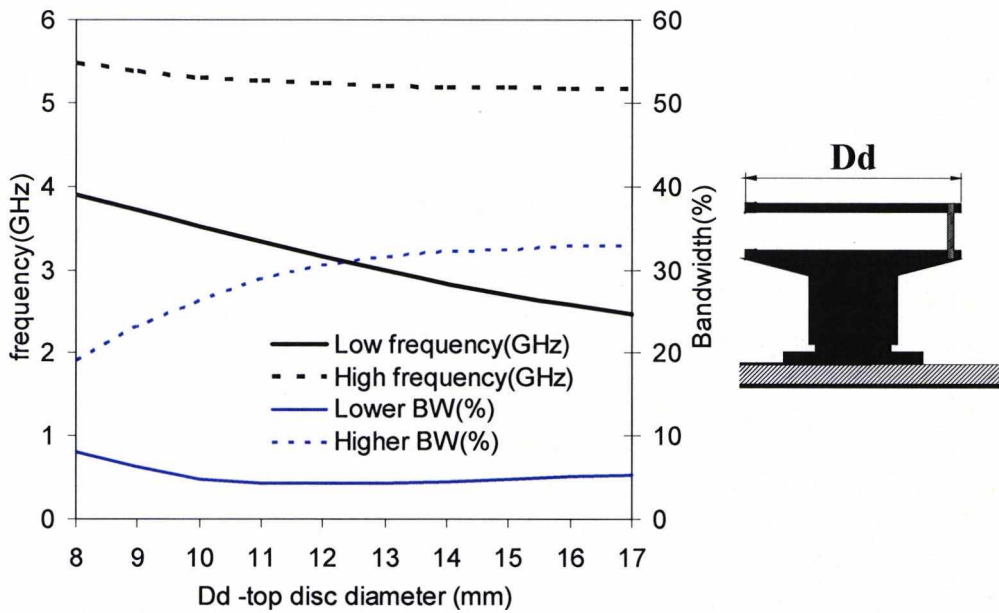


Figure 7.10 Simulated DBSMBA resonances as a function of the top disc diameter D_d . Resonant frequency (black line) and bandwidth (blue line)

Figure 7.10 shows the effect on the resonant modes of the antenna as the top disc diameter D_d is varied from 8mm to 17mm while the plate is kept connected to the via connector V_d . The optimal tuning of the antenna was found for values of D_d between

13mm to 17mm where changes in the top disc diameter D_d do not change significantly the matched higher frequency, while the lower frequency decreases.

It can be concluded from the parametric analysis carried out on the DBSMBA that the antenna offers the ability to be tuned without making it highly sensitive to small fluctuations in physical dimensions.

7.2.5 DBMBA using a SMB – Radiation Patterns

The measured radiation patterns of the DBSMBA with microstrip feed both on/off body are shown in Figs.7.11 to 7.16. The plane cutting the user's body waist shows there to be reasonable forward coverage with a centre null of around 20dB and there is a deep null in the rear direction.

The gain obtained for the DBSMBA was 1.7 dBi at 2.48 GHz, 4.1 dBi at 5.25 GHz and 4.3 at 5.5 GHz. The microstrip feeding caused high cross-polarization at the Hiperlan 2 band. However, the effect is not expected to affect the overall performance of the antenna as small antennas often have mixed polarization and the communication system normally benefits from multipath.

Placing the antenna on the human body increased the forward gain by 1dB at 2.45GHz, 0.8 dB at 5.25GHz and 0.9 dB at 5.5 GHz. Although the gain difference was not uniform in all angles, an expected decrease in the backward gain of -10dB to -20dB was observed for most of the XZ and YZ radiation patterns, while the side gain increased. The reason for the decrease in gain is the proximity of the human body which blocked any radiation through the body while it guided the waves along the body surface.

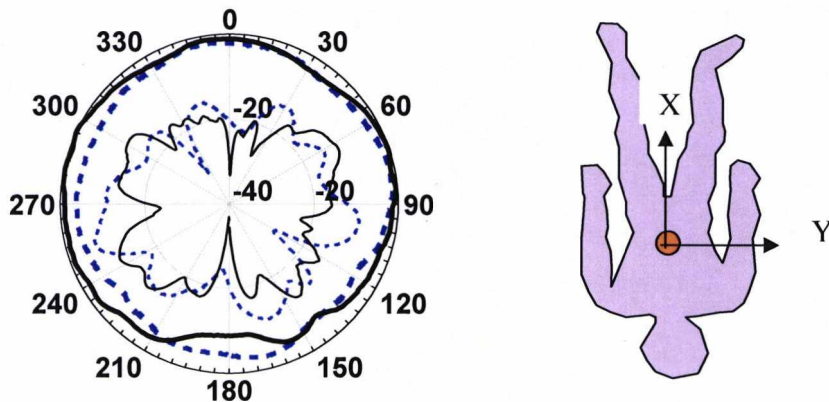


Figure 7.11 Measured far field pattern in the XY plane at 2.45GHz: Co-polar (thick line) and cross-polar (thin line). On body (continuous line), off -body (discontinuous).

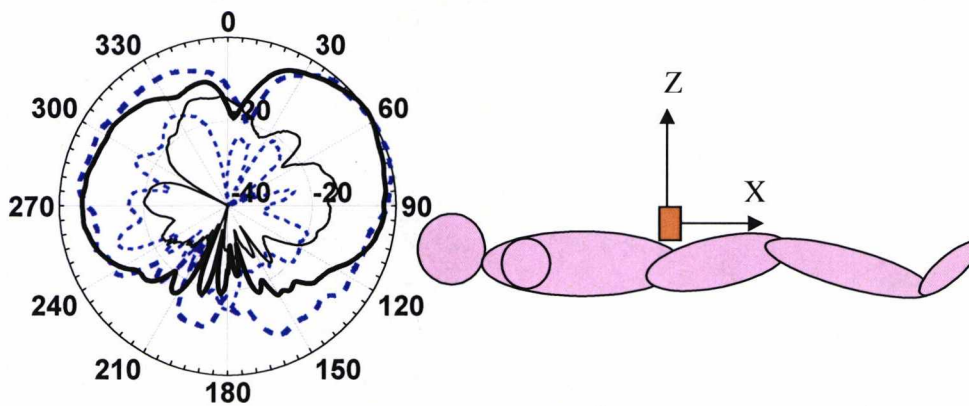


Figure 7.12 Measured far field pattern in the XZ plane at 2.45GHz. Co-polar (thick line) and cross-polar (thin line). On body (continuous line), off -body (discontinuous).

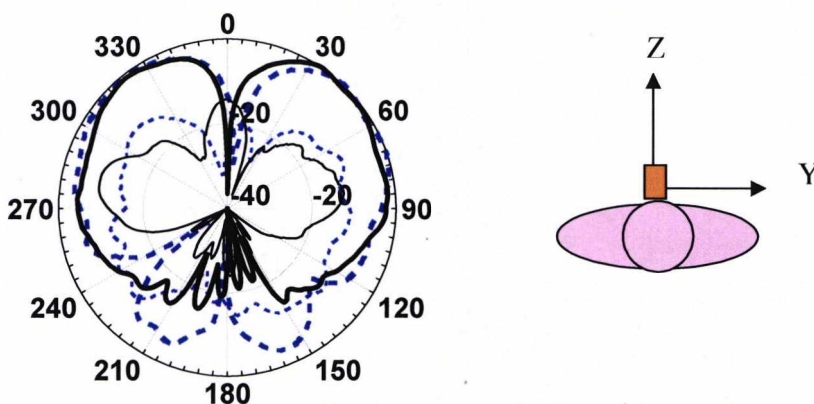


Figure 7.13 Measured far field pattern in the YZ plane at 2.45GHz: Co-polar (thick line) and cross-polar (thin line). On body (continuous line), off -body (discontinuous).

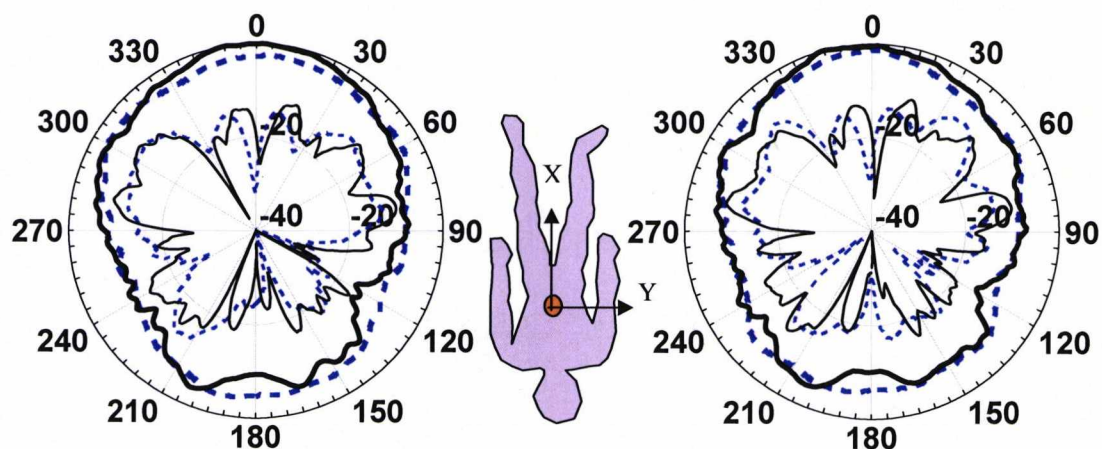


Figure 7.14 Measured far field pattern in the XY plane at 5.25 GHz(left) and 5.5GHz(right): Co-polar (thick line) and cross-polar (thin line).
On body (continuous line), off -body (discontinuous).

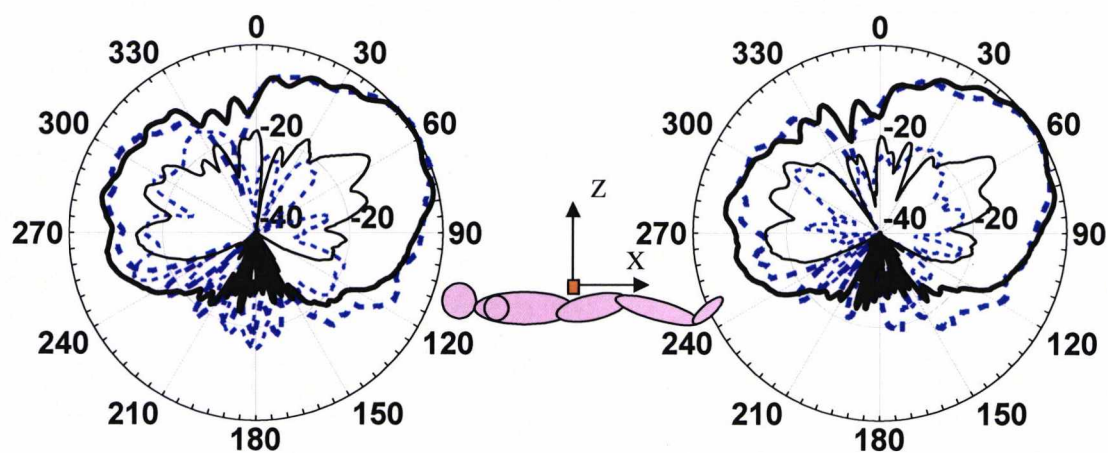


Figure 7.15 Measured far field pattern in the XZ plane at 5.25 GHz(left) and 5.5GHz(right): Co-polar (thick line) and cross-polar (thin line).
On body (continuous line), off -body (discontinuous).

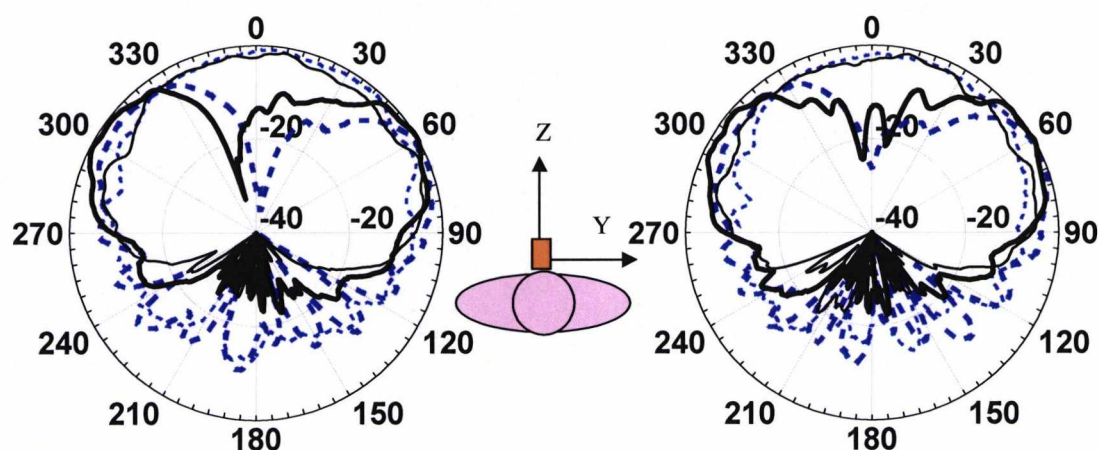


Figure 7.16 Measured far field pattern in the YZ plane at 5.25 GHz(left) and 5.5GHz(right): Co-polar (thick line) and cross-polar (thin line).
On body (continuous line), off -body (discontinuous).

7.3 Miniature Ground Shorted DBMBA

The DBMBA presented in chapter 6 and section 7.1 use an air gap and two metallic parallel plates to create the dual resonance necessary to cover the Bluetooth and Hiperlan bands. The antennas achieve small size and high rigidity while maintaining the physical appearance of denim jeans buttons. However, the use of the top metal plate and the air gap (G) made with honeycomb composite increased the height by 3mm from the size of the standard button and can cause detuning if the antenna is exposed to compression conditions. The DBMBA also needs a Velcro substrate and is attached to it with glue or another sticky material.

The antenna to be presented in this section uses different antenna miniaturization techniques to increase the rigidity of the antenna, achieve smaller size and improve the adherence to clothing. A photograph of the miniature ground shorted DBMBA with a textile material is shown in Fig.17. The antenna, also shown in Fig.7.18, uses a dielectric material between the single band structure and the top plate to increase the rigidity and achieve the lower frequency band. In addition, the top metal plate is shorted to ground to increase the matching in the lower frequency band and improve the attachment to the

clothing material. Velcro substrate has also been used for the antenna, however, other textile materials would be possible with a small re-tuning necessary.

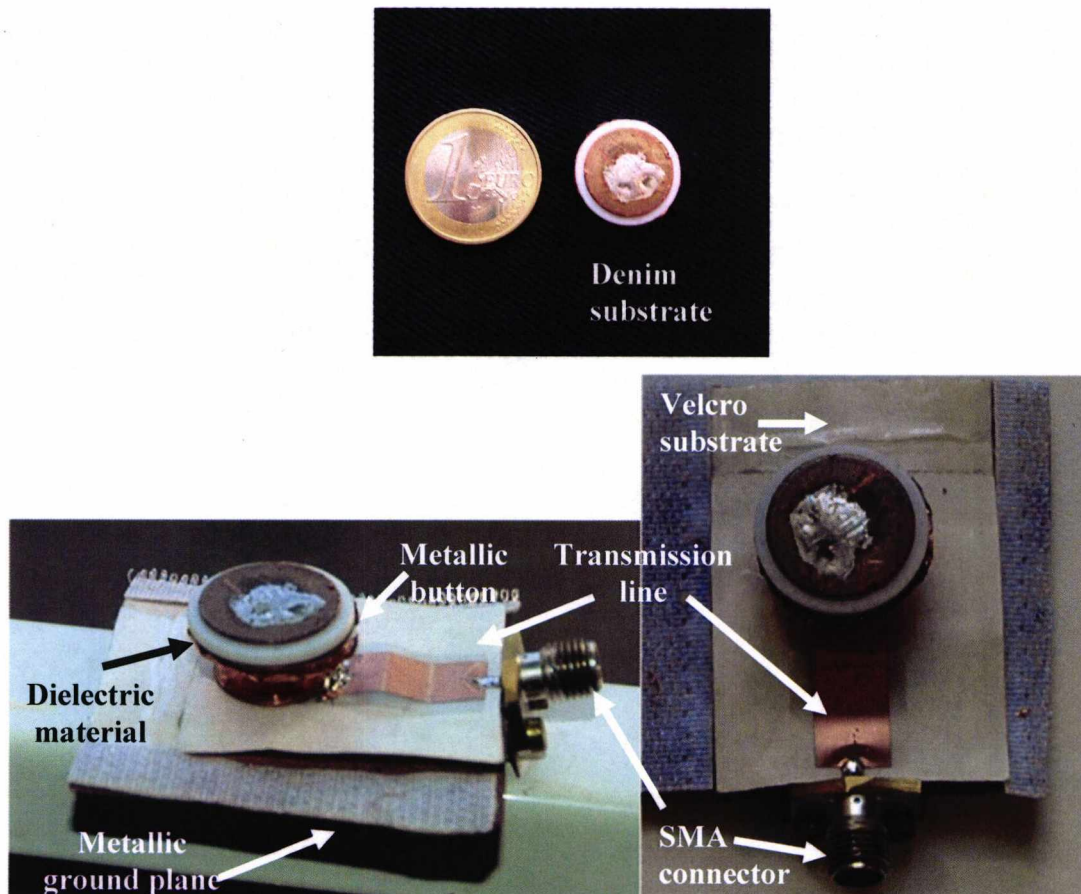


Figure 7.17 Photographs of the miniature ground-shorted DBMBA

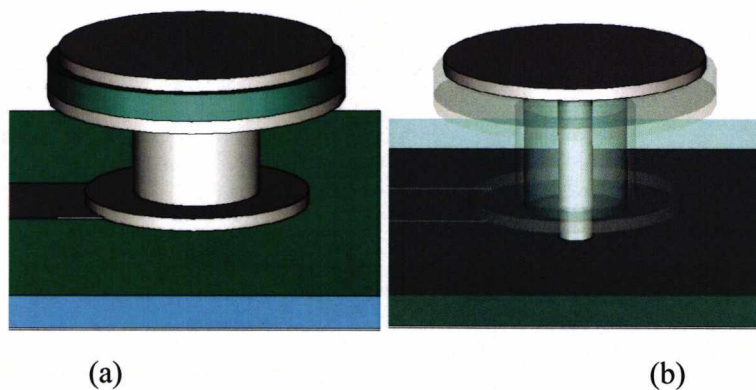


Figure 7.18 Miniature ground-shorted DBMBA structure. (a) with Velcro substrate and outer cylinder shown (b) with Velcro substrate and outer cylinder translucent to show the centre via connected to the metal ground.

7.3.1 Miniature Ground Shorted DBMBA - Dimensions

The main button dimensions are shown in Fig.7.19 and Table 7.2. The total visible height of the antenna is 7.5mm and the top disc diameter is 17mm. The antenna is made up of two main parts: a button shape cylindrical structure fed by a microstrip line and a separate top disc connected to the metal ground through a wire connection. Both parts are separated by a Teflon dielectric material with an overall size of the antenna equivalent of that of a conventional denim jeans button. The antenna is placed on a Velcro substrate and metal ground plate is placed on the other side of the Velcro material. However, due to the monopole antenna characteristics any low permittivity textile material could replace the Velcro with only a small retuning necessary.

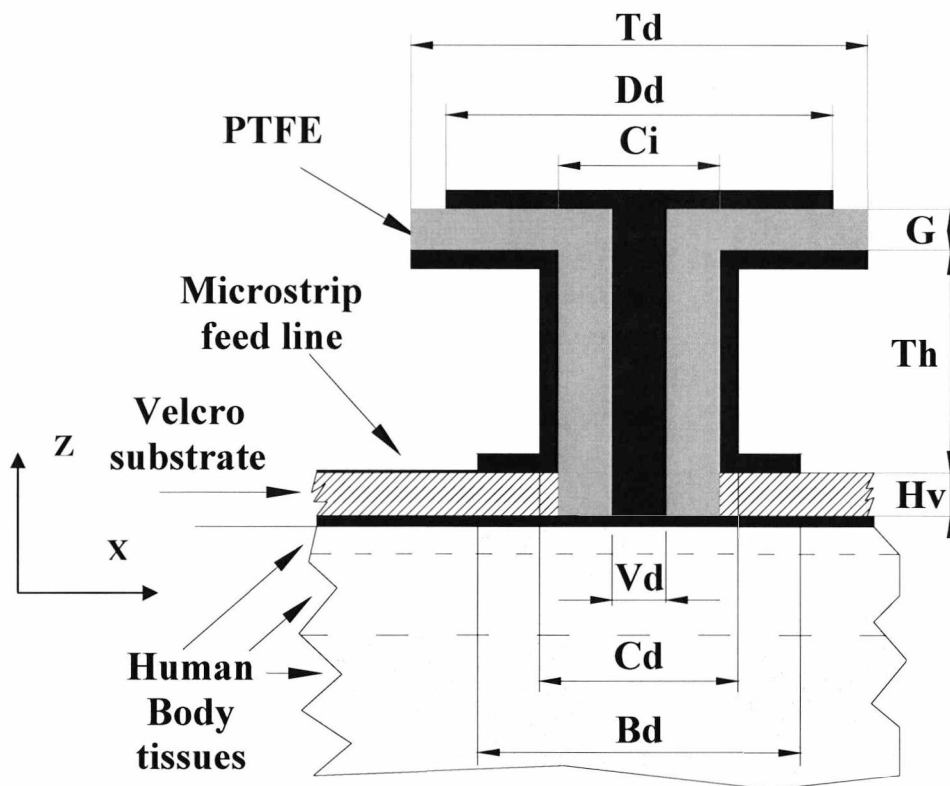


Fig. 7.19 Miniature ground-shortened DBMBA on body representation with principal dimensions

A microstrip feed line was etched in the metal cladding of a Mylar sheet and mounted on Velcro substrate. Velcro makes a convenient substrate for the transmission line as it is plastic based and flexible but is strongly resistant to compression of its height. An alternative excitation method would be to rear feed the base of the antenna using a coaxial cable which could be concealed within the lining of the garment.

Antenna Parameters	Values	Electrical length lower band	Electrical length higher band
Disc diameter, Dd	14.6	0.118 λ	0.271 λ
Top disc diameter, Td	16.4	0.133 λ	0.304 λ
Base diameter, Bd	12.4	0.101 λ	0.230 λ
Cylinder outer diameter, Do	7	0.057 λ	0.130 λ
Cylinder inner diameter, Di	6	0.049 λ	0.111 λ
Centered via diameter, Vd	2	0.016 λ	0.037 λ
lower button height, Th	7.4	0.060 λ	0.137 λ
Gap between discs, G	1.5	0.013 λ	0.028 λ
Disc thickness, Dt	0.7	0.006 λ	0.013 λ
Top disc thickness, Zt	0.7	0.006 λ	0.013 λ
Base thickness, Bt	0.7	0.006 λ	0.013 λ
Substrate height, Hv	1.8	0.015 λ	0.033 λ
Ground plane length	50	0.487 λ	1.113 λ
Ground plane width	40	0.487 λ	1.113 λ
Coaxial impedance, Zp	50 Ω		
Substrate material - Velcro	($\epsilon_r \sim 1.37$)		

Table 7.3 Main dimensions of the miniature ground-shortened DBMBA

7.3.2 Miniature Ground Shorted DBMBA - Measurement Results. S11

The simulated and measured reflection coefficient (S11) on and off body for the dual band button antenna with top disc ground connection is shown in Figs. 7.20 and 7.21 and Table 7.3. CST microwave studio was used for the computer calculation of the antenna with good agreement between simulation and measurements. Simulations were carried out initially with a Perfect Electric Conductor below the antenna and then the presence of

the human body was accounted for by including a three layer tissue representation, [6]. The measurements were carried out using an Anritsu ME7808A vector network analyzer.

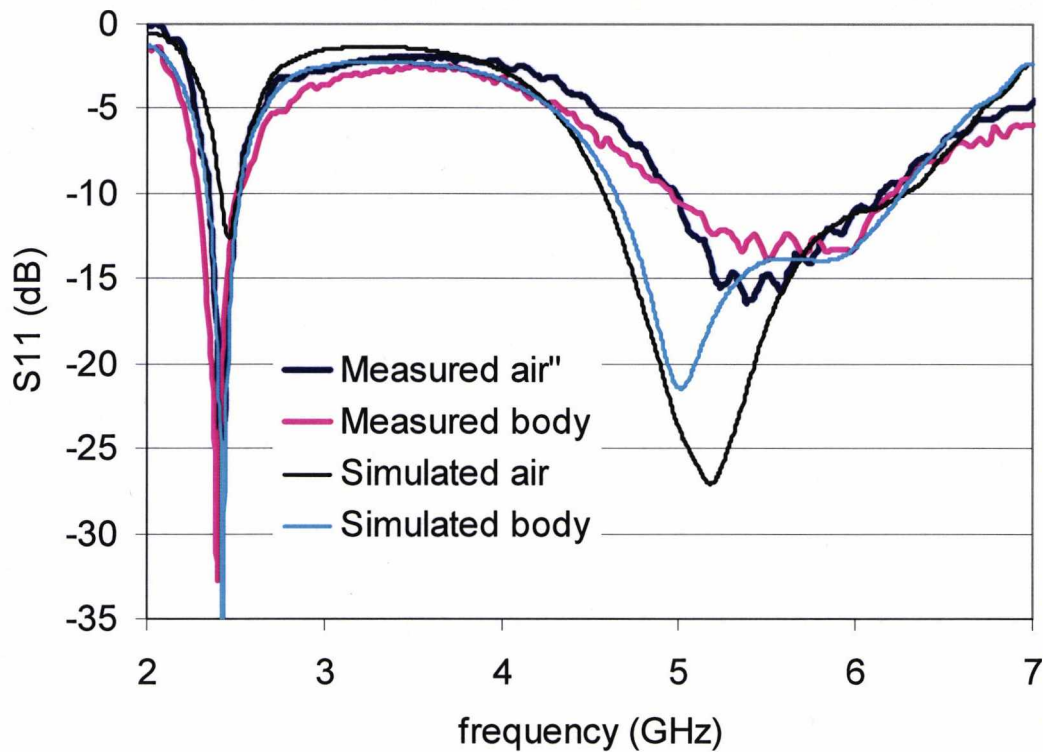


Figure 7.20. Simulated and Measured S11 of the ground shorted DBMBA

The antenna achieved -10dB impedance matching bandwidth of 6.8% at a lower 2.45GHz resonant mode and 21.1% at a higher 5.5GHz resonant mode when the antenna is in free space. In the case of the antenna placed on the body, the measured lower frequency bandwidth increased by nearly 1%, while the upper frequency band increased by 1.3%. The frequency bands achieved on and off-body are sufficient to cover the Bluetooth and WLAN bands (2.45 GHz, 5.250 GHz and 5.5 GHz).

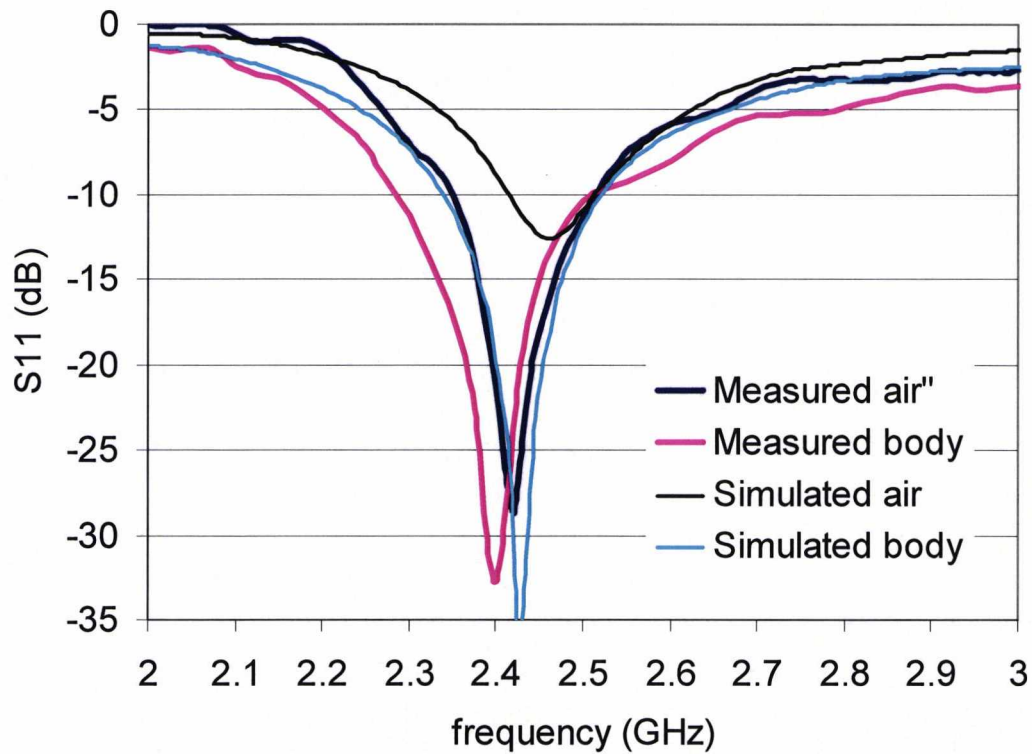


Figure 7.21. Measured and calculated S11 curves of the ground shorted DBMBA

	Low band	BW low band- %	High band	BW high band -%
Simulated air	2415-2515	100 - 4.1%	4580-6275	1695 - 31.2%
Simulated body	2340-2520	150 - 7.4%	4640-6256	1616 - 29.7%
Measured air	2350-2515	165 - 6.8%	4990-6140	1420 - 20.7%
Measured body	2300-2510	210 - 8.7%	4970-6200	1230 - 22.0%

Table 7.4 Simulated and Measured S11 of the ground shorted DBMBA

7.3.3 Miniature Ground Shorted DBMBA - Surface Currents

A simulation study of the surface currents of the antenna was carried out to determine the hot surface areas at each resonant frequency. The results are shown in Figs.7.22-7.24. As can be seen from the surface current plot, there is a high current flowing through the

centred via connection at the lower frequency band. At the higher frequency band, the surface currents seem to be stronger in the outer cylinder and main body of the antenna.

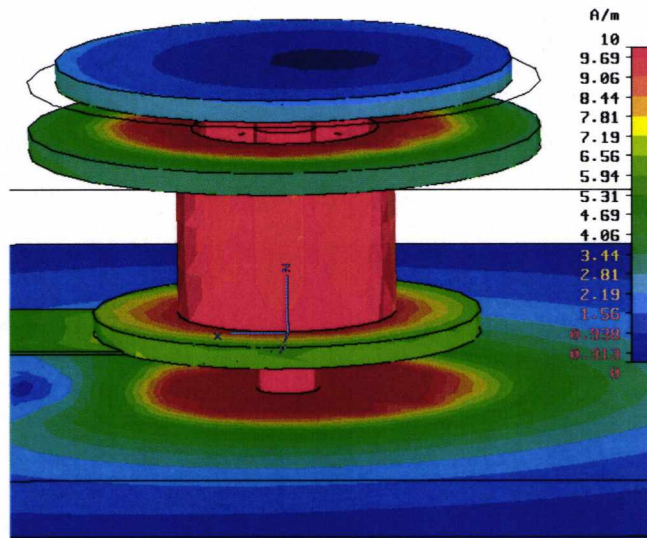


Figure 7.22 Surface currents of the ground shorted DBMBA at 2.45 GHz

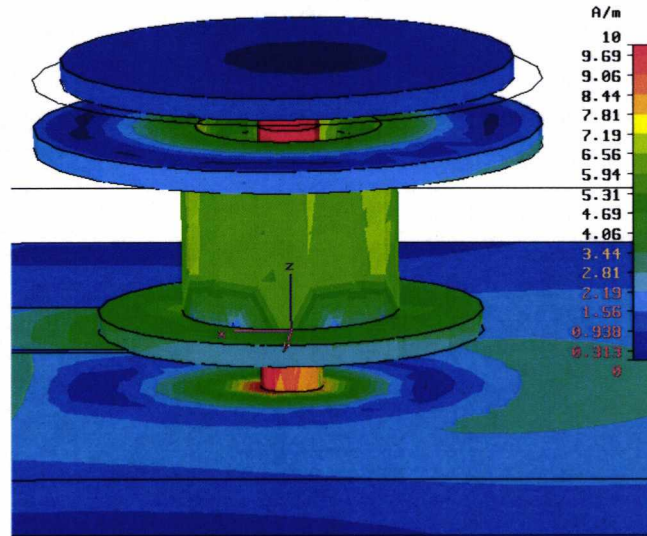


Figure 7.23 Surface currents of the ground shorted DBMBA at 5.0 GHz

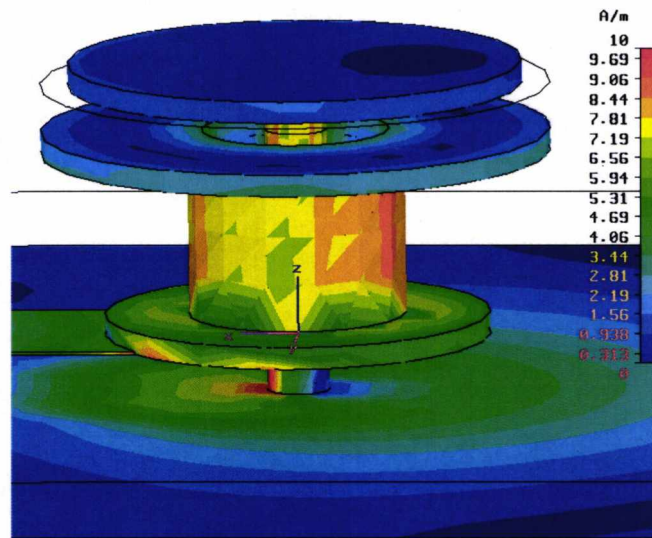


Figure 7.24 Surface currents of the ground shorted DBMBA at 5.5 GHz

7.3.4 Miniature Ground Shorted DBMBA - Parametric Analysis

A parametric analysis was carried out to determine the characteristics of the miniature ground-shortened DBMBA. The main parameters considered for the analysis were the top disc diameter D_d and T_d , the diameter of the base B_d , the diameter of the cylinder C_d , the diameter of the via connector V_d the height of the lower part of the antenna T_h and the dielectric filled gap G between the top discs D_d and T_d .

The effect of varying the top disc diameter D_d of the ground shorted DBMBA between 6mm to 18mm on the resonant frequency and bandwidth is illustrated in Fig.7.25. As can be seen from the figure, there is no lower band matching for values of D_d lower than 8mm. As the top diameter is increased further ($D_d > 8\text{mm}$), the lower frequency becomes matched while the frequency of the lower band mode decreases. The higher frequency band, however, increases its resonant frequency and bandwidth altogether. It was also observed that values of D_d higher than 14mm decrease the lower frequency bandwidth at a constant rate while the higher frequency and bandwidth increase at a lower pace. The range of values of D_d between 10mm to 14mm is optimal since the frequency of the lower band decreases while its bandwidth remains fairly constant. The value of D_d , equal

to 14.6 mm, is only 0.6mm from the optimal range and allows the antenna to resonate at the desired Bluetooth and Hiperlan bands.

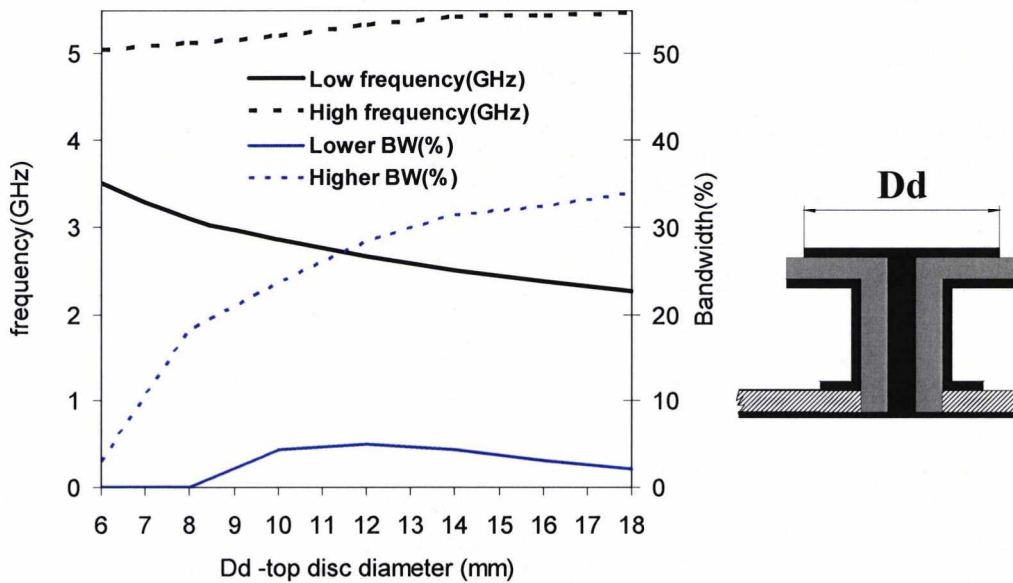


Figure 7.25 Simulated ground-shorted DBMBA resonances as a function of the top disc D_d diameter. Resonant frequency (black line) and bandwidth (blue line)

The effect of varying the lower top disc diameter T_d of the ground shorted DBMBA on the resonant frequency and bandwidth is shown in Fig.7.26. Changes in T_d between 10mm and 20mm produce a decrease in the frequency of the lower band and a marginal increase in the higher band frequency. The lower frequency bandwidth followed a wide parabolic curve with maxima at T_d of 10mm (5% bandwidth) and T_d of 20mm (4.6%) and a minimum at the centre T_d of 16mm with 3.8% bandwidth. The higher frequency bandwidth curve followed a high slope linear curve with a value of 0% at 10mm and 43.9% at 20mm. The value of T_d of 16.4mm achieves sufficient bandwidth (4.1%) at the lower band to cover the Bluetooth system and at the same time serves as a filter for frequencies above and below the working frequency. The higher band covers broadly the Hiperlan band.

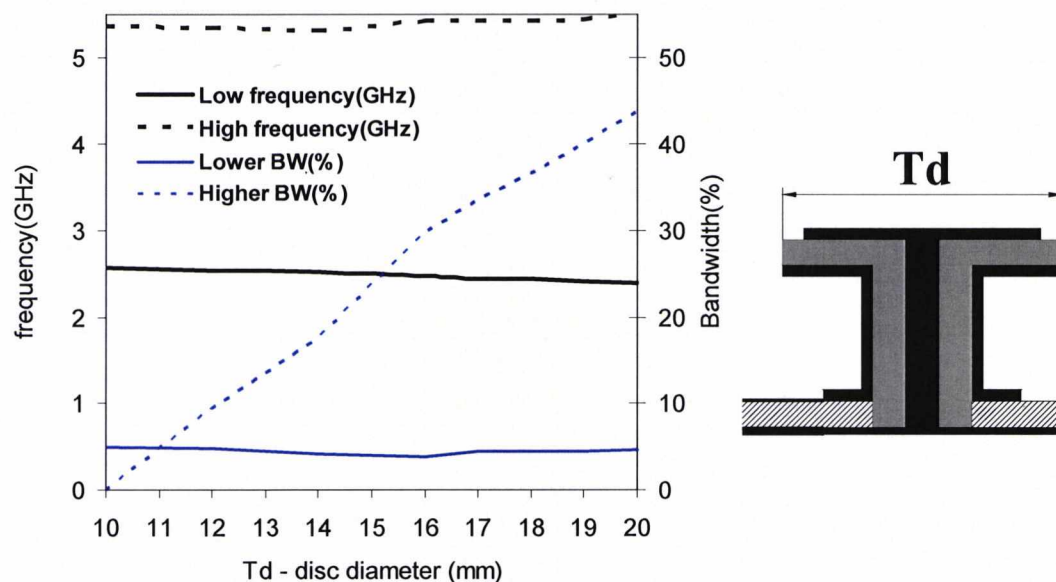


Figure 7.26 Simulated ground-shorted DBMBA resonances as a function of the top disc T_d diameter. Resonant frequency (black line) and bandwidth (blue line)

The effect of varying the diameter of the base disc B_d on the resonant frequency and bandwidth is illustrated Fig.7.27. The lower resonant frequency decreases and the higher frequency increases when B_d is increased from 7mm to 16mm. The lower frequency bandwidth followed an inverse parabolic curve with maximum at a value of B_d of 9mm with a bandwidth of 5.1% and minimum at the limits 7mm (BW= 3.7%) and 16mm (BW=2.7%) considered for the study. The higher frequency bandwidth also follows an inverse parabolic curve with a small deviation at B_d of 12mm. The higher frequency band was not matched for values of B_d lower than 7mm and achieves a second minimum at B_d of 16mm with 13.4% bandwidth. The value of B_d of 12.4mm chosen for the antenna falls within a region of wide high frequency bandwidth while maintaining sufficient lower band bandwidth.

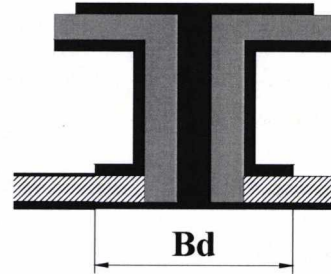
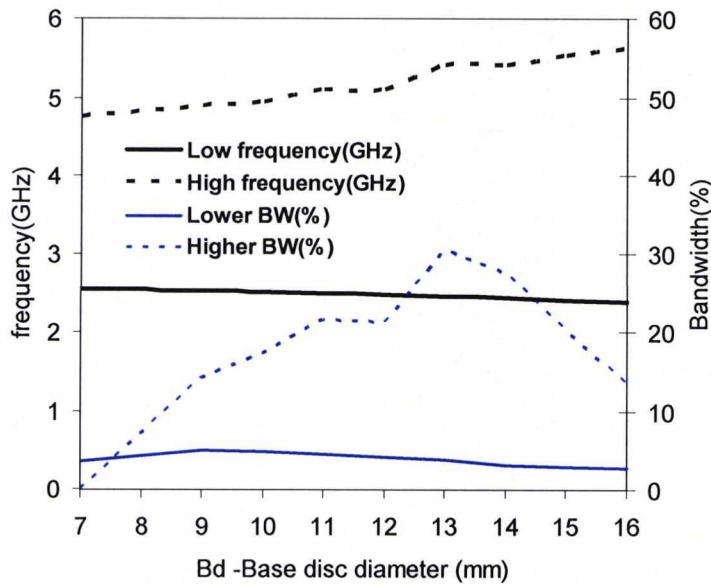


Figure 7.27 Simulated ground-shorted DBMBA resonances as a function of the top disc Dd diameter. Resonant frequency (black line) and bandwidth (blue line)

Figure 7.28 shows the effect of varying the ground shorted via diameter V_d between 0.5mm and 4mm on the resonant frequency and bandwidth. The resonant frequency increases and the higher frequency decreases (with some fluctuations) when the via diameter (V_d) is increased within the range studied. Values of V_d lower than 1.1mm did not match the lower frequency band while values of V_d greater than 3mm produced a decrease in the same band which becomes again mismatched for values of V_d greater than 4mm. The higher frequency band, however, fluctuates around a level of 30% up to a V_d of 2.5 mm. For values greater than those the bandwidth experiences a sharp decrease. The value of V_d of 2mm chosen for the antenna falls within the range of increased bandwidth at the lower band and wide bandwidth at the higher band.

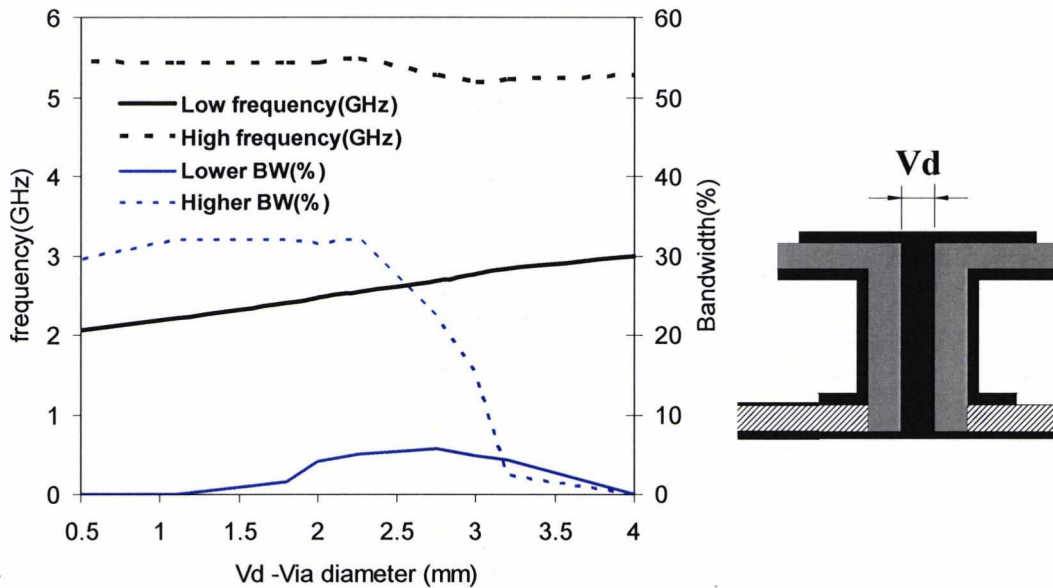


Figure 7.28 Simulated ground-shorted DBMBA resonances as a function of the V_d via diameter. Resonant frequency (black line) and bandwidth (blue line)

The effect of varying the gap (G) between the parallel plates at the top of the antenna is illustrated in Fig.7.29. For values of G considered in the study ($0.5\text{mm} < G < 5\text{mm}$), the lower frequency decreases at a constant rate while the higher frequency remains almost constant at a centre frequency of 5.44 GHz and a maximum deviation of 0.4%. No matching (-10dB) is found at the lower frequency band for values of G less than 1 mm and values of G greater than 1 mm cause an increase in the lower frequency bandwidth up to a peak of 4.9% for G of 2.5 mm. If G is increases further ($G > 2.5\text{mm}$), the lower frequency bandwidth decreases at a rate of 1% per mm(approx.). The higher frequency bandwidth decreases at an almost constant rate for the distances between discs considered for the study. However, the Hiperland/2 band target for the antennas at the higher frequency band is achieved for the values of G between 0.5mm and 5mm. This allows an independent tuning of the lower frequency band for the range considered. The value of G of 1.5mm chosen for the antenna falls within the range wide lower band bandwidth while the antenna structure maintains small physical dimensions.

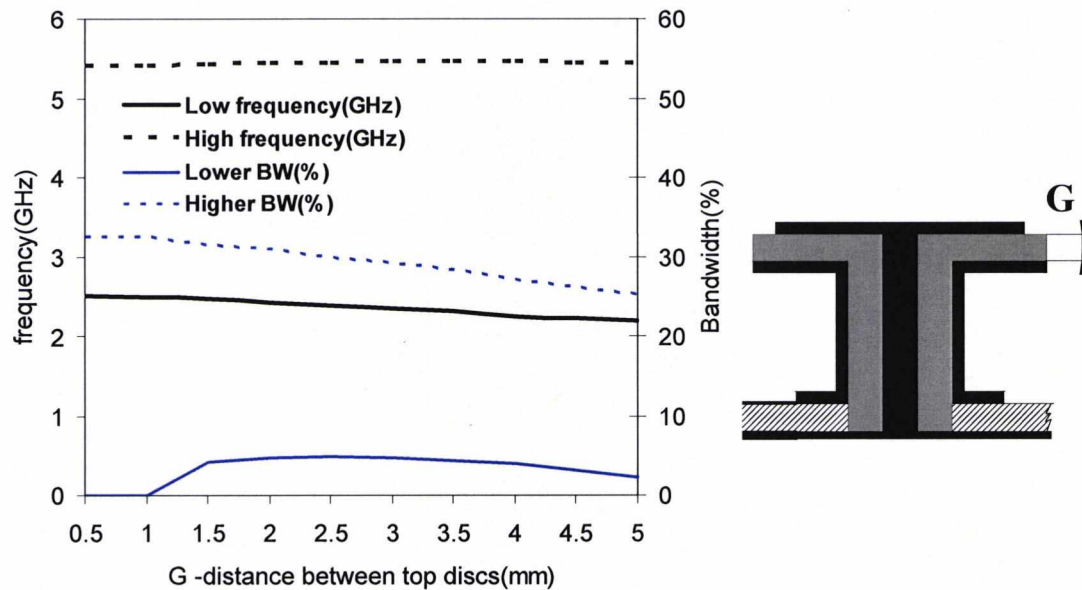


Figure 7.29 Simulated ground-shorted DBMBA resonances as a function of the G distance between top plates. Resonant frequency (black line) and bandwidth (blue line)

Figure 7.30 shows the effect of varying the height T_h of the lower part of the antenna while keeping the distance between discs G constant at 1.5 mm. As can be seen from the figure, as T_h is increased from 5 mm to 10 mm the lower frequency decreases while the higher frequency fluctuates around a centre frequency of 5.25 GHz up to T_h of 8.5 mm where the higher frequency splits in two modes, one following an increasing trend while the other one decreases. The lower frequency bandwidth increases at a nearly constant rate of 0.18% per mm for increases of T_h between 5 mm to 10 mm. The higher frequency bandwidth increases sharply up to the value of T_h of 8.5 mm when the higher frequency band splits in two modes with a declining bandwidth trend. The value of T_h of 7.4 mm falls within the range of increasing lower and higher band bandwidth conveniently achieving the bandwidth required for the WLAN bands targeted.

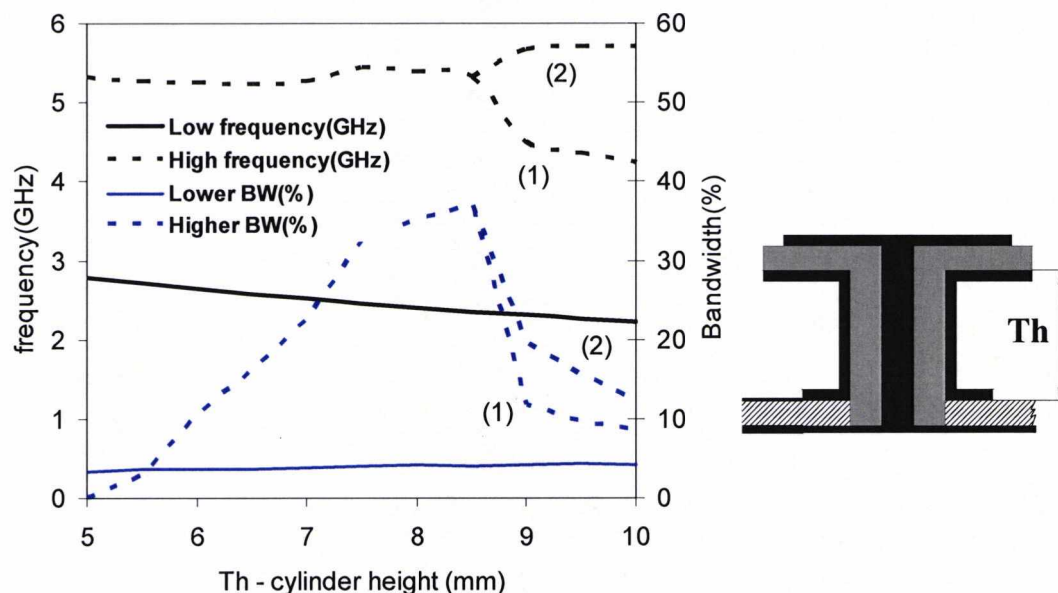


Figure 7.30 Simulated ground-shorted DBMBA resonances as a function of the Th height. Resonant frequency (black line) and bandwidth (blue line)

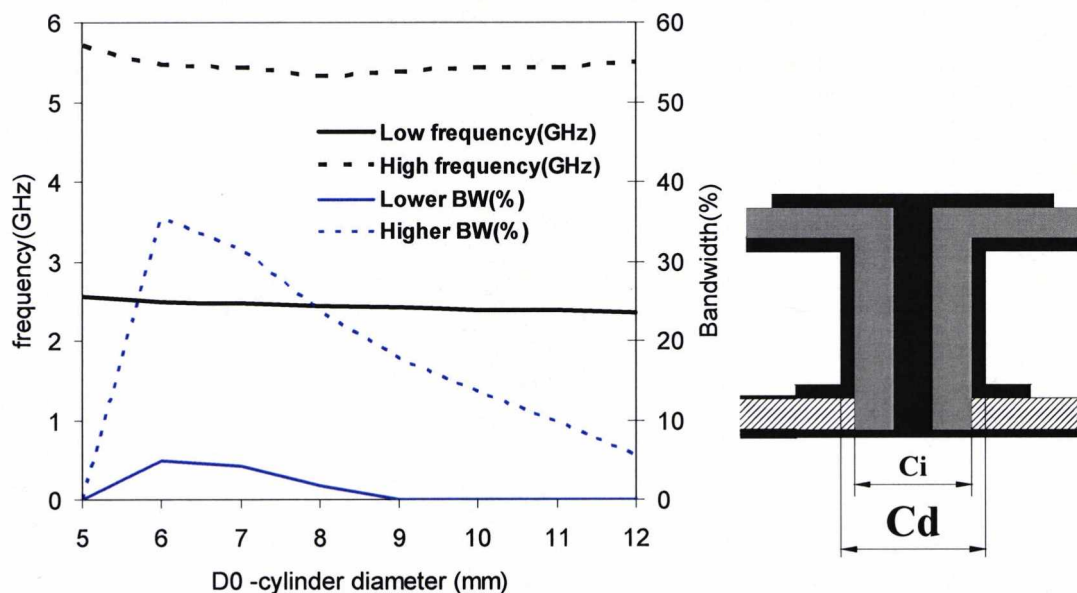


Figure 7.31 Simulated ground-shorted DBMBA resonances as a function of the Cd middle cylinder diameter. Resonant frequency (black line) and bandwidth (blue line)

Figure 7.31 shows the effect of varying the centre cylinder diameter Cd on the resonant frequency and bandwidth. As the cylinder diameter is increased from 5 mm to 12 mm,

the lower resonant frequency decreases at an almost constant rate of 30MHz per mm. However, the higher resonant frequency follows a parabolic curve with a minimum value of 5.315 GHz for D0 of 8mm and maximum values 5.697GHz for D0 of 5mm and 5.4895GHz for D0 of 12mm. The lower frequency bandwidth is only matched (-10dB) for values of D0 between 5mm and 9mm., although bandwidth level of over 4% is only achieved for values of D0 between 5.5mm and 7.2mm. The higher frequency bandwidth increases sharply from D0 of 5mm and reaches a peak of 36% for D of 6mm. For larger values of D, the higher frequency band bandwidth experiences a constant decrease.

In conclusion, the parametric analysis of the ground-shortened DBMBA has shown a higher sensitivity to variation of their principal dimension than previous DBMBA presented in chapter 6 and section 7.1. However, the lower and higher frequency bands seem to be matched (-10dB) and show sufficient bandwidth to withstand small variations which will be normally expected in mass production manufacturing.

7.3.5 Miniature Ground Shorted DBMBA - Radiation patterns

The measured radiation patterns for the ground-shortened DBMBA antenna on/off body at 2.45 GHz, 5.250 GHz and 5.500 GHz are shown in Figs.7.32-7.37. The radiation patterns were measured on an adult male and compared with the antenna in free space. The antenna was mounted as a waist height front trousers button and the two polarizations in the XY, XZ and YZ were measured. The z-axis is normal to the user's body which means that wireless connection may be made between the button antenna and other body worn devices. The plane cutting the user's waist shows there to be reasonable forward coverage with centre nulls and there is a deep null in the rear direction. The good omni-directional pattern observed in the XY plane will allow the antenna to communicate with other devices and sensors place on the body.

The gain obtained for the ground shorted DBMBA microstrip fed was 2.05dB at 2.45GHz, 3.8dB at 5.25GHz and 4.1dB at 5.5GHz. The side feeding caused the gain to be higher for the DBMBA microstrip fed at the 5GHz band as the width of the microstrip

line creates an asymmetry in the radiating structure in the XZ and YZ planes as shown in Figs. 7.36 and 7.37.

Placing the antenna on the human body increased the forward gain by 0.6dB at 2.45GHz, 0.8dB at 5.25GHz and 1 dB at 5.5GHz. However, the gain difference was not uniform in all the angles and while there was a decrease in backward gain when the antenna was placed on the body, the gain increased in both sides (90 and 270 in XZ and YZ planes) of the human body.

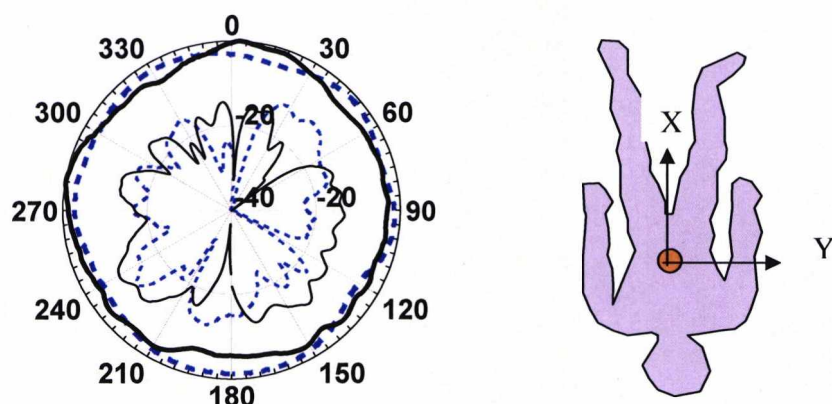


Figure 7.32 Measured far field pattern in the XY plane at 2.45GHz: Co-polar (thick line) and cross-polar (thin line). On body (continuous line), off-body (discontinuous).

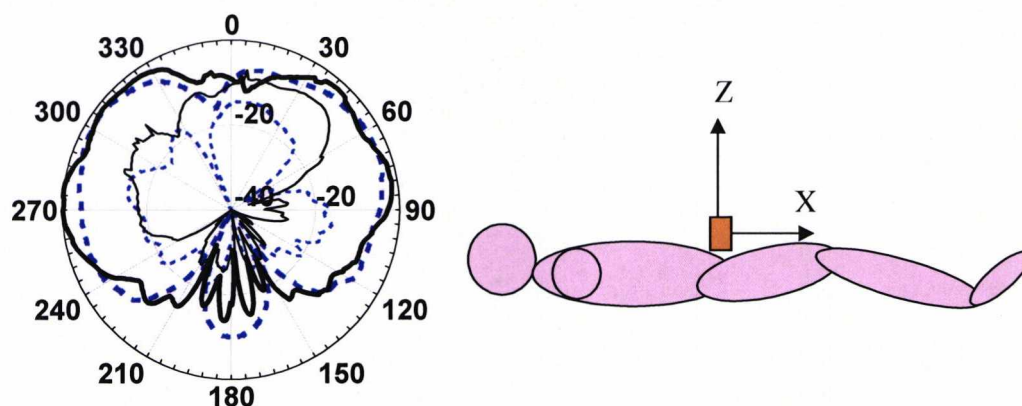


Figure 7.33 Measured far field pattern in the XZ plane at 2.45GHz: Co-polar (thick line) and cross-polar (thin line). On body (continuous line), off-body (discontinuous).

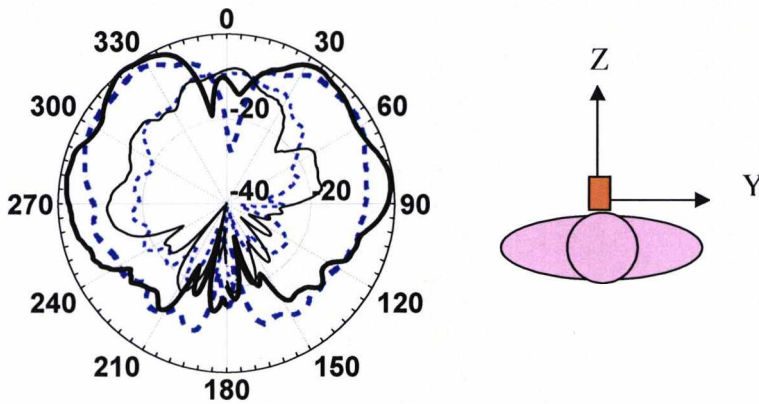


Figure 7.34 Measured far field pattern in the YZ plane at 2.45GHz: Co-polar (thick line) and cross-polar (thin line). On body (continuous line), off-body (discontinuous).

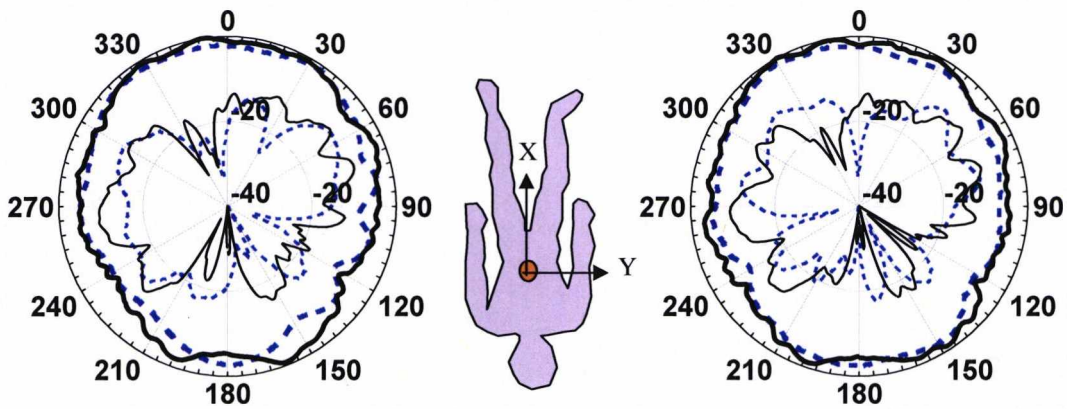


Figure 7.35 Measured far field pattern in the XY plane at 5.25 GHz(left) and 5.5GHz(right): Co-polar (thick line) and cross-polar (thin line). On body (continuous line), off-body (discontinuous).

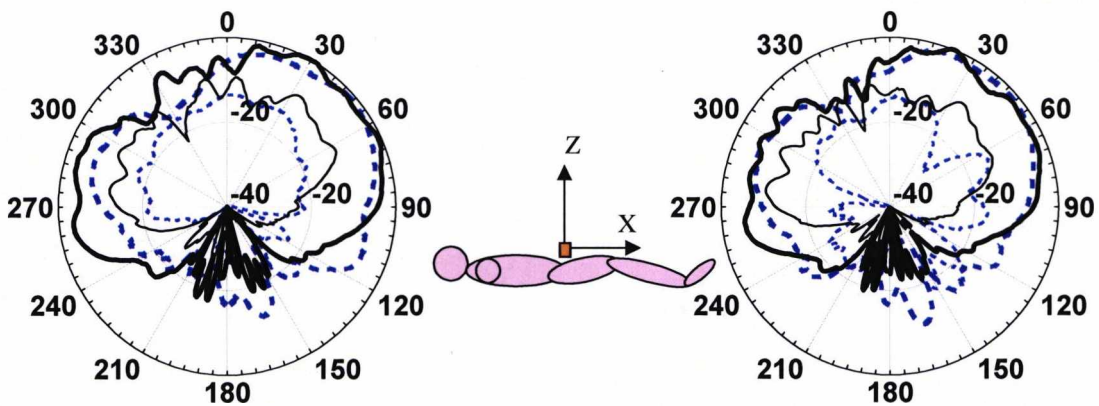


Figure 7.36 Measured far field pattern in the XZ plane at 5.25 GHz(left) and 5.5GHz(right): Co-polar (thick line) and cross-polar (thin line). On body (continuous line), off-body (discontinuous).

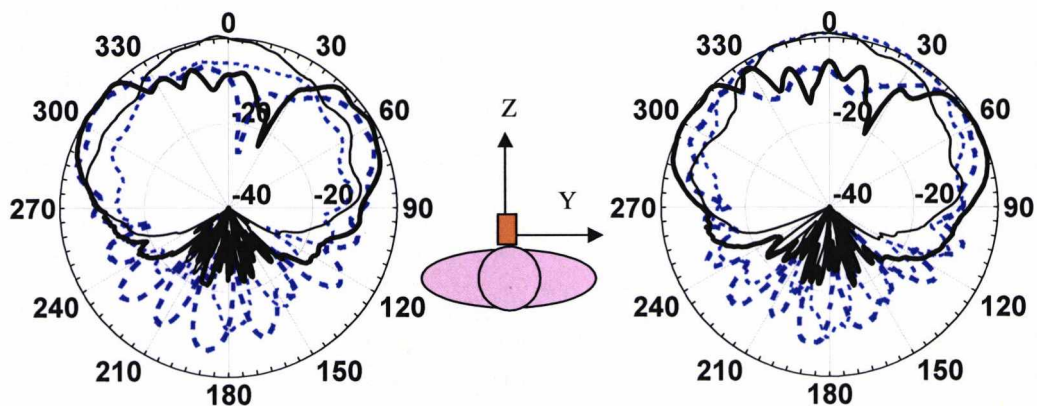


Figure 7.37 Measured far field pattern in the YZ plane at 5.25 GHz(left) and 5.5GHz(right): Co-polar (thick line) and cross-polar (thin line). On body (continuous line), off-body (discontinuous).

7.4 Summary of Button antennas

A summary of the button antennas developed in chapter 6 and 7 is shown in Table 5. The disc diameter and the button height of the antenna have been the dimensions of interest in the study. As can be seen from the table, a single band button structure of 16mm diameter and 8.5mm height with a coaxial feeding achieves the hiperlan/2 band with a bandwidth of over 45.6% and a gain of 3.8dBi. The dual band wearable button antenna with dual disc and centre via and coaxial feeding is 3.1mm higher than the single button structure and achieves the Bluetooth and Hiperlan/2 bands with 12% and 35% (-10dB) bandwidth respectively. The gain for this first dual band antenna was 2.2dBi for the lower band and 3.6dBi for the higher band. A dual band button structure with microstrip feeding had 17mm top disc diameter and was 11.7mm height. The bandwidth for this dual and structure off body was 6.3% (low band) and 7.9% (high band) lower than the antennas with coaxial feeding. The bandwidth of the antenna mounted on the body increased by 0.1% at the lower band while it decreased by 6.9% at the higher frequency band. The gain of the antenna off body was similar to the antenna with coaxial feeding with 2.18dBi at the lower band and 3.5dBi at the higher band. In the case of mounting the antenna on the human body, the gain decreased by 0.52 dB and 1 dB at the lower and higher band respectively.


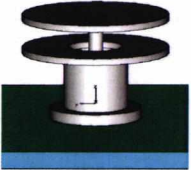
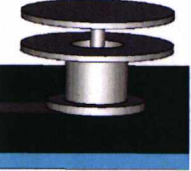
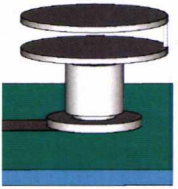
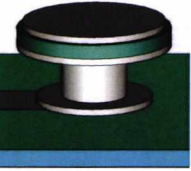
Antenna	SIZE Button (mm)	S11- Off body		S11- On body		Gain- Off body		Gain-On body	
		Low band BW	High band BW	Low band BW	High band BW	Low band BW	High band BW	Low band BW	High band BW
Single band 	16 x 8.5	-----	45.6%	-----	-----	-----	3.8dB	-----	-----
Dual band button 	16 x 11.6	12.0%	35%	-----	-----	2.2dB	3.6dB	-----	-----
Dual band button microstrip (1) 	17 x 11.7	5.7%	27.1%	5.8%	20.2%	2.18dB	3.5dB	2.6dB	4.5dB
Dual band button microstrip (2) 	17 x 12.1	6.1 %	32.7%	6.4%	33.5%	1.7dB	4.1dB	2.7dB	5.0dB
Compact dual band button 	17 x 9.6	6.8%	20.7%	8.7%	22.0%	2.05dB	3.8dB	2.6dB	4.6dB

Table 5. Summary of wearable button antennas

The dual band antenna using standard metallic button structure with microstrip feeding was 0.3mm higher than the antenna with centre via. However, it achieved 0.4% and 5.6% wider bandwidths than the first antenna with microstrip feeding. The gain of the antenna off body was 1.7dBi and 4.1Bi at the lower and higher band respectively. The gain of the antenna on the human body increased by 1.0dB and 0.9dB at the lower and higher frequency bands.

Finally, the miniature, ground shorted metallic button structure is 2 mm smaller than the best dual band metallic button structure previously developed. The antenna achieves 6.8% and 20.7% bandwidth at the lower and higher frequency bands respectively. The gain of the antenna off body was 2.05dBi and 3.8dBi at the lower and higher frequency bands. In the case of placing the antenna on the human body, the gain of the antenna increased by 0.55dB and 0.8dB at the lower and higher frequency bands.

7.5 Conclusions

Two dual band button antennas have been presented in chapter 7. The first antenna evolves from the DBMBA antenna presented in chapter 6 and uses a simple denim jeans trouser button, a top metal disc and via connector to create a very simple dual band metallic button antenna. The antenna was fed by a microstrip line and achieves good omni-directional patterns in the XY plane which is desirable for communication with other body worn devices.

The second antenna presented in this chapter is the miniature ground shorted DBMBA which is a miniaturized and optimized version of the DBMBA. The antenna uses two crucial miniaturization techniques: the addition of dielectric material between the two resonant plates and the ground shorting of the top disc. The antenna achieves significant reduction in size while keeping its electrical performance. In addition, the antenna achieves higher rigidity which is desirable for everyday on body usage. Good omnidirectional pattern in the XY plane was also observed for the miniature ground shorted DBMBA when the antenna was placed on the human body waist or in free space.

References:

- [1] www.gsmworld.com
- [2] Hsiao-Hwa Chen , Mohsen Guizani , “Next Generation Wireless Systems and Networks”, Chapter 3, pp.120, John Wiley & Sons, Inc, 2006
- [3] K. Fujimoto and J.R. James, Mobile Antenna Systems Handbook., Norwood, MA: Artech House, 1994
- [4] Constantine A.Balanis “Antenna Theory”, Chapter 10, pp. 509 John Wiley&Sons, 1982
- [5] John D. Kraus, Ronald J. Marhefka, “Antennas”, McGraw-Hill Publishing Co.
- [6] R. King, C. Harrison, and D. Denton, “Transmission-line missile antennas," *IRE Trans. on Antennas and Propagation*, vol. 8, pp. 88-90, January 1960. -- Ballanis
- [7] T.Tagar, “Analysis of planar inverted-F antennas and antenna design for portable radio equipment”in K.Hirasawa and M. Haneishi, eds., Analysis, Design and Measurement of Small and Low-Profile Antennas, Artech House, Norwood, MA, 1992, pp. 161-180
- [8] Zi Dong Liu; Hall, P.S.; Wake, D, “Dual-frequency planar inverted-F antenna”, *IEEE Transactions on Antennas and Propagation*, Volume 45, Issue 10, Oct. 1997, Page(s):1451 - 1458
- [9] Rowell, C.R., Murch, R.D., “A capacitively loaded PIFA for compact mobile telephone handsets”, *IEEE Transactions on Antennas and Propagation*, Volume 45, Issue 5, May 1997 Page(s):837 - 842
- [10] Di Nallo, C.; Faraone, A.,” Multiband internal antenna for mobile phones”, *Electronics Letters* , Volume 41, Issue 9, 28 April 2005 Page(s):514 – 515
- [11] www.antenova.com
- [12] Maciej Klemm, Istvan Z. Kovacs, Gert F. Pedersen, Gerhard Tröster , “Novel Small-Size Directional Antenna for UWB WBAN/WPAN Applications”, , *IEEE Transactions on Antennas and Propagation* , vol.53, issue 12, Dec. 2005, pages: 3883-3896;
- [13] <http://niremf.ifac.cnr.it/tissprop/htmlclie/htmlclie.htm> .*ITALIAN NATIONAL RESEARCH COUNCIL Institute for Applied Physics "Nello Carrara" - Florence*
- [14] C. Gabriel, “Compilation of the dielectric properties of body tissues at RF and microwave frequencies, ”, *AL/OE-TR-1996-0037 Rep., Jun.1996.*

Chapter 8.

Conclusions and Future Work

The research presented has investigated techniques and methodologies employed when designing antennas for wireless communication systems. It has also introduced new multiband antennas for wireless indoor communications and wearable transceivers. Many mobile communications systems have been introduced over the last few years; such as UMTS, Bluetooth, Hiperlan and UWB systems. These new communication systems aim to provide the transmission of large amounts of digital data employed in multimedia applications. The systems are so called “always on” with access to information “any time, any where“ which is also driving the telecommunications sector in recent years.

Single antennas are being required to operate at many frequency bands and cover different technologies. In addition, there is an ongoing trend to miniaturize antennas and make devices unobtrusive which can be easily carried or even be embedded on

everyday clothing. Both trends, multiband and wearable antennas, have been covered in the present research work.

This chapter concludes the doctor of Philosophy thesis on “Compact antennas for wireless communications” and looks at future work on multiband and wearable antennas.

8.1 Electromagnetic Simulators

Before the 1990's electromagnetic simulators used by scientists and antenna engineers were mostly written in house and for a specific application. Simulations used to be time consuming and highly costly and were limited to the academic community. The development and expansion of existing commercial electromagnetic software in the 1990's such as ANSOFT's Ensemble and HFSS, Zealand Software's IE3D, HP EEsof's ADS and the introduction of CST microwave studio has facilitated the design of antennas and other microwave related components.

The three main mathematical methods dominant in the commercial electromagnetic software market for antenna applications are: Method of Moments, Finite Element Method (FEM) and Finite-Difference Time-Domain (FDTD).

Method of Moments (MoM) is a numerical computational method of solving linear partial differential equations which have been formulated as integral equations. It examines the eddy currents flowing through a metal interconnect such as an antenna, then looks at the radiation fields these surface currents create and determines their impact on adjacent fields.

The finite element method (FEM) is used for finding approximate solution of Partial Differential Equations (PDE) and integral equations. The solution approach is based either on eliminating the differential equation completely (steady state problems), or rendering the PDE into an equivalent ordinary differential equation, which is then solved using standard techniques such as finite differences.

Finite-Difference Time-Domain (FDTD) is a time-domain method which belongs to the general class of differential time-domain numerical modeling methods. Maxwell's equations (in partial differential form) are modified to central-difference equations, discretized, and implemented in software. The electric field is solved at a given

instant in time, then the magnetic field is solved at the next instant in time, and the process is repeated over and over again.

Two different computational software packages have been used to calculate the antennas developed for the present research:

- Zealand Software's IE3D which is based on the method of moments and is ideal for the multiband planar or semi-planar structures in chapters 4 and 5.
- Computer Simulation Technology's CST MICROWAVE studio software is general purpose software that uses Finite Integration Technique (FIT) which is similar to the Finite Difference Time Domain Technique (FDTD). This software has been used to calculate the 3D wearable antennas presented in chapters 6 and 7 with good agreement between calculation and measurements.

8.2 Multiband Antennas for Indoor Communication Systems

Chapters 4 and 5 have studied multiband antennas for wireless indoor communications.

Chapter 4 focused on 3D multiband antennas made up of planar elements which use the planar inverted F antenna (PIFA) concept. Starting from a dual band PIFA developed at the University of Kent operating at the GSM900 and DCS1800 bands, a new parasitic resonator was introduced in the ground plane to create two new resonant modes at the higher band and allow the antenna to cover the DCS, DECT and UMTS bands. The new multiband antenna was further enhanced by adding two extra side resonators, resulting in one additional mode at the higher band which increases the bandwidth of the novel multiband antenna. The addition of this new mode allows the coverage of the 2.4GHz Bluetooth band. The size of the antenna was reduced further by relocating the side elements and extending the ground plane to the side of the antenna. The final 3D antenna in chapter 4 achieves the GSM900, DCS 1800, DECT, UMTS and Bluetooth bands and offers good quality radiation patterns at all bands.

In Chapter 5, the first antenna with the parasitic element developed in chapter 4 was transposed to a planar form. The transposition is explained in detail and it is shown that the resulting antenna had similar modes to the original 3D antenna but the modes were cancelling each other, resulting in poor S11 matching. The problem was solved

by folding a section of the antenna, producing a smaller size structure and creating a path for the currents to add together. The novel planar PIFA, however, had balancing problems when fed by a coaxial feeding, which were more pronounced at the lower frequency band. A novel solution was applied to the balancing problem by duplicating the metallic pattern on the other side of an FR4 substrate. The result was a good match at the lower, middle and higher frequency bands for any coaxial cable length and cable curvature. The final dual layer planar PIFA antenna was able to cover the GSM900, DCS1800, DECT, UMTS, Bluetooth and Hiperlan bands with good quality radiation patterns.

8.3 Multiband Antennas for Wearable Applications

Chapters 6 and 7 have studied wearable antenna designs for WLAN on body applications.

Chapter 6 began a study the electrical characteristics of a metallic button structure when is fed by a coaxial feed line. It was found that a standard denim jeans button was resonant at the 5GHz ISM band. A novel wearable antenna was later designed by adding a second top loaded monopole and a centred wire which connects to the base of a hollow metallic button structure. The novel antenna achieved operation at the 2.4GHz and 5.25 GHz ISM bands with radiation patterns of a monopole antenna on a small ground plane. A small redesign was necessary to feed the antenna with a microstrip line which is ideal for on body measurements. The antenna with the microstrip feeding was simulated on a 3 layer tissue model of a human body and later compared with the measurements, finding that the antenna maintains its bandwidth matching in both cases isolated and on body. On body radiation patterns were measured and compared to the antenna isolated and on the human body with the expected increase in the forward gain and decrease in the backward gain.

In chapter 6, two new metallic button antennas were presented. The first metallic button structure is similar to the one presented in chapter 5 but with the via connection off-set from the centre of the antenna. This allowed the use of a standard, solid metallic button structure with an added a top metallic plate and via connector to achieve the 2.45GHz and 5.25GHz WLAN bands. The second metallic button

structure achieved smaller size and higher rigidity by adding dielectric material and shorting the centre plate to ground. The two novel metallic button antennas performed well when in isolation and on body with good quality radiation patterns at both bands. A final table in chapter 6 compares all the wearable antennas developed for the present research.

8.4 Future Work on Multiband and Wearable Antennas

Multiband antennas are widely used these days in mobile communication systems. Some of the early challenges encountered when developing multiband and wideband antennas have been overcome with the help of new, more powerful electromagnetic software packages. At present, the main difficulty found by antenna engineers is the integration of the antennas with more circuitry around them (ie, speakers, cameras). There is also an increasing interest in developing antennas with multiple feeding for different frequencies and in MIMO antennas where many antennas are closed to each other to achieve higher throughput and range for the same bandwidth. In addition, several standards are attracting strong interest in recent years, such as ultrawideband and WIMAX systems. All this technologies and the decrease in price for millimetre wave components will drive the developments of wideband and multiband antennas in the next few years.

Wearable electronics are seen as the next step on the integration of electronics into our everyday life. There are already jackets in the market with plug and volume control for MP3 players and even trainers that can send information about speed to a handheld device. The trend of wearable electronics and computing is also driving the research and development of antennas suitable for these applications. Antennas based on metallic button structures are attractive for these applications as they can direct waves across the surface of the body to other worn devices. There is a good scope for future research work on the interaction and communication between wearable antennas and antennas in portable devices placed in different parts on the body. There is also potential for creating antenna arrays based on button structures with improved feeding transmission lines. The study of the antennas on flexible ground plane and mesh ground planes will also provide useful information for future on-body

communication networks. In addition, ultrawideband metallic button antennas and the propagation of short pulse on the human body offer a good prospect for future work in the field of wearable antennas.

Chapter 8.

Conclusions and Future Work

The research presented has investigated techniques and methodologies employed when designing antennas for wireless communication systems. It has also introduced new multiband antennas for wireless indoor communications and wearable transceivers. Many mobile communications systems have been introduced over the last few years; such as UMTS, Bluetooth, Hiperlan and UWB systems. These new communication systems aim to provide the transmission of large amounts of digital data employed in multimedia applications. The systems are so called “always on” with access to information “any time, any where“ which is also driving the telecommunications sector in recent years.

Single antennas are being required to operate at many frequency bands and cover different technologies. In addition, there is an ongoing trend to miniaturize antennas and make devices unobtrusive which can be easily carried or even be embedded on

everyday clothing. Both trends, multiband and wearable antennas, have been covered in the present research work.

This chapter concludes the doctor of Philosophy thesis on “Compact antennas for wireless communications” and looks at future work on multiband and wearable antennas.

8.1 Electromagnetic Simulators

Before the 1990's electromagnetic simulators used by scientists and antenna engineers were mostly written in house and for a specific application. Simulations used to be time consuming and highly costly and were limited to the academic community. The development and expansion of existing commercial electromagnetic software in the 1990's such as ANSOFT's Ensemble and HFSS, Zealand Software's IE3D, HP EEsof's ADS and the introduction of CST microwave studio has facilitated the design of antennas and other microwave related components.

The three main mathematical methods dominant in the commercial electromagnetic software market for antenna applications are: Method of Moments, Finite Element Method (FEM) and Finite-Difference Time-Domain (FDTD).

Method of Moments (MoM) is a numerical computational method of solving linear partial differential equations which have been formulated as integral equations. It examines the eddy currents flowing through a metal interconnect such as an antenna, then looks at the radiation fields these surface currents create and determines their impact on adjacent fields.

The finite element method (FEM) is used for finding approximate solution of Partial Differential Equations (PDE) and integral equations. The solution approach is based either on eliminating the differential equation completely (steady state problems), or rendering the PDE into an equivalent ordinary differential equation, which is then solved using standard techniques such as finite differences.

Finite-Difference Time-Domain (FDTD) is a time-domain method which belongs to the general class of differential time-domain numerical modeling methods. Maxwell's equations (in partial differential form) are modified to central-difference equations, discretized, and implemented in software. The electric field is solved at a given

instant in time, then the magnetic field is solved at the next instant in time, and the process is repeated over and over again.

Two different computational software packages have been used to calculate the antennas developed for the present research:

- Zealand Software's IE3D which is based on the method of moments and is ideal for the multiband planar or semi-planar structures in chapters 4 and 5.
- Computer Simulation Technology's CST MICROWAVE studio software is general purpose software that uses Finite Integration Technique (FIT) which is similar to the Finite Difference Time Domain Technique (FDTD). This software has been used to calculate the 3D wearable antennas presented in chapters 6 and 7 with good agreement between calculation and measurements.

8.2 Multiband Antennas for Indoor Communication Systems

Chapters 4 and 5 have studied multiband antennas for wireless indoor communications.

Chapter 4 focused on 3D multiband antennas made up of planar elements which use the planar inverted F antenna (PIFA) concept. Starting from a dual band PIFA developed at the University of Kent operating at the GSM900 and DCS1800 bands, a new parasitic resonator was introduced in the ground plane to create two new resonant modes at the higher band and allow the antenna to cover the DCS, DECT and UMTS bands. The new multiband antenna was further enhanced by adding two extra side resonators, resulting in one additional mode at the higher band which increases the bandwidth of the novel multiband antenna. The addition of this new mode allows the coverage of the 2.4GHz Bluetooth band. The size of the antenna was reduced further by relocating the side elements and extending the ground plane to the side of the antenna. The final 3D antenna in chapter 4 achieves the GSM900, DCS 1800, DECT, UMTS and Bluetooth bands and offers good quality radiation patterns at all bands.

In Chapter 5, the first antenna with the parasitic element developed in chapter 4 was transposed to a planar form. The transposition is explained in detail and it is shown that the resulting antenna had similar modes to the original 3D antenna but the modes were cancelling each other, resulting in poor S11 matching. The problem was solved

by folding a section of the antenna, producing a smaller size structure and creating a path for the currents to add together. The novel planar PIFA, however, had balancing problems when fed by a coaxial feeding, which were more pronounced at the lower frequency band. A novel solution was applied to the balancing problem by duplicating the metallic pattern on the other side of an FR4 substrate. The result was a good match at the lower, middle and higher frequency bands for any coaxial cable length and cable curvature. The final dual layer planar PIFA antenna was able to cover the GSM900, DCS1800, DECT, UMTS, Bluetooth and Hiperlan bands with good quality radiation patterns.

8.3 Multiband Antennas for Wearable Applications

Chapters 6 and 7 have studied wearable antenna designs for WLAN on body applications.

Chapter 6 began a study the electrical characteristics of a metallic button structure when is fed by a coaxial feed line. It was found that a standard denim jeans button was resonant at the 5GHz ISM band. A novel wearable antenna was later designed by adding a second top loaded monopole and a centred wire which connects to the base of a hollow metallic button structure. The novel antenna achieved operation at the 2.4GHz and 5.25 GHz ISM bands with radiation patterns of a monopole antenna on a small ground plane. A small redesign was necessary to feed the antenna with a microstrip line which is ideal for on body measurements. The antenna with the microstrip feeding was simulated on a 3 layer tissue model of a human body and later compared with the measurements, finding that the antenna maintains its bandwidth matching in both cases isolated and on body. On body radiation patterns were measured and compared to the antenna isolated and on the human body with the expected increase in the forward gain and decrease in the backward gain.

In chapter 6, two new metallic button antennas were presented. The first metallic button structure is similar to the one presented in chapter 5 but with the via connection off-set from the centre of the antenna. This allowed the use of a standard, solid metallic button structure with an added a top metallic plate and via connector to achieve the 2.45GHz and 5.25GHz WLAN bands. The second metallic button

structure achieved smaller size and higher rigidity by adding dielectric material and shorting the centre plate to ground. The two novel metallic button antennas performed well when in isolation and on body with good quality radiation patterns at both bands. A final table in chapter 6 compares all the wearable antennas developed for the present research.

8.4 Future Work on Multiband and Wearable Antennas

Multiband antennas are widely used these days in mobile communication systems. Some of the early challenges encountered when developing multiband and wideband antennas have been overcome with the help of new, more powerful electromagnetic software packages. At present, the main difficulty found by antenna engineers is the integration of the antennas with more circuitry around them (ie, speakers, cameras). There is also an increasing interest in developing antennas with multiple feeding for different frequencies and in MIMO antennas where many antennas are placed close to each other to achieve higher throughput and range for the same bandwidth. In addition, several standards are attracting strong interest in recent years, such as ultrawideband and WIMAX systems. All these technologies and the decrease in price for millimetre wave components will drive the developments of wideband and multiband antennas in the next few years.

Wearable electronics are seen as the next step on the integration of electronics into our everyday life. There are already jackets in the market with plug and volume control for MP3 players and even trainers that can send information about speed to a handheld device. The trend of wearable electronics and computing is also driving the research and development of antennas suitable for these applications. Antennas based on metallic button structures are attractive for these applications as they can direct waves across the surface of the body to other worn devices. There is a good scope for future research work on the interaction and communication between wearable antennas and antennas in portable devices placed in different parts on the body. There is also potential for creating antenna arrays based on button structures with improved feeding transmission lines. The study of the antennas on flexible ground plane and mesh ground planes will also provide useful information for future on-body

communication networks. In addition, ultrawideband metallic button antennas and the propagation of short pulse on the human body offer a good prospect for future work in the field of wearable antennas.

